A one-dimensional quantum gas with tunable interactions

Dissertation
by

Elmar Haller

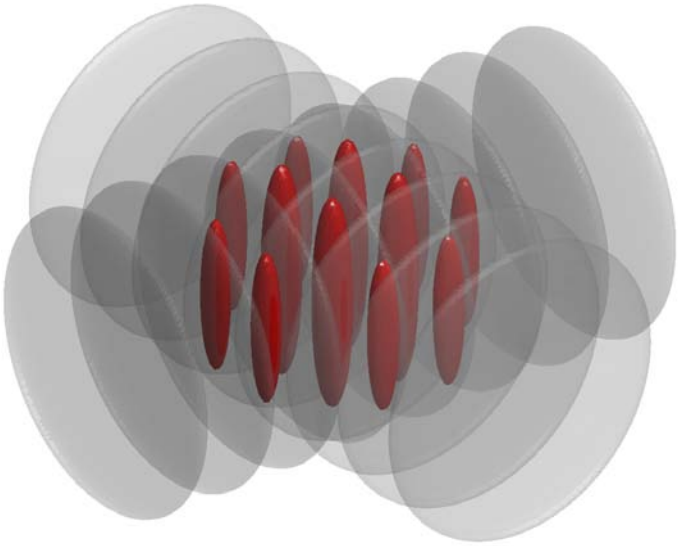

submitted to
the Faculty of Mathematics, Computer Science and Physics
of the University of Innsbruck

Advisor: a. Univ. Prof. Dr. Hanns-Christoph Nägerl

Innsbruck, July 2010

Abstract

Many-body quantum systems with strong interactions give rise to some of the most intriguing phenomena in physics. This is especially true when the system's dimensionality is reduced and when quantum correlations dominate the system's behavior. Ultracold atoms in optical lattices present a model system to study many-body physics. They offer control over almost all system parameters, they provide clean external potentials and they allow for a direct detection process. In particular, ultracold atoms in optical lattice potentials permit the study of quantum physics in low-dimensional geometry.

This thesis presents a series of experiments that study a quantum gas of strongly interacting cesium atoms in one-dimensional (1D) geometry. We employ optical lattice potentials to confine a Bose-Einstein condensate to an array of 1D tubes. Within each tube the confining potential "freezes out" any transversal motion of the particles, and thus creates a quasi 1D system. Furthermore, the confinement strongly affects the atomic scattering process along the tubes, giving rise to a new type of scattering resonance, called confinement induced resonance (CIR). We observe CIRs by an increase in particle loss and heating. They allow us to tune interparticle interactions in 1D geometry and to access regimes with strong particle correlations.

For increasing interactions we access the regimes of a non-interacting gas, the 1D Thomas Fermi regime and we approach the limit of a Tonks-Girardeau (TG) gas, i.e. a gas of impenetrable bosons. Quickly crossing a CIR preserves and even strengthens the correlations of the many-body state from one side of the resonance to the other. As a result an excited, strongly-correlated phase is formed, called the super Tonks-Girardeau (STG) gas, which is metastable despite strong attractive interactions. The interaction regimes and the existence of the STG phase are verified by observing characteristic changes in hydrodynamic properties of the gas.

We add a shallow lattice potential along the axis of the 1D systems and drive a phase transition from a TG gas to a Mott insulator. For commensurate density, i.e. for an average density of one atom per lattice site, and for sufficiently large repulsive interactions an arbitrarily small periodic perturbation "pins" the atoms immediately. This so-called "pinning transition" is driven by tuning interactions. We observe the appearance of an energy gap in the excitation spectrum and a change in the transport properties of the gas. The complete phase diagram of the Mott insulator transition is determined all the way from vanishingly small lattice depth to the tight binding regime. As a result, we connect the physics of two important models of condensed-matter physics, the Bose-Hubbard model and the sine-Gordon model.

Zusammenfassung

Quantenmechanische Vielteilchensysteme mit starker Teilchenwechselwirkung zeigen erstaunliche Effekte. Besonders deutlich wird dies in Systemen mit reduzierter räumlicher Dimensionalität und in Systemen deren Eigenschaften stark von Teilchenkorrelationen dominiert werden. Ultrakalte Atome in optischen Gittern bilden ein ideales Testsystem, um diese Effekte der Vielteilchenphysik zu untersuchen. Fast jeder Parameter kann hier frei gewählt werden. Sie ermöglichen komplexe, externe Potentiale, und sie erlauben einen direkten Detektionsprozess der Atome. Insbesondere ermöglichen sie es, quantenmechanische Effekte in niedrigen Dimensionen zu untersuchen.

Diese Arbeit diskutiert eine Reihe von Experimenten zu eindimensionalen (1D) Quantengasen aus stark wechselwirkenden Cäsium Atomen. Die eindimensionalen Systeme werden dabei mit Hilfe eines optischen Gitters erzeugt, das die Atome entlang eines röhrenförmigen Potentials einschließt und die transversale Bewegung der Teilchen komplett "ausfriert". Wir transferieren ein Bose-Einstein Kondensat in diese Anordnung aus 1D Fallen und untersuchen die atomaren Streuprozesse innerhalb der 1D Systeme. Der starke Einschluss modifiziert dabei die Wechselwirkung zwischen den Atomen und möglicht uns über die Beobachtung von Teilchenverlusten und Heizeffekten den Nachweis einer sogenannten Einschlussresonanz. Diese Resonanz kann dazu verwendet werden, die Wechselwirkung der Teilchen zu kontrollieren und stark korrelierte Systeme zu erzeugen.

Wir untersuchen die hydrodynamischen Eigenschaften eindimensionaler Quantengase mit unterschiedlich starker Wechselwirkung. Für repulsive Wechselwirkung werde drei Regime beobachtet: nicht wechselwirkende Teilchen, das von Wechselwirkungen dominierte Thomas-Fermi Regime und im Grenzfall starker Wechselwirkung das sogenannte Tonks-Girardeau Gas. Ein schneller Wechsel von repulsiver zu attraktiver Wechselwirkung mit Hilfe der Einschlussresonanz erzeugt einen angeregten, stark korrelierten Zustand. Dieser sogenannte super Tonks-Girardeau Zustand ist trotz starker attraktiver Wechselwirkung zwischen den Teilchen metastabil.

Ein zusätzliches schwaches optisches Gitter ermöglicht uns, einen Phasenübergang vom Tonks-Girardeau Gas zu einem Mott Isolator zu untersuchen. Stimmt der mittlere Abstand der Atome mit dem Gitterabstand überein, reicht ein beliebig schwaches Gitterpotential, um die Atome zu lokalisieren. Wir treiben diesen sogenannten „Pinning-Übergang" mit Hilfe der Wechselwirkung und weisen den Mott Isolator Zustand über eine Energielücke im Anregungssprektrum und über das Transportverhalten der Atome nach. Wir bestimmen das komplette Phasendiagram des Mott Isolator Übergangs von schwachen zu tiefen Gitterpotentialen und verbinden somit zwei wichtige Modelle der Physik der kondensierten Materie, das Bose-Hubbard Model und das sine-Gordon Model.

CONTENTS

CHAPTER 1

INTRODUCTION

> *"... Place a penny on the middle of one of your tables in space; and leaning over it, look down upon it. It will appear a circle. But now, drawing back to the edge of the table, gradually lower your eye - thus bringing yourself more and more into the condition of the inhabitants of Flatland - and you will find the penny becoming more and more oval to your view, and at last ... the penny will then have ceased to appear oval at all, and will have become, so far as you can see, a straight line."*
>
> Flatland, Edwin A. Abbott

In 1884, E. A. Abbott pictured in his novel "Flatland" a two-dimensional (2D) world that is inhabited by various geometrical objects. Partially due to the constrained perception and partially due to the rigid social structure, the inhabitants of this world show a complete ignorance towards scientific progress and a lack of insight. Despite the fact that Abbott mainly allegorized and criticized the social hierarchy of Victorian culture in the 19^{th} century, he visualized the consequences of a change of dimensionality. Our everyday life is based on one temporal and three spatial dimensions - but what would it be like with one, two or four spatial dimensions? Of course, there are recent theories that employ higher dimensions to introduce additional physical quantities, e.g. [Kle26], but usually, those theories provide a particular process of dimensionality reduction that allows to associate 3+1 of these dimensions with our familiar space-time structure [Tip86].

E. A. Abbot's novel is a writers answer to the question: "How do our physical laws change with the number of spatial dimensions?" This question has a long history, dating back to the Greek philosophers [Tip86], and has generated valuable insight to our physical

laws. In modern physics Immanuel Kant was one of the first who commented on the role of dimensionality in physical laws. He realized a connection between the inverse square law of gravity and the number of spatial dimensions [Han79]. In 1917, Ehrenfest published a famous article *"In what way does it become manifest in the fundamental laws of physics that space has three dimensions?"* [Ehr17]. He demonstrated that the existence of stable planetary orbits, the stability of atoms and molecules, and the properties of wave operators depend on exactly three dimensions. A more recent quantum mechanical treatment of a generalized d-dimensional hydrogen atom [Gur71] indicates that no stable orbits for bound electrons can exist for d larger than three, which places an upper bound on the number of spatial dimensions of a life-supporting universe. A lower bound, on the other hand, is given by the necessity to construct complex, connected objects in two dimensions. For example, a neural network in two dimensions allows to connect only four nerve cells without intersecting the joins [Whi59]. There are countless examples that demonstrate that our physical laws are unique in three spatial dimensions [Tip86].

Since we live in a three-dimensional (3D) world with unique physical properties, why is it important to study systems with a different dimensionality? One reason is exactly the aforementioned strong dependence of physical laws on dimensionality. A change of the number of dimensions is particularly well suited to test theoretical models, especially since many models get much simpler in reduced dimensionality. Another reason is the frequent occurrence of objects that behave as if they existed in a system with a different dimensionality. Whereas it is probably not possible to increase the number of spatial dimensions, there are numerous examples of objects in a reduced dimensionality. Typically their motion is restricted by an external constraint or confinement, e.g. the one-dimensional (1D) flow in a water pipe or the 2D spreading of oil on a water surface. There is an important difference between these "quasi" low-dimensional systems and the mathematical concept of low-dimensionality. In our world, low-dimensionality is always just an approximation. For example, in classical physics, the dimensionality of a model depends strongly on the observed length scale. The trip of a sailboat on the ocean can be modeled in two dimensions, but in rough weather and with high waves the sailor himself will be strongly effected by the third dimension. For quantum systems this approximation of a reduced dimensionality improves strongly. The trapping of a quantum mechanical object along one direction provides a set of discrete energy levels and it provides an absolute length scale. If the energy of the object is insufficient to bridge the gap to the next trap level, the motion of the object along the trapped direction will effectively be "frozen out". But even in low-dimensional quantum systems reminiscent 3D effects are usually present as will be demonstrated later. The term "quasi" low-dimensional system has as strict denotation in the context of ultracold atoms. It is assigned to a gas that is confined along one or two directions with the particle motion "cooled down" to the lowest trap level [Ols98]. In the context of condensed matter physics

the definition is less stringent. There, the term quasi low-dimensional is already used when particles are confined to a length scale that is comparable to the de Broglie wavelength of the particle, and when the motion along the confined direction is influenced by quantum mechanics [Bar01, Kan95].

This work studies the motion of quantum objects in 1D geometry. Here, atoms that are cooled down to quantum degeneracy by means of laser cooling and by forced evaporation move in 1D geometry, which is provided by optical lattice potentials. Of course, the motion of a single atom along a straight line is not particularly elucidating, but the 1D motion of several interacting atoms shows intriguing many-body effects, which have been at the center of interest for decades [Gia03]. The understanding of these many-body effects in low dimensions is crucial to explain the transport of electrons in certain materials, e.g. to understand the phenomenon of high temperature superconductivity [Tin96] or the conduction in carbon nanotubes [Tan01]. In real solids those transport phenomena are extremely complex. The band structure of allowed energy states, the Coulomb interaction of electrons, the disorder and defects of the crystal lattice and lattice vibrations, have to be accounted for. Unlike in solid state physics, ultracold atoms in optical lattices offer the possibility to tune almost any system parameter, including the external potential and particle interactions. This makes ultracold atoms in optical lattices an ideal tool to study yet unobserved concepts and theories that were originally developed in condensed matter physics [Gre08].

This thesis contains a collection of articles, which were published in the framework of this doctoral work. The main results are the observation of an excited quantum many-body phase, called the super Tonks-Girardeau (STG) phase (chapter 3), and the demonstration of the "pinning" quantum phase transition, which connects a Tonks-Girardeau (TG) gas and a Mott insulator (chapter 4). The first chapter is intended as a broad introduction to ultracold atoms in low-dimensional systems. It introduces important methods and parameters that are employed in the following articles. Although a brief summary of the results of each publication is provided, it is the main intent of this chapter to supply background information and concepts that are not included in the articles.

Optical lattice potentials can be employed to confine the motion of a particle to one dimension, but the actual interparticle scattering process maintains a 3D character. This combination of 1D motion and 3D scattering induces a new type of scattering resonance, a so-called confinement induced resonance (CIR), which was observed and studied in [Hal09, Hal10b] (chapter 2,3). CIRs allow tuning of particle interactions in 1D geometry, and, in particular, approaching the limit of a TG gas, i.e. a gas of impenetrable bosons. Quickly crossing a CIR preserves some properties of a many-body state from one side of the resonance to the other. As a result, the strongly correlated STG phase is formed, which is metastable despite strong attractive interactions. The existence of the STG phase is verified by the observation of a change in the hydrodynamic properties of the gas [Hal09] (chapter 3). In chapter 4 we

add a shallow lattice potential along the axis of the 1D system. This additional potential is employed to drive a phase transition from the TG gas to a Mott insulator. We determine the complete phase diagram of this Mott insulator transition ranging from shallow lattice potentials, described within the framework of the sine-Gordon model, to the tight binding regime, covered by the Bose-Hubbard model. In the chapters 5 to 7 the atomic motion in a 1D lattice potential is studied as a result of an external driving force. Here, as opposed to the previous chapters, the atoms are just weakly confined in the transversal direction. We study the effect of interparticle interactions on Bloch oscillations and, for a periodically modulated driving force, we observe a novel type of oscillations, so-called super Bloch oscillations (sBOs).

During the time of this thesis, the second experimental objective of our team was the creation of a BEC of Cs_2 molecules in the rovibronic ground state. Starting from a BEC of single Cs atoms, a Mott insulator state with a maximum of two atoms per lattice site is formed. We associate the atoms on a magnetic Feshbach resonance to weakly bound molecules, and we transfer the atoms to the rovibronic ground state by means of a two-step Stimulated Raman Adiabatic Passage (STIRAP) technique. Chapter 8 lists our publications that are connected to this second experimental branch.

1.1 Quantum gases in 3D geometry

With the development of laser cooling and trapping of atoms during the 1980s [Met99] atomic gases became available at ultracold temperatures on the order of microkelvin. At sufficiently low temperatures the description of collisions between atoms simplifies greatly and two-body interactions are completely characterized by a single parameter, the s-wave scattering length a_{3D}. Magnetic Feshbach resonances (FBR), which were first observed in [Ino98], allow for the control of a_{3D} by external fields [Chi10]. Especially the heaviest stable alkali atom, cesium (Cs), offers very favorable scattering properties and magnetic FBRs at low magnetic field strengths [Chi04].

In 1995, a combination of laser cooling and evaporative cooling led to the formation of the first Bose-Einstein condensate (BEC) [And95, Dav95]. This novel state of matter is a result of quantum statistics and energy quantization at low temperatures. For overlapping wave functions, bosonic particles will show an effective "bunching" that eventually leads to a macroscopic occupation of the energetic ground state [Bos24, Ein25]. BECs constitute macroscopic quantum objects, which can be employed to verify fundamental ideas of quantum mechanics. Outstanding achievements are the observation of macroscopic matter wave interference [And98] and the creation of vortices [Mat99, Mad00] and solitons [Bur99, Den00, Kha02].

Especially Cs atoms offer a rich structure of magnetic FBRs and provide a magnetic tunability of the interaction strength. The first Cs BEC was formed in 2002 in Innsbruck [Web03].

Cs atoms have been employed to generate a degenerate gas of Feshbach molecules [Her03]. It has been possible to observe collisions between Cs_2 dimers as a function of magnetic field strength, thus indicating a molecular Feshbach resonance [Chi05]. Recently, Cs trimer states, so called Efimov states, were detected [Kra06] and evidence for universal four-body states was reported [Fer09].

1.2 Low-dimensional systems

There are surprisingly many examples for low-dimensional systems in our everyday life. In classical physics, they usually originate from a separation of length scales and time scales, which allows to model the motion of objects in reduced dimensions. This is different in quantum mechanics. The main motivation for studying low-dimensional quantum many-body effects with ultracold atoms stems from the interest in electron gases in condensed matter physics. An improved understanding of the conduction process in solid states physics could result in the design and fabrication of novel materials with far-reaching technological impact, for example superconductors at room temperature.

1.2.1 Examples of low-dimensional systems

Two-dimensional systems. The class of 2D systems that is most common in nature are surfaces. The study of the interface between two phases of matter constitutes a whole subcategory of condensed matter physics and chemistry, called surface science. Topics of current interest are for example chemical reactions at interfaces, transport processes across and between the phases and surface excitations [Zan88]. Surfaces often facilitate a direct experimental test on the dependence of a theoretical model on dimensionality, since many phenomena in bulk materials provide surface counterparts, such as surface superconductivity [Fos04] and surface magnetism [Kan90].

For bulk materials, an important class of 2D systems is given by an electron gas in semiconductors or metals. Here, the electron motion can be confined to a 2D band structure, either naturally, due to the crystal structure as exemplified by graphite [Rot95], or artificially due to the manufacturing process. Recent advances in semiconductor growth and processing techniques, such as molecular beam epitaxy, render it possible to "grow" compositionally graded semiconductors [Bar01]. Sublimated elements, for example gallium and arsenic, slowly condense on a substrate and form thin layers of varying composition. Such semiconductor heterostructures provide the building blocks for low-dimensional nanostructures. They allow the design of spatially varying electronic conduction bands and to construct position dependent potentials with length scales that are comparable to the de Broglie wavelength of the electron. 2D nanostructurs and superlattices [Esa70] can be generated by a stack of several heterostructures.

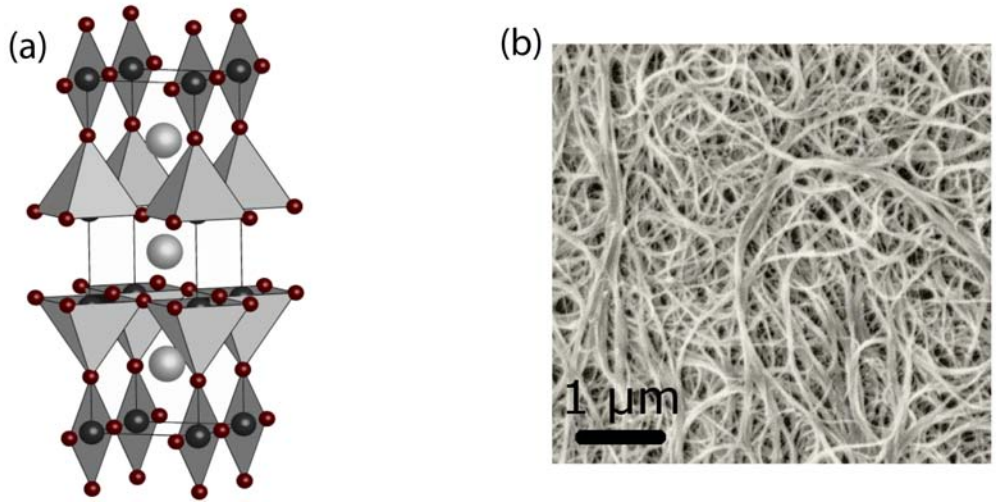

Figure 1.1: Examples of low-dimensional systems. (a) Crystal structure of the 123 superconductor $YBa_2Cu_3O_7$. Oxygen is represented as small red spheres and Cu as small black spheres. Y and Ba are represented by large gray spheres. The 123 superconductor shows both one-dimensional systems (vertical chains of corner-shared CuO_4 squares) and two-dimensional systems (two layers of CuO_2 planes in close proximity). Figure adapted from Ref. [Cav00]. **(b)** Scanning electron microscope image of a carpet of multiwall carbon nanotubes on a silicon substrate. Figure from Ref. [wik09].

An important example of 2D electron gases is provided by high-temperature superconductors. In 1986 it was discovered that certain oxide ceramics show exceptionally high superconducting transition temperatures [Bed86]. The first compound with a transition temperature above the temperature of liquid nitrogen (77 K) was the 123 superconductor $YBa_2Cu_3O_7$. The crystal structure of this superconductor shows both the existence of 2D and 1D systems Fig. 1.1a [Cav00]. It contains two 2D layers of CuO_2 planes as well as 1D chains of corner-shared CuO_4 squares. The 2D planes are separated by additional layers that control the number of electrons in the CuO_2 planes. It is currently believed that those so-called "charge reservoir layers" hold the key to the understanding of superconductivity in the 2D planes and to the determination of the superconducting transition temperatures [Cav00].

One-dimensional systems. 1D systems result from a strong confinement in two directions and allow free motion along the third direction. Typically, the confinement is either determined by the external geometrical shape of the object, e.g. carbon nanotubes, or by the alignment of atoms and atomic bounds that can form very elongated chains, e.g. conducting polymers. A taxonomy of one-dimensional systems in solid states physics can be found in Ref. [Rot95].

Carbon nanotubes are an example for a 1D system that has received tremendous attention during the last two decades. They were observed in 1991 in the carbon soot of graphite electrodes during an arc discharge [Iij91]. Nowadays they are usually grown by chemical vapor deposition [Rot95]. Carbon nanotubes are hollow cylinders of graphite and can be described as a single cylindrical carbon molecule or as a carbon crystal with translational

symmetry. It is possible to form single wall or multi-walled tubes and to form bundles or arrays of tubes, Fig. 1.1b. Carbon nanotubes are among the strongest and stiffest materials ever discovered in terms of tensile strength and elastic modulus [Yu00]. They present a promising candidate for miniaturizing electronics, in particular since they can exhibit superconductivity [Tan01, Tak06].

1.2.2 Optical lattice potentials

To model the transport of electrons in real carbon nanotubes or in the 2D planes of the 123 superconductor one has to account for a multitude of effects, such as Coulomb interactions between electrons, lattice defects, lattice vibrations and complicated band structures of allowed energy states. In general, real condensed matter systems require a "top-down" approach in complexity. It is challenging to separate those effects experimentally and to deduce simplified theoretical models. On the other hand, optical lattices in combination with ultracold atoms constitute a "bottom-up" approach [Gre08]. They provide the possibility to start from an experimental model system, i.e. with a well known band structure and free of lattice defects, and then to increase the complexity of the system step by step. In a way, optical lattices represent a realization of Richard Feynman's idea of a "quantum simulator", a quantum system that can be used to model other quantum systems [Fey82, Gre08].

Optical lattice potentials rely on the interaction between an induced atomic dipole moment and an external electric field. The alternating electric field of a laser beam induces an ac-stark shift of the electronic ground state of the atom. This shift in potential energy depends on the intensity of the laser beam and can be used to trap cold atoms [Gri00]. In optical lattices atoms move towards the intensity maxima or minima of the interference pattern formed by the laser beams. A multitude of lattice configurations can be realized depending on the number, the orientation, the relative polarization and the relative phase of the laser beams. The standing wave of two counter propagating beams, a so-called 1D lattice configuration, generates a series of pancake like 2D systems. Two standing waves at an angle of 90^o, a 2D lattice configuration, form a potential of an array of elongated tubes, which confine atoms to 1D systems. Other beam configurations allow for more complicated lattice structures like Bravais lattices [Pet94] or Kagomé lattices [San04].

Even before ultracold atoms became readily available, optical lattice potentials have been used in various experiments in atomic physics, e.g. Bragg scattering of atoms on lattice beams [Mar88] and the Kapitza-Dirac effect [Gou86]. Direct cooling in an optical lattice potential is possible by means of Raman sideband cooling [Vul98, DeP99, Ker00, Han00]. However, up to now quantum degeneracy of the complete atomic cloud has not been reached by Raman sideband cooling alone. Instead, BECs are usually first formed by evaporative cooling techniques and later transferred into the optical lattice potential [Gre02]. Starting with a BEC allows to adiabatically transfer the atoms to the lowest energy band of the lattice

potential. Once loaded to the lattice potential, the atoms are said to be confined to a low-dimensional system if both kinetic energy and potential energy are insufficient to transfer the atoms to excited energy levels [Ols98]. Along the strongly confined direction the atoms are in the potential ground state and usually show a gaussian density distribution. Any motion along this direction is effectively frozen out. Following this idea, it has been possible to create both 1D and 2D systems with ultracold atoms. Systems with a strong transversal confinement in elongated traps have been created with a quantum degenerate mixture of ^{6}Li/^{7}Li [Sch01] and with ^{23}Na [Gör01]. Both experiments probed the 3D/1D crossover regime. The 1D condition was first fulfilled in [Gre01] by loading a BEC of Rb^{87} atoms into a 2D lattice potential. In the same year, a stack of 2D systems were created in a 1D lattice potential [Orz01].

1.2.3 Scattering resonances

Even if the motion of a particle is confined to a low-dimensional system, there are usually some particle properties that rely on independent length scales and that can preserve 3D character. For example, in case of an 1D electron gas in a metal, several 1D systems are positioned in parallel and are thus coupled by means of long range Coulomb interaction or by electron tunneling between the systems [Geo00]. Ultracold neutral atoms interact by short range contact interaction, and the tunneling between the 1D tubes can be suppressed by sufficiently deep lattice potentials. However, ultracold atoms show a reminiscence of 3D scattering physics for collisions within the 1D system.

For bosons, only waves without orbital angular momentum, so called s-waves, contribute to low energy scattering . In this regime, the scattering process can usually be described by a single parameter, the s-wave scattering length a_{3D}. There are two additional length scales, the confinement length $a_\perp$, which for a harmonic confinement is given by the harmonic oscillator length, and the effective range R_e of the scattering potential. Both length scales are indicated in Fig. 1.2. The effect of the confining potential on the scattering process can be neglected if $a_\perp$ is much larger than both the R_e and a_{3D}. This is typically the case for scattering of ultracold atoms in 3D systems, i.e. in magnetic traps or single beam dipole traps. If on the other hand $a_\perp$ is of the same order as R_e, the actual shape of the scattering potential will be altered by the confinement and the original 3D scattering length becomes meaningless [Kim05]. The experiments described in publications 1 and 2 are in an intermediate regime, $R_e \ll a_{3D} \approx a_\perp$, in which case the confinement provides a type of boundary condition for the scattering process but the important region of the scattering potential is not altered [Kim05].

During the scattering process two atoms, both of them in the transversal ground state, approach each other along the axis of the 1D system. Within a certain radius the spherical symmetry prevails and the actual 3D scattering process can be described by means of the

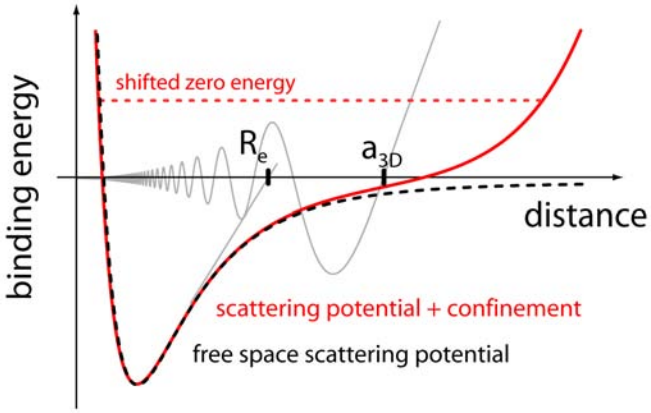

Figure 1.2: Effect of a confining potential on the scattering process. In a collision of ultracold atoms the 3D scattering potential (black dashed line) can be sufficiently described by two parameters, the effective range of the potential R_e and the s-wave scattering length a_{3D}. An additional confining potential (red solid line) allows to introduce a third length scale, the confinement length $a_\perp$. The ratios of $a_\perp$, R_e and a_{3D} determine the scattering regime and the effect of the confinement. As a result of strong confinement the zero energy of two colliding atoms, i.e. the energy of the two particle ground state, is shifted.

3D scattering length a_{3D}. After the collision, the departing particles are again "stabilized" by the confinement to the transversal ground state [Ols98, Kim05]. Although higher transversal modes are forbidden for a single particle, during the collision process virtual excitations may occur and coupling to transversally excited molecular states is possible. Similar to 3D Feshbach resonances (FBRs) [Chi10], those states allow for tuning the 1D interaction strength.

A theoretical model describing atomic scattering under strong transversal confinement was developed by M. Olshanii in 1998 [Ols98]. Analogous to the scattering process in three dimensions, he introduced an effective contact potential with a 1D scattering length and a 1D coupling constant. This coupling constant displays a resonance-like divergence at $a_{3D} \approx a_\perp$, which was called a confinement induced resonance (CIR). Its close connection to 3D FBRs was suggested in [Ber03]. M. Olshanii's original model was supported by further theoretical studies [Tie00, Blu02, Ber03, Kim05, Yur05, Nai07, Blo08]. It is possible to extend the model to a two component gas of ultracold atoms [Pea05, Sae08], to include non-zero collision energy [Mel07] and to include an anharmonicity in the trapping potential [Kes10]. Furthermore, CIRs are predicted to exist in 2D geometry [Pet00, Pet01, Nai07, Blo08] and in 0D geometry [Fed04, Büc10].

First experimental evidence for a change of scattering properties close to a magnetic FBR in 1D systems was observed in 2005 in the group of T. Esslinger [Gün05, Köh05, Mor05]. For a degenerate gas of fermions, a shift of the zero energy due to transversal confinement was observed in 1D and 2D geometry. This shift in energy is indicated by a shift of the position of a p-wave FBR [Gün05]. In [Köh05], the fraction of atoms that are transferred to excited bands

during a magnetic field ramp across a magnetic FBR was studied in a 3D lattice. Maximum transfer efficiency was reached for ramps with a final magnetic field value that was larger than the pole position of the 3D FBR. In [Mor05], the binding energy of molecules in 1D geometry was determined by radio-frequency spectroscopy. Contrary to molecules in free space, these bound states exist irrespective of the sign of the 3D scattering length. This fact was indicated by the term "confinement induced molecules".

In chapter 2 and 3 we report on the observation of CIRs in form of atomic loss resonances. A BEC of cesium atoms is loaded into a 1D or 2D lattice, and the properties of CIRs are studied by measuring particle loss and heating. In 1D systems, the observed position of the CIR agrees well with theoretical predictions [Ols98] and can be shifted by changing the strength of the confinement or by changing a_{3D}. A transversal anisotropy in the trapping potential can be introduced by changing the relative power of the laser beams, which form the 2D lattice. We observe a second loss minimum, which we attribute to the creation of a second CIR. The formation of such a double resonance can be explained by the loss of degeneracy of the energy levels of the transversal confining potential. For strongly anisotropic confinement and for positive values of a_{3D} we observed a broad spectrum of loss resonances. One of these loss resonances even persists in the limit of a 2D system. This is surprising, since CIRs in 2D geometry are predicted to require attractive interactions [Pet01, Nai07].

Recently, it was demonstrated that the concept of CIRs can be extended to scattering in mixed dimensions [Lam10, Nis08]. Species-selective dipole potentials allow confining one species, here ^{41}K, to 2D geometry while having a negligible effect on the other, ^{87}Rb. The confinement shifts the zero energy of both Rb atoms and RbK molecules. As a result, it is possible to control the position of the interspecies resonance and to observe a series of additional resonances. Furthermore, fermionic Efimov physics is predicted to exist in a 1D-3D system for a ^{40}K and ^{6}Li mixture [Nis09].

1.3 Quantum physics in low-dimensional systems

1.3.1 Quantum degeneracy and interaction regimes

In quantum physics, the properties of a system strongly depend on its dimensionality. Most striking is the absence of a true BEC in a uniform 1D Bose gas with contact interaction. Since all transverse degrees of freedom are effectively frozen out, fluctuations can only propagate along a single dimension. As a result the effect of fluctuations is greatly enhanced and no long range order can exist in the thermodynamic limit, not even at zero temperature [Caz04]. An intuitive explanation, given in many textbooks [Pit03, Pet07], is based on the energy scaling of the density of states $\rho(E) \sim E^{d/2-1}$, with dimensionality d and total energy E. A macroscopic occupation of the ground state occurs if the number of atoms exceeds the number of states available. Thus, in a uniform 3D system with $\rho(E) \sim \sqrt{E}$, Bose-Einstein

condensation is a direct consequence of the reduction of E. However, $\rho(E)$ is constant in two dimensions and even diverges in one dimension and the phenomenon of condensation is absent. Fortunately, this is not the end of the story.

W. Ketterle, and N. van Druten pointed out that the arguments above only apply in the thermodynamic limit [Ket96]. With a finite atom number and with a confining potential, Bose Einstein condensation is possible in 1D systems. In a way, the finite size of the sample provides a low-momentum cut-off for phase and density fluctuations and it reduces the influence of fluctuations as compared to the uniform case [Pet07]. The discrete structure of trap levels allows for a sharp cross-over to a BEC. However, this sharp crossover can be smeared out by particle interactions, which broaden the structure of energy levels. As a result, a sharp crossover to a BEC in 1D systems requires weak interactions and low particle numbers [Pet00].

A gas of bosons in one dimension, interacting via a repulsive contact-potential, was studied by Lieb and Liniger in 1963. In particular, the ground state energy and the excitation spectrum were calculated in [Lie63b, Lie63a]. The only free parameter in this model is called the Lieb-Liniger γ-parameter and can be used to characterize the interparticle interaction strength. The particles are non-interacting for $\gamma = 0$ and get impenetrable for $\gamma \to \infty$. In this limit of infinitely strong interactions the system can be described by M. D. Girardeau's model of hard-core bosons [Gir60], the so-called Tonks-Girardeau (TG) gas. For ultracold atoms in one dimension the γ-parameter is given by $\gamma = mg/(\hbar^2 n)$ [Pet00], where m, g and n correspond to the particle mass, the 1D coupling parameter and the 1D density, respectively. For weak interactions, γ can be interpreted as the ratio of the interaction energy and the kinetic energy of the gas. The concept of a parameter that relates interaction energy and kinetic energy is not restricted to bosons in 1D systems, but can be applied to interacting gases in general. For example, in plasma physics the coupling parameter Γ relates the Coulomb interaction energy to the kinetic energy [Ich04].

Interpreting the γ-parameter as a ratio of energies is correct within the mean field regime, but it fails for a strongly correlated gas as, for example, the TG gas. This failure is particularly evident for $g \to \infty$. For diverging repulsive interactions, i.e. $\gamma \to \infty$, one would expect that the ratio of interaction energy to kinetic energy diverges as well. Instead, the energy of the system "saturates" at a finite value [Gan03]. An intuitive explanation is provided by the fact that the interaction energy depends on both the interaction strength and the overlap of the single particle wave functions. The two-particle correlation function g_2 scales for $\gamma \gg 1$ with $1/\gamma^2$ [Gan03], which indicates a vanishing particle overlap for large γ-values. A different interpretation of the γ-parameter is provided in [Pet07]. Repulsive interactions between the particles reduce the extend of their relative wave function, called the interaction length $r_g = \hbar^2/(mg)$. Thus, the γ-parameter can be interpreted as the ratio of the mean interparticle separation $1/n$ to r_g, i.e. $1/\gamma$ corresponds to the average number of particles per interaction

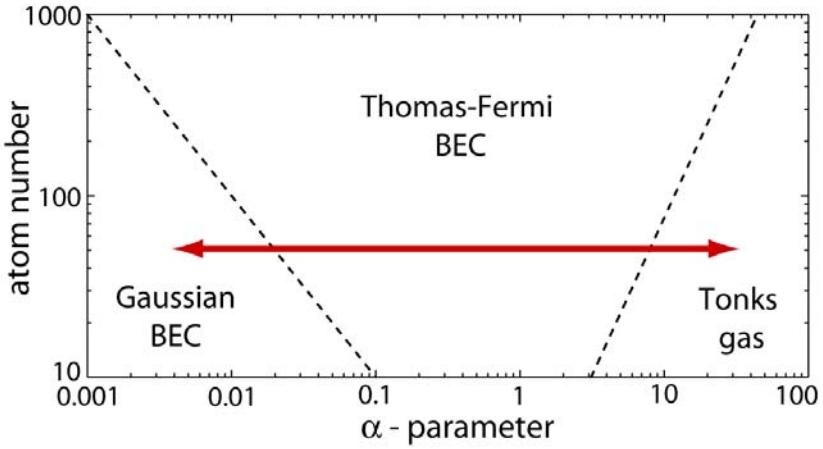

Figure 1.3: Interaction regimes in 1D. Increasing both the γ-parameter (uniform system) or the α parameter (harmonic potential) correspond to an increase of interactions. For $T = 0$ there are three interaction regimes: an ideal BEC with a gaussian density profile for $\alpha = 0$, a TG gas in the limit $\alpha \to \infty$ and a Thomas-Fermi regime with a parabolic density profile in between. Figure adapted from Ref. [Pet07].

length. For a BEC with weak interactions this number is large as r_g is of the same order of magnitude as the size of the BEC, but it is small in the limit of a strongly interacting TG gas.

Although the γ-parameter is just defined for uniform 1D systems, it is commonly applied to systems with a harmonic trapping potential [Kin04, Kin06, Stö04, Hal09]. A conservative estimate for the γ-value can be calculated by approximating the constant density of the uniform system by the center density of a trapped atom cloud. For particles in a 1D system with a harmonic potential a complementary parameter α can be defined as the ratio of the harmonic oscillator length $a_{||}$ and the previously introduced interaction length r_g, with $\alpha = mga_{||}/\hbar^2$. Since the system is finite, it is necessary to state both α and the total atom number N to determine the interaction regime. A third interaction parameter A is introduced in [Men02, Ast04]. The parameter A includes both the total atom number and the harmonic confinement and is defined for attractive and repulsive interactions. It is related to α by $A^2 = 4\hbar^2 N/\alpha^2$. In chapter 3 we employ the parameters γ and A to allow for a direct comparison with the theoretical predictions [Men02, Ast04].

For a harmonically trapped Bose gas at $T = 0$ fluctuations are small and the system is described by the Gross-Pitaevskii equation [Pet07]. Fig. 1.3 shows three different interaction regimes for a varying α-parameter at zero temperature. Similar to a 3D system, a true condensate with a gaussian density profile can form for sufficiently weak interactions with $\alpha \ll 1$. In a harmonic trap this requires that the mean field interaction energy is much smaller than the spacing of the energy levels, i.e. $N \ll 1/\alpha$ [Pet07]. For sufficiently large atom number and interaction strength the kinetic energy can be omitted and the system is in the Thomas-Fermi regime with a parabolic density distribution. For $\alpha \gg 1$ and low atom numbers, i.e. $N \ll \alpha^2$, the system is strongly interacting and forms a TG gas. Here,

the system can be mapped to a gas of free fermions with the corresponding density profile [Gir60, Ols98].

A TG gas of ultracold atoms was first created in 2004 with ^{87}Rb atoms [Kin04]. The strongly interacting regime was reached by tight transversal confinement and by low atomic densities. For an increasing interaction strength a saturation of the expansion energy and of the spatial extend of the cloud was observed. In [Par04] a lattice potential was added along the 1D system to enhance the effective particle mass and thereby to increase the γ-parameter. Taking the previously discussed interpretation, which is restricted to weak interactions, an effective γ-value was determined as the ratio of the on-site interaction energy U to the tunneling energy J. Effective γ-values up to $\gamma \approx 200$ were reached.

In chapter 3 we tune interactions by means of a CIR. As originally suggested in [Ols98], the CIR allows us to increase the interaction strength and to reach γ-values up to 500. We probe those three interaction regimes by measuring the oscillation frequency of two collective modes. A collective "sloshing" motion of all atoms can be initiated by applying a small magnetic force for a short amount of time. The oscillation frequency ω_D of this mode is independent of interactions and matches the trap frequency. An interaction quench or a fast change of the trap frequency can excite a "breathing" mode of the atoms. The frequency of this mode ω_C increases with interactions as the system gets "stiffer". The ratio of both frequencies, ω_D/ω_C, is independent of trap properties and can be calculated analytically for certain interaction regimes [Men02]. This experimental technique was demonstrated for weakly interacting atoms in [Mor03a]. In chapter 3 we determine ω_D/ω_C in the non-interacting regime, in the Thomas Fermi regime and in the TG regime and find excellent agreement with theoretical predictions [Men02].

1.3.2 Quantum liquids

Within the last 100 years a set of phenomenological theories was developed to describe interacting and non-interacting quantum gases [Pin66]. These theories do not provide exact, microscopic solutions but describe a fluid with few excitations close to an equilibrium state. Models of a free gas of non-interacting particles were successfully employed to study electrons in metals. The Drude model describes conductivity, the Lorentz model comprises a temperature dependence and quantized free electron theories include the Fermi-Dirac statistics and Pauli's exclusion principle [Bla04]. This success was surprising since all of these theories completely neglect interactions between the electrons. An explanation was offered in the 1950s by Landau who introduced the idea of a Fermi liquid [Lan57, Lan59].

Non-interacting fermions at zero temperature will occupy all momentum states that are available within the Fermi surface. Removing or adding a fermion close to the Fermi surface will result in elementary excitation of either a hole or a particle on the corresponding side of the surface. For an interacting Fermi gas this picture does not change much. Due to interac-

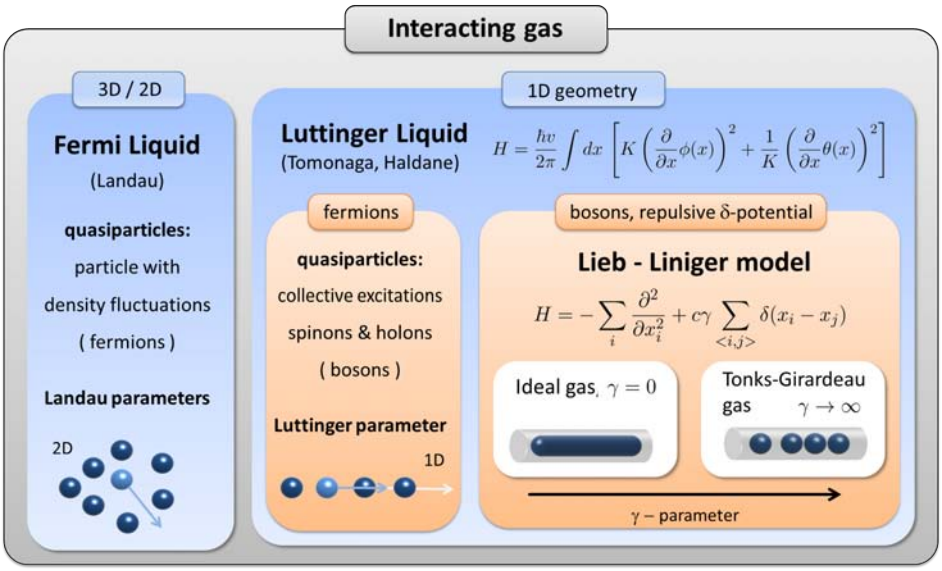

Figure 1.4: Overview of quantum liquid theories. For 1D systems the Fermi liquid theory, which is usually employed to model interacting quantum gases, fails due to geometry arguments. Instead the theory of Luttinger liquids, developed by Luttinger, Tomonaga and Haldane, describes fermions and bosons in 1D systems.

tions an additional particle will distort the surrounding density distribution. Those particles, dressed by density fluctuations, provide elementary excitations of the interacting system and are called quasiparticles. They behave as fermions, they possess an effective mass and they scatter with each other [Pin66]. Landau realized that an adiabatic "turn on" of interactions can lead to a one-to-one correspondence between the eigenstates of the non-interacting and the interacting system. Interactions between quasiparticles can be described by Landau parameters [Pin66]. In 3D and 2D systems the lifetime of those quasiparticles diverges close to the Fermi surface and, for sufficiently low temperatures, quasiparticles can be regarded as well-defined, long-lived free excitations of the system [Gia04, Pin66].

Landau's theory of Fermi liquids fails in 1D geometry. One reason is illustrated in Fig. 1.4. For interacting particles in a 1D system the motion of a single particle is not possible without pushing its neighbors [Gia04]. Excitations are no longer given by local quasiparticles but correspond to a collective motion of the particles. Sound wave-like excitations of the density (or charge) and spin wave-like excitations are possible, called holons (chargons) and spinons. Those excitations possess bosonic particle character and are free to separate [Gia03, Gia04]. In analogy to Fermi liquids, interacting 1D gases of bosons or fermions that show gapless collective spin or charge excitations are called Tomonaga-Luttinger liquids [Hal81, Gia03, Voi08]. This concept of describing an interacting gas by bosonic quasiparticles in the framework of quantum field theory is called 'bosonization'. The corresponding Hamiltonian of the system, as given in Fig. 1.4, consists of two terms: the first term is proportional to K and accounts for the kinetic energy whereas the second term is related to the interaction

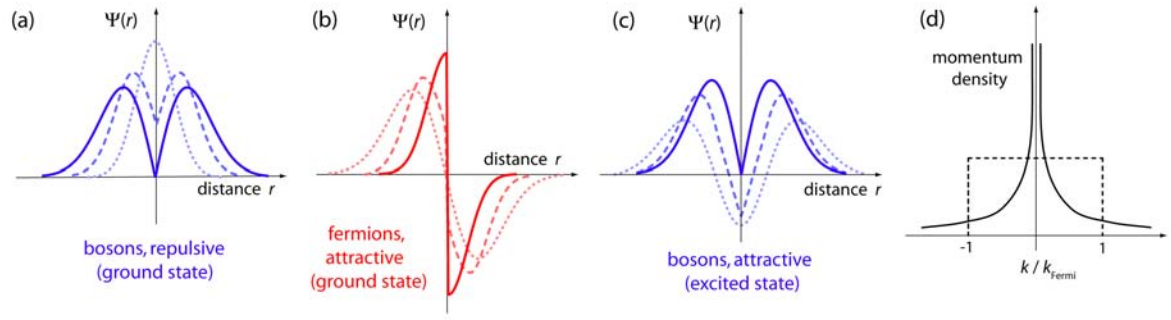

Figure 1.5: (a-c) Sketch of the wave function of two particles in a harmonic potential. The dotted, dashed and solid lines indicate zero, medium and infinitely strong interactions. **(a)** Bosons with repulsive interactions in the ground state of the harmonic potential. **(b)** Fermions with attractive interactions in the ground state. **(c)** Bosons with attractive interactions in the excited state. **(d)** Sketch of the momentum distribution of bosons (solid line) and fermions (dashed line). k_F is the Fermi momentum. Figure (d) adapted from [Ols98].

energy. The velocity v of the excitations and the parameter K completely characterize the macroscopic properties of the system for low energies. The dimensionless parameter K is called Luttinger parameter and depends on the interaction strength. For fermions a K-value of one corresponds to non-interacting particles, whereas $K < 1$ signals repulsive interactions and $K > 1$ attractive interactions.

A surprising property of 1D systems is the absence of a well defined concept of statistics. Bosons exhibit fermion-like properties and vice versa [Caz04]. This Bose-Fermi mapping is illustrated in Fig. 1.5 by means of the two-particle wave function $\psi(r)$ in a harmonic potential. Non-interacting bosons exhibit a symmetric, gaussian wave function (a, dotted line), which develops a characteristic kink for increasing repulsive interactions (a, dashed line). The absolute value of the wave function of bosons in the limit of infinitely strong repulsive interaction (a, solid line) matches to the absolute value of the wave function of non-interacting fermions (b, dotted line). Similarly, the absolute value of the wave function of fermions with infinitely strong attractive interaction (b, solid line) corresponds to the wave function of non-interacting bosons (a, dotted line). In 1D systems, the Bose-Fermi mapping works well for the spatial distribution of the atoms, whereas it fails for the momentum distribution, see Fig. 1.5d.

The Lieb-Liniger parameter γ can be connected to the Luttinger liquid parameter K. $K = 1$, representing non-interacting fermions, corresponds to a diverging parameter $\gamma \to \infty$, whereas $K \to \infty$, representing fermions with infinitely strong attractive interaction, matches $\gamma = 0$ for non-interacting bosons, see Fig. 1.6. Even a bosonic analogue for repulsively interacting fermions exists. The super Tonks-Girardeau phase in chapter 3 exhibits a K-parameter smaller than one.

An important result of the theory of Luttinger liquids are the correlation functions of the

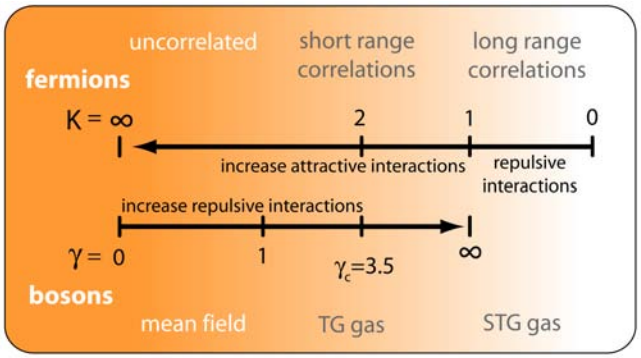

Figure 1.6: Relation between γ and K. Particle interactions in 1D systems can be quantified by the Luttinger liquid parameter K, in case of fermions, and by the γ-parameter in case of bosons. Both parameters are related due to the Bose-Fermi mapping and a common description in LL theory. In particular, the correlation functions of both, bosons and fermions, are identical for corresponding interaction regimes.

system. For example, the density correlation function $\langle n(x)n(0)\rangle$ can be described by a series of harmonics of a momentum p. In case of fermions, p is given by the Fermi momentum and in case of bosons p is πn_0, where n_0 denotes the equilibrium density. The first important term of this series scales with $\sim \cos(2\pi p\, x)/x^{2K}$, i.e. correlations show a power law decay with an exponent $2K$. As a result, strongly attractive fermions (non-interacting bosons) are not correlated and non-interacting fermions (strongly repulsive bosons) show a $1/x^2$ decay of the correlation function. Surprisingly, bosons in the STG regime (repulsive fermions with $K < 1$) show long range correlations. How is this possible for bosons with a contact potential?

The STG phase is created with a trick [Ast05]. The system is not in the ground state but in an excited, quantum many-body state with attractive interactions. Intuitively, N attractively interacting atoms in the ground state form a N-body cluster state or a bright soliton [Tem08]. Possible excited states can have hybrid character, i.e. they contain some clusters and some free atoms, or they consist of free atoms only. The STG state corresponds to the energetically lowest gas-like state, i.e. a state of free atoms [Ast05]. It is prepared by quickly crossing a CIR, thus switching from strongly repulsive to strongly attractive interactions. This preparation process does not destroy the correlations present in a TG gas ($\sim 1/x^2$), but even strengthens them ($\sim 1/x^m,\ m < 2$). The many-body wave function and the correlation function of a STG gas are calculated in [Tem08, Gir09] and the energy and the stability of a STG state are estimated in [Ast05]. The relative wave function of two non-interacting bosons in an excited state is illustrated in Fig. 1.5c, dotted line. With increasing attractive interactions, the center node of the wave function develops a characteristic kink. For infinitely strong attraction the wave function of bosons in the excited state matches the wave function of strongly repulsive bosons in the ground state. It is this correspondence of the wave functions that allows us to smoothly connect the ground state to the excited state by crossing the CIR. In chapter 3, we determine the frequency ratio ω_C/ω_D in the STG regime and demonstrate that it increases

beyond the value of 2 [Ast05]. This increase is a clear experimental signature of the STG regime since the frequency ratio of strongly correlated bosons (non-interacting fermions) is limited to 2 in a TG gas [Men02].

1.3.3 Quantum phase transitions

The physics of phase transitions is particularly effected by the system's dimensionality. In general, transitions between phases, i.e. between states of matter with essentially uniform physical properties, play an important role in our every day life. Well known examples are the boiling of water, the melting of ice or the ferromagnetic to paramagnetic transition of iron. Even the universe itself evolved in a succession of phase transitions, as the high-temperature plasma formed by the Big Bang cooled down [Voj03].

During a phase transition the common characteristics of a system change qualitatively as a result of the variation of an external control parameter. Phase transitions can be classified into first-order and continuous transitions. A typical example for a first-order transition is the melting of ice. Here, both phases co-exist at the transition point and the system absorbs a certain amount of energy, the latent heat, at a fixed transition temperature. Continuous transitions on the other hand show a gradual change in the macroscopic order when approaching the transition point. This change can be characterized by an order parameter, which is a thermodynamic quantity that is zero in the disordered phase and non-zero in the ordered phase [Sac00, Voj03]. For example, an order parameter for the ferromagnetic to paramagnetic transition of iron is the magnetization. Above the Curie temperature of 770° C, thermal fluctuations destroy the regular ordering of the magnetic moments of the spins and the magnetization vanishes. Usually, the loss of order is accompanied by a gain in symmetry. In the example of a ferromagnetic system, the Hamiltonian shows a rotational symmetry in spin-space, which, in the disordered phase, results in the lack of any preferred direction for the magnetic moments. Below the Curie temperature the magnetic moments orientate themselves in a common but arbitrary direction and the symmetry of the system is said to be spontaneously broken [Bel00].

Any system in thermodynamic equilibrium shows local variations of the thermodynamic variables around equilibrium values, in particular it shows variations of the order parameter. In the previous example, it is a local fluctuation of the magnetization or of the spin orientation, which is driven by thermal energy. It is those fluctuations, which allow for a reordering of the system close to the transition point. They appear on a length scale that can be quantified by the spatial correlation function of the order parameter and they occur on a time scale, which is given by the equilibration time τ_c. Close to the critical point of a continuous phase transition, both, correlation length and equilibration time, diverge and the system effectively averages over all length scales that are smaller than the correlation length [Sac00, Voj03]. Due to the divergence of the correlation length, microscopic details of the

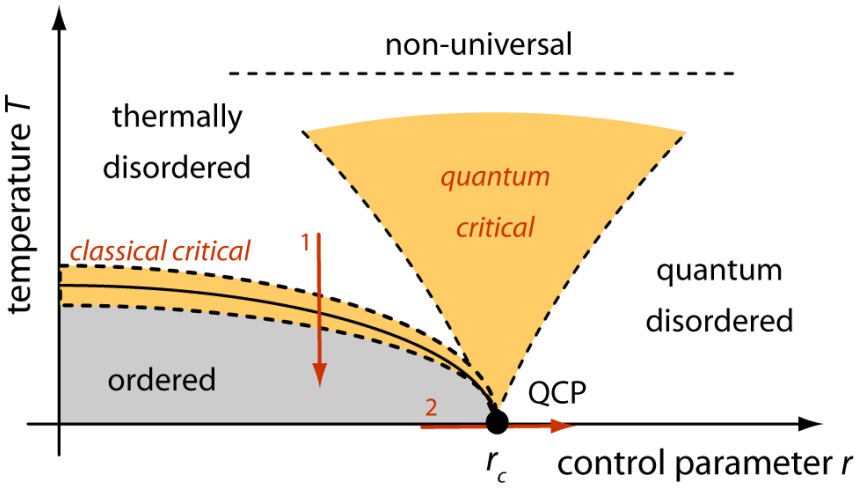

Figure 1.7: Quantum phase transitions. Phase transitions connect ordered and disordered states of matter. A classical and a quantum phase transition are indicated by the red arrows 1 and 2. Experiments usually probe the quantum critical region close to the quantum critical point QCP. Figure adapted from Ref. [Voj03].

system can be neglected and universal classes of continuous phase transitions can be introduced. Each universality class provides a set of so-called critical exponents, which describe the scaling of thermodynamic variables, like the order parameter or the susceptibility, close to the transition point. Usually, the universality class of a system is determined by the basic symmetries of the underlying Hamiltonian and by the spatial dimensionality of the system [Voj03].

The origin of the fluctuations of the order parameter is not necessarily thermal. Quantum fluctuations or zero point motion are a direct consequence of Heisenberg's uncertainty principle and lead to the reordering of the system. For example, they result in a certain probability for a spin to flip its orientation or for a non-zero particle momentum. Phase transitions that are driven by quantum fluctuations are called quantum phase transitions and occur at at temperature of zero. Quantum mechanics will dominate the system as long as the energy scale of those fluctuation, determined by the equilibration time τ_c, exceeds the thermal energy. Close to the transition point, τ_c diverges and any phase transition at finite temperatures can be described classically [Voj03]. A generalized phase diagram with classical and quantum phase transitions is shown in Fig. 1.7. Here, the horizontal dashed line indicates that for sufficiently low temperatures a universal description is applicable, since the correlation length exceeds any microscopic length scales of the system. Within a certain range of the control parameter r, it is possible to drive a classical phase transition from a thermally disordered to an ordered phase by lowering the temperature (red arrow 1). At $T = 0$, a quantum phase transition from an ordered phase to a quantum disordered phase is driven by increasing the control parameter across a critical value r_c at the quantum-critical point (QCP) (red

arrow 2). For temperatures that are finite but close to zero, the system is in the quantum-critical region. Here, the system is effected by both types of fluctuations and shows thermal excitations of the quantum-critical ground state [Voj03]. It is this quantum-critical region that is usually probed in experiments, e.g. in chapter 4.

Classical and quantum phase transitions exhibit a generic mapping to the same universality class. Usually, for classical systems the kinetic part and the potential part of the Hamiltonian commute and thus allow for a time-independent descriptions of phase transitions. This is usually not the case for a quantum mechanical Hamilton operator, for which statics and dynamics are coupled. It is often possible to map a quantum phase transition in d spatial dimensions to a classical transition in (d+z) dimension, where z is the dynamical critical exponent of the transition [Bel00]. However, despite this mapping, it is still necessary to develop an additional theory of quantum phase transitions. This is mainly due to the difficulty of obtaining realtime dynamics within the (d+z) dimensional mapping [Sac00] and due to the need to include quantum effects that lack a classical counterpart, as for example the phase coherence time [Voj03].

1.3.4 Metal-insulator transitions

In chapter 4 we probe a specific type of phase transition, which belongs to the class of "metal-insulator transitions". The term "metal-insulator transition" usually refers to a quantum phase transition that connects an electrically conducting phase in a metal to an insulating phase. Several effects exist that influence the transport of electrons in crystals: electrons can interact with the potential of the ions, they can interact with other electrons or they are affected by external fields. Usually, the insulating behavior relies on an energy gap in the excitation spectrum either of single electrons or, in case of interacting systems, of the quasiparticles discussed previously.

Figure 1.8 lists typical metal-insulator transitions. It is possible to distinguish between insulators that rely on single electron effects and on many-body electron effects. A typical example of a single electron insulator is the Bloch-Wilson insulator. Due to the periodic ion potential, the electron motion is confined to certain energy bands. Depending on the filling and the overlap of the bands the material is either conducting, semiconducting or insulating. In case of a Bloch-Wilson insulator, the valence band and the conduction band are disjunct and the energy gap for an electron-hole excitation prevents conduction [Geb97]. In the calculation of the band structure the position of the ions, which create the lattice potential, is usually assumed to be constant. For real materials with an electron-ion interaction, the electrons will induce a static lattice deformation and a new lattice periodicity, called the Peierls effect. These static lattice deformations can lower the total energy of lattice and electrons and may result in an excitation gap. At a temperature, corresponding to this gap energy, a thermodynamic phase transition from a metal to an insulator can occur, called the Peierls

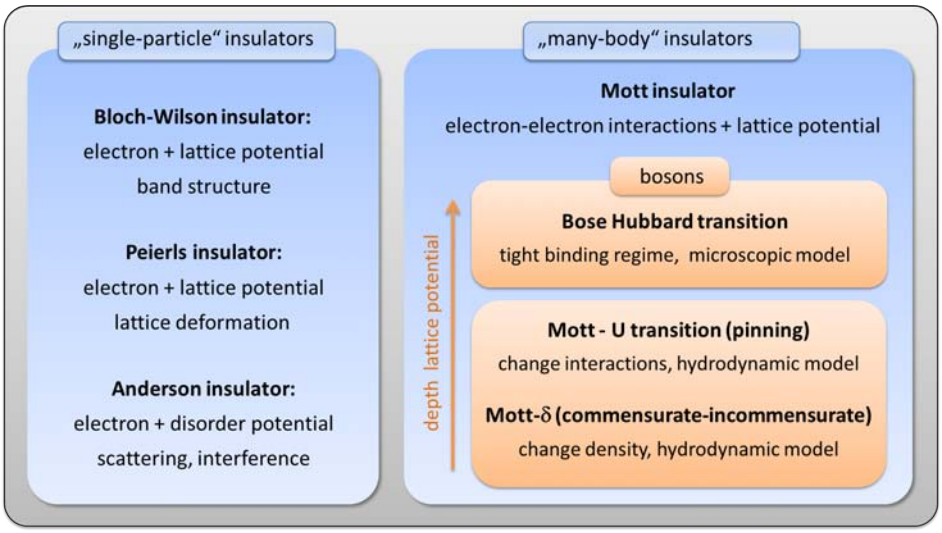

Figure 1.8: Examples of metal-insulator transitions. For details see text.

transition [Geb97]. The third metal-insulator transition mentioned in Fig. 1.8 is the Anderson transition. In lattices with strong structural disorder or with strong impurity scattering a coherent scattering of electron waves can result in the localization of electrons. Anderson localization was recently observed in cold atom experiments [Roa08, Bil08].

In 1949, N. F. Mott suggested that many-body effects and interactions can cause an insulating behavior [Mot49]. On the one hand, repulsive electron-electron interactions tend to keep electrons apart from each other and lead to localization. On the other hand, the kinetic energy "tries" to spread the electrons over the whole crystal. This competition between interaction energy and kinetic energy can result in a quantum phase transition between a metal and an insulator [Geb97]. A simplified model that assumes local interactions and considers only a single lattice band was introduced by J. Hubbard [Hub63]. The Hubbard model was originally intended to describe fermions, but in 1989 M. Fisher and co-workers extended it to a much simpler model for spinless bosons [Fis89]. Within this Bose-Hubbard model tunneling between lattice sites results in a delocalization of the particles and in a reduction of phase fluctuations, while repulsive interactions tend to localize the particles and to reduce density fluctuations. The resulting continuous phase transition connects a superfluid (SF) phase and a Mott insulating (MI) phase, Fig. 1.9a. In 1998, D. Jaksch and co-workers suggested to experimentally realize the Bose-Hubbard model by means of ultracold atoms in deep optical lattice potentials [Jak98]. Here, neutral atoms move in the lowest band of the lattice potential and the control parameter is given by the ratio between the on-site interaction energy U and the kinetic energy J. Since U/J increases exponentially with the lattice depth, it is possible to drive the phase transition experimentally by changing the laser power in the optical lattice beams. For commensurate density, e.g. on average one atom per lattice site, the SF-MI transition falls into the universality class of a (d+1)-dimensional XY model [Fis89].

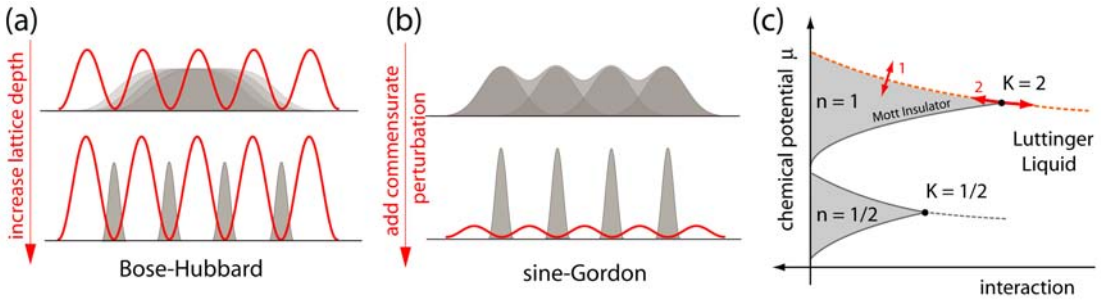

Figure 1.9: Sketch of the Mott insulator phase transition. (a,b) Schematic density distributions (grey) in the presence of a periodic potential (red solid line). **(a)** For weak interactions the system is still superfluid at finite lattice depth (top), and the Mott-Hubbard-type phase transition to the insulating state is induced by increasing the lattice depth (bottom). **(b)** The sine-Gordon-type phase transition exists for a system with strong interactions. In the absence of any perturbation, the system is a strongly correlated superfluid (top). An arbitrarily weak perturbation by a lattice potential commensurate with the system's granularity induces the transition to the insulating Mott state (bottom). **(c)** Sketch of the phase diagram. The red arrows 1 and 2 indicate the Mott-δ or commensurate-incommensurate transition and the Mott-U or pinning transition, respectively. Figure (c) adapted from [Gia03]

In the context of ultracold atoms the SF-MI transition was first observed in 2002 with ^{87}Rb atoms in a 3D optical lattice potential [Gre02]. Later experiments used the tight confinement, provided by optical lattice beams, to demonstrate the SF-MI transition in 1D geometry [Stö04] and in 2D geometry [Spi07]. Various properties of the SF-MI transition have been probed experimentally. The loss of phase coherence as the system enters the MI phase was observed via the matter wave interference pattern of the particles after release from the optical lattice [Gre02]. The MI phase shows a gapped excitation spectrum while the spectrum is continuous in the SF phase. The existence of the gap was experimentally demonstrated by applying a potential gradient [Gre02], by amplitude modulation spectroscopy [Stö04] and by Bragg spectroscopy [Fab09]. The energy gap in the excitation spectrum causes the insulating properties and the incompressibility of the MI phase [Gem09, Hun10].

In real experimental setups important modifications from the original phase diagram of a uniform system are necessary due to the external trapping potential. In a uniform system the SF-MI phase transition can only be driven by the control parameter J/U if the atom density is commensurate with the lattice spacing. For a finite size system this would require an experimental control of the atom number down to the level of single atoms. Luckily, the confining potential of the external trap alleviates this restriction by allowing for a locally varying chemical potential [Gre03]. As a result both SF and MI phases can be present at the same time and spare atoms are "taken up" by the SF phase. In the limit $J/U \rightarrow 0$ the superfluid fraction vanishes and the remaining MI phase shows regions with a varying integer occupation number per lattice site. The resulting "shell structure" of the density profile was predicted in [Jak98] and was experimentally demonstrated in [Föl06, Cam06, Gem09].

The Bose-Hubbard model follows a microscopic approach to describe bosons in a deep lattice potential. This constraint to the tight-binding regime is necessary since the model relies on the localization of particles at certain lattice sites, on the occupation of the lowest energy band and on a well defined tunneling energy J and interaction energy U. The Mott insulator transition itself is not restricted to deep lattice potentials, but does also exists for shallow lattice depths in 1D systems [Gia97]. In a way, strong interactions and correlations can replace the lattice potential Fig. 1.9b. Interacting quantum liquids in 1D systems can be described by the theory of Luttinger liquids, as introduced in section 1.3.2. The approach to model Luttinger liquids with an additional lattice potential differs for fermions and bosons. However, the resulting Hamilton operators agree with each other as expected from the Bose-Fermi mapping. For fermions close to the Fermi surface only collisions that include an exchange of momentum with the lattice potential can lead to a finite resistivity [Gia04]. Similar to other collective excitations, these so-called Umklapp processes can be expressed in terms of bosonic operators and result in an additional term in the system's Hamiltonian [Gia91]. For bosons the shallow lattice potential can be treated as a perturbation. Both approaches result in a Hamiltonian that maps to the sine-Gordon model [Büc03b, Gia03]. The corresponding phase diagrams are discussed in [Gia97, Gia04, Gia03]. Figure 1.9c shows a sketch of the phase diagram for bosons as a function of the chemical potential and interactions. The dotted lines correspond to commensurate filling with one boson per site and per two sites, respectively. Two types of Mott insulator transitions are indicated by red arrows. Adding or removing particles drives the system away from commensurability and is called Mott-δ transition or commensurate-incommensurate transition, red arrow 1. For commensurate filling, a change of the interaction strength drives a Mott-U transition or pinning transition, red arrow 2. This is the Mott insulator transition that was observed in the publication in chapter 4. We perform modulation spectroscopy and transport measurements to map out the phase diagram. Our data in the strongly interacting regime agrees well with the predictions from the sine-Gordon model [Büc03b]. We trace the phase boundary all the way from the strongly interacting to the weakly interacting regime where we find good agreement with the predictions of the 1D Bose-Hubbard model.

1.4 Single particle motion in periodic potentials

Unlike chapters 3 and 4, which study static properties of strongly interacting bosons, chapters 5 to 7 focus on the aspect of dynamics. Here, we examine the motion of interacting bosons in a 1D lattice as a result of a driving force. Usually, bosons in a 1D lattice do not fulfill the definition of a 1D quantum system as introduced in section 1.2.2. They are not restricted to the transverse ground state of the lattice potential, but they rather form a quantum liquid with transversal excitations and density fluctuations. However, if the transversal mo-

tion of the particles can be neglected, it is possible to reduce the transversal density profile to a single parameter, and to describe the axial dynamics with an effective 1D wave equation [Sal02]. In this respect, chapters 5 to 7 study 1D Bloch oscillations of bosons with repulsive interactions within the mean field description.

The concept of Bloch oscillations was first introduced by Bloch and Zener [Blo28, Zen34], who describe the motion of a single electron in an effective periodic lattice potential, which is formed by ionic cores and by the background distribution of other electrons. Assuming that the eigenstates of such a system are periodic in space, it is possible to solve the Schrödinger equation directly. The energy of the electron is no longer continuous, as in the case of a free particle, nor is it discrete, as expected for a particle trapped in a potential well. But instead the possible eigenenergies are grouped in bands, which are separated by forbidden energy gaps. These Bloch bands form the basis for a multitude of effects in solid state physics ranging from the transport of electrons in conductors, semiconductors or insulators to optical properties of metals [Ash76].

One surprising consequence of the band theory is the existence of Bloch oscillations [Blo28, Zen34]. When a particle in a lattice potential is subject to an external force, it will not be accelerated towards infinity, but rather start to oscillate both in position and in momentum space. Bloch oscillations are directly linked to the Bloch state's spatial periodicity, which limits the possible values of the quasi-momentum to the first Brillouin zone [Bri30]. According to Bloch's acceleration theorem, a particle will get accelerated until it reaches the maximum quasi-momentum at the edge of the first Brillouin zone. It is then Bragg scattered [Bra12] by the lattice potential and acquires a quasi-momentum of opposite value. This process repeats itself periodically thus resulting in a saw-tooth like time evolution of the velocity and a spiked oscillation in position space. Counterintuitive, constant acceleration in a periodic potential leads to the localization of the particle and the suppression of transport [Kan95, Wac02].

Bloch oscillations have not been observed until 1993 [Was93]. This is mostly due to the fact that the motion of an electron in a metal is strongly dominated by scattering processes. Elastic scattering on lattice defects or electrons and inelastic scattering on lattice phonons interrupt the Bloch cycle of the electron. In bulk metals the electric field, which is necessary to reduce the value of the Bloch period below the scattering time, exceeds the break down field of a crystal. In 1970, Esaki and Tsu suggested that superlattice structures can be realized by the periodically repeated deposition of alternate layers from different semiconductor materials [Esa70]. In superlattices, with a spacing much larger than the lattice constant of each constituent, minibands are formed and the Bloch period is reduced. Bloch oscillations in superlattices were observed by transient four-wave mixing [Fel92], by the observation of THz emission [Was93] and by directly measuring the dipole shift induced by the oscillating electrons [Lys97]. Since the original proposal by Esaki and Tsu, one of the main goals has been

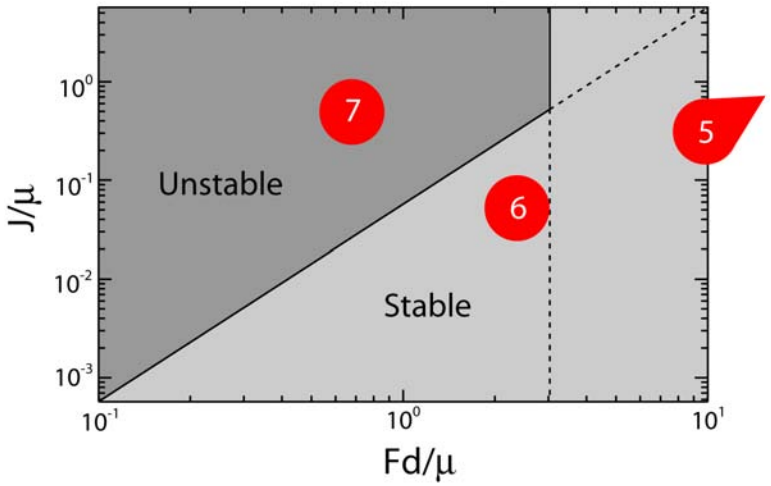

Figure 1.10: Stability diagram. A BEC in an optical lattice potential under a constant force F can show a dynamically instable time evolution. Depending on the system parameters, like tunneling energy J, chemical potential μ, force F and the lattice spacing d, there are stable and unstable regions [Zhe04]. The parameter space used in the chapters 5-7 is indicated by numbers.

to build amplifiers and oscillators that operate at THz frequencies [Ale05]. Unfortunately, due to dephasing processes and charge domain formation, only transient signals have been observed so far [Wac02].

An interesting alternative approach to observe and study Bloch oscillations comprises ultracold atoms in optical lattice potentials. In optical lattices dissipation is essentially absent and decoherence can be well-controlled. Essentially all relevant system parameters are tunable, e.g. lattice depth and spacing, particle interaction strength, and external force. An important difference between Bloch oscillations of electrons and neutral atoms is the absence of the long range Coulomb interaction. For ultracold atoms with contact-interactions, magnetic Feshbach resonances can be employed to tune the interaction strength while avoiding complicated, self-energizing many-body effects like charge domain formation [Wac02]. Furthermore, ultracold atoms yield a well-defined, narrow momentum distribution, which can be imaged directly. Bloch oscillations have been observed for thermal samples [Ben96, Bat04, Fer06], for atoms in weakly-interacting BECs [And98, Mor01, Gus10], for ensembles of non-interacting quantum-degenerate fermions [Roa04], and for non-interacting BECs [Gus08, Fat08].

In case of an interacting BEC, a rapid broadening of the momentum distribution in the first Brillouin zone was observed. For typical atomic densities, this "smearing out" of the momentum width reduces the number of observable Bloch cycles and thereby limits possible applications of Bloch oscillations in metrology. It is possible to identify two classes of instabilities that broaden the momentum distribution of particles in lattice potentials: Landau instabilities and dynamical instabilities [Mor06]. In references [Wu01, Phy03], it is demonstrated that Bloch states close to the edge of the Brillouin zone are dynamically unstable and

small perturbations grow exponentially with time. However, the stability of the system can be increased by adding a force F that drives Bloch oscillations. Depending on the system parameters, there are stable and unstable regions [Zhe04]. Figure 1.10 illustrates these regions and indicates the parameter regimes that correspond to the measurements in chapter 5 to 7. The experiment in chapter 5 is based on the absence of dynamical instabilities for vanishingly small interactions, while the experiment in chapter 6 relies on the existence of a stable region for deep lattice potentials and strong forces. Despite the fact that experiment in chapter 7 is clearly carried out in an unstable region, we observe a strong suppression of dynamical instabilities. This effect, which is related to an additional periodic modulation of the driving force, still has to be explained.

In chapter 5 we tune the s-wave scattering length by means of a broad magnetic FBR and we demonstrate a reduction of the rate of interaction induced dephasing by several orders of magnitude. A clear minimum of the dephasing can be identified, which allows us to determine the zero-crossing of the s-wave scattering length with high precision. At the interaction minimum, more than 2×10^4 oscillations can be observed with high contrast, thus surpassing the formerly achieved record value of 4000 Bloch oscillations of a thermal cloud of ^{89}Sr atoms [Fer06]. For non-zero interactions, we quantify the dephasing of Bloch oscillations and find excellent agreement with the predictions in [Wit05].

Bloch waves and the acceleration theorem are well suited to model the atomic motion in a shallow lattice potential with a weak force. For deep lattices and large forces it is advantageous to introduce a new basis of localized eigenstates, called Wannier-Stark states [Kan95]. A large force shifts the harmonic oscillator energy levels of the lattice sites and forms an array of independent BECs. Within this model, Bloch oscillations are a result of the matter wave interference of independent BECs, where the phase evolution at each site is driven by the local potential. Matter wave interference was first observed as a single particle effect for electrons [Dav27], neutrons [Hal36], atoms and molecules [Est30]. More than half a century later it was possible to demonstrate matter wave interference of macroscopic objects by means of two independent atomic BECs [And98]. Matter wave interferometers [Ber97, Cro09, Har07], in particular for precision measurements, are typically operated in the dilute single particle limit [Wic02, Cla06a, Fix07] to avoid particle-particle interactions. Atom interferometers based on BECs are expected to benefit from the extremely low momentum spread, the exceptional brightness, and the low spatial extent of the BEC [Gup02], but they enter the nonlinear matter wave regime as a result of the interaction-induced mean field potential. While chapter 5 offers a possible solution by operating the interferometer in the non-interacting limit, we demonstrate in chapter 6 that a BEC-based multipath atom interferometer is possible, where the dynamics is dominated by interaction-induced phase shifts. In addition to the linear phase shift due to the lattice tilt, which leads to Bloch oscillations, there are phase shifts caused by interactions and by the external trapping potential. We observe a charac-

teristic time-evolution and revivals of the interference pattern, which are closely connected to the theory of quantum carpets [Kap00] and Talbot effects [Ber97, Den99]. The ability to tune interactions allows us to reverse the nonlinear phase evolution and thereby to refocus the wave function of the BEC in momentum space. By means of the external potential we cancel the dominant mean field contribution to the phase evolution and we become sensitive to beyond-mean field effects. Recently, coherent phase shifts due to interparticle interactions have been observed in Ramsey interferometry experiments with a two-component BEC [And09].

Bloch oscillations result from a constant force, but what is the effect of a periodically forced driving? The amplitude, frequency and phase of the driving force effect the evolution of the particle's wave function both in position and momentum space. Important effects, already observed in solid state superlattices, constitute dynamic localization and resonant tunneling [Kea95]. Dynamic localization occurs for certain values of the driving amplitude, when an initially localized wave packet remains perpetually localized [Eck09]. It has been observed for matter waves in optical lattices [Lig07] and can be employed to drive a superfluid to Mott insulator like phase transition [Zen09]. The frequency of the drive can be used to control the probability of tunneling between lattice sites showing certain resonance frequencies [Eck05]. This effect of resonant tunneling of matter waves in optical lattices has been observed between nearest and next nearest neighboring sites [Iva08] and in form of a two-phonon resonance [Sia08]. There is a close analogy to photon-assisted tunneling in microwave-driven superconducting Josephson junctions [Eck05, Kea95]. In chapter 8 we extend the observation tunneling resonances up to the 16^{th}-phonon resonance to the nearest and up to the 5^{th}-phonon resonance to the next nearest neighboring site.

Unlike references [Lig07, Iva08, Sia08, Alb09], which study the broadening of an atomic cloud due to periodic driving, in chapter 7 we focus on the center-of-mass motion of a weakly-interacting atomic BEC in a tilted lattice potential. We demonstrate that harmonic driving can lead to a directed center-of-mass motion. If the modulation frequency of the driving force is close but not equal to the Bloch frequency, we observe giant matter-wave oscillations that extend over hundreds of lattice sites. These super Bloch oscillations result from a beat between the usual Bloch oscillations and the drive, and they represent rescaled Bloch oscillations in position space. We study the dependence of sBOs on lattice depth, modulation amplitude, and modulation frequency and find excellent agreement with the theoretical prediction in [Kol09]. It is commonly assumed that Bloch oscillations or Wannier-Stark localization prevent transport on a single particle level [Kan95] and that additional dissipative effects such as scattering from lattice defects or lattice phonons are necessary to ensure conductance [Ash76]. We demonstrate that super Bloch oscillations provide two mechanisms to circumvent localization and to induce coherent transport in an otherwise insulating context [Hal10a]. Recently, a different method to achieve dissipationless transport was demon-

strated, which relies on the ability to shape and to control the lattice potential [Sal09]. A sawtooth-like optical lattice potential with a periodically modulated amplitude resembles the quantum analog of a ratchet, and it allows for directed motion of the atoms.

1.5 Outlook

All experiments within this thesis rely on contact-interactions. The scattering potential of contact-interactions can be approximated by a δ-function, it is isotropic in space and, not surprisingly, of short range. How do the properties of a gas in 1D geometry change for a different type of scattering potential?

Especially dipole-dipole interactions are a promising candidate to answer this question with experiments in the near future. Atoms with a large magnetic dipole moment, like chromium [Gri06], allow adjusting the relative strength of the contact potential and the dipole potential via magnetic FBRs. For finite scattering length quantum degeneracy can be reached via evaporative cooling, whereas magnetic dipole interactions dominate at a scattering length close to zero [Lah07]. A different approach is taken for polar molecules. Usually, only molecule-molecule collisions in the rovibronic ground state preserve the internal state and they allow for sufficient stability of the sample. Here, unbound atoms are first brought to quantum degeneracy by conventional cooling methods, they are then converted to Feshbach molecules [Her03] and finally transferred to the rovibronic ground state by means of a STIRAP technique [Dan08, Ni08]. It is suggested to tune the dipole interaction strength with a combination of DC and AC microwave fields [Mic07]. In Innsbruck a quantum gas of Cs_2 molecules in the rovibronic ground state has been realized [Dan10], and recently polar RbCs Feshbach molecules have been created. The expected dipole moment of ground state RbCs molecules is 1.25 D. An experiment with Erbium atoms with an effective dipole moment of 0.065 D is currently set up.

A dipole potential adds two new aspects to many-body physics in low-dimensional systems. The dipole-dipole interaction is not spherically symmetric in space but depends on the relative orientation of both dipole moments. Secondly, the scattering potential shows a spatial $r^{-\beta}$ dependence, with $\beta = 3$ to 5 depending on the relative orientation of the dipoles. Due to its "slow" decay, the scattering potential it is often called long range. There are several definition of the term "long range". Often a potential is called long range if the resulting chemical potential is an extensive quantity, i.e. more than local particles contribute towards the interaction energy. It follows immediately from this definition that β must be smaller or equal to the dimensionality of the system [Ast08]. As a result the dipole potential is long range in 3D geometry, but it is short range in 1D systems.

Most of the concepts introduced in this chapter still hold for dipolar interactions. The theory of Luttinger liquids is introduced phenomenologically and it is not based on the exact

shape of the interaction potential. For $\beta > 1$ the power law scaling of the interaction potential changes the Luttinger parameter K, but the correlations and the hydrodynamic properties of the system are set for a particular value of K . A relation between β and K can be found in [Dal10]. For both, fermions and bosons, a dipole potential with $\beta = 3$ results in $1 \geq K > 0$, where $K = 1$ corresponds to non-interacting fermions and $K = 0$ corresponds to a system with long range order. In this respect, dipolar systems provide direct access to the super Tonks Girardeau regime. No CIR and no preparation trick is necessary as it is the true ground state of the system. The frequency of the breathing mode is calculated in [Ast08] and it shows similar properties as demonstrated in chapter 3.

Effects of the dipole potential become apparent if another potential with a comparable length scale is introduced, e.g. an optical lattice potential. Here, several Mott insulating phases are possible, which differ in the filling fraction. In fact, a filling with q atoms distributed over p sites results in Mott phases for any rational fraction $\nu = q/p$. For each phase the system is stable over a finite interval of the chemical potential μ, with a dependence $\mu(\nu)$. This monotonically increasing function, which exhibits steps at each rational number, is called devil's staircase or cantor function [Bur09]. As a result, the phase diagram is strongly enriched. Already for singly occupied lattice sites, it contains an infinite number of Mott-insulating lobes for various filling factors. A further increase of complexity is possible by allowing for double occupancy [Bur09].

1.6 List of publications

- *Pinning quantum phase transition for a Luttinger liquid of strongly interacting bosons.*
  E. Haller, R. Hart, M. J. Mark, J. G. Danzl, L. Reichsöllner, M. Gustavsson, M. Dalmonte, G. Pupillo, and H.-C. Nägerl, arXiv:1004.3168 accepted to Nature (2010).

- *Confinement-induced resonances in low-dimensional quantum systems.*
  E. Haller, M. J. Mark, R. Hart, J. G. Danzl, L. Reichsöllner, V. Melezhik, P. Schmelcher, and H.-C. Nägerl, Phys. Rev. Lett. **104**, 153203 (2010).

- *An ultracold high-density sample of rovibronic ground-state molecules in an optical lattice.*
  J. G. Danzl, M. J. Mark, E. Haller, M. Gustavsson, R. Hart, J. Aldegunde, J. M. Hutson, and H.-C. Nägerl, Nature Physics **6**, 265 (2010).

- *Inducing transport in a dissipation-free lattice with super Bloch oscillation.*
  E. Haller, R. Hart, M.J. Mark, J.G. Danzl, L. Reichsöllner, and H.-C. Nägerl, Phys. Rev. Lett. **104**, 200403 (2010).

- *Realization of an excited, strongly correlated quantum gas phase.*
  E. Haller, M. Gustavsson, M. J. Mark, J. G. Danzl, R. Hart, G. Pupillo, and H.-C. Nägerl, Science **325**, 1224 (2009).

- *Precision molecular spectroscopy for ground state transfer of molecular quantum gases.*
  J. G. Danzl, M. J. Mark, E. Haller, M. Gustavsson, N. Bouloufa, O. Dulieu, H. Ritsch, R. Hart, and H.-C. Nägerl, Faraday Discuss. (2009).

- *Deeply bound ultracold molecules in an optical lattice.*
  J. G. Danzl, M. J. Mark, E. Haller, M. Gustavsson, R. Hart, A. Liem, H. Zellmer, and H.-C. Nägerl, New J. Phys. **11**, 055036 (2009).

- *Dark resonances for ground state transfer of molecular quantum gases.*
  M. J. Mark, J. G. Danzl, E. Haller, M. Gustavsson, N. Bouloufa, O. Dulieu, H. Salami, T. Bergeman, H. Ritsch, R. Hart, and H.-C. Nägerl, Appl. Phys. B **95**, 219 (2009).

- *Interference of interacting matter waves.*
  M. Gustavsson, E. Haller, M. J. Mark, J. G. Danzl, R. Hart, A. J. Daley, and H.-C. Nägerl, New J. Phys. **12**, 065029 (2010).

- *Quantum gas of deeply bound ground state molecules.*
  J. G. Danzl, E. Haller, M. Gustavsson, M.J. Mark, R. Hart, N. Bouloufa, O. Dulieu, H. Ritsch, and H.-C. Nägerl, Science **321**, 1159909 (2008).

- *Control of interaction-induced dephasing of Bloch oscillations.*
  M. Gustavsson, E. Haller, M. J. Mark, J.G. Danzl, G. Rojas-Kopeinig, and H.-C. Nägerl, Phys. Rev. Lett. **100**, 080404 (2008).

CHAPTER 2

PUBLICATION

Confinement-induced resonances in low-dimensional quantum systems

Phys. Rev. Lett. **104**, 153203 (2010)

E. Haller[1], M. J. Mark[1], R. Hart[1], J. G. Danzl[1], L. Reichsöllner[1],
V. Melezhik[2], P. Schmelcher[3], H.-C. Nägerl[1]

[1]*Institut für Experimentalphysik und Zentrum für Quantenphysik, Universität Innsbruck, 6020 Innsbruck, Austria*

[2]*Bogoliubov Laboratory of Theoretical Physics, Joliot-Curie 6, 141980 Dubna, Russia*

[3]*Theoretische Chemie, Physikalisch-Chemisches Institut, Universität Heidelberg, Im Neuenheimer Feld 229, 69120 Heidelberg, Germany*

We report on the observation of confinement-induced resonances in strongly interacting quantum-gas systems with tunable interactions for one- and two-dimensional geometry. Atom-atom scattering is substantially modified when the s-wave scattering length approaches the length scale associated with the tight transversal confinement, leading to characteristic loss and heating signatures. Upon introducing an anisotropy for the transversal confinement we observe a splitting of the confinement-induced resonance. With increasing anisotropy additional resonances appear. In the limit of a two-dimensional system we find that one resonance persists.

2.1 Introduction

Low-dimensional systems have recently become experimentally accessible in the context of ultracold quantum gases. For a two-dimensional (2D) geometry, the Berezinskii-Kosterlitz-Thouless (BKT) transition has been observed [Had06], and in one dimension the strongly-correlated Tonks-Girardeau (TG) [Gir60, Kin04, Par04, Sya08, Hal09] and super-Tonks-Girardeau (sTG) gases [Hal09] have been realized. In these experiments steep optical potentials freeze out particle motion along one or two directions and restrict the dynamics to a plane or to a line. Such quasi-2D or quasi-1D systems can be realized with ultracold gases when the kinetic and the interaction energy of the particles are insufficient to transfer the particles to transversally excited energy levels. Whereas the confinement removes motional degrees of freedom, it also provides an additional structure of discrete energy levels that can be used to modify scattering along the unconfined direction and by this to effectively control the interaction properties of the low-dimensional system [Ols98, Pet00, Ber03]. In this Letter, we investigate the few-body scattering processes that give rise to the capability to tune interactions and hence to drastically alter the properties of low-dimensional many-body quantum systems [Hal09].

In three-dimensional (3D) geometry magnetically-induced Feshbach resonances (FBRs) [Chi10] allow tuning of the inter-particle interaction strength. A FBR occurs when the scattering state of two atoms is allowed to couple to a bound molecular state. Typically, scattering state and bound state are brought into degeneracy by means of the magnetically tunable Zeeman interactions. For particles in 1D and 2D geometry a novel type of scattering resonance occurs. Coupling between the incident channel of two incoming particles and a transversally excited molecular bound state generates a so-called confinement-induced resonance (CIR) [Ols98, Pet00, Ber03, Tie00, Yur05, Mel07, Sae08, Kim05, Nai07]. A CIR occurs when the 3D scattering length $a_{3\mathrm{D}}$ approaches the length scale that characterizes the transversal confinement, i.e. the harmonic oscillator length $a_\perp = \sqrt{\hbar/(m\omega_\perp)}$ for a particle with mass m and transversal trapping frequency $\omega_\perp$. This causes the 1D coupling parameter $g_{1\mathrm{D}} = \frac{2\hbar^2 a_{3\mathrm{D}}}{m a_\perp^2} \frac{1}{1 - C a_{3\mathrm{D}}/a_\perp}$ to diverge at $a_\perp = C a_{3\mathrm{D}}$, where $C = 1.0326$ is a constant [Ols98, Ber03]. The CIR allows tuning of interactions from strongly repulsive to strongly attractive and thus represents a crucial ingredient for the control of interactions in a low-dimensional system. Modification of scattering properties due to confinement has been measured near a FBR for fermions [Gün05], and, recently, a CIR has been observed for a strongly-interacting 1D quantum gas of bosonic Cs atoms and was used to drive the crossover from a TG gas with strongly repulsive interactions to an sTG gas with strongly attractive interactions [Hal09]. Here, for an ultracold quantum gas of Cs atoms with tunable interactions, we study the properties of CIRs by measuring particle loss and heating rate and, in particular, confirm the resonance condition $a_\perp = C a_{3\mathrm{D}}$ for symmetric 1D confinement. For the case of transversally anisotropic confinement we find that the CIR splits and,

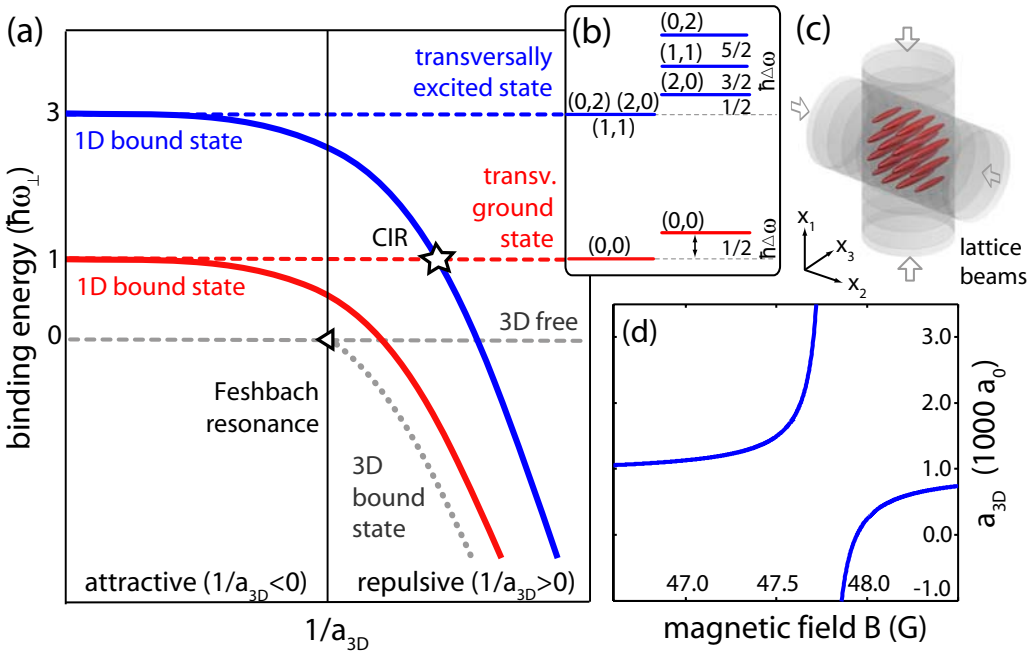

Figure 2.1: (color online) (a) Illustration of the mechanism responsible for a CIR, see Ref.[Ber03] and text for details. The energy levels near a scattering resonance are plotted as a function of $1/a_{3D}$. The CIR occurs for $Ca_{3D} = a_\perp$ when scattering atoms are allowed to couple to transversally excited bound states. (b) indicates the shift and splitting for anisotropic confinement characterized by $\Delta\omega$. (c) Experimental configuration. Two laser beams create an optical lattice that confines the atoms to an array of approximately 3000 independent, horizontally-oriented elongated 1D tubes. (d) Tuning of a_{3D} is achieved by means of a FBR with a pole at $B = 47.78(1)$ G [Lan09].

to our surprise, persists for positive a_{3D} even when the anisotropy reaches the limit of a 2D system.

2.2 Confinement induced resonances

Figure 2.1(a) reviews the basic mechanism that causes a CIR for zero collisional energy in 1D [Ber03]. It is assumed that in 3D the scattering potential supports a single universal bound state for strong repulsive interactions (dotted line) [Chi10]. The point where the incoming channel of two colliding atoms and the universal dimer state are degenerate marks the position of a 3D FBR (triangle). In 1D, strong transversal confinement shifts the zero-energy of the incoming channel (middle dashed line) and introduces a transversally excited state (upper dashed line). As a result of the strong confinement, the universal dimer state with binding energy E_B (lower solid line) exists also for attractive interactions [Mor03a] whereas the original 3D FBR has disappeared. Instead, there is a CIR (star) when the incoming scattering channel becomes degenerate with the transversally excited molecular bound state (upper solid line). It is assumed that the binding energy of this state is also E_B, shifted by

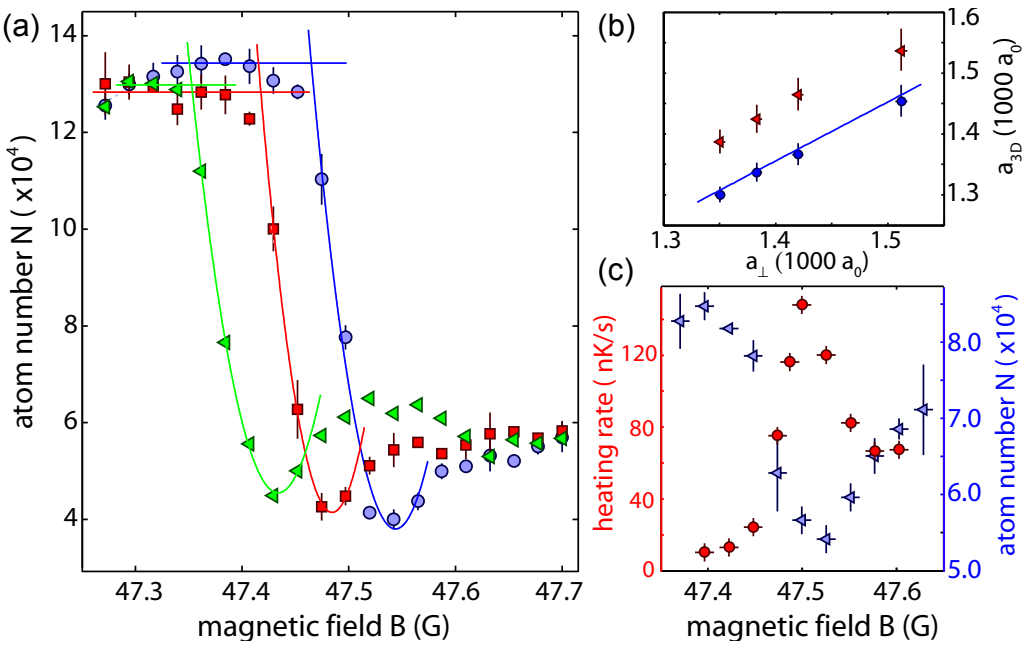

Figure 2.2: (color online) Particle loss and heating rates in the vicinity of a CIR. (a) The number N of remaining atoms after $\tau = 200$ ms shows a distinct drop ("edge") when B is scanned across the CIR. A clear shift of the position of the edge to lower values for B can be observed when the transversal confinement is stiffened, $\omega_\perp = 2\pi \times (0.84, 0.95, 1.05) \times 14.2(2)$ kHz (circles, squares, triangles). (b) Position of the edge (circles) as determined from the intersection point of a second-order polynomial fit to the minimum for N and the initial horizontal baseline as shown in (a), converted into values for a_{3D}. For comparison, the position of the minimum (triangles) is also shown. The solid line is given by $Ca_{3D} = a_\perp$. (c) Heating rates near the CIR (circles). For comparison, N is also shown (triangles). Here, $\omega_\perp = 2\pi \times 12.0(2)$ kHz. All error bars reflect 1σ statistical uncertainty.

$2\hbar\omega_\perp$[Ols98]. In more detail, as depicted in Fig. 2.1(b), we assume that the energy levels of non-interacting atoms, as a result of cylindrically symmetric transversal confinement, can be approximated by those of a 2D harmonic oscillator with $E_{n_1,n_2} = \hbar\omega_\perp(n_1+n_2+1)$ and quantum numbers n_1 and n_2 belonging to the two Cartesian directions. Scattering atoms [Sep] in the transversal ground state $(0,0)$ can couple to the excited states (n_1,n_2) if the parity of the total wave function is preserved [Kim05]. The energetically lowest allowed excited states are threefold degenerate with an energy $E = 3\hbar\omega_\perp$ and with quantum numbers $(1,1)$, $(2,0)$ and $(0,2)$. For the transversally symmetric confinement, they contribute towards a single CIR [Ber03]. However, the contribution of the state (1,1) is negligible due to the zero contact probability of the atoms and the short-range character of the interatomic interaction. Unequal transversal trapping frequencies ω_1 and $\omega_2 = \omega_1 + \Delta\omega$ lift this degeneracy and shift the energy levels according to $E_{n_1,n_2} = \hbar\omega_1(n_1+n_2+1) + \hbar\Delta\omega(n_2+1/2)$. One thus expects a splitting of the CIR.

2.3 Experimental procedure

We start from a tunable Bose-Einstein condensate (BEC) of 1.0 to 1.4×10^5 Cs atoms in the energetically lowest hyperfine sublevel [Kra04] confined in a crossed-beam optical dipole trap and levitated against gravity by a magnetic field gradient of $|\nabla B| \approx 31.1$ G/cm. Tunability of a_{3D} is given by a FBR as shown in Fig. 2.1(d) with its pole at $B_0 = 47.78(1)$ G and a width of 164 mG [Kra04, Lan09]. The BEC is produced at $a_{3D} \approx 290\ a_0$. We load the atoms within 300 ms into an optical lattice, which is formed by two retro-reflected laser beams at a wavelength of $\lambda = 1064.49(1)$ nm, one propagating vertically and one propagating horizontally as illustrated in Fig. 2.1(c). These lattice beams confine the atoms to an array of approximately 3000 horizontally oriented, elongated 1D tubes with a maximum occupation of 60 atoms at a linear peak density of approximately $n_{1D} \approx 2/\mu$m. Weak longitudinal confinement results from the Gaussian-shaped intensity distribution of the beams. We raise the lattice to a depth of typically $V = 30\ E_R$, where $E_R = h^2/(2m\lambda^2)$ is the photon recoil energy. At this depth, the resulting transversal and longitudinal trap frequencies are $\omega_\perp = 2\pi \times 14.5$ kHz and $\omega_\parallel = 2\pi \times 16$ Hz and we then have $a_\perp \approx 1370\ a_0$. After loading we slowly ramp down $|\nabla B|$ in 50 ms and adiabatically increase a_{3D} to 915 a_0 in 100 ms to create a TG gas with well-defined starting conditions near the CIR [Hal09]. To detect the CIR as a function of B, manifested by a loss resonance, we quickly set B in less than $200\ \mu$s to the desired value, wait for a hold time of typically $\tau = 200$ ms, and then measure the number N of remaining atoms by absorption imaging. For this, we re-levitate the atoms, ramp down the lattice beams adiabatically with respect to the lattice band structure, and allow for 50 ms of levitated expansion and 2 ms time-of-flight. Note that τ is chosen to be much longer than the lifetime of the sTG phase [Hal09].

2.4 Transversally symmetric confinement

We observe the CIR in the form of an atomic loss signature as shown in Fig. 2.2. We attribute the loss near the resonance to inelastic three-body collisions [Web03], which lead to molecule formation and convert binding energy into kinetic energy, causing trap loss and heating, similar to the processes observed near a FBR [Chi10]. In Fig. 2.2(a) the CIR can be identified as a distinct "edge" for the atom number N. Initially, in the TG regime losses are greatly suppressed, but increase rapidly on the attractive side of the CIR. N drops to a minimum when B is increased and then recovers somewhat. A clear shift of the loss signature to lower values for B and hence lower values for a_{3D} can be discerned when the confinement is stiffened. When we identify the position of the edge with the position of the CIR, we find good agreement with the analytical result $Ca_{3D} = a_\perp$ as shown in Fig. 2.2(b). As we have no theoretical description of the detailed shape of the loss resonance, we also plot, for comparison, the position of the minimum, which is shifted accordingly.

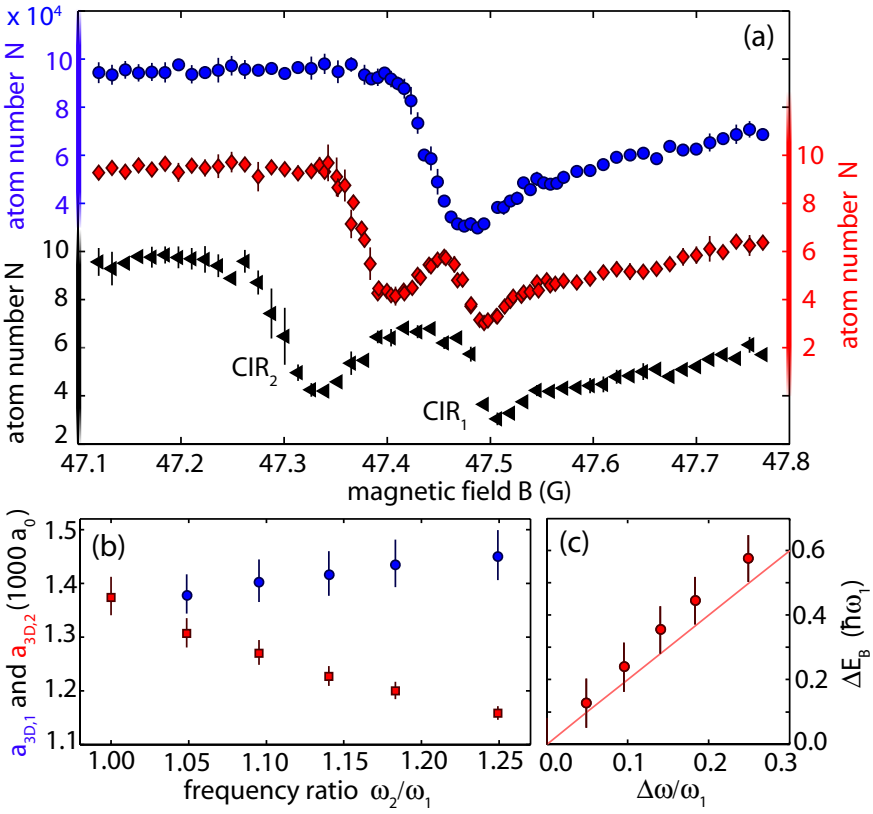

Figure 2.3: (color online) Splitting of a CIR for a 1D system with transversally anisotropic confinement. (a) As the horizontal confinement is stiffened, $\omega_2/\omega_1 = 1.00, 1.10, 1.18$ (circles, diamonds, triangles) for $\omega_1 = 2\pi \times 13.2(2)$ kHz, the CIR splits into CIR_1 and CIR_2. (b) Position of CIR_1 ($a_{3\mathrm{D},1}$, circles) and CIR_2 ($a_{3\mathrm{D},2}$, squares) as a function of the frequency ratio ω_2/ω_1. (c) Binding energy difference ΔE_B as determined from the implicit equation (see text) in comparison to the expectation from the simple harmonic oscillator model (solid line).

In Fig. 2.2(c) we juxtapose the loss and the heating rate that we measure in the vicinity of the CIR. For this, we measure the increase of the release energy within the first 100 ms. After holding the atoms for time τ at a given value of B, we decrease $a_{3\mathrm{D}}$ back to $250\ a_0$ in 20 ms, switch off the lattice potential and determine the release energy in the direction of the tubes from the momentum distribution in free space expansion. We observe an increase for the heating rate when the CIR is crossed. From a low value of 10 nK/s in the TG regime it rises to a maximum of approximately 150 nK/s and then drops to settle at some intermediate value. The position of the maximum agrees well with the maximum for atom loss. We check that the system's increase in energy is sufficiently small so that its 1D character is not lost. The release energy, even at maximal heating, remains below $k_B \times 30$ nK, which is far below the energy spacing of the harmonic oscillator levels, $\hbar\omega_\perp \approx k_B \times 600$ nK.

2.5 Transversally asymmetric confinement

We now examine 1D systems with transversally anisotropic confinement. Starting from a lattice depth of $V = 25\ E_R$ along both transversal directions, yielding $\omega_\perp = \omega_1 = \omega_2 = 2\pi \times 13.2(2)$ kHz, we increase the horizontal confinement to frequencies up to $\omega_2 = 2\pi \times 16.5(2)$ kHz, corresponding to a lattice depth of $39\ E_R$, while keeping the depth of the vertical confinement constant. Fig. 2.3(a) shows a distinct splitting of the original CIR into two loss resonances, CIR_1 and CIR_2. The splitting increases as the anisotropy is raised. In Fig. 2.3(b) we plot the 3D scattering length values $a_{3\mathrm{D},1}$ and $a_{3\mathrm{D},2}$ that we associate with the positions of CIR_1 and CIR_2 as a function of the frequency ratio ω_2/ω_1. For this, as it becomes difficult to assign an edge to both of them, we simply determine the associated atom number minima and subtract a constant offset of $88(7)\ a_0$ as determined from the measurement shown in Fig. 2.2(b). One of the resonances, CIR_2, exhibits a pronounced shift to smaller values for $a_{3\mathrm{D}}$ as the horizontal confinement is stiffened. The second resonance, CIR_1, shows a slight shift towards higher values for $a_{3\mathrm{D}}$. We now use the lifting of the degeneracy for the energy levels as indicated in Fig. 2.1(b) to model the observed splitting of the CIR. We assume that the implicit equation $\zeta(1/2, -E_\mathrm{B}/(2\hbar\omega_\perp) + 1/2) = -a_\perp/a_{3D}$ for the binding energy E_B [Ber03] remains approximately valid for sufficiently small $\Delta\omega$, taking $\omega_\perp = \omega_1$. Here, ζ is the Hurwitz zeta function. We translate the scattering length values $a_{3\mathrm{D},1}$ and $a_{3\mathrm{D},2}$ into binding energies and calculate the energy difference $\Delta E_\mathrm{B} = E_\mathrm{B}(a_{3\mathrm{D},1}) - E_\mathrm{B}(a_{3\mathrm{D},2})$, shown in Fig. 2.3(c). While this model does not explain the upward deviation seen for CIR_1, the difference ΔE_B is in reasonable agreement with the expected energy shift caused by the shifts of the excited harmonic oscillator states $(E_{0,2} - E_{2,0}) = 2\hbar\Delta\omega$ (solid line in Fig. 2.3(c)). We thus attribute CIR_2 to the stiffened confinement along the horizontal direction and hence to state $(0, 2)$, while CIR_1 corresponds to the unchanged confinement along the vertical direction and hence to state $(2, 0)$.

2.6 Limit of a 2D-system

We observe the appearance of additional structure in the measured loss curves when we increase the transversal anisotropy by weakening the confinement along one axis, here along the vertical direction. Fig. 2.4(a) shows the atom number after $\tau = 300$ ms for trapping frequency ratios ω_1/ω_2 from 0.67 to 0.45. Multiple loss resonances appear close to the position of CIR_1. The number of resonances increases and the positions shift continuously as the confinement is weakened. We speculate that those resonances are a result of a coupling to additional excited states, resulting in a multi-channel scattering situation. Also the weakening of the confinement could induce sufficient anharmonicity to allow for violation of the parity rule [Pea05].

Surprisingly, we find that one of the CIRs persists in the limit of a 2D system. Previous

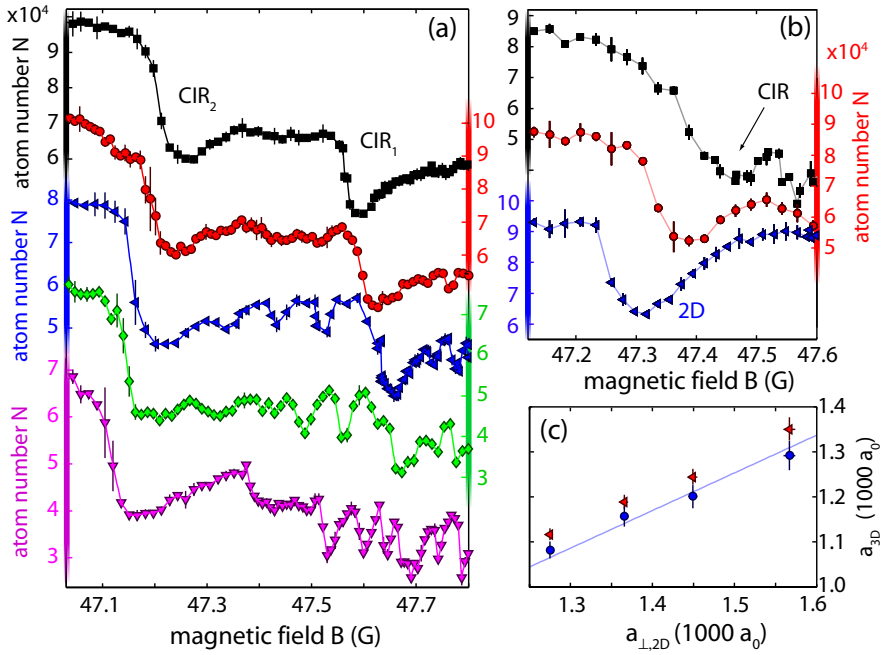

Figure 2.4: (color online) (a) Appearance of additional structure in the vicinity of CIRs for strongly anisotropic transversal confinement. The trap frequencies are $\omega_2 = 2\pi \times 16.6(2)$ kHz and $\omega_1/\omega_2 = 0.67, 0.60, 0.53, 0.49, 0.45$ from top to bottom. (b) Transition from 1D to 2D confinement. As the horizontal lattice is ramped down, CIR_2 shifts and persists, while CIR_1 disappears ($\omega_1 = 2\pi \times 13.0(2)$ kHz and $\omega_2/\omega_1 = 0.58, 0.42, 0.00$ for squares, circles, and triangles). (c) Scaling of the CIR's position in 2D, in analogy to the 1D case shown in Fig. 2.2(b). The position of the CIR as determined from the edge (circles) and, alternatively, from the minimum in atom number (triangles) shifts to lower values for a_{3D} as the confinement is stiffened and $a_{\perp,2D}$ is reduced. The solid line is a linear fit according to $C_{2D} a_{3D} = a_{\perp,2D}$ with $C_{2D} = 1.19(3)$.

theoretical studies on 2D systems have predicted the appearance of a CIR for negative a_{3D}, but not for positive a_{3D} [Pet01, Nai07]. In the experiment, we reduce the horizontal confinement while keeping the vertical confinement constant to probe the transition from the array of tubes to a stack of pancake-shaped, horizontally-oriented 2D systems. Trapping in the horizontal direction is still assured, now by the Gaussian profile of the vertically propagating laser beam, for which $\omega_2 = 2\pi \times 11$ Hz. Fig. 2.4(b) shows that the CIR associated with the tight confinement shifts to lower values for B and hence for a_{3D} as the horizontal confinement is weakened. In the limit of 2D confinement, one of the CIRs, and in fact all the additional structure observed above, have disappeared, but one resonance persists. To check that the observed resonance is indeed the result of the 2D confinement, we vary the confinement along the tight vertical direction. Fig. 2.4(c) plots the positions of edge and minimum of the loss signature as a function of $a_{\perp,2D}$, the confinement length associated with this direction. When we again associate the edge with the pole of the resonance, we obtain $C_{2D} a_{3D} = a_{\perp,2D}$ with $C_{2D} = 1.19(3)$, where C_{2D} is a scaling factor similar to C for the 1D

case. Further scattering experiments are needed to elucidate the energy dependence of this 2D scattering resonance.

In summary, we have investigated the properties of CIRs, which appear in low-dimensional quantum systems as a result of tight confinement and which replace "conventional" 3D Feshbach resonances to tune the effective atomic interaction strength. We observed a splitting of the CIR for anisotropic transversal confinement, the appearance of multiple resonances for strongly anisotropic confinement, and the survival of one resonance for positive a_{3D} in the limit of 2D confinement. We expect that CIRs will not only be used in 1D geometry to tune the effective interaction strength as recently demonstrated [Hal09], but also in 2D geometry and mixed dimensions [Lam10] for the study of strongly-interacting quantum systems.

We thank W. Zwerger for discussions and R. Grimm for generous support. We acknowledge funding by the Austrian Science Fund and by the European Union within the framework of the EuroQUASAR collective research project QuDeGPM. R.H. is supported by a Marie Curie Fellowship within FP7. P.S. acknowledges financial support by the DFG. Financial support by the Heisenberg-Landau Program is appreciated by P.S. and V.M.

CHAPTER 3

PUBLICATION

Realization of an Excited, Strongly-Correlated Quantum Gas Phase

Science **325**, 1224 (2009).

E. Haller, [1] M. Gustavsson, [1] M. J. Mark,[1] J. G. Danzl, [1] R. Hart,[1]
G. Pupillo,[2,3] H.-C. Nägerl [1]

[1]*Institut für Experimentalphysik und Zentrum für Quantenphysik, Universität Innsbruck, Technikerstraße 25, A–6020 Innsbruck, Austria*

[2]*Institut für Theoretische Physik, Universität Innsbruck, Technikerstraße 25, A–6020 Innsbruck, Austria*

[3]*Institut für Quantenoptik und Quanteninformation der Österreichischen Akademie der Wissenschaften, Technikerstraße 21a, A–6020 Innsbruck, Austria*

Ultracold atomic physics offers myriad possibilities to study strongly correlated many-body systems in lower dimensions. Typically, only ground state phases are accessible. Using a tunable quantum gas of bosonic cesium atoms, we realize and control in one dimensional geometry a highly excited quantum phase that is stabilized in the presence of attractive interactions by maintaining and strengthening quantum correlations across a confinement-induced resonance. We diagnose the crossover from repulsive to attractive interactions in terms of the stiffness and the energy of the system. Our results open up the experimental study of metastable excited many-body phases with strong correlations and their dynamical properties.

3.1 Introduction

In many-body quantum physics the interplay between strong interactions and confinement to a low-dimensional geometry amplifies the effects of quantum fluctuations and correlations. A remarkable example in one dimension is the Tonks-Girardeau (TG) gas, where bosons with strong repulsive interactions minimize their interaction energy by avoiding spatial overlap and acquire fermionic properties [Gir60, Lie63b]. Evidence for this ground state phase was found using Bose-Einstein condensates (BEC) loaded into optical lattices [Par04, Kin04]. While many-body quantum systems are usually found in their ground state phases, long-lived excited state phases are responsible for some of the most striking physical effects, examples ranging from vortex lattices in superfluids to subtle topological excitations in spin liquids [Ale06]. However, the experimental realization of excited phases is difficult, as these usually quickly decay by intrinsic effects or by coupling to the environment. In this context, cold atoms [Pet00, Mor03a, Par04, Kin04, O'H04, Pet07, Hof07, Sya08, Blo08] may provide unique opportunities for the realization of long-lived, strongly interacting, excited many-body phases due to the excellent decoupling from the environment and the tunability of interactions via, for example, Feshbach resonances.

For an ultracold one-dimensional (1D) system of bosons, we prepare a highly-excited many-body phase known as the super-Tonks-Girardeau (sTG) gas [Ast05]. In this highly-correlated quantum phase, interactions are attractive, and rapid decay into a cluster-type ground state is in principle possible. However, a surprising property of this many-body phase is its metastability. Attractive interactions strengthen correlations between particle positions and ensure, similar to an effective long-range repulsive interaction, that particles rarely come together. To realize this exotic phase, we observe and exploit a 1D confinement-induced resonance (CIR) [Ber03, Ols98]. This resonance allows us to first enter deeply into the repulsive TG regime to establish strong particle correlations and then to switch interactions from strongly repulsive to strongly attractive. The frequency ratio of the two lowest-energy collective modes [Men02] provides accurate diagnostics for the crossover from the TG to the sTG regime. In particle loss and expansion measurements we study the time evolution of the system through the crossover.

3.2 Scattering in 1D systems

We tune the strength of the interaction as characterized by the three-dimensional (3D) scattering length $a_{3\mathrm{D}}$ by means of a magnetically-induced Feshbach resonance [Ino98]. For a 1D system, a CIR arises and strongly modifies the 1D scattering properties when $a_{3\mathrm{D}}$ approaches the harmonic oscillator length $a_\perp = \sqrt{\hbar/(m\omega_\perp)}$ of the transversal confinement with trap frequency $\omega_\perp$ [Ols98, Ber03]. Here, m is the mass of the particles and $\hbar$ is Planck's constant divided by 2π. More precisely, the coupling constant $g_{1\mathrm{D}}$ of the 1D δ-function contact poten-

tial $U_{1D}(z) = g_{1D}\delta(z)$ behaves as [Ber03]

$$g_{1D} = -\frac{2\hbar^2}{m a_{1D}} = \frac{2\hbar^2 a_{3D}}{m a_\perp^2} \frac{1}{1 - C\, a_{3D}/a_\perp}, \tag{3.1}$$

where a_{1D} is the 1D scattering length defined by this equation and $C = 1.0326$ is a constant. Thus, the CIR allows tuning of g_{1D}. For values of a_{3D} less but close to $a_\perp/C$ ($a_{3D} \lesssim a_\perp/C$) the coupling parameter g_{1D} is large and positive, and for $a_{3D} \gtrsim a_\perp/C$ it is large and negative, leading to an effectively attractive interaction. For homogenous systems with $g_{1D} > 0$, it is customary to characterize the strength of interactions by the Lieb-Liniger parameter $\gamma = g_{1D}m/(\hbar^2 n_{1D})$, where n_{1D} is the linear 1D density of the system [Lie63b, Pet00]. The TG gas corresponds to the limit $\gamma \gg 1$ or $g_{1D} \to \infty$. As interactions are increased, the system becomes strongly correlated and is fully dominated by its kinetic energy. In previous experiments, without the capability to tune a_{3D}, a maximum of $\gamma \approx 5.5$ was achieved [Kin04], while an effective strength $\gamma_{\text{eff}} \approx 200$ was reached with an additional shallow lattice potential along the longitudinal direction [Par04]. In the former experiment, a saturation for the size and energy of the 1D system was observed, and in the latter experiment the momentum distribution was studied.

But what happens in the case of strong attractive interactions $g_{1D} \to -\infty$, i.e. $a_{1D} \gtrsim 0$? The ground state for a system of N attractively interacting bosons in 1D is a cluster state [McG65, Tem08], which one would expect, in a cold atom system, to decay quickly via molecular channels. However, by crossing the CIR from the TG side, i.e. switching interactions from $g_{1D} = +\infty$ to $g_{1D} = -\infty$, an excited gas-like phase, the sTG gas, should be accessible [Ast05]. Is this excited phase stable, i.e. does it exist at all? The expectation is that the large kinetic energy inherited from the TG gas, in a Fermi-pressure like manner, prevents the gas from collapsing [Bat05]. This stability can most simply be inferred from a Bethe-ansatz solution to the Lieb-Liniger model with attractive interactions [Ast04, Bat05]. This ansatz yields for the energy per particle $E/N \approx \hbar^2\pi^2 n_{1D}^2/[6m(1 - n_{1D}a_{1D})^2]$, corresponding to the energy of a gas of hard rods [Gir60], for which a_{1D} represents the excluded volume. This results in a positive inverse compressibility and also in an increased stiffness of the systems as long as $n_{1D}a_{1D}$ is sufficiently small. Interestingly, in this phase the density correlations are even stronger than in the TG gas, as they show a power-law decay that is slower than for a TG gas [Ast05], indicating an effective long-range interaction.

We realize the crossover all the way from a non-interacting gas via the 1D mean-field Thomas-Fermi (TF) regime to a TG gas and then to a sTG gas. We exploit the fact that our 1D systems possess weak harmonic confinement along the axial direction characterized by the confinement length $a_\parallel$. Whereas the frequency ω_D of the lowest dipole mode depends only on the confinement, the frequency ω_C of the lowest axial compressional mode is sensitive to the various regimes of interaction [Men02]. For the non-interacting system one expects

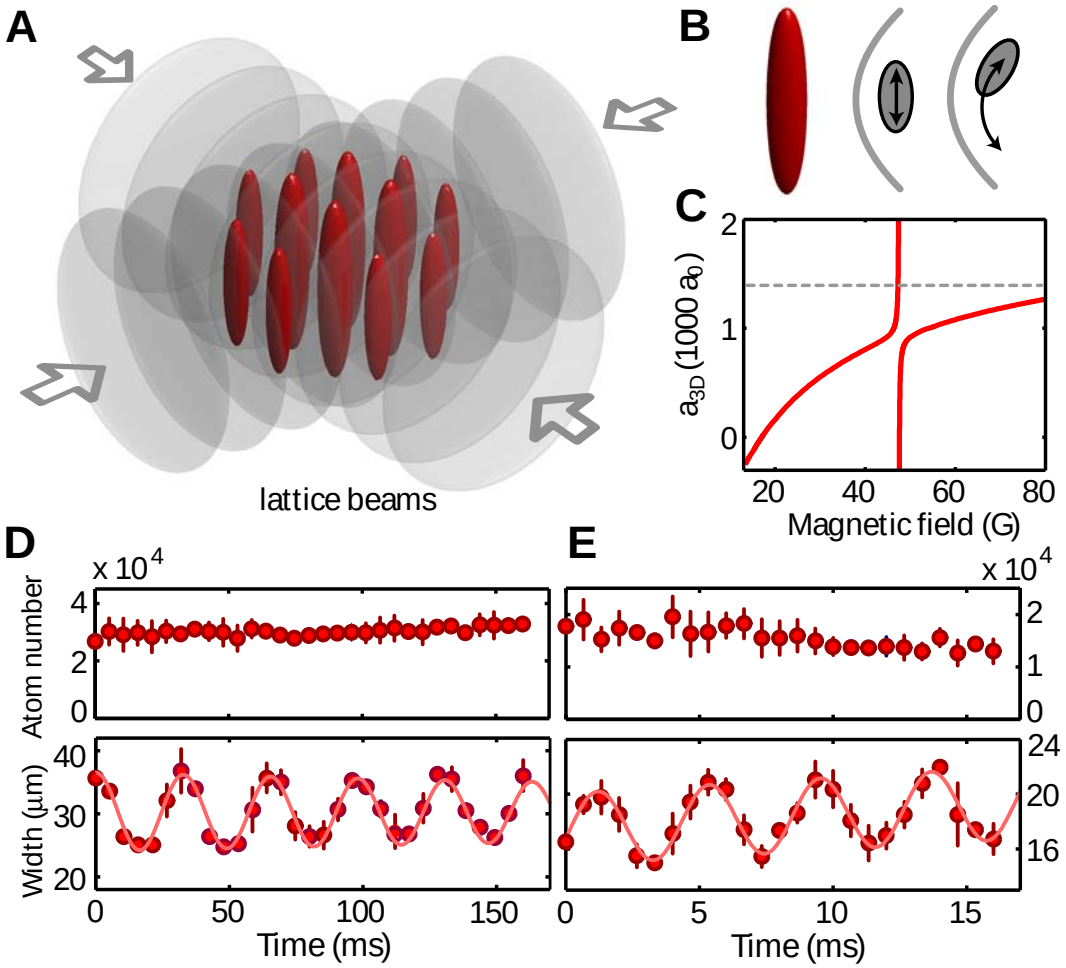

Figure 3.1: (color online) **A**, Experimental setup. The lattice potential is created by two retro-reflected laser beams confining the atoms to an array of one-dimensional tubes with equipotential surfaces shown in red. **B**, Along each tube (left) we excite the lowest compressional mode (center) and compare its frequency to the dipole mode (right). **C**, The strength of the interatomic interaction is adjusted by tuning the s-wave scattering length a_{3D}. The background scattering length rises gently from 0 to 1240 a_0 when the magnetic field B is tuned from 17 to 76 G. Further tuning is possible near a Feshbach resonance at $47.78(1)$ G to absolute values beyond 4000 a_0. The dashed line indicates $a_\perp/C$ for a transversal trap frequency of $\omega_\perp = 2\pi \times 13.1$ kHz. **D** and **E** present typical data sets for the compressional mode in the TG and sTG regime at $a_{3D} = 875(1)$ a_0 and $a_{3D} = 2300(200)$ a_0, respectively. The upper panels show the atom number, the lower panels show the $1/e$-cloud-width after time-of-flight. The solid lines in the lower panels are sinusoidal fits (see online material), yielding the oscillation frequencies $\omega_C = 2\pi \times 30.6(3)$ Hz and $\omega_C = 2\pi \times 241(1)$ Hz, respectively.

$R \equiv \omega_C^2/\omega_D^2 = 4$. This value then changes to $R = 3$ for weakly repulsive interactions in a 1D TF regime [Mor03a]. For increasing positive interaction strength, R is expected to change smoothly to 4 when entering the TG regime as the system becomes fermionized and hence effectively non-interacting. A rise beyond the value of 4, after crossing the CIR, would then constitute clear evidence for the sTG regime [Ast05]. As $a_{1\mathrm{D}}$ is further increased, the system will finally become unstable and R is expected to turn over and drop towards zero. For a harmonically confined system, the point of instability is reached when the overall length of the system of hard rods, $Na_{1\mathrm{D}}$, becomes of the order of the size $\sqrt{N}a_\parallel$ for the wave function of N non-interacting fermions, i.e. $A \equiv Na_{1\mathrm{D}}/(\sqrt{N}a_\parallel) \approx 1$. We use A^2 as an alternative parameter to γ to characterize the strength of the interaction as it accounts for the harmonic confinement.

3.3 Experimental procedure

We start from a 3D Bose-Einstein condensate (BEC) with up to 2×10^5 Cs atoms with no detectable thermal fraction in a crossed-beam dipole trap with magnetic levitation [Web03]. Depending on the interaction regime to be studied, we then set the number of atoms in the BEC to values in the range of $(1-4) \times 10^4$ by means of forced radio-frequency evaporation. To confine the atoms in 1D, i.e. to freeze out transversal motion, we use a two-dimensional optical lattice [Blo08], which forms an array of vertically oriented elongated tubes with an aspect ratio that we set to values between 100 and 1000 (Fig. 3.1A). We occupy between $3000-6000$ independent tubes with 8-25 atoms in the center tube. The interaction strength $g_{1\mathrm{D}}$ is controlled by magnetic tuning of $a_{3\mathrm{D}}$ by means of a combination of a broad and a narrow Feshbach resonance (Fig. 3.1C) with poles at $B = -11.1(6)$ G and $B = 47.78(1)$ G and widths of about 29.2 G and 164 mG, respectively [Lan09]. The broad resonance provides a slow variation of $a_{3\mathrm{D}}$, allowing us to gently tune $a_{3\mathrm{D}}$ from 0 a_0 near 17.119 G to about 1240 a_0 near 76 G, while the narrow resonance allows us to tune $a_{3\mathrm{D}}$ to absolute values beyond 4000 a_0 given our magnetic field control. We convert the applied magnetic field B into $a_{3\mathrm{D}}$ using the fit formula of Ref. 23. A magnetic field gradient, used to levitate the atomic sample [Mat], introduces a small spread in the value of $a_{3\mathrm{D}}$ across the sample.

To determine the oscillation frequencies ω_C and ω_D of the fundamental modes (Fig. 3.1 B), we excite each mode separately at a given value of the magnetic field B [Mat] and let the atoms evolve for a varying amount of hold time. The distribution is then imaged in momentum space by taking an absorption picture after release and expansion. To avoid possible broadening effects due to interaction during the initial expansion, $a_{3\mathrm{D}}$ is set to zero near $B = 17.119$ G at the moment of release. To extract the frequency, we determine for each hold time the axial $1/e$-width of the distribution and then fit a damped sinusoid with linear offset to this data. Typical measurements of ω_C are shown in Fig. 3.1 D and E. Whereas

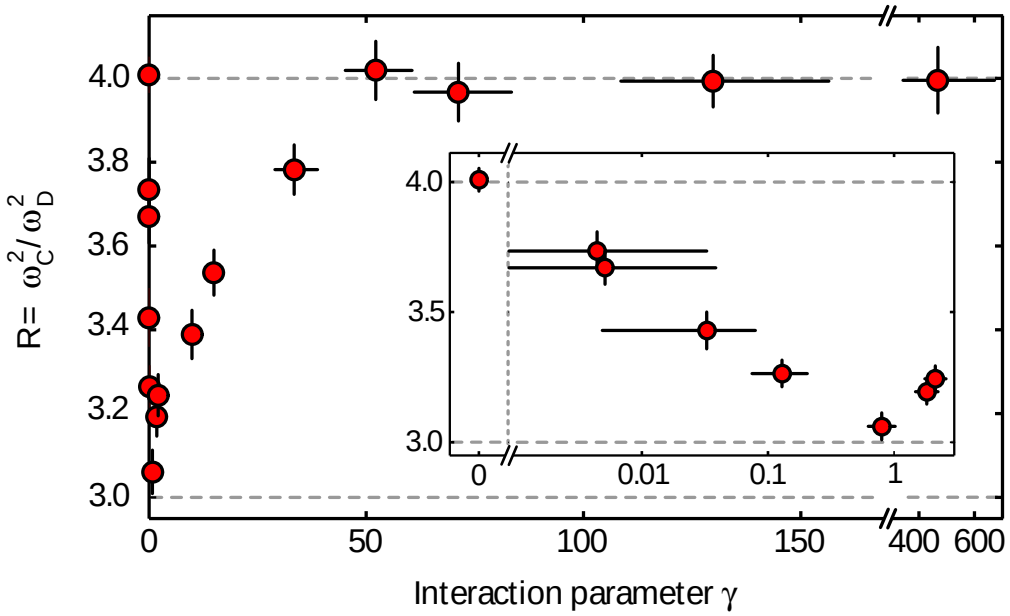

Figure 3.2: (color online) Transition from the non-interacting regime via the mean-field TF regime into the TG regime. The squared frequency ratio $R = \omega_C^2/\omega_D^2$ of the lowest compressional mode with frequency ω_C and the dipole mode with frequency ω_D serves as an indicator for the different regimes of interaction. For increasing interactions from $\gamma = 0$ to $\gamma \approx 500$ the system passes from the ideal gas regime ($R = 4$) to the 1D TF regime ($R \approx 3$) and then deeply into the TG regime ($R = 4$). The inset shows the transition from the non-interacting regime to the mean-field regime in more detail. The vertical error bars refer to standard error and the horizontal error bars reflect the uncertainty in determining a_{1D} and n_{1D} (see online material). The horizontal error bar on the data point at $\gamma = 0$ (not shown in the inset) is ± 0.03 a_0 .

the atom number remains constant for $g_{1D} > 0$, we observe some atom loss and a slight broadening of the distribution for attractive 1D interactions. In all parameter regimes, the 1D system is sufficiently stable to allow a reliable measurement of ω_C.

3.4 Transitions between the mean field, TG and STG regimes

First, we show that we can tune the system from the non-interacting regime deeply into the repulsive TG regime (Fig. 3.2). In agreement with expectations, the value for $R = \omega_C^2/\omega_D^2$ first drops from 4 to 3 and then increases back to 4 as γ is tuned by means of the gently-varying background scattering length. We find that the TG regime is fully reached for $\gamma > 50$. A further increase to values up to $\gamma \approx 500$ does not lead to changes for R. Note that, as a_{3D} approaches $a_\perp$, the divergence of g_{1D} according to Eq. 1 has to be taken into account when determining γ [Mat]. Heating of the system can be excluded as we can return to a 3D BEC without significant thermal background when ramping down the lattice potential.

The attractive regime is entered by crossing the CIR on the low-field wing of the 47.78 G Feshbach resonance. a_{1D} is now small and positive. The central results of this work are sum-

marized in Fig. 3.3A and compared to the theoretical work of Ref. 13. We plot $R = \omega_C^2/\omega_D^2$ as a function of the interaction parameter A^2. For reference, Fig. 3.3B plots a_{3D}, a_{1D}, and g_{1D} in the vicinity of the Feshbach resonance as a function of the magnetic field B. As the CIR is crossed and A^2 is increased, R rises beyond the value of 4. This provides clear evidence for the sTG regime as $R = 4$ is the maximal value for bosons with repulsive contact interaction. This increase is expected from the model of a gas of hard rods, and our data initially follows the prediction from this model. However, as A^2 is increased, R reaches a maximum and then starts to drop. The maximum of about 4.5 is reached for $A^2 \approx 3 \times 10^{-2}$. The existence of the maximum is in qualitative agreement with the results obtained from Monte-Carlo simulations [Ast05]. The theoretical prediction, however, underestimates the measured R. This is probably due to the local density approximation, which may not be applicable to our system with low particle numbers. For comparison, the results from Fig. 3.2 for $\gamma \geq 1$ are shown. Note that $\gamma \approx 500$ corresponds to small values of $A^2 \approx 10^{-4}$. For this data, at higher particle numbers, there is excellent agreement with the theoretical prediction (solid line) in the entire crossover from the mean-field regime to the TG regime[Men02].

3.5 Losses and heating

We study the stability of the system in the crossover from the TG to the sTG regime and find further evidence for the existence of the CIR by recording particle loss and measuring the axial width of the atomic cloud after release from the tubes. The axial width is a measure for the kinetic energy of the system as interactions are instantly switched off upon release. Similar conditions are used as for the measurements on the sTG regime presented in Fig. 3.3. The TG regime is entered adiabatically to avoid the excitation of collective modes. The system is prepared at $a_{3D} = 887(1)$ a_0 at a magnetic field of $B = 42.77(2)$ G with about 11 atoms in the central tube. The magnetic field is then ramped to a specific value within 0.2 ms and the sample is held at this value for a variable hold time τ from 10 to 200 ms. $a_\perp$ is set to $1523(6)$ a_0. The results (Fig. 3.4) for different hold times τ in the tubes show that, for $\tau = 10$ ms, corresponding to the timescale of the measurements in the sTG regime shown in Fig. 3.3, the transition from the TG to the sTG regime appears very smooth. There is essentially no particle loss when the system is deep in the TG regime and close to the CIR. The loss gradually increases in the attractive regime as one moves to larger values of B and towards the pole for a_{1D}. Correspondingly, the width of the sample exhibits a smooth behavior across the CIR, showing a slight increase for larger B. This behavior is consistent with the expectation of an increased energy in the sTG regime [Ast05].

For longer hold times, the data for the atom number and the sample width develop distinct features at the calculated position of the CIR. Evidently, the system is in a transient state. For $\tau = 50$ ms, the number of remaining atoms shows a dip that correlates with a peak

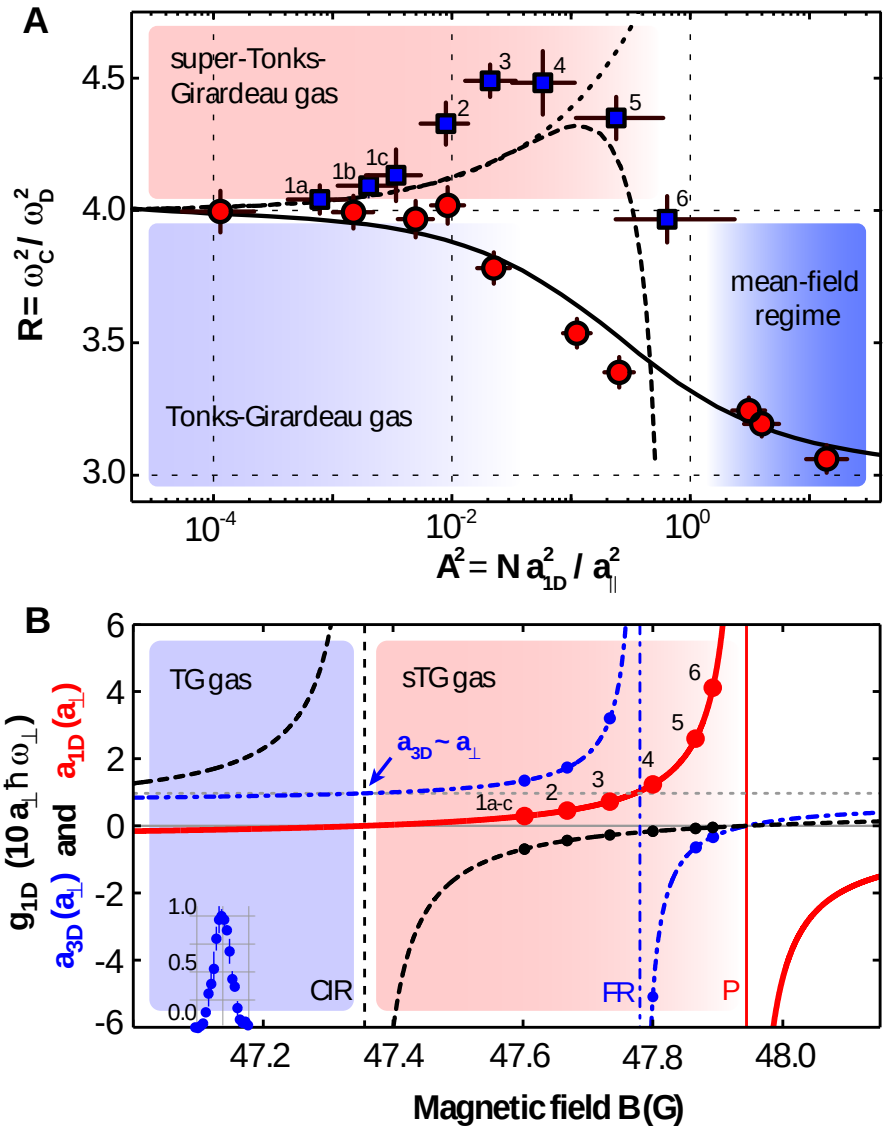

Figure 3.3: (color online) **A**, The ratio $R = \omega_C^2/\omega_D^2$ is plotted as a function of the interaction parameter $A^2 = Na_{1D}^2/a_\parallel^2$. The squares show the measurements in the attractive regime ($g_{1D} < 0$), providing evidence for the super-Tonks-Girardeau gas. The circles show the transition from the TF to the TG regime ($g_{1D} > 0$, same data as in Fig. 3.2 for $\gamma > 1$). The solid (dashed) line presents the theoretical data for $g_{1D} > 0$ ($g_{1D} < 0$) by Astrakharchik et al.[Ast05]. The dotted line corresponds to the model of hard rods. For reference, the measurements for $g_{1D} < 0$ are numbered. Data points 1c to 6 are taken at $\omega_D = 2\pi \times 115.6(3)$ Hz. For data points 1a and 1b the trap frequency is $\omega_D = 2\pi \times 22.4(1)$ Hz and $\omega_D = 2\pi \times 52.3(1)$ Hz, respectively. For all measurements in the sTG regime $a_\perp = 1346(5)$ a_0. **B**, The parameters a_{3D} (dashed-dotted), a_{1D} (solid), and g_{1D} (dashed) are plotted in the vicinity of the Feshbach resonance (FR) at $47.78(1)$ G. The horizontal dotted line indicates the value of $a_\perp/C$. The pole of the CIR is at $47.36(2)$ G. a_{1D} has a pole (P) at $47.96(2)$ G. The bell-shaped curve at the bottom left indicates the atomic distribution as a function of the magnetic field determined from high-resolution microwave spectroscopy.

in the kinetic energy of the sample. Both features become more prominent and asymmetric for longer hold times ($\tau = 100$ and 200 ms). Note that, in comparison, no pronounced effects are visible at the pole of the Feshbach resonance for a_{3D}. Our results must be connected to the fact that the energy spectrum of the system changes dramatically across the CIR, from the TG to the sTG regime [Tem08]. The system acquires a deeply lying ground state together with a family of lower lying many-body excited states, potentially opening up new decay channels. Also, the CIR strongly modifies the two-body scattering problem, making formation of confinement-induced molecules in transversally excited trap states [Ber03] possible.

3.6 Summary

The non-trivial time evolution observed in this system raises intriguing questions on possible coupling and decay mechanisms for strongly interacting excited many-body systems, in particular in the context of integrability of 1D systems [Kin06]. Our results offer an example of the counter-intuitive effects that occur in many-body systems, and open up the possibility to study the dynamical properties of strongly-correlated systems with effective long-range interactions [Boc99, Ste08] under conditions where all parameters are tunable and, in fact, can be changed dynamically. Similar to magnetic Feshbach resonances in atomic scattering, we expect the confinement-induced resonance demonstrated here to serve as a general tool to tailor interactions in 1D and possibly also in 2D systems [Pet00], allowing for the further investigation of strongly correlated phases in the context of cold atomic gases.

We thank S. Giorgini and C. Menotti for helpful discussions and for providing the theory curves shown in Fig. 3.3A. We are indebted to R. Grimm for generous support and to H. Häffner and his group for the loan of a CCD camera. We gratefully acknowledge funding by the Austrian Ministry of Science and Research (Bundesministerium für Wissenschaft und Forschung) and the Austrian Science Fund (Fonds zur Förderung der wissenschaftlichen Forschung) in form of a START prize grant and by the European Union through the STREP FP7-ICT-2007-C project NAME-QUAM (Nanodesigning of Atomic and MolEcular QUAntum Matter) and within the framework of the EuroQUASAR collective research project QuDeGPM. R.H. is supported by a Marie Curie International Incoming Fellowship within the 7th European Community Framework Programme.

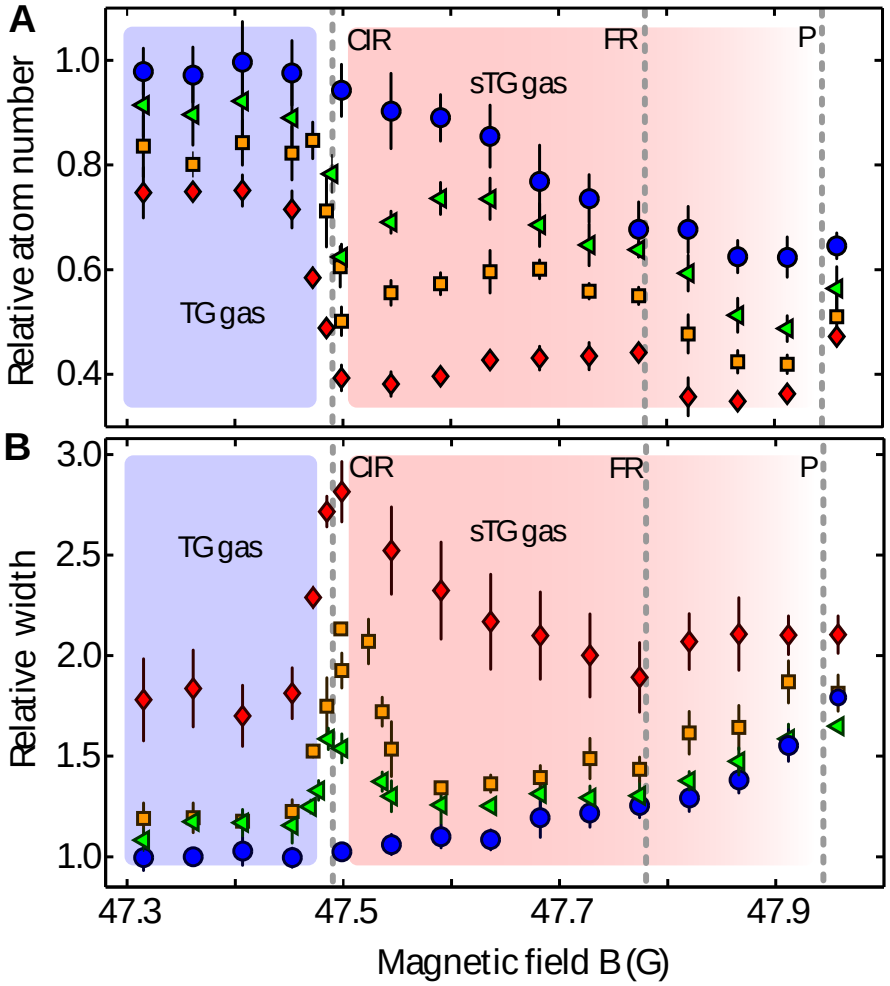

Figure 3.4: (color online) Stability and kinetic energy in the TG and sTG regimes. **A**, relative number of atoms remaining and **B**, relative $1/e$-width along the axial direction after 10 ms expansion, after a hold time $\tau = 10$, 50, 100, and 200 ms (circles, triangles, squares, and diamonds, respectively) at a given magnetic field B. The position of the CIR, the pole of the Feshbach resonance (FR), and the pole for a_{1D} (P) are as indicated. For these measurements $a_\perp = 1523(6)$ a_0 and $\omega_D = 2\pi \times 115.6(3)$ Hz. The atom number is normalized to the initial value of $1.7(1) \times 10^4$ and the width is normalized to the initial value in the TG regime.

3.7 Materials and Methods

3.7.1 Lattice loading

We produce a BEC of Cs atoms in the lowest hyperfine sublevel with hyperfine quantum numbers $F = 3$ and $m_F = 3$ in a crossed beam dipole trap with trap frequencies $\omega_{x,y,z} = 2\pi \times (15, 20, 13)$ Hz, where z denotes the vertical direction. The BEC is adiabatically transferred from the dipole trap to the array of tubes by exponentially ramping up the power in the lattice laser beams with waists ~ 350 μm within 500 ms. The repulsive interaction causes the atoms to move radially outwards during the initial phase of the lattice loading in response to the strong local compression. We use this effect to vary the total number of tubes loaded and hence the atom number per tube by setting $a_{3\mathrm{D}}$ for the loading process to values between 40 a_0 and 350 a_0. For the data set in the repulsive regime (Fig. 3.3A, circles), we exponentially ramp down the crossed beam dipole trap during the loading process and reach longitudinal and transversal trap frequencies of $\omega_D = 2\pi \times 15.4(1)$ Hz and $\omega_\perp = 2\pi \times 13.1(1)$ kHz with a transversal confinement length $a_\perp = 1440(6)$ $\mathrm{a_0}$. Here, depending on the regime of interaction to be studied, the number of atoms in the central tube is set to values between 8 and 25. For the data set in the sTG regime (Fig. 3.3A, squares) we increase ω_D to $2\pi \times 115.6(3)$ Hz to reduce the vertical extent of the sample and hence the variation of the magnetic field across the atom cloud, see below. For this, we keep the depth of the crossed beam dipole trap constant during the loading process and then ramp up the power in one of the beams within 100 ms. In this regime we choose $\omega_\perp = 2\pi \times 15.0(1)$ kHz, corresponding to $a_\perp = 1346(5)$ $\mathrm{a_0}$. The number of atoms in the central tube is set to values between 8 and 11.

3.7.2 Array of 1D tubes

The atom number per tube becomes fixed once tunneling is suppressed during the loading process and can be determined by integrating a Thomas-Fermi profile along the tubes (1). The number of atoms in tube (i, j) is given by

$$N_{i,j} = N_{0,0} \left[1 - \left(i \frac{d_{\mathrm{lat}}}{R_x} \right)^2 - \left(j \frac{d_{\mathrm{lat}}}{R_y} \right)^2 \right]^{3/2} \qquad \text{with} \quad N_{0,0} = \frac{5 N_{\mathrm{tot}} d_{\mathrm{lat}}^2}{2\pi R_x R_y},$$

where N_{tot} is the total atom number, $N_{0,0}$ is the occupation of the central tube, $d_{\mathrm{lat}} = \lambda/2$ is the lattice spacing at a wavelength $\lambda = 1064.5$ nm, and $R_{x,y}$ are the Thomas-Fermi radii in the horizontal directions. To calculate the effective atom number per tube N, we average over the tubes, weighting each tube by its atom number. This procedure accounts for the fact that we measure an averaged frequency ω_C, as ω_C is expected to slightly vary from tube to tube. The result for ω_C should be dominated by the more heavily occupied tubes close to the center of the array.

3.7.3 Magnetic levitation

To hold the $(F = 3,\ m_F = 3)$ atoms in the vertically oriented tubes, magnetic levitation by means of a magnetic field gradient of 31.1 G/cm is applied. The gradient introduces a small field spread over the atomic sample. This sets our precision to tune the interaction strength. For the measurements in the sTG regime the distribution has a full width at half maximum (FWHM) of 30 mG. We measure the atom distribution in the magnetic field by driving a magnetic-field-dependent microwave transition. A typical distribution is shown in the bottom left corner of Fig. 3.3B.

3.7.4 Excitation of collective modes

We use two different methods to excite the lowest compressional mode. For a measurement in the mean-field regime, we use a rapid change of the interaction strength to excite the oscillation. For this, we ramp the scattering length adiabatically in 100 ms to a value that is approximately 50 a_0 from the desired final value and then perform the last part of the ramp non-adiabatically. For a measurement in the sTG regime, we use an analogous method. We simply ramp sufficiently quickly, within about 5 ms, all the way from the mean-field across the TG into the sTG regime. For the TG regime, we chose to excite the mode by compressing the cloud adiabatically with an additional dipole trap laser beam, starting the motion by rapidly ramping down the power of this beam. In all cases, we adjust the ramp speeds so that the measured oscillation amplitude is within 10-20$\%$ of the initial cloud size. To excite the dipole mode at frequency ω_D, we adiabatically lower the levitating magnetic field gradient and hence displace the cloud along the vertical direction. Quickly readjusting the gradient back to full levitation leads to excitation of the dipole oscillation.

3.7.5 Determination of γ

We make a conservative estimate to determine the Lieb-Liniger interaction parameter γ

$$\gamma = \frac{m\, g_{1\mathrm{D}}}{\hbar^2\, n_{1\mathrm{D}}} = \frac{2}{n_{1\mathrm{D}}\, |a_{1\mathrm{D}}|}.$$

To take into account that the atom number varies according to $N_{i,j}$, we first calculate $\gamma_{i,j}$ for every tube separately. We calculate the center density for each tube both in the mean-field and in the TG regime and use the larger value to determine $\gamma_{i,j}$. We then take γ as the weighted average over $\gamma_{i,j}$. The error in determining γ largely comes from the determination of $a_{1\mathrm{D}}$, reflecting the magnetic field distribution across the sample.

CHAPTER 4

PUBLICATION

Pinning quantum phase transition for a Luttinger liquid of strongly interacting bosons

arXiv:1001.1206 (2010)
accepted for publication in Nature

Elmar Haller[1], Russell Hart[1], Manfred J. Mark[1], Johann G. Danzl[1], Lukas Reichsöllner[1], Mattias Gustavsson[1], Marcello Dalmonte[2,3,4,5], Guido Pupillo[2,3], and Hanns-Christoph Nägerl[1]

[1] *Institut für Experimentalphysik und Zentrum für Quantenphysik, Universität Innsbruck, Technikerstraße 25, A-6020 Innsbruck, Austria*
[2] *Institut für Theoretische Physik, Universität Innsbruck, Technikerstraße 25, A-6020 Innsbruck, Austria*
[3] *Institut für Quantenoptik und Quanteninformation der Österreichischen Akademie der Wissenschaften, Technikerstraße 21a, A–6020 Innsbruck, Austria*
[4] *Dipartimento di Fisica dell'Università di Bologna, via Irnerio 46, 40127 Bologna, Italy*
[5] *Istituto Nazionale di Fisica Nucleare, via Irnerio 46, 40127 Bologna, Italy*

One of the most remarkable results of quantum mechanics is the fact that many-body quantum systems may exhibit phase transitions even at zero temperature [Sac00]. Quantum fluctuations, deeply rooted in Heisenberg's uncertainty principle, and not thermal fluctuations, drive the system from one phase to another. Typically, the relative strength of two competing terms in the system's Hamiltonian is changed across a finite critical value. A well-known example is the Mott-Hubbard quantum phase transition from a superfluid to an insulating phase [Jak98, Gre02], which has been observed for weakly interacting bosonic atomic gases. However, for strongly interacting quantum systems confined to lower-dimensional geometry a novel type of quantum phase transition may be induced for which an arbitrarily weak perturbation to the Hamiltonian is sufficient to drive the transition [Gia03, Gog98]. Here, for a one-dimensional (1D) quantum gas of bosonic caesium atoms with tunable interactions, we observe the sine-Gordon quantum phase transition from a superfluid Luttinger liquid to a Mott-insulator [Büc03b, Pok79]. For sufficiently strong interactions, the transition is induced by adding an arbitrarily weak optical lattice commensurate with the atomic granularity, which leads to immediate pinning of the atoms. We map out the phase diagram and find that our measurements in the strongly interacting regime agree well with a quantum field description based on the exactly solvable sine-Gordon model [Col75]. We trace the phase boundary all the way to the weakly interacting regime where we find good agreement with the predictions of the 1D Bose-Hubbard model. Our results open up the experimental study of quantum phase transitions, criticality, and transport phenomena beyond Hubbard-type models in the context of ultracold gases.

4.1 Introduction

Ultracold atomic gases are a versatile tunable laboratory system for the investigation of complex many-body quantum phenomena [Blo08]. The study of quantum phases and quantum phase transitions is greatly enriched by the possibility to independently control the kinetic energy and the interactions. In deep optical lattice potentials the many-body dynamics for a weakly interacting gas is, to a very good approximation, governed microscopically by a Hubbard Hamiltonian [Jak98] with a local onsite interaction energy U and kinetic energy J, which corresponds to tunneling of atoms from one lattice site to the next. Experiments with Bose-Einstein condensates (BEC) of Rb atoms have demonstrated the quantum phase transition from a superfluid phase for large J to an insulating Mott-Hubbard (MH) phase [Gre02]. The transition between these two phases was obtained by quenching J in a lattice of finite depth. Recent experiments with fermionic atoms have demonstrated the presence of a fermionic MH insulating state [Jör08, Sch08], potentially opening the way to the study of high-temperature superconductivity in proximity of the MH phase in 2D.

While the focus in the study of quantum phase transitions in the context of ultracold atoms has so far been on Hubbard-type physics in the weakly interacting regime, novel quantum phenomena occur in lower dimensions, where the effects of quantum fluctuations and correlations are enhanced. In a 1D bosonic gas, strong repulsive interactions lead to the

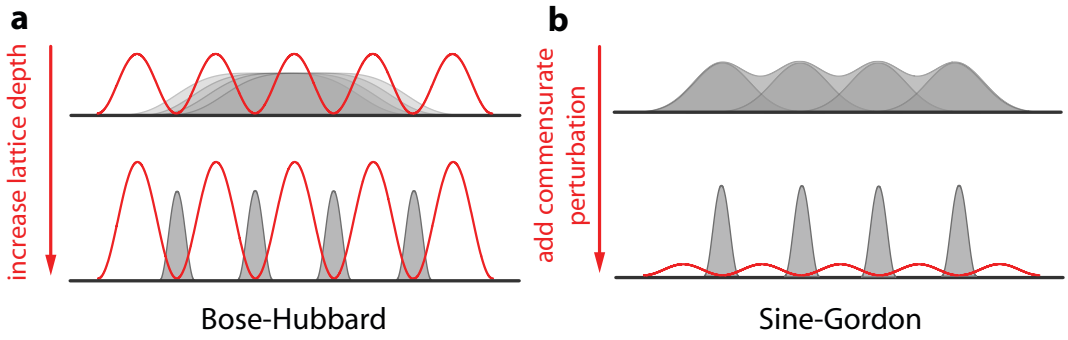

Figure 4.1: Comparing two types of superfluid-to-Mott-insulator phase transitions in 1D. Schematic density distributions (grey) in the presence of a periodic potential (red solid line). **a**, Mott-Hubbard type quantum phase transition for weak interactions [Gre02]. The system is still superfluid at finite lattice depth (top). The transition to the insulating state is induced by raising the lattice depth above a finite critical value (bottom). **b**, Sine-Gordon type quantum phase transition for strong interactions [Büc03b]. In the absence of any perturbation, the system is a strongly correlated superfluid (top). For sufficiently strong interactions, not necessarily infinitely strong, an arbitrarily weak perturbation by a lattice potential commensurate with the system's granularity induces the transition to the insulating Mott state (bottom).

formation of a Tonks-Girardeau (TG) gas, where bosons minimize their interaction energy by avoiding spatial overlap and acquire fermionic properties [Gir60, Kin04, Par04, Hal09]. The addition of an arbitrarily weak lattice potential commensurate with the atomic density, i.e. $n \sim 2/\lambda$, where n is the linear 1D density and $\lambda/2$ is the lattice periodicity, is expected to lead to a novel kind of quantum phase transition [Gia03, Büc03b]: the strongly correlated 1D gas is immediately pinned by the lattice and the superfluid TG phase is turned into an insulating, gapped phase. Figure 4.1 contrasts the Hubbard-type superfluid-to-Mott-insulator transition to this pinning transition. Given the universality of 1D quantum physics, the pinning transition will occur for interacting bosons as well as for fermions in 1D and has been discussed with respect to a variety of quantum models in low dimensions [Gia03].

4.2 The pinning transition

The pinning transition is described by the (1+1) quantum sine-Gordon (sG) model, which is an exactly solvable quantum field theory, extensively studied in high energy, condensed matter, and mathematical physics [Gog98]. The sG Hamiltonian reads

$$\mathcal{H} = \frac{\hbar v_s}{2\pi} \int dx[(\partial_x\theta)^2 + (\partial_x\phi)^2 + \mathcal{V}\cos(\sqrt{4K}\theta)]. \tag{4.1}$$

Here, $\partial_x\theta$ and $\partial_x\phi$ are the fluctuations of the long-wavelength density and phase fields θ and ϕ, respectively, of the hydrodynamic description of the 1D liquid with commutation relation $[\partial_x\theta(x), \phi(y)] = i\pi\delta(x-y)$, v_s is the velocity of the soundlike excitations of the 1D

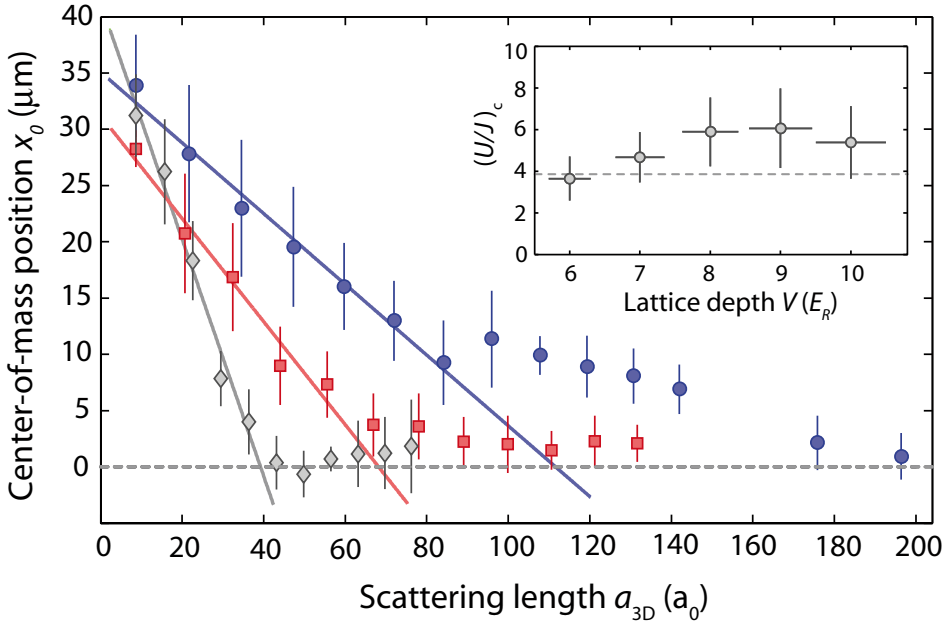

Figure 4.2: Transport measurements on the 1D Bose gas. Center-of-mass displacement x_0 as a function of a_{3D} for different values of V ($V = 9.0(5)E_R$ (diamonds), $V = 5.0(3)E_R$ (squares), $V = 2.0(1)E_R$ (circles)). We extrapolate the linear slope at small values for a_{3D} and associate the transition point with the axis intercept. For the data with $V = 2.0(1)E_R$ transport is not fully quenched as the condition of commensurability is not fulfilled for all atoms. All errors are the 1σ statistical error. The inset plots the mesured critical ratio $(U/J)_c$ at the transition point as a function of lattice depth V. The dashed line indicates the theoretical result $(U/J)_c \approx 3.85$ for the 1D Bose-Hubbard regime [Rap99].

gas, $\mathcal{V} = Vn\pi/(\hbar v_s)$ is proportional to the depth V of a weak lattice [Gia03, Büc03b], and $\hbar$ is Planck's constant h divided by 2π. For vanishing lattice $\mathcal{V} = 0$, Eq. (4.1) describes a Luttinger liquid, where the strength of interactions is parameterized by the dimensionless parameter $K = \hbar\pi n/(mv_s)$, which determines the long-distance power-law decay of the correlation functions, e.g. $\langle n(x)n(x')\rangle \sim n^2 + cK/(x-x')^2 + c'\cos(2\pi n * (x-x'))/(x-x')^{2K} + \ldots$, with c and c' constants and m the atomic mass. The sG model with a weak but finite lattice predicts a quantum phase transition of the Berezinskii-Kosterlitz-Thouless (BKT) type between a superfluid state for $K > K_c = 2$, where the shallow lattice is an irrelevant perturbation, to an insulating Mott phase for $K < K_c$, for which the spectrum is gapped for any value of $\mathcal{V}$.

While in general K is a phenomenological parameter, in the case of a 1D bosonic gas it can be microscopically related to the Lieb-Liniger parameter $\gamma = mg/(\hbar^2 n)$, which characterizes interactions in a homogenous 1D system [Lie63b] (see Methods). Here, $g \simeq 2\hbar\omega_\perp a_{3D}$ is the coupling constant of the 1D δ-function interaction potential $U(x) = g\delta(x)$, where $\omega_\perp$ is the frequency of transverse confinement and a_{3D} is the 3D scattering length. The strength of interactions, and thus K, can be tuned by varying a_{3D} near a Feshbach resonance [Chi10]. The TG regime corresponds to $\gamma \gg 1$. Using the relation between K and γ, Büchler and

coworkers [Büc03b] have shown that particles are pinned for experimentally accessible values of $\gamma > \gamma_c \simeq 3.5$ in the limit of a vanishingly weak lattice. The pinning transition is expected to continuously transform into the MH-type quantum phase transition, which occurs for the weakly interacting gas when the lattice depth becomes sufficiently large. Here, using a quantum gas of caesium (Cs) atoms with tunable interactions confined to an array of independent 1D tubes (see Methods), we drive the superfluid-to-Mott-insulator phase transition by varying γ and determine the phase boundary all the way from the strongly to the weakly interacting regime using modulation spectroscopy and measurement of transport. For shallow lattices under conditions of commensurability, we observe immediate pinning of the particles for strong interactions when $\gamma > \gamma_c$.

4.3 Experimental procedure

We first discuss our experiments in the strongly interacting regime. We start with a 3D Bose-Einstein condensate (BEC) of typically 1.3×10^5 Cs atoms without detectable thermal fraction in a crossed-beam dipole trap with magnetic levitation [Kra04] and initialize our system by creating a conventional 3D MH-state in a deep 3D lattice at $U/(6J) \approx 75$ with precisely one atom per lattice site [Gre02]. We find, by reversing the loading, that the procedure does not lead to heating of the sample. The array of 1D tubes is obtained by reducing the lattice depth V along one direction. Our procedure ensures that a majority of tubes has a near-commensurate number density (see Methods). A Feshbach resonance allows us to control a_{3D} with a precision of $3\ a_0$ limited by the presence of the magnetic field gradient. Here, a_0 is Bohr's radius. For the case of the shallow lattice, we probe the state of the system by amplitude modulation spectroscopy [Stö04, Iuc06]. We determine the presence of an excitation gap E_g by testing whether energy can be deposited into the 1D system at a given excitation frequency f. The lattice depth V is modulated at f by 25% to 45% for $40 - 60$ ms. After ramping down the lattice beams adiabatically with respect to the lattice band structure and after a levitated expansion time of $40 - 60$ ms [Kra04], we detect the atoms by time-of-flight absorption imaging. We determine the spatial width of the atomic sample from a gaussian fit to the absorption profile and obtain the change δ of the spatial width compared to the unmodulated case as a function of f. Two typical measurements are shown in Fig. 4.3(a), one in the superfluid phase and one deep in the 1D Mott phase at the same value for the lattice depth, $V = 1.5(1)E_R$, where $E_R = h^2/(2m\lambda^2)$ is the photon recoil energy. For weak interactions the system exhibits a linear increase for δ as a function of f, which we attribute to the superfluid character of the gas. For strong interactions, the increase, after a slow rise, shows a clear kink. We attribute the initial slow rise to excitation of residual superfluid portions of our inhomogeneous system and the sudden change in slope to the presence of an excitation gap. We associate the axis intercept f_g obtained from a linear fit to the steep part

of the spectrum with the frequency of the gap. To determine the phase transition from the 1D Mott state to the superfluid state, we repeat this measurement for a given depth V as we scan γ by changing a_{3D}. A typical result is shown in Fig. 4.3(c). The gap closes as γ is reduced. For values $V \leq 2.0E_R$, the transition point is identified with the abrupt step, i.e. we determine the critical value $\gamma_{c,V}$ at which the transition happens by an error-function fit to the data. Note that we always observe some small residual value for f_g of about 120 Hz for weak interactions. In general, we find that the measured value for the frequency of the gap is robust against variations of modulation amplitude, while the slope increases with stronger modulation.

For comparison, we present in Fig. 4.3(b) and (d) excitation spectra for an intermediate value of the lattice depth and for the case of a deep lattice, respectively. For $V = 3.0(2)E_R$ the spectrum shows additional structure for high frequencies as band structure comes into play. We find that for $V > 2.0E_R$ the gap opens up approximately linearly as a function of γ beyond a critical $\gamma_{c,V}$, see inset to Fig. 4.3(c). For deep lattices and for comparatively weak interactions the spectrum exhibits a broad distribution characteristic of a superfluid. For stronger interactions we recover the discrete excitation spectrum of the Mott phase in the Hubbard regime [Gre02, Stö04] with a pronounced peak at $f = 1.0\ U/h$. Additional peaks [Cla06b] can be found at $f = 0.5\ U/h$ and above $f = 1.5\ U/h$.

For the case of a deep lattice, we find that the state of the system is very sensitively probed by transport measurements [Fer05, Mun07]. A characteristic property of the Mott state is the inhibition of particle motion. In our experiment with the capability to tune interactions we expect the phase transition to manifests itself, at fixed V, through a strong suppression of transport when the strength of the interaction is raised above a certain critical value. Essentially, we test whether momentum can be imparted to the 1D system as a function of interaction strength. For a given V we apply a weak axial magnetic force for a brief time to the interacting system, chosen such that the imparted momentum would be approximately $0.2\hbar k$ if the system were non-interacting. Then, as a function of a_{3D}, we determine the center-of-mass displacement x_0 of the sample after a fixed time of flight. Fig. 4.2 shows that x_0 decreases monotonically with a_{3D}. For the case of a deep lattice with $V = 9.0(5)E_R$ the quenching of transport is abrupt. At a certain critical value for a_{3D} transport is fully inhibited [Alt05, Sch10]. We find the critical a_{3D} by a linear fit to the decreasing data and by determining the axis intercept and derive from this a critical $\gamma_{c,V}$. Reducing the lattice depth to $V = 5.0(3)E_R$ and $V = 2.0(1)E_R$ leads to a less abrupt quenching of transport. For stronger interactions, the decrease starts to level off. Nevertheless, the initial decrease is still linear, allowing us to determine the critical $\gamma_{c,V}$ by an extrapolation of the initially linear decrease to zero. The inset to Fig. 4.2 shows the measured critical ratio $(U/J)_c$ determined by our transport method as a function of lattice depth V. When we compare our results with the predicted value [Rap99] of $(U/J)_c \approx 3.85$ for the transition in 1D, we find a slight sys-

tematic overestimation of the transition point. This, however, is expected in view of e.g. the spatial inhomogeneity of the sample and the BKT-type nature of the transition in a finite size system.

4.4 Phase diagram

We summarize our results in Fig. 4.4, where we present the phase diagram as a function of $1/\gamma$ and V. The set $\{\gamma_{c,V}\}$ defines the phase boundary between the 1D Mott insulator and the 1D superfluid. The measurements based on modulation spectroscopy cover a range from $V = 4E_R$ down to $0.5E_R$ (circles), while the transport measurements extend from $V = 2E_R$ to $10E_R$ (squares). In the weakly interacting regime, $1/\gamma > 2$, our data are in good agreement with the prediction of the MH model (dashed line). In the strongly interacting regime, $1/\gamma < 1$, the measured phase boundary extrapolates to a finite critical value $1/\gamma_c$ for the Lieb-Liniger parameter as the lattice depth V is reduced to zero. Our results are in excellent quantitative agreement with the theory for a commensurate system based on the sine-Gordon model (solid line, see Methods), for which $\gamma_c = 3.5$. We also find good agreement between our two types of measurement techniques in the intermediate regime ($V = 2E_R$ to $4E_R$). Our results demonstrate the striking consequence of strong interactions in 1D geometry in the presence of a lattice: Beyond a critical value γ_c, an insulating Mott state exists for vanishingly small lattice depth V. The particles are immediately pinned by the lattice.

We measure a finite gap energy E_g for $\gamma > \gamma_c$ in the regime of a shallow lattice. In the limit of $\gamma \to \infty$ and $V \to 0$ one would expect the simple relation $E_g = V/2$ as the bosonic system has become fully fermionized and the lattice effectively induces a band insulator of fermions [Büc03b]. In the inset to Fig. 4.4 we plot the measured E_g as a function of V at fixed $\gamma = 11(1)$. For $V < 1E_R$ our data is in good agreement with the analytical result for the gap energy at finite γ (see Methods). Note that, for $V \geq 1E_R$, we observe a deviation for E_g away from the predicted values. This deviation occurs at rather shallow lattices. However, one does expect the curve to have a reduced slope for deeper lattices, for which E_g becomes of order U and is only weakly dependent on V.

Our results are a benchmark realization of quantum field theory models with tunable parameters in cold atomic systems. These results open up the experimental study of the out-of-equilibrium properties of sine-Gordon-type models. In particular, thermalization in integrable models beyond the Luttinger liquid model, quenches across quantum phase transitions, and their relations to the breakdown of the adiabatic theorem in low dimensions can now be investigated with full tunability of system parameters.

4.5 Methods Summary

4.5.1 Sample preparation.

We begin with a BEC with no detectable thermal fraction of typically 1.3×10^5 Cs atoms in the $|F = 3, m_F = 3 >$ hyperfine ground state in a crossed-beam dipole trap with magnetic levitation. Details of the BEC preparation are presented elsewhere [Kra04]. The BEC is adiabatically transferred to the 3D lattice by exponentially ramping up the power in the lattice laser beams within 300 ms. We create a 3D Hubbard-type Mott insulator with precisely one atom per site in the central region of the trap by adjusting the external dipole trap confinement prior to loading into the lattice. The array of vertically oriented tubes is created by ramping down the power in the vertically propagating beam pair. Typical trapping frequencies for the tubes are $\omega_{r,z} = 2\pi \times (12300(200), 21.9(3))$ Hz along the transversal and longitudinal directions, respectively.

It is not necessary to strictly adhere to the commensurate density condition to observe the pinning transition at very weak lattices [Büc03b]. However, we prepare our sample such that the commensurability condition is on average best fulfilled over the inhomogeneously populated array of tubes. We find this optimal configuration when the total atom number is chosen such that the peak density of the center tube is approximately $1.2\, n_{\mathrm{c}}$, where $n_{\mathrm{c}} = 2/\lambda$ is the commensurate 1D density. Typically there are about 60 atoms in the center tube.

4.5.2 Phase transition line.

For the case of a 1D Bose gas in a weak optical lattice the effective sine-Gordon Hamiltonian Eq. (4.1) is realized. In this regime, the BKT transition line between the superfluid and the Mott-insulating phases can be derived in terms of V and $\gamma = \gamma_{\mathrm{c},V}$ as

$$\frac{V}{E_{\mathrm{R}}} = 2\left(\frac{\pi}{\sqrt{\gamma - \gamma^{3/2}/(2\pi)}} - 2\right).$$

When the system is weakly interacting, $\gamma \ll 1$, and for deeper lattices, $V \gg 1E_{\mathrm{R}}$, the system can be described by the Bose-Hubbard Hamiltonian [Jak98]. In this regime, the quantum phase transition between a superfluid and a MH state occurs at [Rap99] $(U/J)_{\mathrm{c}} \approx 3.85$, which determines a transition line in the (V, γ) - plane via

$$\frac{4V}{E_{\mathrm{R}}} = \ln^2\left[\frac{2\sqrt{2}\pi}{\gamma}\left(\frac{U}{J}\right)_{\mathrm{c}}\sqrt{\frac{V}{E_{\mathrm{R}}}}\right].$$

Here, J is the hopping energy, and U is onsite interaction energy of the Bose-Hubbard model.

We thank W. Zwerger for discussions. We are indebted to R. Grimm for generous support. We gratefully acknowledge funding by the Austrian Ministry of Science and Research (Bundesministerium für Wissenschaft und Forschung, BMWF) and the Austrian Science Fund (Fonds zur Förderung der wissenschaftlichen Forschung, FWF) in form of a START prize grant and by the European Union through the STREP FP7-ICT-2007-C project NAME-QUAM (Nanodesigning of Atomic and MolEcular QUAntum Matter) and within the framework of the EuroQUASAR collective research project QuDeGPM. R.H. is supported by a Marie Curie International Incoming Fellowship within the 7th European Community Framework Programme.

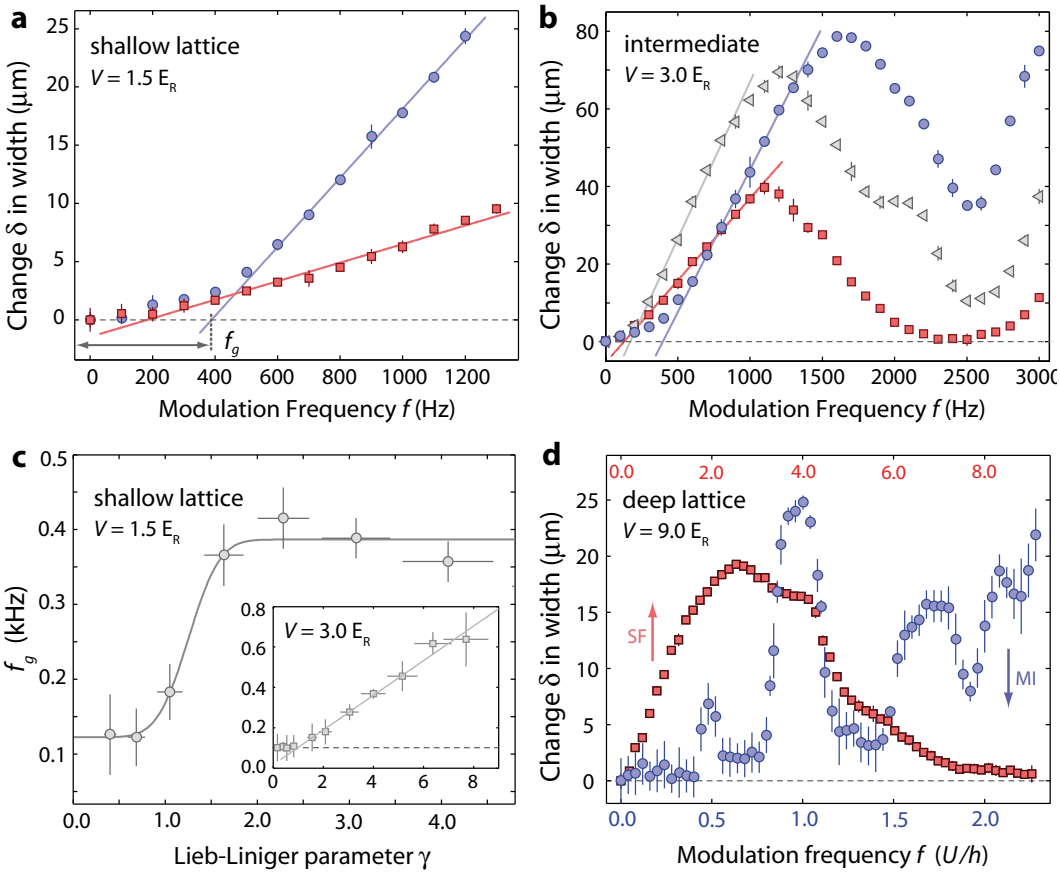

Figure 4.3: Modulation spectroscopy on bosons in 1D. a, b, d, Excitation spectra for low, intermediate, and high lattice depth V. The change δ of the spatial width after amplitude modulation is plotted as a function of the modulation frequency f for different values of γ. **a**, Characteristic spectra for $V = 1.5(1)E_{\mathrm{R}}$ in the superfluid (squares, $a_{3\mathrm{D}} = 115(2)\ a_0$, $\gamma = 1.0(1)$) and in the Mott regime (circles, $a_{3\mathrm{D}} = 261(2)\ a_0$, $\gamma = 3.1(2)$). The solid lines are linear fits to the high-frequency part of the spectrum. We determine the axis intercept f_{g} as indicated. **b**, Spectra for $V = 3.0(2)E_{\mathrm{R}}$. The system is superfluid at $\gamma = 0.51(6)$ (squares), while it exhibits a gap for $\gamma = 1.6(1)$ (triangles) and $\gamma = 4.1(3)$ (circles). **c**, Determination of the transition point for the case of the shallow lattice with $V = 1.5(1)E_{\mathrm{R}}$. The frequency f_{g} is plotted as a function of γ. The solid line is an error-function fit to the data. The inset plots f_{g} as a function of γ for $V = 3.0(2)E_{\mathrm{R}}$. **d**, Spectra for $V = 9.0(5)E_{\mathrm{R}}$ for weak (squares, $\gamma = 0.10(3)$) and strong (circles, $\gamma = 8.1(4)$) interactions in the superfluid (SF) and Mott insulator (MI) regimes. Here, f is in units of U. Modulation parameters and errors bars are discussed in the Methods.

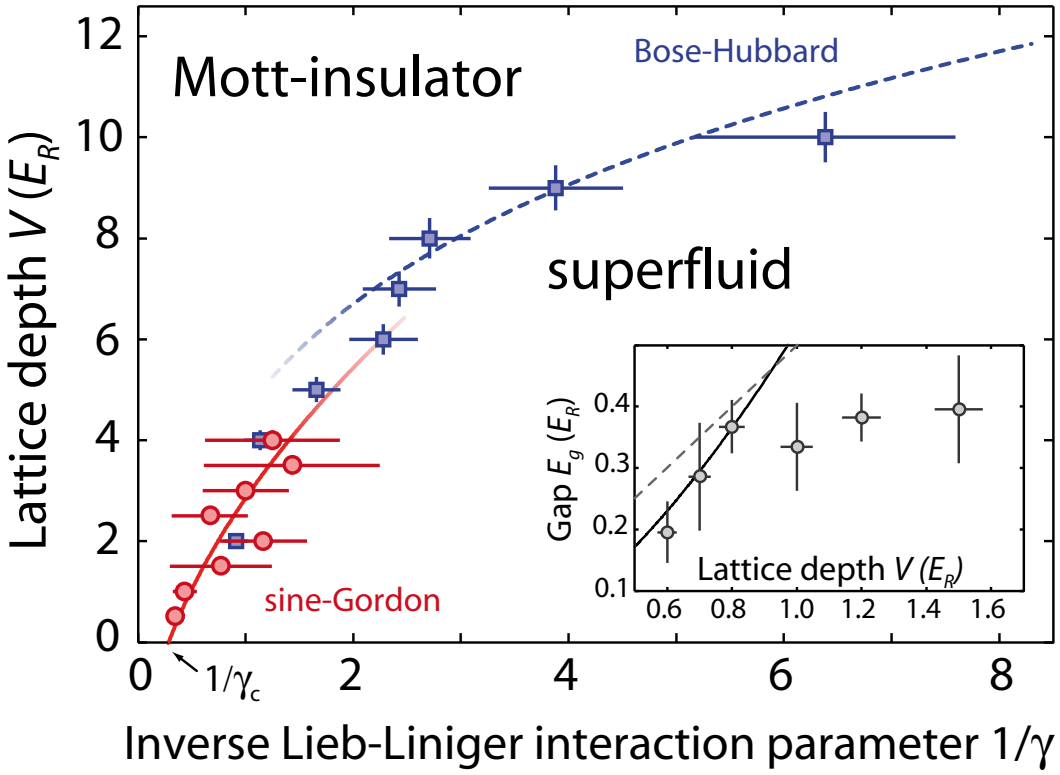

Figure 4.4: Phase diagram for the strongly interacting 1D Bose gas. Superfluid and Mott insulating phases in 1D versus inverse Lieb-Lininger interaction parameter $1/\gamma$ and optical lattice depth V in units of the photon recoil energy E_{R}. The critical interaction parameter is γ_{c}. For strong interactions and shallow lattices we determine the transition by amplitude modulation spectroscopy (circles). For weak interactions and deep lattices we probe the phase boundary by transport measurements (squares). The solid (dashed) line is the prediction from the sine-Gordon (Bose-Hubbard) model. Error bars are discussed in the Methods. The inset plots the measured gap energy $E_{\mathrm{g}} = hf_{\mathrm{g}}$ as a function of V for $\gamma = 11(1)$ and compares our data to the analytical result for finite γ as given by the sine-Gordon model (solid line, see Methods). Also shown is the universal behavior $E_{\mathrm{g}} = V/2$, which is valid for non-interacting fermions (dashed line).

4.6 Methods

4.6.1 1D Bose gas in a weak optical lattice.

In the absence of the optical lattice, $V = 0$, the Luttinger liquid parameter K can be expressed in terms of the Lieb-Liniger parameter $\gamma = gm/(\hbar^2 n)$ for all strengths of interactions [Lie63b, Caz04]. For $\gamma \leq 10$ and $\gamma \gg 10$ one gets $K \simeq \pi/\sqrt{\gamma - \gamma^{3/2}/(2\pi)}$ and $K \simeq (1+2/\gamma)^2$, respectively. The addition of a weak but finite commensurate optical lattice with $V \leq 1E_{\mathrm{R}}$ realizes the effective sine-Gordon Hamiltonian Eq. (4.1). Using a perturbative renormalization group approach, the BKT transition line between the superfluid and the Mott-insulating phases can be derived in terms of V and $\gamma = \gamma_{\mathrm{c},V}$ as

$$\frac{V}{E_{\mathrm{R}}} = 2\left(\frac{\pi}{\sqrt{\gamma - \gamma^{3/2}/(2\pi)}} - 2\right).$$

For small lattice depths, the integrable structure of the sine-Gordon model [Zam79, Zam95] allows one to derive the following analytical expression for the dependence of the spectral gap E_{g} on V and K

$$\frac{E_{\mathrm{g}}}{E_{\mathrm{R}}} = \frac{8\Gamma[\frac{\pi K}{2(2-K)}]}{\sqrt{\pi}\Gamma[\frac{1}{2}\frac{2+K(\pi-1)}{2-K}]}\left[\left(\frac{K^2 V}{16 E_{\mathrm{R}}}\right)\frac{\Gamma[1-\frac{K}{2}]}{\Gamma[1+\frac{K}{2}]}\right]^{\frac{1}{2-K}}.$$

Here, Γ is the gamma function. For strong interactions $K \simeq 1$, the dependence of the gap on V is linear, and E_{g} approaches the free fermion value $E_{\mathrm{g}} = V/2$. In the vicinity of $K = 2$, the gap closes exponentially approaching the BKT transition line.

4.6.2 Deep lattice: the Bose-Hubbard model.

In the weakly interacting regime $\gamma \ll 1$, for $V \gg 1E_{\mathrm{R}}$, when all atoms occupy the lowest vibrational state in each potential well of the lattice, the system can be described by the following Bose-Hubbard model [Jak98]

$$H = -J\sum_i (b_i^\dagger b_{i+1} + h.c.) + \frac{U}{2}\sum_i b_i^\dagger b_i^\dagger b_i b_i.$$

Here, b_i ($b_i^\dagger$) is the operator destroying (creating) a bosonic particle at the position of the i^{th}-well, $J = 4E_{\mathrm{R}}(V/E_{\mathrm{R}})^{\frac{3}{4}}\exp[-2\sqrt{V/E_{\mathrm{R}}}]/\sqrt{\pi}$ is the hopping energy, and $U = \sqrt{2\pi}g(V/E_{\mathrm{R}})^{1/4}/\lambda$ is onsite interaction energy. The quantum phase transition between a superfluid and a MH state occurs at [Rap99] $(U/J)_{\mathrm{c}} \approx 3.85$, which determines a transition line in the (V, γ) - plane

via

$$\frac{4V}{E_{\mathrm{R}}} = \ln^2\left[\frac{2\sqrt{2}\pi}{\gamma}\left(\frac{U}{J}\right)_{\mathrm{c}}\sqrt{\frac{V}{E_{\mathrm{R}}}}\right].$$

4.6.3 Magnetic Feshbach resonance

The strength of interaction can be tuned by means of a broad magnetic Feshbach resonance with a pole at -11.7 G and with a zero crossing for the scattering length near 17 G [Kra04]. To hold the atoms in the vertically oriented tubes, magnetic levitation by means of a magnetic field gradient is applied. For a cesium atom in the hyperfine state $|F = 3, m_F = 3\rangle$ a magnetic field gradient of 31.1 G/cm cancels the gravitational force.

4.6.4 Lattice loading and array of 1D tubes.

We create a 3D optical lattice by interference of 3 pairs of counterpropagating dipole trap laser beams at wavelength $\lambda = 1064.5$ nm with $1/e^2$ beam waists of ~ 350 μm. The atomic BEC, initially trapped in a crossed-beam dipole trap, is adiabatically transferred to the 3D lattice by exponentially ramping up the power in the lattice laser beams within 300 ms. At the same time we increase the interaction strength by linearly raising the magnetic field strength and finally reach a 3D Hubbard-type Mott insulator with precisely one atom per site in the central region. The array of vertically oriented tubes is created by linearly ramping down the power in the vertically propagating beam pair in 100 ms reaching lattice depths from 10 to 0.5 E_R. At the same time we linearly reduce the magnetic field strength to set $a_{3\mathrm{D}}$. Typical trapping frequencies for the tubes are $\omega_{r,z} = 2\pi \times (12300(200), 21.9(3))$ Hz along the transversal and longitudinal directions, respectively. The depth of the lattice along the tubes is calibrated by the pulsed Raman-Nath technique [Gou86]. The transversal trapping frequencies of the tubes are determined by parametric heating measurements. The distribution of the atom number per tube can be directly determined from the density distribution in the Mott-insulating phase and shows an occupation of about 60 atoms in the center tube. Here, we assume a constant filling factor of one atom and no thermal or superfluid components. In view of our inhomogeneous system we calculate γ, for a given tube, by assuming a 1D Thomas-Fermi distribution and taking the center density. The reported γ is a weighted average over all tubes.

4.6.5 Commensurability.

To observe the pinning transition it is not necessary to fulfill the condition of commensurability precisely [Büc03b]. A finite commensurability parameter $Q = 2\pi(n - n_{\mathrm{c}})$ corresponds to a shift $\delta\mu$ of the chemical potential. Here, $n_{\mathrm{c}} = 2/\lambda$ is the commensurate 1D density. The system stays locked to the Mott insulating phase as long as $\delta\mu$ remains smaller than the

energy necessary to add another atom. When Q rises beyond a critical value $Q_c(\gamma, V)$, the system develops finite density excitations, which destroy the long range order of the Mott insulator. We find that, for the array of 1D tubes, the commensurability condition in the superfluid regime is fulfilled best when the total atom number is chosen in such a way that the peak density of the center tube is approximately $1.2\ n_c$.

4.6.6 Modulation parameters and error bars.

For the data in Fig. 4.3 **a, b, d** we chose the following modulation times and amplitudes: **a** 40 ms, 35%, **b** 40 ms, 30%, **d** 30 ms, 35% for the superfluid phase and 25% for the Mott phase. In Fig. 4.3 **a, b, d**, the error bars for δ reflect the 1σ statistical error. In Fig. 4.3 **c**, the error bars for f_g are derived from the 1σ error on the fit parameters. The error for γ results from the 1σ statistical error of the independent input variables and the spread of γ due to the distribution of tubes. For the data in Fig. 4.4 the error in γ is derived from the 1σ error of the fit parameters for the modulation measurements. For the transport measurements, the error in γ results from the 1σ statistical error of the independent input variables and the spread of γ due to the distribution of tubes.

CHAPTER 5

PUBLICATION

Control of Interaction-Induced Dephasing of Bloch Oscillations

Phys. Rev. Lett. **100**, 080404 (2008).

M. Gustavsson, E. Haller, M. J. Mark, J. G. Danzl, G. Rojas-Kopeinig, H.-C. Nägerl

Institut für Experimentalphysik und Zentrum für Quantenphysik, Universität Innsbruck, Technikerstraße 25, A–6020 Innsbruck, Austria

We report on the control of interaction-induced dephasing of Bloch oscillations for an atomic Bose-Einstein condensate in an optical lattice under the influence of gravity. When tuning the strength of the interaction towards zero by means of a Feshbach resonance, the dephasing time is increased from a few to more than twenty thousand Bloch oscillation periods. We quantify the dephasing in terms of the width of the quasi-momentum distribution and measure its dependence on time for different values of the scattering length. Minimizing the dephasing allows us to realize a BEC-based atom interferometer in the non-interacting limit. We use it for a precise determination of a zero-crossing for the atomic scattering length and to observe collapse and revivals of Bloch oscillations when the atomic sample is subject to a spatial force gradient.

5.1 Introduction

Ultracold atomic systems have initiated a revolution in the field of precision measurements. Laser cooled thermal samples are used for ultra-high resolution laser spectroscopy [Did04], they are at the heart of modern atomic fountain clocks [Biz05, Boy07], and they allow the realization of matter-wave interferometers for high-precision inertial sensing [Pet80] and high-precision determination of fundamental constants [Cla06a]. Atomic Bose-Einstein con-

densates (BEC), the matter-wave analoga to the laser, combine high brightness with narrow spatial and momentum spread. In general, the resolution is limited only by the quantum mechanical uncertainty principle, and BECs could thus serve as ideal sources for precision measurements and in particular for matter wave interferometers [Gup02]. Atom-atom interactions, however, have to be taken into account, as they lead to collisional dephasing and give rise to density dependent mean-field shifts in the interferometric signal. It is thus advisable to either operate a BEC-based atom interferometer in the dilute density limit, possibly sacrificing a high signal-to-noise ratio, or to find ways of reducing or even nulling the strength of the interaction altogether. Precisely the latter is feasible in the vicinity of magnetically induced Feshbach resonances where the atomic s-wave scattering length and hence the strength of the atom-atom contact interaction go through a zero crossing [Köh06]. It is thus possible to experimentally investigate the reduction and even disappearance of interaction-induced effects on the interferometric signal as the scattering length is tuned towards zero by means of an externally controlled magnetic field.

A paradigm atom interferometric effect is the well-known phenomenon of Bloch oscillations [Ben96]. Bloch oscillations for the mean quasi-momentum are the result of single atom interference as the atomic wavepacket, subject to a constant force, is Bragg reflected in the presence of a periodic optical lattice potential. They have been observed for ultracold thermal samples [Ben96, Bat04, Cla06a, Fer06], for atoms in interacting BECs [Mor01, Roa04], and for ensembles of non-interacting quantum-degenerate fermions [Roa04]. For the case of the interacting BEC, strong dephasing is found as evidenced by a rapid broadening and apparent smearing out of the momentum distribution in the first Brillouin zone, limiting the observation of Bloch oscillations to a few cycles for typical atomic densities in a BEC. In addition, the measured initial width of the momentum distribution is comparable to the extent of the Brillouin zone, as interaction energy is converted into kinetic energy upon release of the BEC from the lattice potential, thus greatly reducing the contrast of the oscillations [Roa04].

In this Letter, we report on the control of interaction induced dephasing of Bloch oscillations for a BEC in a vertically oriented optical lattice under the influence of gravity. Control is obtained by means of a zero crossing for the atomic s-wave scattering length a. We observe the transition from an interacting BEC to a non-interacting BEC by measuring the rate of dephasing, given by the change of the width of the momentum distribution, as a function of a. We identify a clear minimum for the dephasing which we associate with the zero crossing for a. At the minimum more than 2×10^4 oscillations can be observed with high contrast, and the zero crossing can be determined with high precision. For our measurements at non-zero scattering length, we greatly reduce broadening of the momentum distribution by rapidly switching the interaction strength to zero upon release from the lattice potential. Our measurements indicate that BECs can indeed be used as a source for precision atom interferometry, as effects of the interaction can be greatly reduced. For a non-interacting BEC,

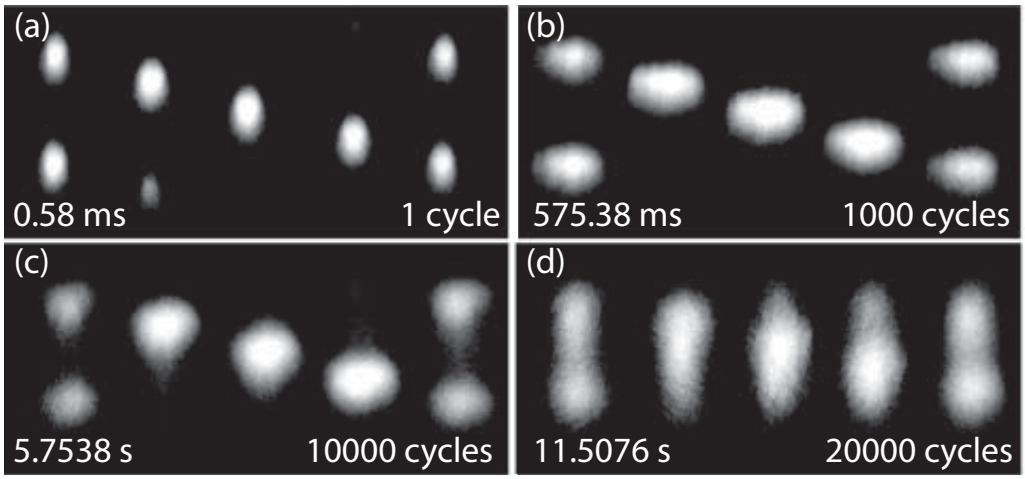

Figure 5.1: Long-lived Bloch oscillations for a non-interacting BEC with Cs atoms in the vertical lattice under the influence of gravity. Each picture shows one Bloch cycle in successive time-of-flight absorption images corresponding to the momentum distribution at the time of release from the lattice. Displayed are the first (a), the 1000^{th} (b), the 10000^{th} (c), and the 20000^{th} (d) Bloch cycle for minimal interaction near the zero crossing for the scattering length.

we intentionally induce dephasing by means of a weak optical force gradient and observe collapse and revivals of Bloch oscillations.

5.2 Experimental procedure

The starting point for our experiments is an essentially pure BEC with typically 1×10^5 Cs atoms in the $|F = 3, m_F = 3\rangle$ hyperfine ground state sublevel confined in a crossed-beam dipole trap generated by one vertically (L_1, with $1/e^2$-beam diameter 256 μm) and one more tightly focused horizontally (L_2, with diameter 84 μm) propagating laser beam at a wavelength near 1064 nm. We support the optical trapping by magnetic levitation against gravity [Web03]. For BEC preparation, we basically follow the procedure described in Ref. [Web03, Kra04]. The strength of the interaction can be tuned by means of a broad Feshbach resonance, which causes a zero crossing for the scattering length a near an offset magnetic field value of 17 G with a slope of $61\,a_0$/G [Jul]. Here, a_0 denotes Bohr's radius. The lattice potential is generated by a vertically oriented standing laser wave generated by retro-reflection, co-linear with L_1, but with much larger diameter of 580 μm. This allows independent control of lattice depth and radial (i.e. horizontal) confinement. The light comes from a home-built single-mode fiber amplifier [Lie03] seeded with highly-stable light at $\lambda = 1064.4946(1)$ nm. We turn on the optical lattice potential exponentially to a depth of $7.9\ E_R$ within 1000 ms, where $E_R = h^2/(2m\lambda^2) = k_B \times 64$ nK is the photon recoil energy and m is the mass of the Cs atom. The slow ramp assures that the BEC is adiabatically loaded into the lowest Bloch band of the lattice. We load between 40 to 65 lattice sites, depending on the initial vertical extent of

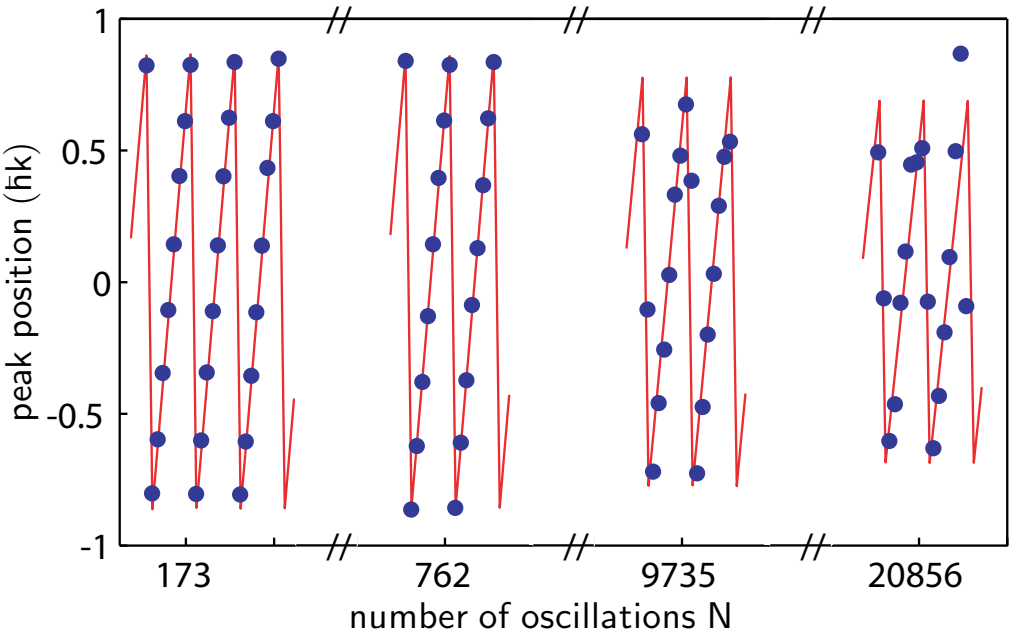

Figure 5.2: (color online). Position of the strongest peak in the momentum distribution as a function of the number N of Bloch oscillations (dots). More than 20000 cycles can be followed with high contrast. A fit to the data (solid curve) yields a Bloch period of $0.5753807(5)$ ms.

the BEC. We then reduce the power in L_2 to zero within $300\,\mu$s. Subsequently, the magnetic field gradient needed for levitation is ramped down and a bias magnetic field is tuned to the desired value within $100\,\mu$s. For the present experiments, we adjust a in the range from -2 to $300\,a_0$ with magnetic bias fields from 17 to 23 G. We control the average bias field to about 1 mG. The confinement of the BEC in the lattice as given by L_1 gives horizontal trapping frequencies in the range of 5 to 10 Hz. We then let the atoms evolve in the lattice under the influence of the gravitational force for variable hold time T. Finally, we switch off the horizontal confinement and ramp the lattice depth adiabatically to zero within $300\,\mu$s to measure the momentum distribution by the standard time-of-flight technique, taking an absorption picture on a CCD camera. For some of the data we turn on the magnetic levitation field to allow for longer expansion times up to 100 ms. To minimize broadening of the distribution as a result of interaction we switch the scattering length to zero during the release and the initial time-of-flight.

5.3 Bloch oscillations with weak interactions

We observe persistent Bloch oscillations when minimizing the effect of interactions at a magnetic field value of 17.12 G (see below). Fig. 5.1 (a)-(d) show the evolution of the momentum distribution during the first, the 1000^{th}, the 10000^{th}, and the 20000^{th} Bloch cycle. Initially, the momentum distribution exhibits narrow peaks. Their full width Δp [Wid] is as narrow as

about $0.15\ \hbar k$, where $k = 2\pi/\lambda$. Very little broadening along the vertical direction is seen after the first 1000 cycles. Initial excitation of horizontal motion as a result of ramping the power in L_2 and switching the scattering length leads to some horizontal spreading. After 20000 cycles the distribution has started to spread out noticeably along the vertical direction.

Fig. 5.2 highlights the high number of Bloch oscillations, which we can observe for the case of minimal interaction strength. It shows how the strongest peak of the momentum distribution cycles through the first Brillouin zone with the typical sawtooth behavior [Ben96]. More than 20000 cycles can easily be followed. From a fit to the data we determine the Bloch period to $0.5753807(5)$ ms. Assuming that no additional forces act on the sample, the local gravitational constant is $g = 9.804450(9)\ \mathrm{m/s^2}$.

5.4 Interaction induced dephasing

In order to quantify the dephasing of Bloch oscillations we determine for each Bloch period the width Δp of the momentum distribution at the instant in time when the peak of the distribution is centered at zero momentum, i.e. for the central picture of each series shown in Fig. 5.1. Fig. 5.3 (a) displays Δp up to the 300^{th} Bloch cycle for different interaction strengths ranging from 0 to $300\ a_0$. For minimal interaction strength ($a \approx 0\ a_0$), we see no broadening of the distribution. Broadening can clearly be seen for $a = 25\ a_0$, and the rate of broadening then increases with increasing interaction strength. For $a \geq 50\ a_0$ the width Δp saturates within the chosen observation time to a value of about $1.3\ \hbar k$ as the momentum distribution completely fills the first Brillouin zone [Str]. To a good approximation, we find that Δp initially increases linearly with time. In Fig. 5.3 (b) we plot Δp as a function of interaction strength for various fixed numbers of Bloch cycles. Δp appears to scale with the square root of the interaction strength. Both observations agree well with a simple model for the dephasing of Bloch oscillations, which predicts $\Delta p \propto \sqrt{a} \times T$ [Wit05] for sufficiently short times T. In order to verify this model, we have performed numerical calculations solving the one-dimensional Gross-Pitaevskii equation in the presence of an optical lattice under the influence of gravity for the typical parameters of our experiment according to the method detailed in Ref. [Sme03]. Via Fourier transform of the spatial wave function we determine the momentum distribution and its width. As shown in Fig. 5.3 (solid lines) we find very good agreement with our measurements with no adjustable parameters when we add a constant offset of $0.1\ \hbar k$ to all the numerical curves. This offset takes into account residual interactions during release from the lattice as a result of the finite magnetic switching speed, which leads to some artificial broadening of the distribution. We attribute the systematic discrepancy for the $N = 50$ data in Fig. 5.3 (b) to the horizontal motion which leads to modulations in the density that adds a modulation onto Δp also seen in Fig. 5.3 (a).

To find the value for the magnetic field that gives minimal broadening we measure Δp

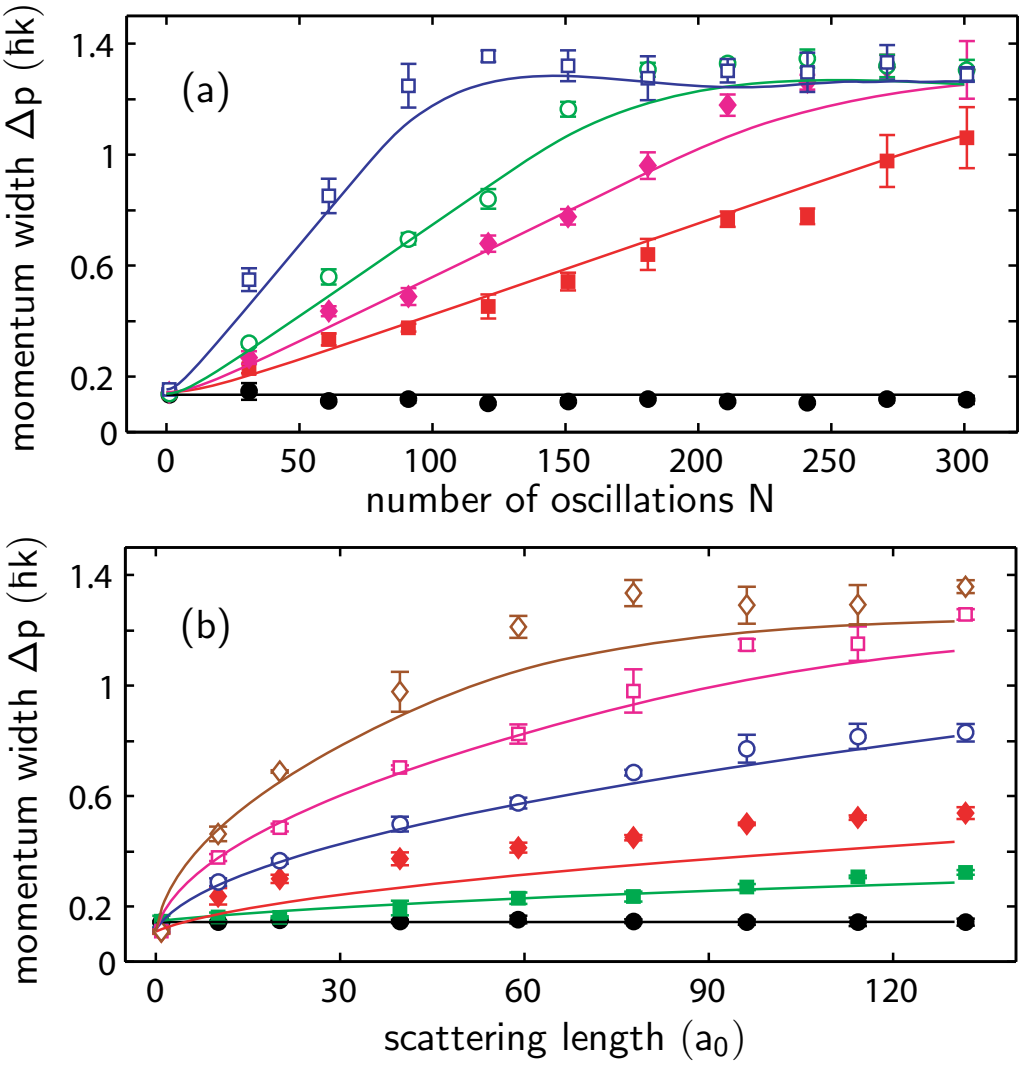

Figure 5.3: (color online). Width Δp of the momentum distribution for different interaction strengths. (a) Evolution of Δp as a function of the number N of Bloch cycles for different values of the scattering length ($a = 0, 25, 50, 100$, and $300\, a_0$ from bottom (full circles) to top (full diamonds). The solid curves are derived from a numerical model calculation, see text. (b) Width Δp for a fixed number of cycles $N = 1$ (full circles), 25 (full squares), 50 (full diamonds), 100 (open circles), 150 (open squares), and 200 (open diamonds) as a function of scattering length. The solid line represents the model calculation. All error bars correspond to $\pm$ one standard deviation resulting from 7 measurements. The data and the simulations correspond to the following parameters: lattice depth: 7.9 E_R, scattering length during lattice loading: 210 a_0, trapping frequencies in L_1 and L_2: 10 and 8 Hz, atom number in the BEC: 5×10^4.

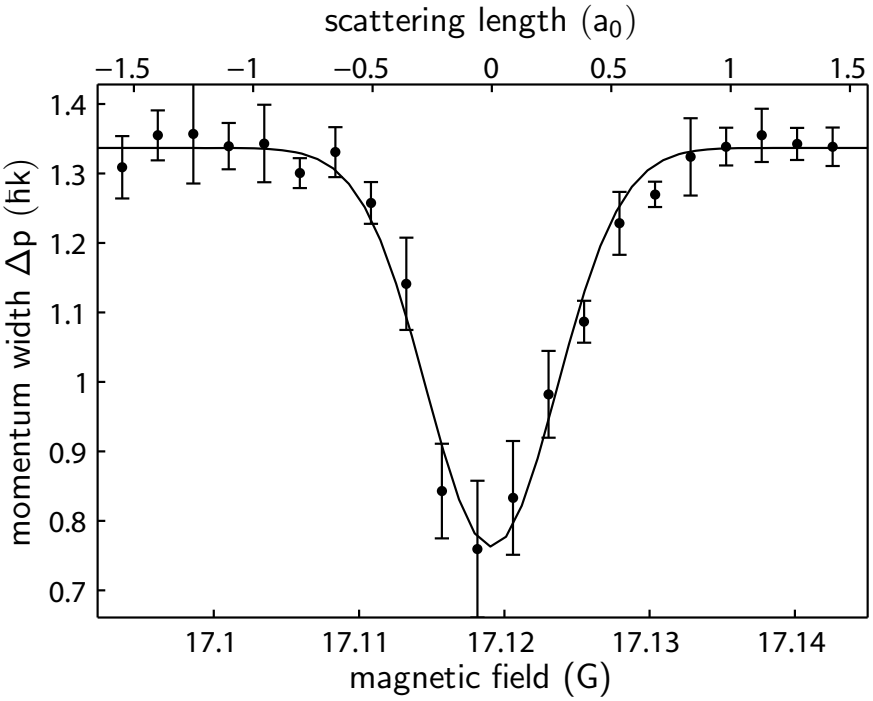

Figure 5.4: Broadening of the momentum distribution as a result of 6951 Bloch oscillations near the zero crossing for the scattering length. The width Δp is plotted as a function of magnetic field (dots). The solid line is a Gaussian fit with a rms-width of 4.5 mG. The fit is centered at $17.119(2)$ G. The zero for the scattering length scale on top was chosen to agree with this value.

after 6951 cycles in the vicinity of the crossing. Fig. 5.4 plots Δp as a function of magnetic field. It shows a clear minimum, which we expect to correspond to the zero crossing for the scattering length. From a Gaussian fit we determine the center position of the minimum to be at $17.119(2)$ G. The one-sigma error takes into account our statistical error in magnetic field calibration. To our knowledge, this is the most precise determination of a minimum for the elastic cross section in ultracold atom scattering. We believe that our measurements are limited by the ambient magnetic field noise, leading to a finite width for the distribution of the scattering length. In fact, a reduction of the atomic density gives longer decay times for the Bloch oscillations. Note that in the scattering length regime considered here the effect of the (magnetic) dipole-dipole interaction [Gio02] should start to play a role.

5.5 Revivals

Our capability to observe Bloch oscillations on extended time scales without interaction-induced dephasing allows us to study the effect of deliberately imposed dephasing. For this we apply a linear force gradient ∇F corresponding to harmonic trapping at $\nu = 40(1)$ Hz along the vertical direction by turning on L_2 during the hold time. Fig. 5.5 shows the widths Δp for two cycle phases separated by π initially corresponding to the single resp. double-

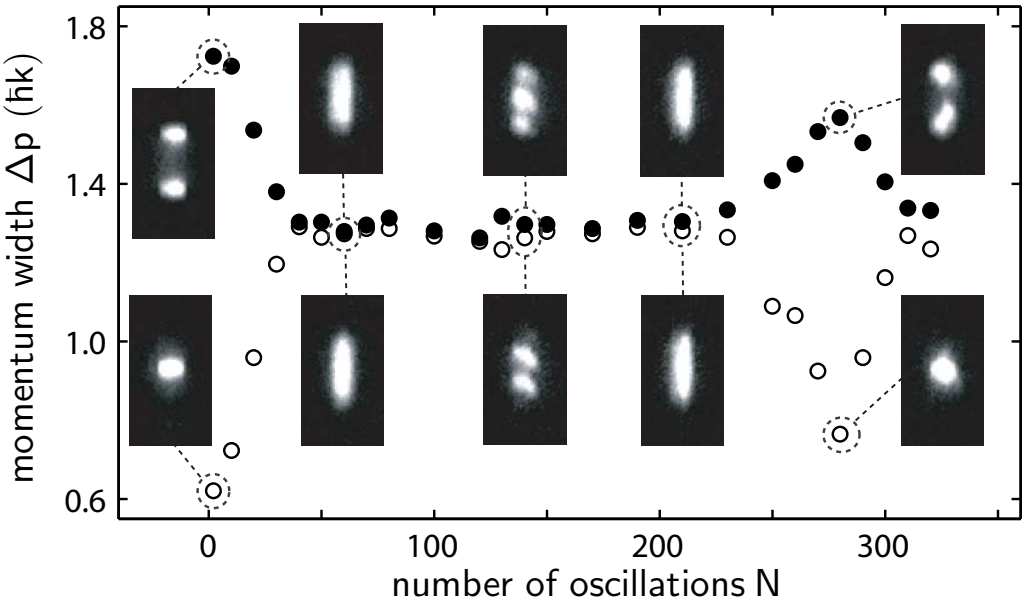

Figure 5.5: Collapse and revival of Bloch oscillations for the case of a non-interacting BEC with a vertical force gradient. For two cycle phases separated by π, the width Δp is plotted as a function of the number N of Bloch cycles. For selected cycles ($N = 1, 70, 140, 210,$ and 280) two absorption images corresponding to the two cycle phases are shown.

peaked distribution as a function of the number N of Bloch cycles. Both widths rapidly increase resp. decrease to the same value of $1.3\ \hbar k$ within about $N = 30$ oscillations. Here the ensemble is dephased. It then remains dephased for about 200 cycles. Partial rephasing at intermediate times not reflected in the widths can be seen from the absorption images. Revival of the oscillations [Pon06] happens around $N = 280$ when the values for both widths separate again [Rev]. This number agrees well with the expected value of $N_{\text{rev}} = 292(15)$ given by $N_{\text{rev}} = F_{\text{grav}}/(\nabla F d) = mg/(m\omega^2 d)$, where F_{grav} is the gravitational force, $\omega = 2\pi\nu$, and $d = \lambda/2$ is the lattice spacing. Subsequently, the widths collapse again to the common value. In further measurements we see up to four collapses and revivals.

5.6 Summary

In summary, we have demonstrated the control of interaction-induced dephasing near a zero-crossing for the scattering length. On the crossing, we have realized a non-interacting BEC, which allows us to observe more than 20000 Bloch cycles, indicating a matter wave coherence time of more than 10 s. The broadening of the momentum distribution agrees well with results from theoretical models. We believe that the number of observable Bloch cycles is limited by residual interactions as a result of magnetic field noise. Our results open up exciting new avenues for precision measurements with quantum degenerate gases. For example, it is now possible to perform sensitive measurements of forces on short length

scales, such as the Casimir-Polder force near a dielectric surface [Car05]. Future experimental work can now address the nature of the dephasing [Buc03a] by studying structure in the momentum distribution.

A similar experiment on long-lasting Bloch oscillations and control of the interaction strength has recently been performed with a BEC of ^{39}K atoms at LENS, Italy. We thank A. Daley for theoretical support and for help with setting up the numerical calculations and A. Buchleitner and his group for useful discussions. We are grateful to A. Liem and H. Zellmer for valuable assistance in setting up the 1064-nm fiber amplifier system. We acknowledge contributions by P. Unterwaditzer and T. Flir during the early stages of the experiment. We are indebted to R. Grimm for generous support and gratefully acknowledge funding by the Austrian Ministry of Science and Research (BMWF) and the Austrian Science Fund (FWF) in form of a START prize grant.

CHAPTER 6

PUBLICATION

Interference of interacting matter waves

New J. Phys. **12** 065029 (2010).

Mattias Gustavsson[1], Elmar Haller[1], Manfred J. Mark[1], Johann G. Danzl[1], Russell Hart[1], Andrew J. Daley[2,3] and Hanns-Christoph Nägerl[1]

[1] *Institut für Experimentalphysik und Zentrum für Quantenphysik, Universität Innsbruck,*
[2] *Institut für Theoretische Physik und Zentrum für Quantenphysik, Universität Innsbruck, Technikerstraße 25, A–6020 Innsbruck, Austria*
[3] *Institut für Quantenoptik und Quanteninformation der Österreichischen Akademie der Wissenschaften, Technikerstraße 21a, A–6020 Innsbruck, Austria*

The phenomenon of matter wave interference lies at the heart of quantum physics. It has been observed in various contexts in the limit of non-interacting particles as a single particle effect. Here we observe and control matter wave interference whose evolution is driven by interparticle interactions. In a multi-path matter wave interferometer, the macroscopic many-body wave function of an interacting atomic Bose-Einstein condensate develops a regular interference pattern, allowing us to detect and directly visualize the effect of interaction-induced phase shifts. We demonstrate control over the phase evolution by inhibiting interaction-induced dephasing and by refocusing a dephased macroscopic matter wave in a spin-echo type experiment. Our results show that interactions in a many-body system lead to a surprisingly coherent evolution, possibly enabling narrow-band and high-brightness matter wave interferometers based on atom lasers.

Matter wave interference has been observed as a single particle effect for electrons [Dav27], neutrons [Hal36], atoms and molecules [Est30]. Macroscopic matter wave interference was first directly observed in the case of two independent atomic Bose-Einstein condensates (BEC) that were brought to overlap [And97]. This experiment validated the notion of the BEC as a macroscopic matter wave and coined the expression of the atom laser in analogy to the laser for the case of photons. Matter wave interferometers [Ber97, Cro09, Har07], in particular for applications to precision measurements, are typically operated in the dilute single particle limit [Wic02, Cla06a, Fix07] to avoid particle-particle interactions. Atom interferometers based on Bose-Einstein condensates (BEC) are expected to benefit from the extremely low momentum spread, the exceptional brightness, and the low spatial extent of the BEC [Gup02], but they readily enter the nonlinear matter wave regime as a result of the interaction-induced mean field potential. A possible solution is to operate BEC-based interferometers in the non-interacting limit [Gus08, Fat08] by exploiting the cancellation of the scattering phase shift near a scattering resonance. This condition, however, is difficult or impossible to fulfill for most atomic species. In the present work we demonstrate a BEC-based multipath atom interferometer where the dynamics is dominated by interaction-induced phase shifts, and we show that full control and also cancellation of these phase shifts is possible. We realize the multipath interferometer by loading an interacting BEC into an optical lattice potential along one dimension, coherently splitting the BEC into several parts that are then each subject to different linear and nonlinear phase shifts. The linear phase shifts due to the gravitational force lead to the the well-known phenomenon of Bloch oscillations [Ben96, And98], whereas the interaction-induced nonlinear phase shifts cause the macroscopic wave function to first spread in momentum space as a function of time and then, surprisingly, to exhibit high-contrast interference. We demonstrate a high degree of coherence by reversing the nonlinear phase evolution, thereby refocusing the BEC momentum wave function. By application of an external potential we cancel the dominant mean-field contribution to the phase evolution and become sensitive to beyond-mean-field effects. A crucial ingredient of our experiments is the capability to tune a, the atomic scattering length which determines the strength of the interaction, by means of a Feshbach resonance [Web03]. In particular, a can be switched to zero to stop the interaction driven part of the evolution in the interferometer or to perform high resolution wave function imaging in momentum space.

6.1 Phase evolution

Our interferometer consists of a BEC adiabatically loaded into a 1D optical lattice potential with a superimposed harmonic trap, as illustrated in figure 6.1a. In the tight-binding regime, it is convenient to write the macroscopic wave function of the condensate, Ψ, in a basis

[Sme03] of wave functions $\Psi_j(z, r_\perp)$ centered at the position $z_j = jd$ of the individual lattice sites j, $\Psi(z, r_\perp, t) = \sum_j c_j(t)\Psi_j(z, r_\perp)$. Here, z is the coordinate along the (vertical) lattice direction, $r_\perp$ is the transverse coordinate, d is the distance between adjacent lattice sites and $c_j(t)$ are time-dependent complex amplitudes.

After the BEC is loaded into the lattice, we tilt the lattice potential by applying a strong force F along the lattice direction. In the limit $Fd \gg J$, where J is the tunnelling matrix element, tunnelling between lattice sites is inhibited. The on-site occupation numbers $|c_j|^2$ are then fixed, and we can write $c_j(t) = c_j(0)e^{i\phi_j(t)}$, where the phase $\phi_j(t)$ evolves in time according to the local potential at each specific lattice site [Wit05],

$$\begin{aligned} \hbar\frac{\partial\phi_j}{\partial t} &= Fdj + V_j^{\mathrm{trap}} + \mu_j^{\mathrm{loc}} \\ &= Fdj + \beta_{\mathrm{tr}}j^2 - \alpha_{\mathrm{int}}j^2. \end{aligned} \tag{6.1}$$

Here, the total potential at each lattice site j consists of three terms. The applied force leads to a term linear in j and causes Bloch oscillations [Ben96, And98] with angular frequency $Fd/\hbar$. The second term comes from an optional harmonic confinement, where $\beta_{\mathrm{tr}} = m\omega_{\mathrm{tr}}^2 d^2/2$ characterizes the strength of the confining potential and ω_{tr} is the trap frequency. Atom-atom interactions give rise to a third term, the local chemical potential μ_j^{loc}, which depends on the scattering length a and the site occupation number as [Sme03] $\mu_j^{\mathrm{loc}} \propto \sqrt{a|c_j|^2}$. When the BEC is loaded in the Thomas-Fermi regime, as is done here, its initial value can be calculated in a simple way. The density distribution will be such that the local chemical potential mirrors the trapping potential that is present during loading into the lattice, $\mu_{\mathrm{loc}}^j = \mu - V_j^{\mathrm{trap}}$, with μ being the (global) chemical potential of the BEC. We then initially have $\mu_j^{\mathrm{loc}} = \alpha_{\mathrm{int}}j^2$, where $\alpha_{\mathrm{int}} = m\omega_{\mathrm{lo}}^2 d^2/2$ and ω_{lo} is the trap frequency during loading. Note that although the initial value of α_{int} is independent of the scattering length used at loading, a later change in scattering length will also change the value of α_{int}.

The phase terms proportional to j^2 lead to a nonlinear relative phase evolution between lattice sites, i.e., dephasing. This results in a time-varying interference pattern of the macroscopic matter wave, as we will demonstrate below. The key in our experiments is that we have full control over these nonlinear terms, not only over β_{tr} via the external trapping potential, but also over the interaction term characterized by α_{int}, both via the initial density distribution, and, more importantly, via the scattering length a. By tuning the scattering length [Web03] from its initial value a to a', we can ramp α_{int} to a new value α'_{int}, which can in particular be set to zero for $a = 0$. Nonlinear phase terms for matter waves are well known in single particle quantum mechanics. They play an important role for matter wave Talbot interferences [Ber97, Den99] and can be visualized in terms of so-called matter wave quantum carpets [Kap00]. In these contexts, the phase terms arise from propagation. In our case, the nonlinear phase terms for $\alpha_{\mathrm{int}} \neq 0$ arise from interactions and thus lead to a density

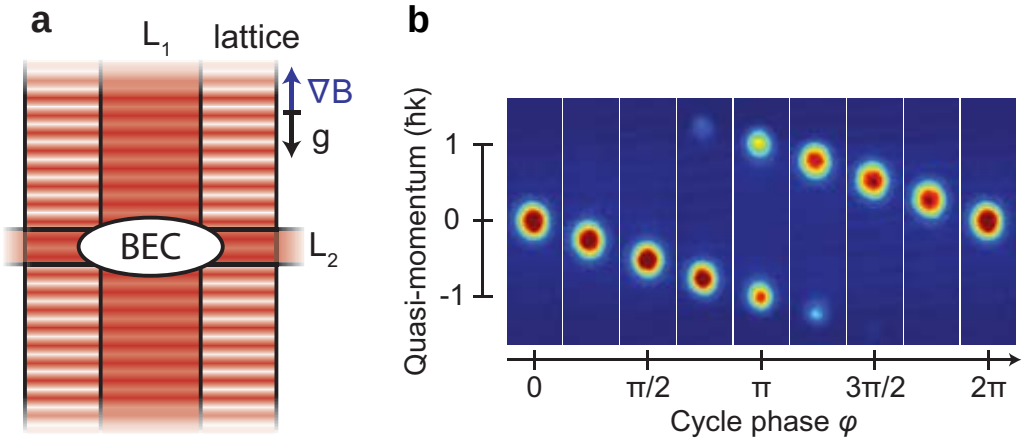

Figure 6.1: BEC-based atom interferometer. a, Experimental configuration: The tunable BEC is formed at the intersection of the vertical guide laser beam L_1 and a horizontal trapping beam L_2. The lattice is oriented along the vertical direction. Gravity, g, is initially compensated by a force due to a magnetic field gradient, ∇B. **b,** Imaging the first Brillouin zone (BZ): One cycle of Bloch oscillations for a non-interacting BEC as seen in time-of-flight absorption imaging, showing narrow peaks cycling through quasi-momentum space for cycle phases $\phi = 0$, $\pi/4$, $\pi/2$, ..., to 2π.

dependent many-body effect in the multipath atom interferometer.

In the preceding discussion, we have assumed that the minimum of the trapping potential is centered directly over one of the lattice minima. If this is not the case, the trapping potential term in equation (1) has to be modified to $\beta_{\mathrm{tr}}(j-\delta)^2 = \beta_{\mathrm{tr}} j^2 - 2\beta_{\mathrm{tr}}\delta j + const.$, where $\delta \in [0,1]$ describes the offset of the trap center in the z-direction with respect to the lattice minima, and an analogous modification has to be done to the interaction term. This adds a small term linear in j and therefore leads to a slight modification of the Bloch oscillation frequency. In our experiments, δ is the only parameter that we do not fully control. It is constant on the timescale of a single experimental run, but it drifts over the course of minutes as the beam pointing of the horizontally propagating laser beam generating the trapping potential is not actively stabilized.

6.2 Interaction-induced matter wave interference

The starting point for our experiments is a BEC trapped in a crossed optical dipole trap and adiabatically loaded into an optical lattice, as illustrated in figure 6.1a. The sample preparation is described in appendix A. The gravitational force acting on the BEC is initially compensated using magnetic levitation [Web03]. We effectively start the multipath atom interferometer and hence the evolution of the interacting macroscopic wave function by turning off magnetic levitation and ramping down the vertical confinement created by laser beam L_2 within 0.3 ms, inducing Bloch oscillations in the lowest band of the lattice. With $Fd/\hbar \approx 2\pi \times 1740$ Hz and $J/\hbar \approx 2\pi \times 40$ Hz the on-site occupation numbers $|c_j|^2$ are fixed

to their initial values. After an evolution time τ, we close the interferometer by ramping down the lattice in 1 ms and directly image the (vertical) quasi-momentum distribution in the first Brillouin zone (BZ). The ramp is adiabatic with respect to the bandgap and maps quasi-momentum onto real momentum [Kas95], which is measured by taking an absorption image after a period of free expansion. Figure 1b shows absorption images of the first Bloch oscillation [Ben96]. The Bloch period is about 0.58 ms and the peaks have a root mean square (rms) width of $0.2\hbar k$, where $k = \pi/d$ is the lattice wave vector, thus being well separated.

We study the evolution of the wave function at high resolution in momentum space by taking snapshots after extended time-of-flight. As illustrated in figure 6.2a, the BEC wave function spreads out in the BZ in about $N = 18$ Bloch cycles. Then, surprisingly, an interference pattern gradually develops at the edge of the BZ and later also becomes visible at the center of the BZ, while the number of interference maxima and minima changes as time progresses. Images are taken after an integer number of Bloch cycles for cycle phase $\phi = 0$, corresponding to the first image in figure 6.1b. The data is acquired with an interacting BEC with the scattering length set to 190 a_0, where a_0 is the Bohr radius, at an initial peak density of $n = 4 \times 10^{13}$ atoms/cm^3, occupying about 35 lattice sites after loading. We can follow the evolution of the interference pattern for more than $N = 100$ Bloch cycles, corresponding to times beyond 60 ms. This is about a factor 10 longer than the timescale for the initial broadening. We find that the number of maxima and minima in the interference pattern as measured after a fixed evolution time τ depends on the number of occupied lattice sites and on the trap frequency of the external harmonic confinement employed when loading the lattice. We also find that the measured quasi-momentum distribution for a given τ is reproducible from one experimental realization to the next, except that the pattern appears slightly shifted within the BZ after several experimental realizations. We attribute this to a drift of δ, the offset of the lattice minima from the dipole trap center, which leads to a small change of the Bloch frequency as noted before. We do not actively stabilize the vertical position of L_2 with respect to the lattice, and hence temperature variations in the laboratory slowly change δ.

We combine two techniques to achieve a high resolution in momentum space and to visualize the interference pattern. First, we minimize broadening of the distribution as a result of interactions by setting a to zero during the release from the lattice and the subsequent free expansion [Gus08]. In addition, we use long expansion times, employing magnetic levitation to prevent the BEC being accelerated by gravity and falling out of the field of view. Figure 3 shows how the contrast emerges during the expansion for a BEC after $N = 40$ Bloch cycles. It takes more than 100 ms of expansion for the interference pattern to acquire full contrast. In general, we find that the contrast is improved when the horizontally confining beam L_1 is not switched off abruptly but is ramped down slowly within the first 55 ms of time-of-flight, reducing the horizontal expansion rate. However, this happens at the cost of some additional momentum broadening along the vertical direction. Our imaging techniques allow us

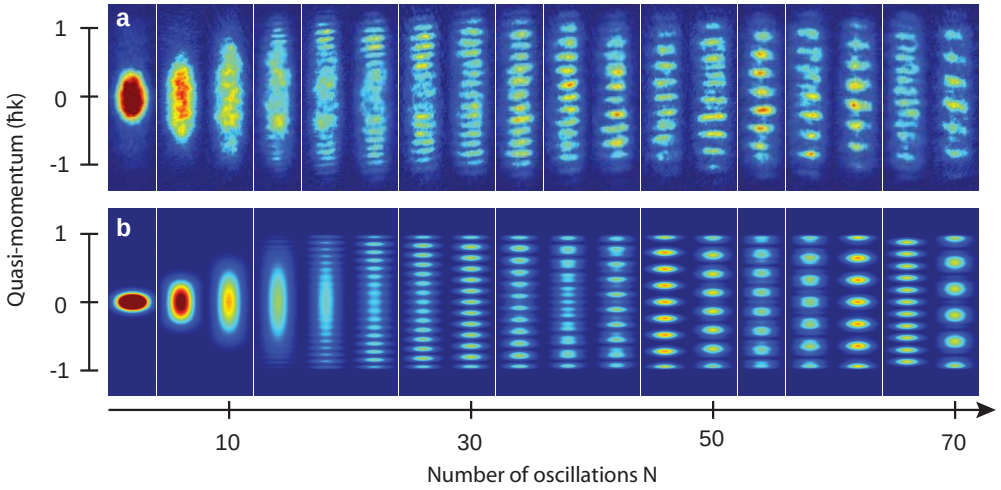

Figure 6.2: Interaction induced macroscopic matter wave interference. a, Experimental results showing the quasi-momentum distribution as a function of evolution time τ given in units of the Bloch period. The absorption images are taken in steps of 4 Bloch cycles for a BEC with an initial peak density of $n = 4 \times 10^{13}$ atoms/cm^3 loaded into about 35 lattice sites with $a = 190$ a$_0$. Each image corresponds to a single realization of the experiment. **b,** Evolution of the wave function in quasi-momentum space when the phase at the individual lattice sites evolves according to equation (1) with $\beta_{\rm tr} = 0$ (no external trap) for $n = 4 \times 10^{13}$ atoms/cm^3 loaded into 35 lattice sites with $a = 190$ a$_0$. $\alpha_{\rm int}$ is slightly rescaled to account for the reduction in density due to transversal dynamics, see text. In **a**, some additional broadening, largely due to the presence of the horizontal trapping potential during expansion, can be seen.

to resolve structure in momentum space on a scale below $0.1\hbar k$ in a single shot absorption image.

To understand the interference structure and its evolution in time, we compute the total BEC wave function in quasi-momentum space for the case where the phase at each lattice site evolves according to equation (1) (details can be found in appendix B). Figure 2b shows the interference pattern for our experimental parameters according to this simple model. The experimental results are qualitatively very well reproduced by the model when we reduce $\alpha_{\rm int}$ by 10 % compared to the value deduced from our experimental parameters. This scale factor accounts primarily for the fact that our simple model does not take into account any horizontal dynamics. In particular, switching off L_2 when starting the evolution leads to an excitation of a radial breathing mode in the horizontal plane, reducing the density at each site and modulating it in time. To a first approximation, rescaling of $\alpha_{\rm int}$ accounts for this. Nevertheless, the agreement between the experiment and the analytical model indicates that the dominant driving mechanism for the wave function spreading and interference is the nonlinear phase evolution. In particular, phase coherence is not lost, in contrast to previous experiments [Mor03b]. We test this coherence and demonstrate control over the phase evolution in two experiments.

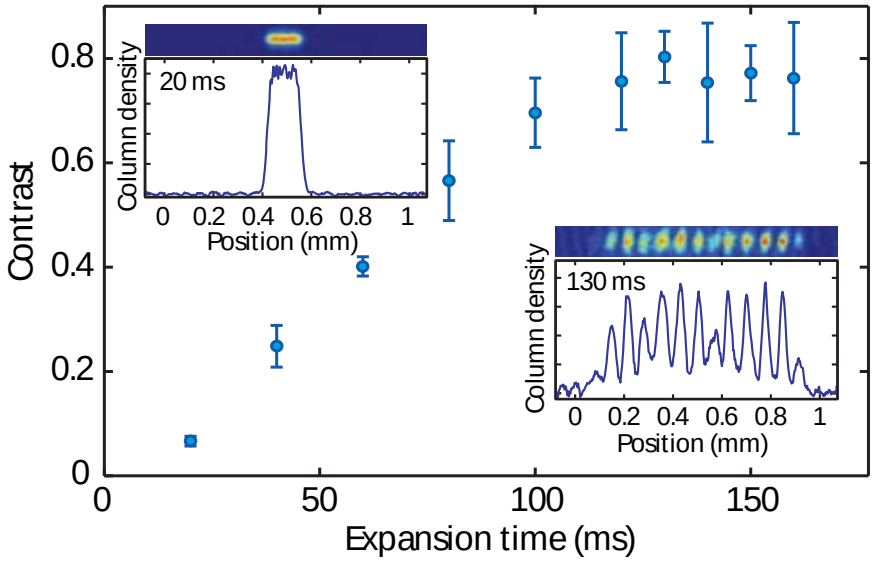

Figure 6.3: Contrast of interference fringes. Contrast of matter wave interference emerging during time-of-flight expansion for a BEC after $N = 40$ Bloch cycles, where the wave function completely fills the BZ. We define the contrast as $(I_{max} - I_{min})/(I_{max} + I_{min})$, where I_{max} (I_{min}) is the average value of the maxima (minima) of the central peak structure. Each data point is the average contrast of 10 experimental runs and the error bars indicate the 1σ statistical error. The insets show measured quasi-momentum distributions integrated along the transverse direction at two expansion times as indicated.

6.3 Cancellation of the dephasing

Equation (1) suggests that the effect of interactions can be cancelled by the application of an external potential [Zha08]. Indeed, choosing this potential to be equal to the initial loading potential, i.e. choosing $\alpha_{int} \approx \beta_{tr}$, allows us to observe persistent Bloch oscillations for an interacting BEC. This demonstrates that the detrimental effects of the mean field phase shift in a BEC matter wave interferometer can be compensated for. The BEC quasi-momentum distribution after $N = 40$ Bloch cycles is shown in figures 6.4a and 6.4b as a function of the strength of the external compensating potential, given by the power in laser L_2. When the external potential does not compensate for interactions, the condensate wave function is dephased and spreads over the whole BZ within less than $N = 20$ Bloch cycles. In contrast, when the external potential balances the effect of interactions, the BEC wave function does not spread out and Bloch oscillations are clearly visible. The time during which Bloch oscillations can be observed is now greatly extended compared to the case when the compensating potential is absent. The transition from a dephased to a non-dephased wave function as a function of confinement strength is quantified in figure 6.4c, where the rms-width Δp of the singly-peaked quasi-momentum distribution after $N = 40$ Bloch cycles is plotted as a function of the laser power in L_2. Figures 4d and 4e show the time evolution of the quasi-momentum distribution without and with the compensating potential while all other pa-

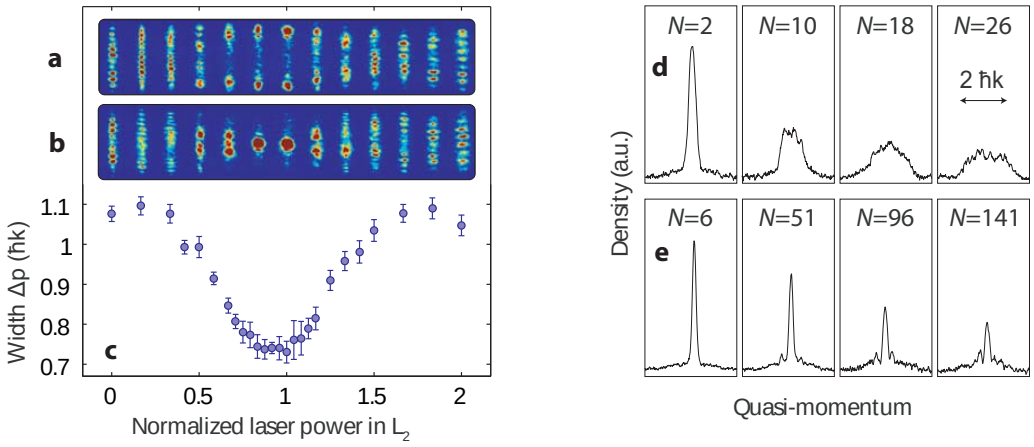

Figure 6.4: Cancellation of interaction induced dephasing and observation of persistent Bloch oscillations. a-c, Absorption images showing the quasi-momentum distribution for cycle phase $\phi = \pi$ (**a**) and $\phi = 0$ (**b**) after $N = 40$ Bloch cycles and (**c**) momentum width Δp for $\phi = 0$ as a function of confinement strength, normalized to the confinement strength at loading. **d** Momentum distribution for $\phi = 0$ as a function of the number N of Bloch cycles when no compensating potential is present, showing fast broadening. **e** The evolution of the momentum distribution for the case of optimum cancellation of interactions.

rameters are kept the same. Figure 4d essentially shows the broadening of the distribution as described before. Interestingly, the condensate wave function in the presence of a compensating potential shown in figure 6.4e dephases in a completely different way. Initially, the central peak shows no broadening. However, it is slowly depopulated, while a much broader background distribution is increasingly populated. After about 100 oscillations, the shape of the central peak starts to develop side lobes or splits in two, with the exact shape varying from one experimental run to the next. The timescale for the loss of interference is a factor 10 larger than the timescale on which the dephasing and hence the initial broadening takes place in the uncompensated case.

6.4 Rephasing of a dephased condensate

Second, we perform a matter wave spin-echo-type experiment. We initially proceed as shown in figure 6.2, letting the wave function evolve for a time corresponding to about $N = 40$ Bloch cycles until it is fully dephased and shows, upon measurement, a regular interference structure. We then essentially remove the effect of interactions by ramping to $a = 10$ a_0 within 10 ms. By not switching the interaction entirely off and by ramping comparatively slowly we avoid excessive excitation of the radial breathing mode as a result of the change in the mean field potential at each site. At the same time, we gradually turn on the harmonic potential as given by the horizontal dipole trapping laser beam L_2 within 4 ms to approximately the same depth as during the initial BEC loading phase. From equation (1) we expect that the

wave function now experiences a phase shift with a quadratic spatial dependence with opposite sign, allowing us to reverse the evolution and to recover the initial condition. Figure 5 shows the resulting quasi-momentum distributions. As time progresses, the wave function indeed refocuses while it continues to perform Bloch oscillations. As we do not control the value of δ for a particular run, we record about 10 distributions for each evolution time and select those that are symmetrical, corresponding to Bloch cycle phase $\phi = 0$ or $\phi = \pi$. For the chosen strength of the potential, refocusing happens after about 24 Bloch cycles after the ramp of a. This confirms that the initial broadening and dephasing mechanism must have been coherent. We note that we cannot avoid some excitation of the radial breathing mode as seen in the absorption images given in figure 6.5.

6.5 Discussion

Our results raise several important questions: To what extent can matter wave interferometry be performed in the presence of interactions? What sets the timescale for the eventual loss of interference contrast? Certainly, our simple analytic model does not predict any loss of contrast. In particular, it should be possible to completely eliminate the effect of interactions with the compensating external potential. However, there are several effects not included in the model that could cause the residual dephasing we observe. Motion in the radial direction, which causes the density and therefore the interaction energy to change over time, could lead to mixing of the different degrees of freedom and hence to additional dephasing. This might apply to our matter wave spin-echo experiment shown in figure 6.5, but in the experiment in figure 6.4 where we compensate interactions by means of the external potential there is hardly any radial excitation and this effect should not play a role. The appearance of dynamical instabilities [Zhe04, Cri04, Fal04] can be ruled out, as the force applied along the lattice is about 2.5 times stronger than the force needed for the instability to disappear [Zhe04]. Going beyond the mean-field treatment, a variety of factors can lead to dephasing. For example, at each lattice site there exists a superposition of number states, accumulating different phases corresponding to their respective interaction energies [Li07, Ima97]. This leads to an effective dephasing, as the phase on a particular lattice site becomes ill-defined. Basic estimates [Li07, Ima97] indicate a dephasing time of about 20 ms for our system, on the same order as we observe.

These experiments constitute a clear demonstration of coherent dynamics in an interacting macroscopic quantum system. This coherence affords a large degree of control over the system, as demonstrated by the possibility to rephase the wave function using an external potential in order to reverse dephasing due to interactions. The control demonstrated here has potential application in matter-wave interferometry, and such a degree of control over the mean-field evolution also opens the possibility to probe beyond-mean-field effects in

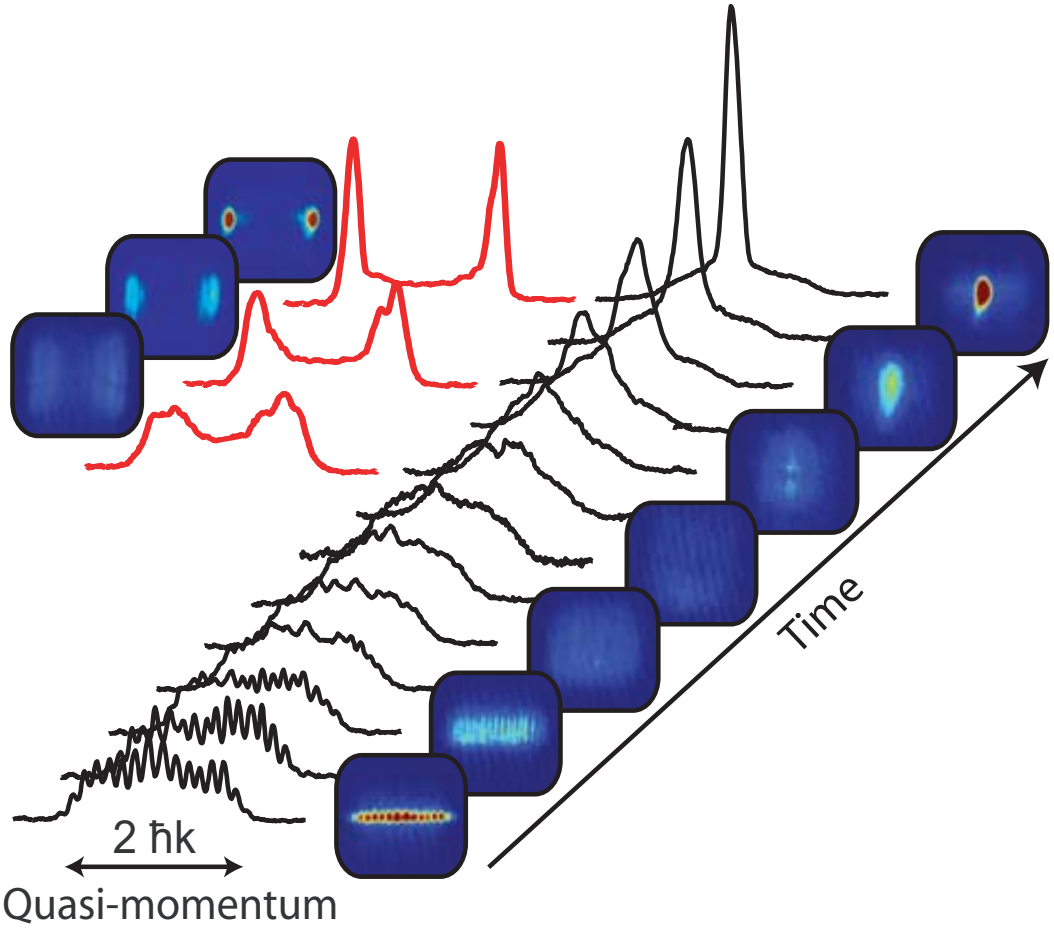

Figure 6.5: Matter wave spin-echo-type experiment. Rephasing of the BEC from a fully dephased wave function back into a narrow distribution after switching interactions to near zero and turning on an external potential. Time progresses from front to back. The black solid lines correspond to selected quasi-momentum distributions that refocus into the characteristic singly-peaked distribution (cycle phase $\phi = 0$), see text. They are separated in time by 1.15 ms or two Bloch cycles, and they are offset for clarity. The red solid lines correspond to selected distributions that refocus into the characteristic double-peaked distribution (cycle phase $\phi = \pi$). The images are absorption images corresponding to the adjacent quasi-momentum distributions. Some radial excitation is also present.

atom interferometers.

We note that coherent phase shifts due to interparticle interactions have also been observed recently in Ramsey interferometry experiments in a two-component BEC [And09].

We thank E. Arimondo, O. Morsch, W. Schleich, A. Smerzi, D. Witthaut and A. Buchleitner and his group for helpful discussions. We are indebted to R. Grimm for generous support and gratefully acknowledge funding by the Austrian Ministry of Science and Research (Bundesministerium für Wissenschaft und Forschung) and the Austrian Science Fund (Fonds zur Förderung der wissenschaftlichen Forschung) in form of a START prize grant and through SFB 15. R.H. is supported by a Marie Curie International Incoming Fellowship within the 7th European Community Framework Programme.

6.6 Appendix

6.6.1 Sample preparation

Our experimental approach initially follows the procedure described in [Gus08]. In brief, within 10 s we produce an essentially pure BEC with tunable interactions [Web03] in the Thomas-Fermi limit with up to 1.5×10^5 Cs atoms. The BEC is trapped in a crossed-beam dipole trap generated by a vertically (L_1) and a more tightly focused horizontally (L_2) propagating laser beam. The BEC is cigar-shaped with the long axis oriented along the direction of L_2. The trap frequencies are $(\omega_x,\omega_y,\omega_z)=2\pi\times(39,5,39)$ Hz, where x denotes the horizontal direction perpendicular to L_2, y is the axial direction along L_2, and z is the vertical direction. We magnetically control the scattering length a in the range between $0\,\mathrm{a_0}$ and $300\,\mathrm{a_0}$ with a resolution of about $0.1\,\mathrm{a_0}$. For BEC production, we work at $a=210$ $\mathrm{a_0}$, where three-body losses are minimized [Kra06]. Initially, we support the optical trapping by magnetic levitation against gravity [Web03]. As shown in figure 6.1a we superimpose an optical lattice with $d=\lambda/2$ along the vertical direction, where $\lambda=1064.5$ nm is the wavelength of the lattice light. To load the BEC into the lattice, we stiffen the horizontal confinement within 1 s, leading to trap frequencies of $2\pi\times(41,13,39)$ Hz, and at the same time turn on the lattice potential exponentially to a depth of $8E_R$. Here, $E_R=h^2/(2m\lambda^2)=k_B\times64\,\mathrm{nK}$ is the photon recoil energy and m the mass of the Cs atom. The BEC is thus gently loaded into the lattice, occupying about 25 to 35 lattice sites, with up to 7000 atoms at the central site.

6.6.2 Derivation of the BEC wave function in momentum space

Here, we outline the method used to calculate the images in figure 6.2b. Due to the comparatively small interaction energies in our system, the atoms are restricted to move in the lowest Bloch band and we can write the local wavefunction at lattice site j as $\Psi_j(r_\perp,z)=$

$w_0^{(j)}(z)\Phi_\perp(\rho_j, r_\perp)$, where $w_0^{(j)}(z)$ is the lowest-band Wannier function localized at the j-th site and $\Phi_\perp(n_j, r_\perp)$ is a radial wave function depending on the occupation number $n_j = |c_j|^2$ at each site [Sme03]. We can then write the total time-dependent wave function in momentum space as

$$\begin{aligned}\Psi(p_z, p_\perp, t) &= \sum_j c_j(t) w_0^{(j)}(p_z)\Phi_\perp(n_j, p_\perp) \\ &= w_0^{(0)}(p_z)\sum_j c_j(t) e^{-ip_z jd}\Phi_\perp(n_j, p_\perp). \end{aligned} \tag{6.2}$$

Transforming to quasi-momentum space and assuming that the phase at each lattice site evolves according to equation (1), we can write [Wit05]

$$\Psi(q_z, p_\perp, t) = \sum_j c_j(0) e^{-i(q+\frac{Ft}{\hbar})jd}\, e^{-i(\beta_{\rm tr} j^2 - \alpha_{\rm int} j^2)t/\hbar}\Phi_\perp(n_j, p_\perp), \tag{6.3}$$

where q_z denotes the quasimomentum. The images in figure 6.2b show the BEC density distribution $|\Psi(q_z, p_\perp, t)|^2$ integrated along one radial direction, using a Thomas-Fermi wave function as radial wave function $\Phi_\perp(n_j, p_\perp)$.

We have compared the result in figure 6.2b with a numerical integration of the discrete nonlinear Schrödinger equation [Sme03], which includes tunnelling between lattice sites, and find essentially identical results, confirming that tunnelling is inhibited.

CHAPTER 7

PUBLICATION

Inducing Transport in a Dissipation-Free Lattice with Super Bloch Oscillations

Phys. Rev. Lett. **104**, 200403 (2010)

E. Haller, R. Hart, M. J. Mark, J. G. Danzl, L. Reichsöllner, and H.-C. Nägerl

Institut für Experimentalphysik und Zentrum für Quantenphysik,
Universität Innsbruck, 6020 Innsbruck, Austria

Particles in a perfect lattice potential perform Bloch oscillations when subject to a constant force, leading to localization and preventing conductivity. For a weakly-interacting Bose-Einstein condensate (BEC) of Cs atoms, we observe giant center-of-mass oscillations in position space with a displacement across hundreds of lattice sites when we add a periodic modulation to the force near the Bloch frequency. We study the dependence of these "super" Bloch oscillations on lattice depth, modulation amplitude, and modulation frequency and show that they provide a means to induce linear transport in a dissipation-free lattice.

7.1 Introduction

Understanding the conduction of electrons through solids is of fundamental concern within the physical sciences. The simplified situation of an electron under a constant force F within a perfect, non-dissipative, periodic lattice was originally studied by Bloch and Zener [Blo28, Zen34] over 70 years ago. Their and subsequent studies revealed that the particle would undergo so-called Bloch oscillations (BOs), a periodic oscillation in position and momentum space, thereby quenching transport and hence resulting in zero conductivity. BOs can be viewed as periodic motion through the first Brillouin zone, resulting in a Bloch period $T_B = 2\hbar k/F$, where $k = \pi/d$ is the lattice wave vector for a lattice spacing d. They result from

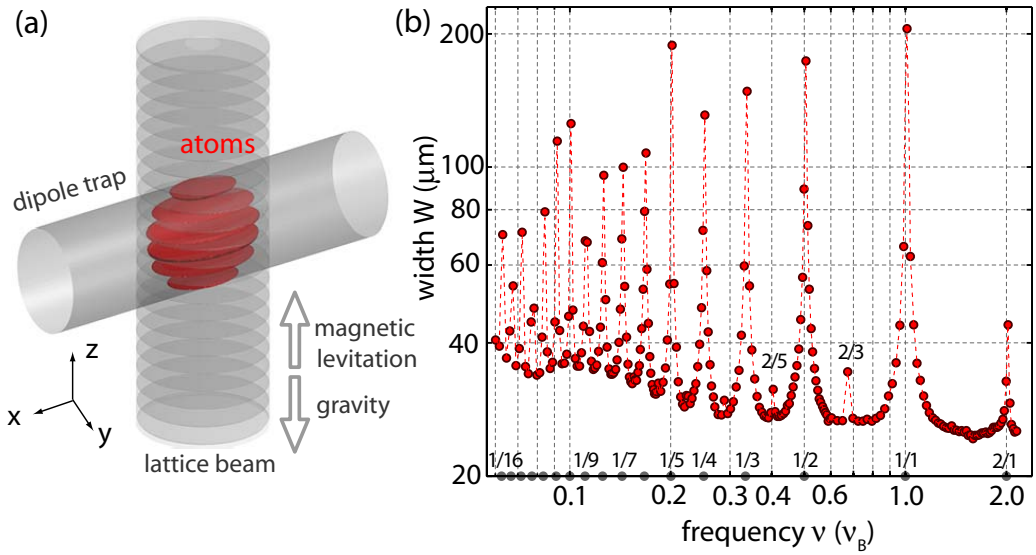

Figure 7.1: (color online) Experimental setup (a) and excitation spectrum (b) for atoms in a tilted periodic potential. The width W is plotted as a function of the drive frequency ν. The resonances correspond to a drastic spreading of the atomic wave packet as a result of modulation-assisted tunneling [Sia08] when $\nu \approx i/j \times \nu_B$, where i, j are integers. The parameters are $F_0 = 0.096(1)mg$, $\Delta F = 0.090(4)mg$, $V = 3.0(3)\ E_R$, and $\tau = 2$ s. The dashed line is a guide to the eye.

the interference of the particle's matter wave in the presence of the periodic lattice structure, requiring a coherent evolution of the wave during the time T_B. Generally, it is believed that conductance is restored via dissipative effects such as scattering from lattice defects or lattice phonons [Kan95, Ash76]. In bulk crystals, relaxation processes destroy the coherence of the system even before a single Bloch cycle is completed. These systems thus exhibit conductivity but prevent the observation of BOs. To observe BOs, the BO frequency $\nu_B = 1/T_B$ must be large compared to the rate of decoherence. In semiconductor superlattices, where the Bloch frequency is enhanced, a few cycles have been observed [Leo92].

A recent approach to observe and study BOs is to use systems of ultracold atoms in optical lattice potentials with a force that is provided by gravity or by acceleration of the lattice potential. In these engineered potentials, generated by interfering laser waves, dissipation is essentially absent, and decoherence can be well-controlled [Gus10]. Essentially all relevant system parameters are tunable, e.g. lattice depth and spacing, particle interaction strength, and external force, i.e. lattice tilt. For sufficiently low temperatures, a well-defined narrow momentum distribution can initially be prepared. BOs have been observed for thermal samples [Ben96, Bat04, Fer06], for atoms in weakly-interacting Bose-Einstein condensates (BECs) [And98, Mor01, Gus10], and for ensembles of non-interacting quantum-degenerate fermions [Roa04]. Non-interacting BECs [Gus08, Fat08] are ideally suited to study BOs as interaction-induced dephasing effects are absent, allowing for the observation of more than 20000 Bloch cycles [Gus08].

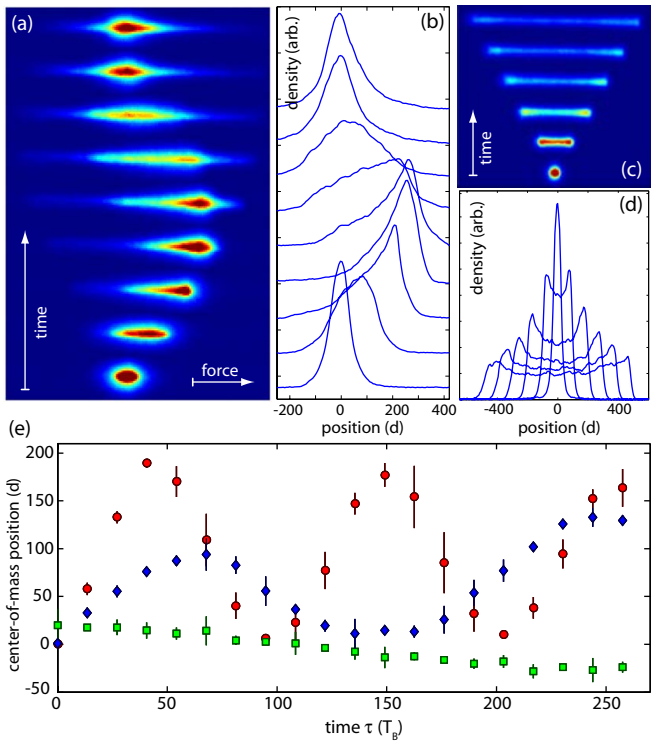

Figure 7.2: (color online) Observation of super Bloch oscillations and modulation-driven wave packet spreading. (a) and (b) In-situ absorption images and density profiles for off-resonant modulation ($\Delta\nu = -1$ Hz), showing giant oscillatory motion across more that 200 sites. (time steps of 120 ms, average of 4 images).(c) and (d) In-situ absorption images and density profiles for resonant modulation ($\Delta\nu = 0$ Hz), showing a wave packet that spreads symmetrically (time steps of 100 ms, average of 4 images). The phase ϕ was adjusted to allow for a symmetric spreading, corresponding to a calculated value of $\phi = \pi/2$. For (a)-(d), the parameters are $F_0 = 0.062(1)mg$, $\Delta F = 0.092(4)mg$, $V = 3.0(3)E_R$, $a = 11(1)$ a$_0$. (e) Center-of-mass motion for $a = 11(1)a_0$ (circles), $a = 90(1)a_0$ (diamonds), $a = 336(4)a_0$ (squares).

As for any oscillator, classical or quantum, it is natural that one investigates the properties of the oscillator under forced harmonic driving. The dynamics of a harmonically driven Bloch oscillator has recently been the subject of several theoretical [Kor03, Har04, Tho02, Kol09] and experimental studies [Wil96, Sia08, Iva08, Alb09]. For example, modulation-enhanced tunneling between lattice sites [Sia08, Iva08] and spatial breathing of incoherent atomic samples [Alb09] have been observed. Here, for a weakly-interacting atomic BEC in a tilted lattice potential, we demonstrate that harmonic driving can lead to directed center-of-mass motion and hence to transport. More strikingly, for slightly off-resonant driving, we observe giant matter-wave oscillations that extend over hundreds of lattice sites. These "super Bloch oscillations" result from a beat between the usual BOs and the drive. They are rescaled BOs in position space and can also be used, by appropriate switching of the detuning or the phase, to engineer transport.

7.2 Super Bloch oscillations

The experimental starting point is a tunable BEC of 1.2×10^5 Cs atoms in a crossed beam dipole trap [Kra04] adiabatically loaded within 400 ms into a vertically oriented 1D optical lattice [Gus08] as illustrated in Fig. 7.1(a). The lattice spacing is $d = \lambda/2$, where $\lambda = 1064.49(1)$ nm is the wavelength of the light. Unless stated otherwise, we work with a shallow lattice with depth $V = 3.0(3)\ E_R$, where $E_R = h^2/(2m\lambda^2)$ is the photon recoil energy for particles with mass m. The atoms are initially levitated against gravity by means of a magnetic field gradient and spread across approximately 50 lattice sites with an average density near 5×10^{13} cm^{-3} in the central region of the sample. We control the strength of the interaction as measured by the s-wave scattering length a near a Feshbach resonance [Kra04]. Throughout this work, unless stated otherwise, we work at $a = 11(1)\ a_0$, where a_0 is Bohr's radius. We initiate BOs by removing, the dipole trap confinement in the vertical direction and by reducing the levitation in 1 ms to cause a force that is a small fraction of the gravitational force mg, for which ν_B is near 100 Hz. An additional harmonic modulation of the levitation gradient then results in an oscillating driving force $F(t) = F_0 + \Delta F \sin(2\pi\nu t + \phi)$, where F_0 is the constant force offset, ΔF is the amplitude of the modulation, ν is the modulation frequency, and ϕ is a phase difference between the BOs and the drive. After a given hold time τ we switch off all optical beams and magnetic fields and take in-situ absorption images after a short delay time of 800μs.

We first determine the excitation spectrum. Fig. 7.1(b) shows the $1/\sqrt{e}$-width W of the matter wave after $\tau = 2$ s as a function of ν. A series of narrow resonances at rational multiples of ν_B can clearly be identified. In agreement with recent experiments [Sia08, Iva08], we attribute these resonances to modulation-enhanced tunneling between lattice sites, leading to dramatic spreading of the atomic wave packet. Tunneling between nearest neighbor lattice sites is enhanced when ν_B is an integer multiple j of ν via a j-phonon process [Eck05], while tunneling between lattice sites i lattice units apart is enhanced when ν is an integer multiple i of ν_B. Even combinations thereof, e.g. $i/j = 2/3$ or $2/5$, are detectable.

We now investigate the dynamics of the wave packet in more detail. For this, we use the resonance with $i=j=1$ and choose $\nu = \nu_B + \Delta\nu$, where $\Delta\nu$ is the detuning. In Fig. 7.2(a)-(d) we present absorption images and spatial profiles for the weakly-interacting BEC. The time evolution for the width, shape, and center position of the BEC is dramatic. On resonance ($\Delta\nu = 0$), (c) and (d), the atomic ensemble spreads as it develops pronounced edges. Also, as we will see below, the center-of-mass motion depends crucially on the phase ϕ. Off resonance, (a) and (b), for small detuning $\Delta\nu = -1$ Hz, the wave packet exhibits giant oscillatory motion across hundreds of lattice sites that we denote as "super Bloch oscillations" (sBO). Note that, for the parameters used here, the amplitude for ordinary BOs corresponds to about $4d = 2.1\ \mu$m. Also the width and higher moments of the distribution show oscillatory behavior. In Fig. 7.2(e) we plot the center-of-mass position as a function of time for $\Delta\nu = -1$

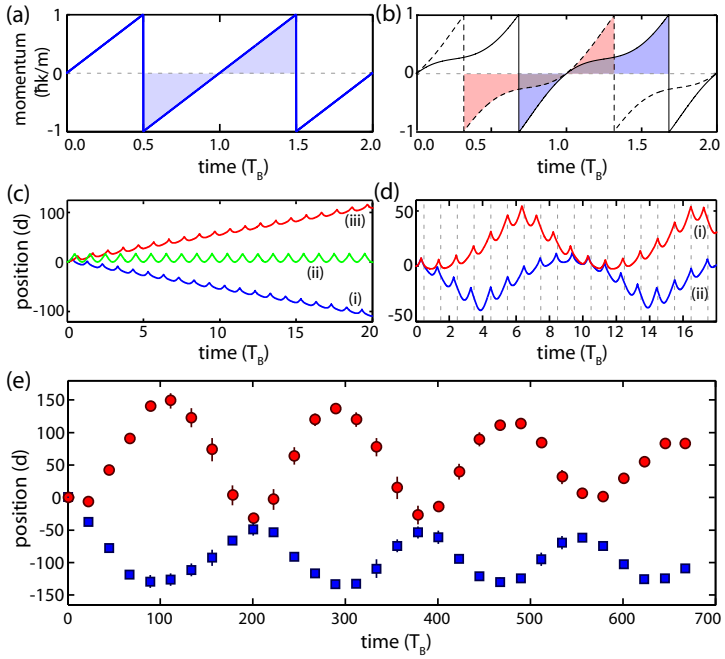

Figure 7.3: (color online) Results from a semi-classical model for sBOs. (a) For a constant force, here $F_0 = 0.06mg$, the velocity (in units of $\hbar k/m$) exhibits a symmetric, saw-tooth-like time evolution, typical for BOs. (b) Resonant modulation, here with $\Delta F = 0.8F_0$, alters the symmetric periodic velocity excursions of normal BOs ($\phi = 0$, solid line, $\phi = \pi$, dashed line), leading to a net-movement, (c), with $\phi = 0$ (i), $\phi = \pi/2$ (ii), and $\phi = \pi$ (iii). An additional detuning $\Delta\nu = \pm 0.1\nu_B$ results in a periodically changing phase difference and hence in giant oscillations in position space, (i) and (ii) in (d). On top of the motion, normal BOs can clearly be seen. The phase of sBOs depends on the sign of $\Delta\nu$, as shown by experimental data in (e), where $F_0 = 0.096(1)mg$, $\Delta F = 0.090(4)mg$, $\Delta\nu = 1$ Hz (circles), -1 Hz (squares).

Hz. At $a = 11(1)\ a_0$ we typically observe sBOs over the course of several seconds. The dynamics of sBOs strongly depends upon the site-to-site phase evolution of the matter-wave. In fact, stronger interactions, e.g. $a = 90(1)\ a_0$, distort the density profile of the driven BEC and alter the BEC's oscillation frequency and amplitude. For sufficiently strong interactions, no sBOs are observed. We also attribute the wave-packet spreading as seen after one cycle in Fig. 7.2(b) mostly to interactions. For the measurements above, we intentionally use a large modulation amplitude ΔF to enhance the amplitude of sBOs. However, all effects equally exist for $\Delta F \ll F_0$, as we will also demonstrate below in Fig. 7.4(b).

7.3 Models and data analysis

It is useful to develop a simple semi-classical model to obtain a qualitative understanding of the origin of sBOs. The only elements of this model are that the wave packet is accelerated by the applied force and that, once the wave packet reaches the edge of the first Brillouin zone, it is Bragg reflected. This model does not include an effective mass and cannot be used

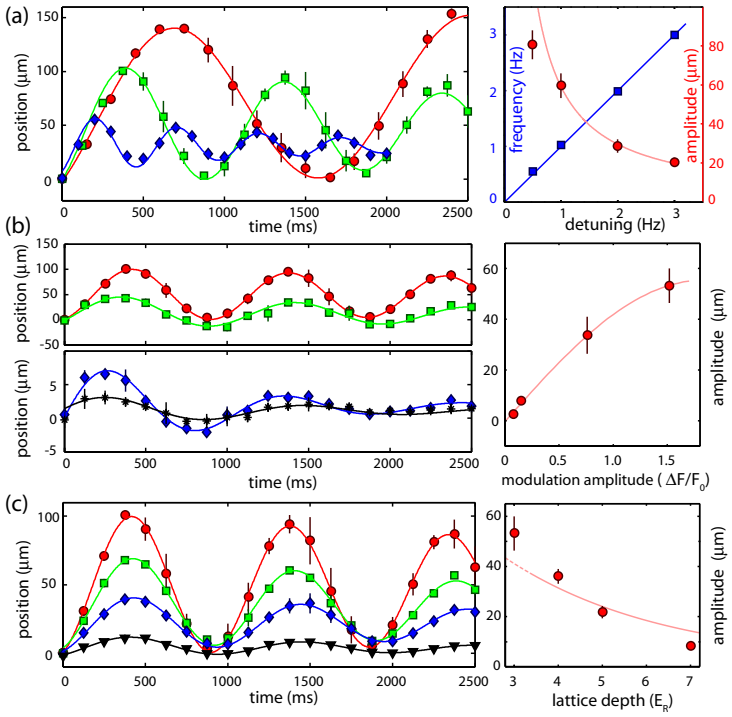

Figure 7.4: (color online) Quantitative analysis of sBOs. (a) The effect of the detuning $\Delta\nu$ on the oscillation frequency and the amplitude of sBOs, with $\Delta\nu = 0.5$ Hz (circles), 1 Hz (squares), 2 Hz (diamonds). Right: The solid lines are fits with linear and $\Delta\nu^{-1}$-dependence, respectively. (b) Dependence of the amplitude of sBOs on $\Delta F/F_0$. The data sets correspond to $\Delta F/F_0 = 1.52$ (circles), 0.76 (squares), 0.15 (diamonds), 0.08 (stars). Right: The solid line is a fit proportional to $B_1(\Delta F/F_0)$. (c) Amplitude of sBOs as a function of lattice depth, V$= 3\ E_R$ (circles), $4\ E_R$ (squares), $5\ E_R$ (diamonds), $7\ E_R$ (triangles). Right: The solid line is a fit proportional to J, for which we omit the first data point for the shallow lattice. If not stated otherwise, the parameters for all measurements shown here are $F_0 = 0.062(1)mg$, $\Delta F = 0.092(4)mg$, $\Delta\nu = -1$ Hz.

to predict quantitative results. Fig. 7.3(a)-(d) shows the result of a numerical integration of the time-dependent acceleration $a(t) = F_0/m + \Delta F/m \sin(2\pi(\nu_B + \Delta\nu)t + \phi)$ with periodic Bragg reflection. For a constant acceleration $\Delta F = 0$, the wave packet's velocity shows the well-known saw-tooth-like time evolution that corresponds to BOs. The curve in (a) is symmetric, hence, there is no net movement, as indicated by the shaded regions of equal area. If, however, there is additional harmonic modulation at $\nu = \nu_B$, the velocity excursions will not be symmetric about zero, (b), and result in a net movement for each period, leading to linear motion, (c). Only for $\phi = \pi/2$ or $\phi = 3\pi/2$ symmetry is restored and no net movement will occur. Note that, in general, the velocity of the linear motion depends non-trivially on ϕ. Off-resonant modulation with $\Delta\nu \ll \nu_B$ induces a slowly-varying phase mismatch between the drive and the original Bloch period. This results in a slow oscillation of the net movement for each Bloch cycle, which finally sums up to a giant oscillation in position space, (d). Evidently, this oscillation is the result of a beat between the drive and the original BO. The initial direction of the motion depends on ϕ and $\Delta\nu$. In particular, a change in the sign of

$\Delta\nu$ at a given ϕ can lead to opposite motion in position space, as verified experimentally in Fig. 7.3(e) for $\Delta\nu = \pm 1$ Hz.

A quantitative understanding of sBOs [Kol09] can be obtained from an approach based on Wannier-Stark states [Tho02]. In essence, the harmonic drive is expected to lead to a rescaling of the tunneling rate $J \rightarrow J_{\text{eff}} = JB_1(\Delta F/F_0)$ and the force $F_0 \rightarrow F_{\text{eff}} = h\Delta\nu/d$ for a stationary lattice with tilt. Here, B_1 is the first Bessel function of the first kind. The amplitude of sBOs is thus given by a new Wannier-Stark localization length $L_{\text{eff}} \approx J_{\text{eff}}/(dF_{\text{eff}})$ [Kol09]. In this sense, sBOs are rescaled BOs. We quantitatively study the dependence of amplitude and period of sBOs on $\Delta\nu$, $\Delta F/F_0$, and V. The results are shown in Fig. 7.4. As expected, the period T is given by $1/\Delta\nu$. Also, the oscillation amplitude scales as $1/\Delta\nu$, and its Bessel-function dependence on $\Delta F/F_0$ is well reproduced. Given our spatial resolution, we can observe sBOs down to $\Delta F/F_0 = 0.08$ (Fig. 7.4(b)). Note that sBOs can only be observed with sufficient wave function coherence and for well-defined initial conditions, i.e. for sufficient wave packet localization in the first Brillouin zone of the lattice. Nevertheless, incoherent atomic samples exhibit a breathing of the spatial distribution [Alb09] as the oscillation period is insensitive to the initial conditions. In the work of Ref.[Alb09], the breathing can be understood in terms of an incoherent sum over localized Wannier-Stark states that individually show a breathing motion with period T [Tho02].

7.4 Inducing transport

The results above provide two mechanisms to circumvent the localization inherent in BOs and to induce coherent transport in an otherwise insulating context. As shown in Fig. 7.5(a), resonant modulation ($\Delta\nu = 0$) causes directed motion of the wave packet's center-of-mass. For longer times, we find that the motion is approximately linear. The mean velocity depends on the relative phase ϕ of the Bloch oscillator and the drive. In the experiment, we varied ϕ via $\phi = \phi_0 + \Delta\phi$, where ϕ_0 is a constant phase offset, which depends on the details how BOs are initiated. For off-resonant modulation, transport can be induced by switching the sign of $\Delta\nu$ before a half-cycle of a sBO is completed. The wave packet then continues to move in the original direction. This motion is shown in Fig. 7.5(b), where we switch the sign after 400 ms. For comparison, Fig. 7.5(c) shows a sBO with $T = 1$ s without switching.

7.5 Conclusion

In summary, we have studied the coherent evolution of matter waves in tilted periodic potentials under forced driving and have observed giant sBOs, which result from a beat of BOs with the drive when a small detuning $\Delta\nu$ from the Bloch frequency is introduced. Localization as a result of BOs is broken, allowing us to engineer matter wave transport over macro-

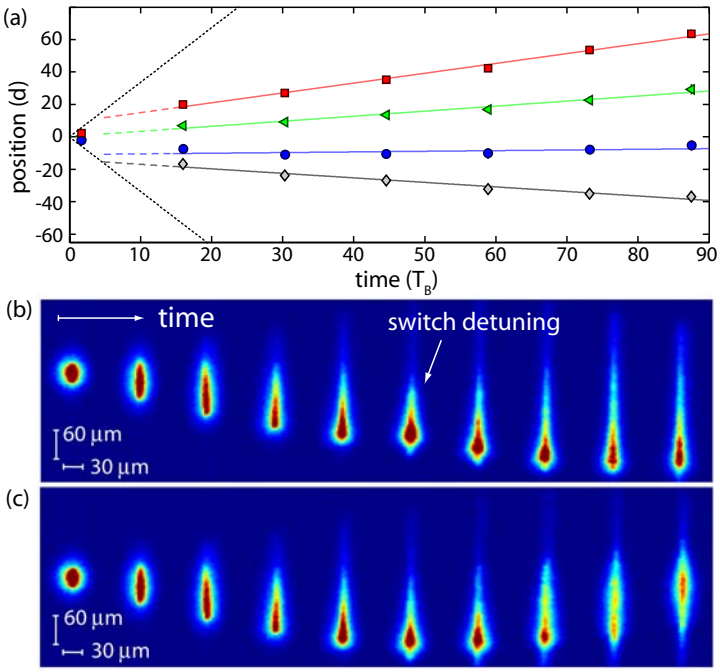

Figure 7.5: (color online) Inducing transport and suppressing interaction-induced dephasing. (a) Linear motion for resonant modulation. $\Delta\phi = 0°$ diamonds, $65°$ circles, $120°$ triangles, $190°$ squares. $\Delta\phi = 0°$ and $\Delta\phi = 190°$ were chosen to maximize the speed in opposite directions. The solid lines are linear fits to the data points excluding the first data point. For comparison we plot the linear motion that corresponds to a tunneling rate of J_{eff}, dotted lines. (b) Directed motion for off-resonant modulation. $\Delta\nu$ was switched from -1 Hz to 1 Hz after 400 ms. For comparison, (c) shows the oscillatory motion without switching (time steps of 80 ms). The parameters are $F_0 = 0.096(1)mg$, $\Delta F = 0.090(4)mg$.

scopic distances in lattice potentials with high relevance to atom interferometry [Cro09]. We are now in a position to investigate the effect of interactions on driven transport, for which subdiffusive and chaotic dynamics have been proposed [Kol09].

During the final preparation of the manuscript we became aware of related work on non-dissipative transport in a quantum ratchet [Sal09]. We thank A. R. Kolovsky, A. Zenesini, and A. Wacker for discussions and R. Grimm for generous support. We acknowledge funding by the Austrian Ministry of Science and Research and the Austrian Science Fund and by the European Union within the framework of the EuroQUASAR collective research project QuDeGPM. R.H. is supported by a Marie Curie Fellowship within FP7.

CHAPTER 8

ADDITIONAL PUBLICATIONS

Quantum Gas of Deeply Bound Ground State Molecules

Science **321**, 1062 (2008)

Johann G. Danzl[1*], Elmar Haller[1], Mattias Gustavsson[1], Manfred J. Mark[1], Russell Hart[1], Nadia Bouloufa[2], Olivier Dulieu[2], Helmut Ritsch[3], Hanns-Christoph Nägerl[1]

[1]*Institut für Experimentalphysik und Zentrum für Quantenphysik, Universität Innsbruck, Technikerstraße 25, 6020 Innsbruck, Austria*
[2]*Laboratoire Aimé Cotton, Université Paris-Sud Bât. 505, 91405 Orsay Cedex, France*
[3]*Institut für Theoretische Physik und Zentrum für Quantenphysik, Universität Innsbruck, Technikerstraße 25, 6020 Innsbruck, Austria*

Molecular cooling techniques face the hurdle of dissipating translational as well as internal energy in the presence of a rich electronic, vibrational, and rotational energy spectrum. Here, we create a translationally ultracold, dense quantum gas of molecules bound by more than 1000 wavenumbers in the electronic ground state. Specifically, we stimulate with 80% efficiency a two-photon transfer of molecules associated on a Feshbach resonance from a Bose-Einstein condensate of cesium atoms. In the process, the initial loose, long-range electrostatic bond of the Feshbach molecule is coherently transformed into a tight chemical bond. We demonstrate coherence of the transfer in a Ramsey-type experiment and show that the molecular sample is not heated during the transfer. Our results show that the preparation of a quantum gas of molecules in specific rovibrational states is possible and that the creation of a Bose-Einstein condensate of molecules in their rovibronic ground state is within reach.

Ultracold samples of molecules are ideally suited for fundamental studies in physics and chemistry, ranging from few-body collisional physics [1, 16, 4, 5], ultracold chemistry [6], and high resolution spectroscopy [2, 3], to quantum gas preparation, molecular Bose-Einstein condensation [3], and quantum processing [4]. For many of the proposed experiments full control over the molecular wave function in specific deeply bound rovibrational states is needed. High densities are required for molecular quantum gas studies. Only in the rovibronic ground state, i.e. the lowest vibrational and rotational energy level of the electronic ground state, is collisional stability assured. However, direct molecular cooling towards high phase space densities seems yet out of reach [11], whereas techniques like Feshbach association [Köh06] and photoassociation [14] either produce molecules exclusively in weakly bound rovibrational levels, or suffer from low production rates and low state selectivity.

In order to produce a quantum gas of molecules in their absolute ground state, Jaksch *et al.* [12] proposed a scheme for homonuclear alkali molecules in which the technique of stimulated two-photon transfer is repeatedly applied to molecules associated from a high-density sample of ultracold atoms. The initially very loosely bound molecules are transferred in successive steps to the rovibrational ground state of the singlet $X^1\Sigma_g^+$ molecular potential. The advantage of this scheme is that it is fully coherent, not relying on spontaneous processes, and that it involves only a very small number of intermediate levels. It promises that a ground state binding energy of typically 0.5 eV can be carried away without heating the molecular sample. It essentially preserves phase space density, allowing the molecular sample to inherit the high initial phase space density from the atomic sample. However, to realize this scheme, several challenges have to be met. First, there is a large difference in internuclear separation that has to be bridged: the overlap between the radial wave function of the least bound molecules with the radial wave functions of deeply bound molecular levels is extremely low, potentially leading to prohibitively low transition rates for the two-photon transitions. Second, the scheme requires the identification of suitable intermediate molecular levels while strictly avoiding parasitic excitations. Third, a large difference in binding energy has to be overcome. On a more technical side, the lasers driving the two-photon transitions at widely different wavelengths need to have extremely low relative short term phase jitter and high long term frequency stability to allow for coherence and reproducibility. In important experiments, Winkler *et al.* [17] and recently Ospelkaus *et al.* [15] demonstrated highly efficient two-photon transfer into lower lying molecular levels starting from weakly bound dimer molecules, which were associated from ultracold atoms on a Feshbach resonance [Köh06]. However, the transferred molecules are still weakly bound. Their binding energy, on the order of the atomic hyperfine splitting, is less than 10^{-4} of the binding energy of the rovibrational ground state, and wave function overlap with this state is still negligible.

Here we demonstrate the crucial step towards full control of the molecular wave function and towards the formation of a Bose-Einstein condensate (BEC) of molecules in their

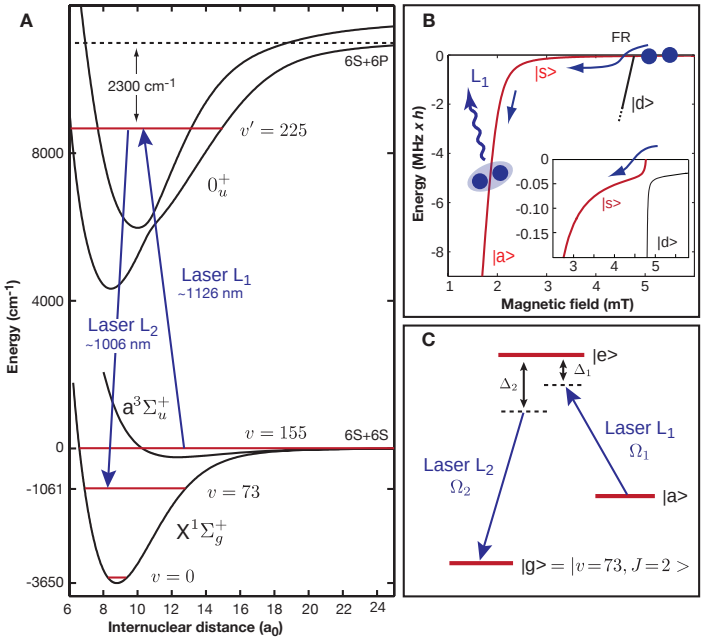

Figure 8.1: A Molecular level scheme for Cs_2. Molecules in a weakly bound Feshbach level are transferred to rovibrational level $|\nu = 73, J = 2>$ of the singlet $X^1\Sigma_g^+$ potential with a binding energy of 1061 cm^{-1} in a two-photon STIRAP process with wavelengths near 1126 nm and 1006 nm via the 225th level of the electronically excited $(A^1\Sigma_u^+ - b^3\Pi_u)\, 0_u^+$ potentials. The $X^1\Sigma_g^+$ potential has about 155 vibrational levels. **B** Zeeman diagram showing the energy of all relevant weakly bound molecular levels for initial Feshbach molecular state preparation [21]. The binding energy is given with respect to the $F=3, m_F=3$ two-atom asymptote. The molecules are produced on a d-wave Feshbach resonance at 4.8 mT (see inset) and then transferred to the weakly bound s-wave state $|s>$ on an avoided state crossing. Further lowering of the magnetic offset field to 1.9 mT transfers the molecules from $|s>$ to state $|a>$, the starting state for the STIRAP transfer. **C** STIRAP transfer scheme [23]. The molecules are transferred from the initial state $|a>$ to the final state $|g>=|\nu = 73, J = 2>$ by means of two overlapping laser pulses for which laser L_2 is pulsed on prior to L_1. The detunings and Rabi frequencies of L_i are Δ_i and Ω_i, $i = 1, 2$.

rovibronic ground state by linking weakly bound molecular states with deeply bound rovibrational states. We coherently transfer an ultracold quantum gas of weakly bound cesium Feshbach molecules to the rovibrational level $|\nu = 73, J = 2>$ of the singlet $X^1\Sigma_g^+$ potential, bound by 1061 cm^{-1} (or $h \times 31.81$ THz), corresponding to more than one fourth of the binding energy of the rovibrational ground state. To achieve this result, we overcome low wave function overlap by using a suitable intermediate excited molecular state while avoiding excitation into loss channels, and we reference the transfer lasers to a frequency comb, allowing us to flexibly bridge binding energy differences of more than 1000 cm^{-1}.

Figure 8.1 shows the energy of the relevant molecular and atomic states. Our experiment starts with a cigar-shaped BEC of cesium atoms in the lowest hyperfine sublevel $F=3, m_F=$

3 in an optical dipole trap. For BEC production, we essentially follow the procedure detailed in [15]. For Feshbach molecule production out of the BEC, we ramp up the offset magnetic field from the initial value of 2.1 mT to about 5.0 mT in 10 ms. We then ramp down, sweeping across a d-wave Feshbach resonance at 4.8 mT after about 1 ms as shown in Figure 8.1B [29, 21]. Our procedure [29] gives an ultracold and dense sample of up to 11000 molecules every 10 s at densities above 1×10^{11} cm^{-3}. For the state transfer experiments discussed here, we do not separate the molecules from the original BEC. Upon lowering the magnetic field, the molecules are transferred from the initial state $|d\rangle$ to a still weakly bound s-wave molecular state $|s\rangle$ of the lowest hyperfine channel $(F_1 = 3, F_2 = 3)$ via an avoided crossing [21]. The index $i = 1, 2$ denotes the i-th atom.

Upon further lowering the magnetic field to about 2.2 mT, the molecules enter into a closed channel s-wave molecular state $|a\rangle$ via a second, broad avoided crossing [21]. This state belongs to the uppermost hyperfine channel $(F_1 = 4, F_2 = 4)$ and thus has an effective binding energy of more than $2 \times h\nu_{\mathrm{Cs}}$. Here h is Planck's constant and $\nu_{\mathrm{Cs}} \approx 9.19$ GHz is the Cs clock frequency. Similar to $|s\rangle$ this state is a mixture of the $X^1\Sigma_g^+$ ground state and the lowest triplet $a^3\Sigma_u^+$ state, coupled by hyperfine interaction, and it has zero rotational angular momentum. At a field of 1.9 mT, it has a binding energy of 5 MHz$\times h$ with respect to the $F = 3, m_F = 3$ two-atom asymptote [21]. As one might expect, we find that optical transition rates as measured below are improved when using this effectively more deeply bound state as the initial state for two-photon transfer instead of state $|s\rangle$. We shut off the trap and perform all subsequent experiments in free flight. This does not affect the particle density immediately, but reduces it during the later detection procedure, which takes about 6ms, in order to avoid collisions between atoms and weakly bound dimers and hence loss. We detect molecules in $|a\rangle$ via states $|s\rangle$ and $|d\rangle$ by first applying a magnetic field gradient for atom-molecule Stern-Gerlach separation, then reversing the magnetic field ramp, and finally dissociating them on the Feshbach resonance at 4.8 mT, and imaging the resulting atoms [29].

Efficient two-photon transfer via the stimulated Raman adiabatic passage (STIRAP) technique [23, 17] relies on a suitable choice for the excited state $|e\rangle$. In our case this state must have singlet character so that it can be used as a transfer state to deeply bound levels of the $X^1\Sigma_g^+$ potential. In general, it must be well separated from other states, which otherwise could be off-resonantly excited. It should thus be situated far to the red of the excited $\mathrm{S}_{\frac{1}{2}}$+$\mathrm{P}_{\frac{1}{2}}$ potential asymptote to avoid the high density of excited molecular states near that asymptote. We have performed optical loss spectroscopy starting from state $|a\rangle$ in the wavelength range from 1120 to 1130 nm, about 2300 cm^{-1} to the red of the cesium D_1 line. For this measurement we recorded the number of remaining molecules in $|a\rangle$ as a function of excitation wavelength and found two progressions of lines, which we assign to the potential curves of the mixed $(A^1\Sigma_u^+ - b^3\Pi_u)\ 0_u^+$ excited states and to the $(1)^3\Sigma_g^+$ excited state, respec-

tively. For the present experiments, we choose for $|e>$ a level of the 0_u^+ progression which is $8879.63(1)$ cm^{-1} above the $F=3, m_F=3$ two-atom asymptote, corresponding to a transition wavelength of $1126.173(1)$ nm (Figure 8.1A). We measure all wavelengths on a home-built wavemeter. We identify this previously unknown level as the 225th one of the 0_u^+ system, with an uncertainty of two in the absolute numbering.

The ground state level $|g>$ with vibrational quantum number $\nu=73$ is well known from conventional molecular spectroscopy [36, 37]. However, its binding energy, as well as the binding energy of all deeply bound vibrational levels, has only been known with an uncertainty of about ± 0.45 cm^{-1} prior to the present experiments [37]. We search for $|g>$ by exciting the transitions from $|a>$ to $|e>$ with laser L_1 and from $|e>$ to $|g>$ with laser L_2 simultaneously. The two light fields create a molecule-molecule dark state. The molecules initially in $|a>$ are lost unless the second laser L_2 is on two-photon resonance, provided that the Rabi frequency Ω_2 on the second transition is equal to or greater than Ω_1, the Rabi frequency on the first transition. For coherence, stability, and reproducibility, we lock both lasers to independent narrow-band optical resonators, which we reference to an optical frequency comb [22]. The comb is not calibrated, but it allows precise differential frequency measurements and provides long-term stability needed for systematic line searches [23]. We find the resonance condition with vibrational level $\nu=73$ at $1005.976(1)$ and $1005.982(1)$ nm, corresponding to rotational quantum numbers $J=0$ and 2. Identification of J is possible since the rotational energy splitting is well known. Figures 8.2 A and B show typical molecular dark resonances when we set L_2 on resonance and step the detuning Δ_1 of L_1 near 1126.173 nm. Figure 8.2C shows a dark resonance involving $\nu=73, J=2$ using a different excited molecular state $|e'>$, which is excited with L_1 near 1123.104 nm.

Figures 8.2 D-F show dark resonances involving the neighboring vibrational levels $\nu=71$ and $\nu=72$. These $X^1\Sigma_g^+$-levels were easily found based on previously acquired Cs_2 spectra [37]. We determine the binding energy of these levels with respect to the atomic $F_1=3, F_2=3$ asymptote at zero magnetic field to be $1060.9694(10), 1088.3101(10), 1115.9148(10)$ cm^{-1} for $\nu=73, 72, 71$ with $J=0$, respectively. The binding energy of the rovibrational ground state $\nu=0$ is thus $3628.7053(14)$ cm^{-1}, which represents an improvement in precision of more than two orders of magnitude compared to the previous determination [37]. Fitting the data for the dark resonances with a three-level model taking into account off-resonant excitations and laser line widths, we determine the molecular transition strengths as given by the normalized Rabi frequencies for the transitions $|a>$ to $|e>$ and $|e>$ to $|\nu=73, J=2>$ to be $\Omega_1=2\pi\times 2$ kHz $\sqrt{I/(\mathrm{mW/cm^2})}$ and $\Omega_2=2\pi\times 11$ kHz $\sqrt{I/(\mathrm{mW/cm^2})}$, respectively. A comparison with a typical atomic transition strength of $\Omega_a=2\pi\times 5$ MHz $\sqrt{I/(\mathrm{mW/cm^2})}$ giving $|\Omega_1/\Omega_a|^2<10^{-6}$ reflects the minuteness of the wave function overlap.

We are now in a position to carry out coherent transfer using the STIRAP technique. For $|g>$ we choose the vibrational level with $\nu=73, J=2$. This level will allow us to reach the

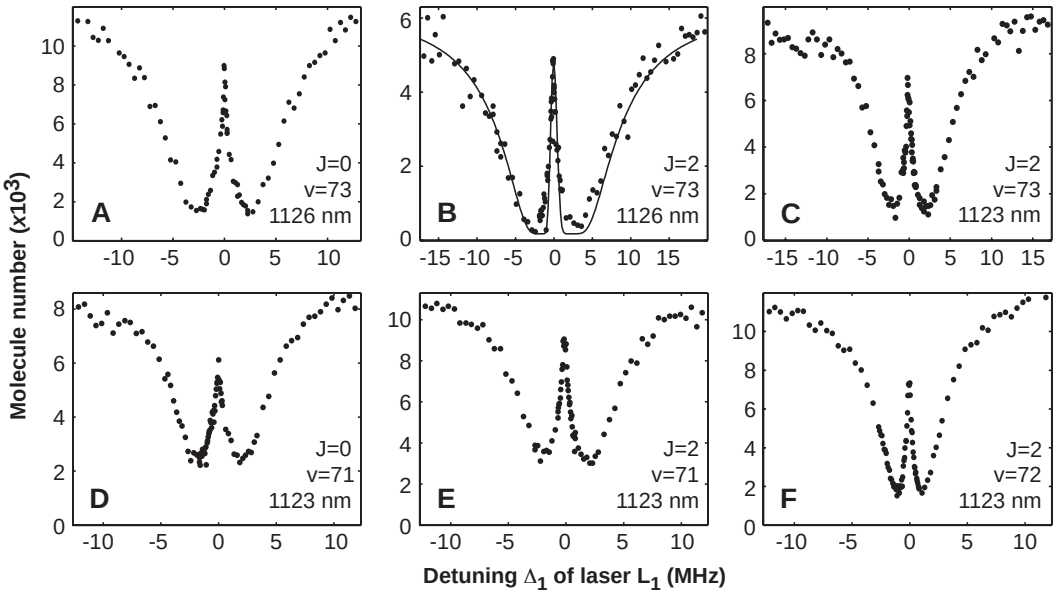

Figure 8.2: Dark resonances for vibrational levels $\nu = 71$, 72, and 73. Laser L_2 is held on resonance, while the detuning Δ_1 of L_1 is scanned. We record the number of molecules in $|a>$ while both lasers are pulsed on simultaneously. **A**, **B**, and **C** show dark resonances involving $\nu = 73$ for excitation with L_1 near 1126 nm into $J = 0$ and 2 and for excitation with L_1 near 1123 nm into $J = 2$, respectively. **D**, **E**, and **F** show the neighboring levels $\nu = 71$ and 72 for excitation near 1123 nm. The solid line in B is the result of a three-level model calculation matched to the data giving $\Omega_1 = 2\pi \times 2$ kHz $\sqrt{I_1/(\mathrm{mW/cm^2})}$ and $\Omega_2 = 2\pi \times 11$ kHz $\sqrt{I_2/(\mathrm{mW/cm^2})}$ for a pulse time of 5 μs at intensities of $I_1 = 4 \times 10^5$ mW/cm^2 for L_1 and $I_2 = 2 \times 10^5$ mW/cm^2 for L_2 assuming a laser linewidth of 2 kHz.

rovibrational ground state $\nu = 0, J = 0$ with a second STIRAP step in view of the selection rule $\Delta J = 0, \pm 2$. STIRAP uses a counterintuitive overlapping pulse sequence in which L_2 is pulsed on prior to L_1. As is well known [23], STIRAP relies on the existence of a dark state of the form $|D> = \alpha(t)|a> + \beta(t)|g>$. With sufficient adiabaticity, the function $|\alpha(t)|^2$ decreases smoothly from 1 to 0, while the function $|\beta(t)|^2$ increases smoothly from 0 to 1. The initial state $|a>$ is thus rotated via $|D>$ into the final state $|g>$. The criterion for adiabaticity is $\tau_p \Omega^2 \gg (2\pi)^2 \Gamma$, where τ_p is the pulse overlap time, $\Omega \approx \Omega_1 \approx \Omega_2$ is the peak Rabi frequency during the pulse, and $\Gamma \approx 2\pi \times 4$ MHz is the (spontaneous) decay rate from the upper state $|e>$ as determined from our loss measurements. This criterion is quite stringent, in particular in view of the low wave function overlap that enters into Ω. An upper (experimental) limit for τ_p is given by the relative laser coherence time for L_1 and L_2. We choose τ_p to be approximately 10 μs. For detection, we apply the reverse STIRAP sequence after a waiting time $\tau_w \approx 10$ μs to transfer the molecules back into $|a>$. During this time we leave laser L_1 on to assure that all possible residual population in state $|a>$ is removed.

We perform double STIRAP about 3 ms after the production of the Feshbach molecules

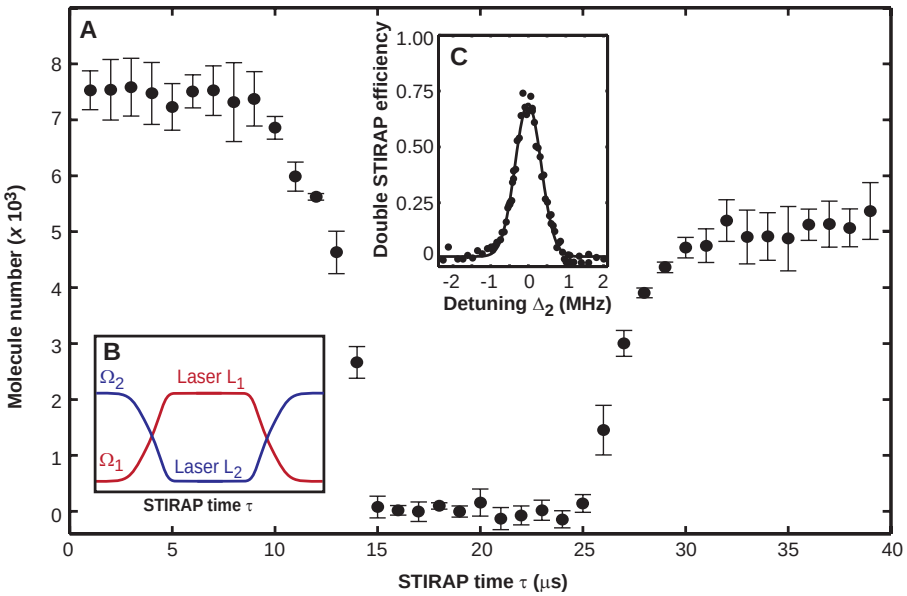

Figure 8.3: STIRAP transfer from the weakly bound state $|a>$ to the deeply bound state $|g>=|\nu=73, J=2>$ and back to $|a>$. A shows the number of molecules in state $|a>$ as a function of STIRAP time τ for $\Delta_1 \approx 0 \approx \Delta_2$. The measured pulse overlap begins at 5 μs and ends at about 15 μs. The second pulse overlap starts at 25 μs and ends at about 33 μs. **B** schematically shows the timing for the Rabi frequencies Ω_i, $i = 1, 2$, during the double STIRAP sequence. Laser L_1 is left on after the first STIRAP sequence to clear out any remaining population in $|a>$. **C** Double STIRAP efficiency as a function of the detuning Δ_2 of laser L_2 for $\Delta_1 \approx 0$. The solid line is a gaussian fit with a FWHM of 811 kHz. The peak Rabi frequencies are $\Omega_1 \approx 2\pi \times 3$ MHz and $\Omega_2 \approx 2\pi \times 6$ MHz. The error bars refer to the 1-sigma error in determining the particle number.

and 1 ms after shutting off the trap. Figure 8.3A shows the molecular population in $|a>$ as a function of the STIRAP time τ, and Figure 8.3B shows the timing sequence for the double transfer scheme. For recording the time evolution of the population we interrupt the transfer process after time τ and measure the remaining population in $|a>$. The molecules in $|a>$ initially disappear during the first STIRAP sequence. They are now in level $|\nu = 73, J = 2>$ of the singlet $X^1\Sigma_g^+$ potential. Then a large fraction of them returns in the course of the reverse STIRAP sequence. For this particular measurement both lasers are on resonance. The peak Rabi frequencies are $\Omega_1 \approx 2\pi \times 3$ MHz and $\Omega_2 \approx 2\pi \times 6$ MHz. We typically obtain an overall efficiency of more than 65% for the double transfer process, corresponding to single pass efficiencies of more than 80%, assuming equal efficiencies for both passes. Figure 8.3C shows the double pass efficiency as a function of detuning Δ_2 of laser L_2. Simulations for the three-level system show that the ~ 800 kHz full width at half maximum of the efficiency curve is compatible with a combination of laser power broadening and Fourier broadening. Our simulations also show that higher transfer efficiencies can be expected for an optimized STIRAP pulse sequence in which both peak Rabi frequencies are equal. Molecules not trans-

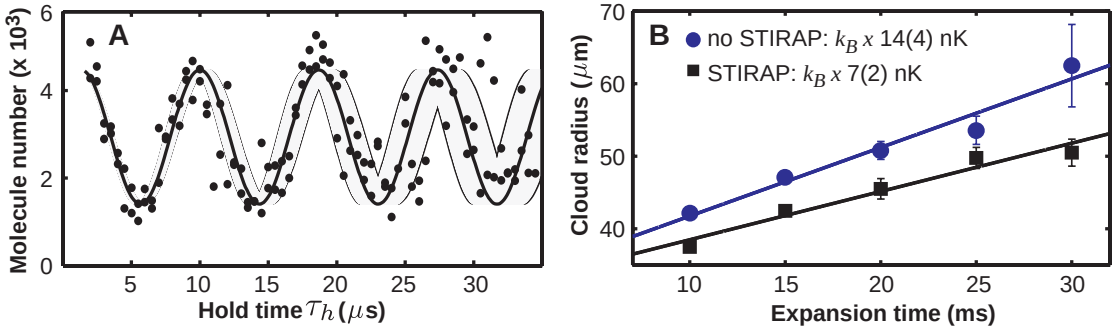

Figure 8.4: A Ramsey-type experiment. The population in the initial state $|a>$ oscillates as the hold time τ_h during which both transfer lasers are off is increased. The solid line is a sinussoidal fit to the data up to $\tau_h = 20$ μs. Its frequency f is $115(2)$ kHz, in good agreement with the expected value of 113 kHz. The thin lines are borders to a region that is given by varying f by ± 6 kHz, illustrating the estimated jitter in the two-photon detuning $|\Delta_2 - \Delta_1|$. **B** Comparison of the rate of expansion in the horizontal direction for the molecular sample without and with STIRAP transfer. The top curve (circles) shows the Thomas-Fermi radius r of the molecular sample as a function of expansion time without STIRAP. The linear fit gives a rate of expansion of $dr/dt = 1.0(1)$ mm/s, corresponding to an energy of $k_B \times 14(4)$ nK. The bottom curve (squares) shows the expansion after double STIRAP with $dr/dt = 0.7(1)$ mm/s, corresponding to $k_B \times 7(2)$ nK.

ferred by STIRAP are resonantly excited to $|e>$ and then lost from our three-level system by spontaneous emission into a multitude of ground state levels.

We demonstrate coherence of the transfer process in a Ramsey-type experiment [17], halting the transfer process by simultaneously shutting off both lasers 12 μs into the first STIRAP sequence when a balanced superposition of $|a>$ and $|g>$ has been created with $|\alpha(\tau)|^2 \approx \frac{1}{2} \approx |\beta(\tau)|^2$. After a hold time τ_h we resume the STIRAP transfer, with the roles of lasers L_1 and L_2 reversed. Thus, for $\tau_h = 0$ the population will simply be rotated back into the initial state. A three-level calculation shows that the population in the initial state $|a>$ is expected to oscillate at the rate of the two-photon detuning $|\Delta_2 - \Delta_1|/(2\pi)$. Figure 8.4A shows the initial state population for $\Delta_1 \approx 0$ and $\Delta_2 \approx 2\pi \times 113$ kHz as a function of τ_h. Indeed, the population oscillates with a frequency at $|\Delta_2 - \Delta_1|/(2\pi)$, however with marked increase in phase jitter on the time scale of 30 μs. We attribute this apparent loss of phase coherence to a slow relative frequency drift of lasers L_1 and L_2, leading to a slightly different two-photon detuning from one experimental run to the next. In Figure 8.4A, we have added a region indicating a frequency jitter of ± 6 kHz. This value is compatible with the present long-term stability of our lasers. Note that the frequency drift does not affect an individual STIRAP process as the transfer efficiency is very robust against laser detuning as shown in Figure 8.3C.

We now show that the molecular sample is not heated during the transfer process and is indeed in the quantum gas regime. Specifically, we measure and compare the rate of expansion of the molecular sample in state $|a>$ without and with the double transfer process.

In our regime the energy scale for expansion is usually set by the mean field of the BEC, resulting in typical expansion energies for the atoms in the range from $k_B \times 2$ nK to $k_B \times 10$ nK, where k_B is Boltzmann's constant, depending on the strength of the atomic interaction [Kra04]. We find that the initial magnetic field ramping excites collective motion of the BEC in the form of a breathing mode as a result of a change in the mean field potential due to a change in atomic interaction strength [15]. The breathing is transformed into expansion of the sample when the trap is shut off. We follow the expansion by monitoring the change of the Thomas-Fermi radius r of the sample. Figure 8.4B shows this radius along the horizontal direction as a function of expansion time without and with STIRAP. Without STIRAP, we obtain from a linear fit an expansion rate of $dr/dt = 1.0(1)$ mm/s, corresponding to an energy of $k_B \times 14(4)$ nK. With STIRAP, the rate is $dr/dt = 0.7(1)$ mm/s, corresponding to an energy of $k_B \times 7(2)$ nK. Both values are compatible with a separate measurement of the expansion of the atomic BEC for the same magnetic field ramp. Interestingly, the rate for the case with STIRAP is lower. We speculate that STIRAP with the tightly focused laser beams L_1 and L_2 preferentially transfers molecules in the center of the sample and is hence responsible for some selection in velocity space.

It should now be possible to add a second STIRAP step for transfer into the rovibrational ground state $\nu = 0, J = 0$. A suitable two-photon transition at readily available laser wavelengths is via the 68th excited state level of the 0_u^+ potential near 1329 nm (up) and 991 nm (down) with comparatively good wave function overlap at the level of $|\Omega/\Omega_a|^2 \approx 10^{-4}$. We expect that searching for dark resonances will be straightforward as now all two-photon transition energies are known to 10^{-3} cm^{-1}. Molecules in $\nu = 0, J = 0$ cannot further decay into a lower state upon a two-body collision, and they are thus expected to allow the formation of an intrinsically stable molecular BEC. The high speed of our STIRAP transfer will allow us to perform in-situ as well as time-of-flight imaging for direct characterization of the spatial and momentum distribution of the molecular ensemble.

With our technique any low-lying vibrational state can be coherently populated in a controlled fashion with full control over the rotational quantum number, allowing, e.g., state-specific collisional studies and high-precision molecular spectroscopy with possible implications for fundamental physics [2, 3]. Our procedure can be adapted to other species, in particular to heteronuclear alkali dimers such as RbCs [18] and KRb [15] for the creation of dipolar quantum gases [28]. For heteronuclear alkali dimers a single two-photon transfer step might suffice as a result of favorable wave function overlap [28]. We expect that the combination of our technique with Feshbach molecule production out of a Mott-insulator state in a three-dimensional lattice [6] will increase the initial Feshbach molecule production efficiency, avoiding collective excitations as a result of magnetic field ramping and inhibiting collisional loss, and will provide full control over all internal and external quantum degrees of freedom of the ground state molecules.

Acknowledgements We thank the team of J. Hecker Denschlag, the LevT team in our group, and T. Bergeman for very helpful discussions and M. Prevedelli for technical assistance. We are indebted to R. Grimm for generous support and gratefully acknowledge funding by the Austrian Ministry of Science and Research (BMWF) and the Austrian Science Fund (FWF) in form of a START prize grant and by the European Science Foundation (ESF) in the framework of the EuroQUAM collective research project QuDipMol.

BIBLIOGRAPHY

[1] C. Chin, T. Kraemer, M. Mark, J. Herbig, P. Waldburger, H.-C. Nägerl, R. Grimm, *Phys. Rev. Lett.* **94**, 123201 (2005).

[2] T. Kraemer, M. Mark, P. Waldburger, J. G. Danzl, C. Chin, B. Engeser, A. D. Lange, K. Pilch, A. Jaakkola, H.-C. Nägerl, R. Grimm, *Nature* **440**, 315 (2006).

[3] P. Staanum, S. D. Kraft, J. Lange, R. Wester, M. Weidemüller, *Phys. Rev. Lett.* **96**, 023201 (2006).

[4] N. Zahzam, T. Vogt, M. Mudrich, D. Comparat, P. Pillet, *Phys. Rev. Lett.* **96**, 023202 (2006).

[5] R. V. Krems, *Int. Rev. Phys. Chem.* **24**, 99 (2005).

[6] T. Zelevinsky, S. Kotochigova, J. Ye, *Phys. Rev. Lett.* **100**, 043201 (2008).

[7] D. DeMille, S. Sainis, J. Sage, T. Bergeman, S. Kotochigova, E. Tiesinga, *Phys. Rev. Lett.* **100**, 043202 (2008).

[8] Ultracold Fermi Gases, Proceedings of the International School of Physics "Enrico Fermi" Course CLXIV, edited by M. Inguscio, W. Ketterle, and C. Salomon (IOS Press, Amsterdam, 2008).

[9] D. DeMille, *Phys. Rev. Lett.* **88**, 067901 (2002).

[10] J. Doyle, B. Friedrich, R. V. Krems, F. Masnou-Seeuws, *Eur. Phys. J. D* **31**, 149 (2004).

[11] T. Köhler, K. Góral, P. S. Julienne, *Rev. Mod. Phys.* **78**, 1311 (2006).

[12] K. M. Jones, E. Tiesinga, P. D. Lett, P. S. Julienne, *Rev. Mod. Phys.* **78**, 483 (2006).

[13] D. Jaksch, V. Venturi, J. I. Cirac, C. J. Williams, P. Zoller, *Phys. Rev. Lett.* **89**, 040402 (2002).

[14] K. Winkler, F. Lang, G. Thalhammer, P. v. d. Straten, R. Grimm, J. Hecker Denschlag, *Phys. Rev. Lett.* **98**, 043201 (2007).

[15] S. Ospelkaus, A. Pe'er, K.-K. Ni, J. J. Zirbel, B. Neyenhuis, S. Kotochigova, P. S. Julienne, J. Ye, D. S. Jin, arXiv:0802.1093 (2008).

[16] T. Weber, J. Herbig, M. Mark, H.-C. Nägerl, R. Grimm, *Science* **299**, 232 (2003).

[17] J. Herbig, T. Kraemer, M. Mark, T. Weber, C. Chin, H.-C. Nägerl, R. Grimm, *Science* **301**, 1510 (2003).

[18] M. Mark, F. Ferlaino, S. Knoop, J.G. Danzl, T. Kraemer, C. Chin, H.-C. Nägerl, R. Grimm, *Phys. Rev. A* **76**, 042514 (2007).

[19] K. Bergmann, H. Theuer, B. W. Shore, *Rev. Mod. Phys.* **70**, 1003 (1998).

[20] W. Weickenmeier, U. Diemer, M. Wahl, M. Raab, W. Demtröder, W. Müller, *J. Chem. Phys.* **82**, 5354 (1985).

[21] C. Amiot and O. Dulieu, *J. Chem. Phys.* **117**, 5155 (2002).

[22] Laser L_1 near 1126 nm and laser L_2 near 1006 nm are continuous-wave grating-stabilized tunable diode lasers with up to 26 mW and 5 mW of power at the sample position, respectively, both focused to a $1/e^2$-waist of about 25 μm for sufficiently high Rabi frequencies. We estimate the laser linewidth for both lasers to be on the order of 1 kHz. The laser beams propagate horizontally at an angle of 80° with the long axis of the BEC with vertical linear polarization. Copropagation assures that the imparted photon recoil during STIRAP is minimal, corresponding to an energy of $k_B \times 0.4$ nK, with Boltzmann's constant k_B. The beam intensity is controlled by acousto-optical modulators, allowing pulse lengths down to 1 μs.

[23] The wavemeter calibration is currently not sufficient to allow absolute numbering of the frequency comb teeth.

[24] T. Kraemer, J. Herbig, M. Mark, T. Weber, C. Chin, H.-C. Nägerl, R. Grimm, *Appl. Phys. B* **79**, 1013 (2004).

[25] J. M. Sage, S. Sainis, T. Bergeman, D. DeMille, *Phys. Rev. Lett.* **94**, 203001 (2005).

[26] K. Góral, L. Santos, M. Lewenstein, *Phys. Rev. Lett.* **88**, 170406 (2002).

[27] W. C. Stwalley, *Eur. Phys. J. D* **31**, 221 (2004).

[28] T. Volz, N. Syassen, D. M. Bauer, E. Hansis, S. Dürr, G. Rempe, *Nature Physics* **2**, 692 (2006).

Dark resonances for ground state transfer of molecular quantum gases

Appl. Phys. B **95** 219-225 (2009)

Manfred J. Mark[1], Johann G. Danzl[1], Elmar Haller[1], Mattias Gustavsson[1], Nadia Bouloufa[2], Olivier Dulieu[2], Houssam Salami[3], Tom Bergeman[3], Helmut Ritsch[4], Russell Hart[1] and Hanns-Christoph Nägerl[1]

[1]*Institut für Experimentalphysik und Zentrum für Quantenphysik, Universität Innsbruck, Technikerstraße 25, A–6020 Innsbruck, Austria*
[2]*Laboratoire Aimé Cotton, CNRS, Université Paris-Sud, Bât. 505, 91405 Orsay Cedex, France*
[3]*Department of Physics and Astronomy, SUNY Stony Brook, NY 11794-3800, USA*
[4]*Institut für Theoretische Physik und Zentrum für Quantenphysik, Universität Innsbruck, Technikerstraße 25, A–6020 Innsbruck, Austria*

One possible way to produce ultracold, high-phase-space-density quantum gases of molecules in the rovibronic ground state is given by molecule association from quantum-degenerate atomic gases on a Feshbach resonance and subsequent coherent optical multi-photon transfer into the rovibronic ground state. In ultracold samples of Cs_2 molecules, we observe two-photon dark resonances that connect the intermediate rovibrational level $|v = 73, J = 2 >$ with the rovibrational ground state $|v = 0, J = 0 >$ of the singlet $X^1\Sigma_g^+$ ground state potential. For precise dark resonance spectroscopy we exploit the fact that it is possible to efficiently populate the level $|v = 73, J = 2 >$ by two-photon transfer from the dissociation threshold with the stimulated Raman adiabatic passage (STIRAP) technique. We find that at least one of the two-photon resonances is sufficiently strong to allow future implementation of coherent STIRAP transfer of a molecular quantum gas to the rovibrational ground state $|v = 0, J = 0 >$.

Introduction

Laser cooling of atoms and the production of quantum degenerate atomic Bose and Fermi gases have revolutionized the field of atomic physics [10]. For molecular systems, ultralow temperatures and high phase space densities are much more difficult to achieve. Laser cooling of molecules has not yet been demonstrated, and with alternative cooling and slowing techniques such as buffer gas cooling and Zeeman slowing high phase space densities are yet out of reach [11, 2, 13]. In photoassociation experiments from magneto-optical traps, [14, 17, 18, 19, 20], cold samples of deeply bound molecules in the lowest vibrational levels have been created. Yet, the phase space densities are far away from the quantum degenerate regime. In the limit of extremely weak binding, molecular Bose-Einstein condensation could

be achieved [3] by using the trick of first cooling an atomic Fermi gas to high phase space densities and subsequently associating pairs of atoms to molecules. For molecules composed of Fermions, collisional stability of the highly excited molecules is assured as a result of a Pauli blocking effect. Here, we are interested in ultracold and dense molecular systems in specific deeply bound rovibrational levels. Such samples are of high interest for fundamental studies in physics and chemistry, ranging from ultracold chemistry [6] and few-body collisional physics [4, 5] to high resolution spectroscopy [2, 3], to applications in quantum processing [4], and to the formation of dipolar quantum gases and dipolar Bose-Einstein condensates [28, 9]. For these experiments full control over the molecular wave function is desired. In addition, high densities are required for molecular quantum gas studies. Only in the rovibronic ground state, i.e. the lowest energy level of the electronic ground state, is collisional stability assured.

For the production of molecular quantum gases in the absolute ground state, we follow a scheme in which the technique of stimulated two-photon transfer is repeatedly applied to molecules associated on a Feshbach resonance from a high-density sample of ultracold atoms such as a Bose-Einstein condensate (BEC). The initially very loosely bound molecules are to be transferred in a few successive steps to the rovibrational ground state, acquiring more and more binding energy. The scheme has several advantages. It is fully coherent, not relying on spontaneous processes, allowing high state selectivity, and it involves only a comparatively small number of intermediate levels. The scheme is expected to allow the removal of a ground state binding energy of typically 0.5 eV for an alkali dimer without appreciably heating the molecular sample. It essentially preserves phase space density and coherence of the particle wave function, allowing the molecular sample to inherit the high initial phase space density from the atomic sample. Ideally, the scheme will ultimately result in the formation of a molecular BEC. A major challenge is given by the low radial wave function overlap between successive molecular levels, potentially leading to prohibitively low transition rates for the two-photon transitions that could only be compensated by the use of further (smaller) transfer steps.

In a crucial experiment, Winkler *et al.* [17] demonstrated that coherent two-photon transfer by means of the stimulated Raman adiabatic passage (STIRAP) technique [23] can efficiently be implemented with quantum gases of weakly bound Feshbach molecules. In this work, the transferred molecules, in this case Rb_2, were still weakly bound with a binding energy of much less than 10^{-4} of the binding energy of the rovibrational ground state. In particular, wave function overlap of the final level with the rovibrational ground state is negligible. Nevertheless, an important result of this experiment was the demonstration that, even with excitation near the excited S+P asymptote, parasitic excitation of unwanted molecular transitions by the STIRAP laser beams could largely be avoided. Recently, Danzl *et al.* [1] showed efficient coherent STIRAP transfer into deeply bound rovibrational levels in the

quantum gas regime. More specifically, transfer into the rovibrational level $|v=73, J=2>$ of the singlet $X^1\Sigma_g^+$ molecular potential of the Cs dimer was demonstrated. This level is bound by 1061 wavenumbers, more than one-fourth of the binding energy of the rovibrational ground state. Here, as usual, v and J denote the vibrational and rotational quantum numbers, respectively. This intermediate level was chosen as to give a balanced distribution for the wave function overlap in a four-photon transfer scheme to the ground state, i.e. to assure that all four dipole transition moments are of comparable magnitude. This level could thus serve as a transfer state towards the rovibrational ground state $|v=0, J=0>$, allowing coherent ground state transfer with two two-photon transitions. Also recently, Ni *et al.* [22] could demonstrate transfer all the way into the rovibrational ground state $|v=0, J=0>$ of the singlet $X^1\Sigma^+$ molecular potential in a quantum gas of KRb molecules. The transfer could be achieved in a single step as a result of the favorable run of the excited state potentials in the case of heteronuclear alkali dimers [28]. Also, the lowest rovibrational level of the Rb_2 triplet $a^3\Sigma_u^+$ potential could recently be populated in the quantum gas regime using the STIRAP technique [18].

Here, in an ultracold and dense sample of Cs molecules, we present two-photon dark resonances connecting the rovibrational level $|v=73, J=2>$ of the Cs dimer singlet $X^1\Sigma_g^+$ molecular potential with the rovibrational ground state $|v=0, J=0>$. Starting from $|v=73, J=2>$, we first perform molecular loss spectroscopy by laser excitation in the wavelength range from 1329 nm to 1365 nm to search for and identify suitable excited state levels of the mixed $(A^1\Sigma_u^+ - b^3\Pi_{0u})\ 0_u^+$ excited molecular potentials. These levels are 9893 to 10091 wavenumbers above the rovibronic ground state, corresponding to a wavelength range from 1011 nm to 991 nm for the transition to the rovibronic ground state. We then perform dark state spectroscopy by simultaneous laser irradiation near 1350 nm and 1000 nm. We find several dark resonances, from which we derive normalized transition strengths and find that at least one of the two-photon transitions is favorable for ground state transfer.

Molecular energy levels and laser transitions

Fig.8.5 shows the energy of the relevant Cs_2 molecular states and the optical transitions for our transfer scheme. State $|1>$ is the initial weakly bound Feshbach state that we populate out of an atomic BEC of Cs atoms via Feshbach association [29]. For the transfer from $|1>$ to the ro-vibrational ground state $|5>= |v=0, J=0>$, three intermediate levels $|2>, |3>$, and $|4>$ are needed. All five molecular levels are coupled by two two-photon transitions in a distorted M-shaped configuration as shown in Fig.8.6. Levels $|2>$ and $|4>$ belong to the excited mixed $(A^1\Sigma_u^+ - b^3\Pi_{0u})\ 0_u^+$ potentials. We have identified level $|2>$ as the 225th one of the coupled 0_u^+ system, with an uncertainty of 2 in the absolute numbering, and $|3>$ is the level with $v=73$ and $J=2$ of the $X^1\Sigma_g^+$ ground state potential [1]. A two-photon laser

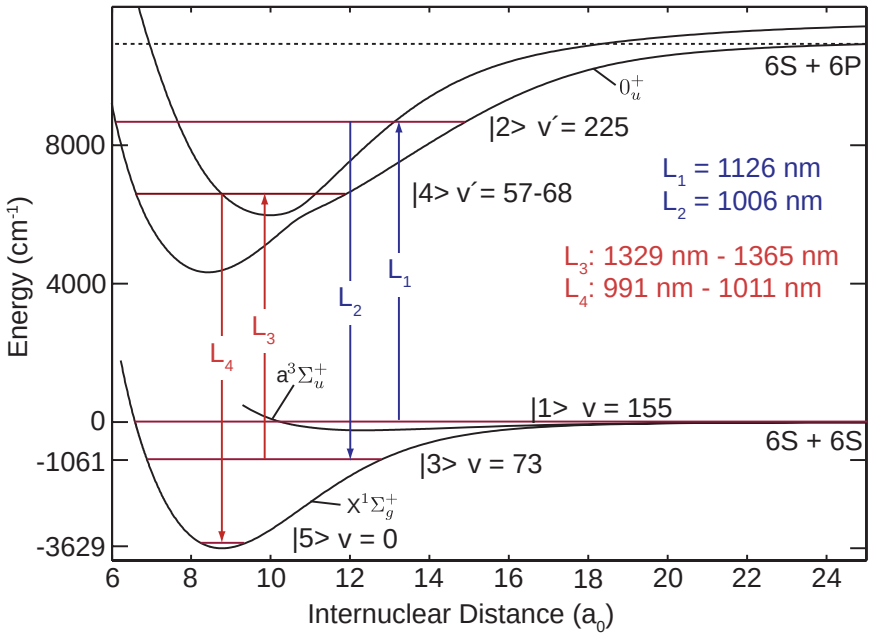

Figure 8.5: Molecular level scheme for Cs_2. Molecules in a weakly bound Feshbach level $|1>= |v \approx 155>$ (not resolved near the 6S+6S asymptote) are transferred to the rovibrational level $|3>= |v = 73, J = 2>$ of the singlet $X^1\Sigma_g^+$ ground state potential with a binding energy of 1061 cm^{-1} by a two-photon STIRAP process [1] involving lasers L_1 and L_2 near 1126 nm and 1006 nm. The following two-photon transition from $|3>$ to $|5>= |v=0, J=0>$ and also to $|v=0, J=2>$ is then probed by lasers L_3 and L_4 near 1350 nm and 1000 nm, respectively. Level $|2>$ is the 225th level of the electronically excited coupled $(A^1\Sigma_u^+ - b^3\Pi_{0u})\ 0_u^+$ potentials. Here, we probe suitable candidate levels for $|4>$, connecting $|3>$ to $|5>$. These candidate levels also belong to the 0_u^+ coupled state system and include levels with coupled channel vibrational numbers $v' = 57$ to 68. The position of the vertical arrows is not meant to reflect the internuclear distance at which the transition takes place.

transition with laser L_1 at 1126 nm and laser L_2 at 1006 nm couples $|1>$ to $|3>$ via $|2>$. There are now several possibilities for coupling $|3>$ to $|5>$, differing in the choice of the excited state $|4>$. The aim of this work is to identify a suitable state $|4>$ from the $(A^1\Sigma_u^+ - b^3\Pi_{0u})\ 0_u^+$ potentials with sufficient wave function overlap with both $|3>$ and $|5>$. We search for state $|4>$ in the energy range of 9893 to 10091 wavenumbers above the rovibrational ground state $|5>$. Molecular structure calculations as outlined in Sec. 8 show that in this range there are candidate states for $|4>$ that have dipole transition matrix elements with both $|3>$ and $|5>$ of comparable magnitude, allowing optimum STIRAP performance. The wavelengths for the lasers L_3 and L_4 driving the associated two-photon transition are near 1350 nm and 1000 nm, respectively. We derive all laser light for driving the molecular transitions from highly stable, widely tunable diode laser systems with kHz linewidths. For short term stability, the lasers are all locked to narrow-band optical resonators. For long term stability, the optical resonators are referenced to an infrared, fiber-laser-based frequency comb, covering the wavelength range from about 980 nm to about 2000 nm.

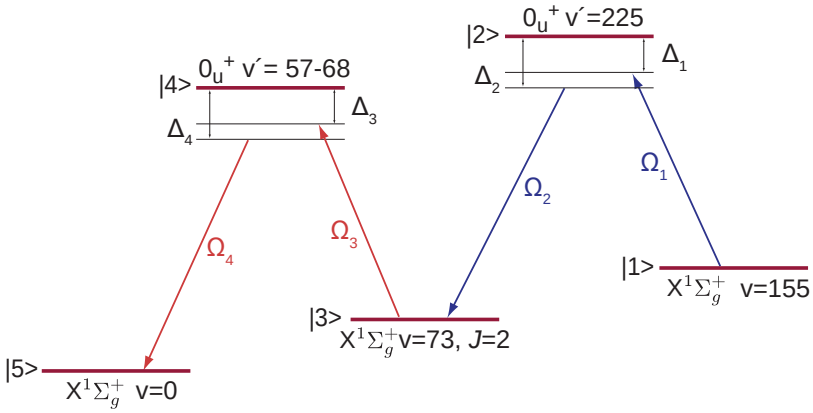

Figure 8.6: 5-level distorted M-scheme. The one-photon-detunings and Rabi frequencies of L_i are Δ_i and Ω_i, $i = 1, 2, 3, 4$. For STIRAP to $|v=73, J=2>$ the detunings for L_1 and L_2 are $\Delta_1 \approx 0 \approx \Delta_2$.

Preparation of a molecular quantum gas in $v=73, J=2$

Our sample preparation procedure follows Ref. [1]. In summary, we first produce a cigar-shaped BEC of typically 1.5×10^5 cesium atoms in the lowest hyperfine sublevel $F=3,\ m_F=3$ in a crossed optical dipole trap. As usual, F is the atomic angular momentum quantum number, and m_F its projection. The trapping light at 1064.5 nm is derived from a single-frequency, highly-stable Nd:YAG laser. Using a d-wave Feshbach resonance at 4.8 mT [21] we then produce a quantum gas of weakly bound Feshbach molecules out of the BEC [29]. For this, we first ramp the magnetic field from the BEC production value of 2.0 mT to 4.9 mT, slightly above the Feshbach resonance. The molecules are produced on a downward sweep at a typical sweep rate of 0.025 mT/ms. The resulting ultracold sample contains up to 11000 molecules, immersed in the bath of the remaining BEC atoms. For the present experiments we shut off the trap and perform all subsequent measurements in free flight. This reduces the particle density, in particular during the later detection stage of the experiment, and hence reduces atom-molecule collisional loss, thus increasing the molecular signal. Following two avoided state crossings while further sweeping the magnetic field to lower values, we transfer the molecules via a weakly bound, open channel s-wave molecular state into the still weakly bound, closed channel s-wave molecular state $|1>$ by magnetic field ramping [1]. This is the starting state for the subsequent optical transfer. As with all other weakly bound Feshbach states, it belongs to both the $X^1\Sigma_g^+$ ground state potential and the lowest triplet $a^3\Sigma_u^+$ potential and is hence of mixed character. It has zero rotational angular momentum. At a field of 1.9 mT, it has a binding energy of 5 MHz$\times h$, where h is Planck's constant, with respect to the $F=3, m_F=3$ two-atom asymptote [21]. We detect molecules in $|1>$ by reverse magnetic field ramping, leading to dissociation on the Feshbach resonance at 4.8 mT, and by

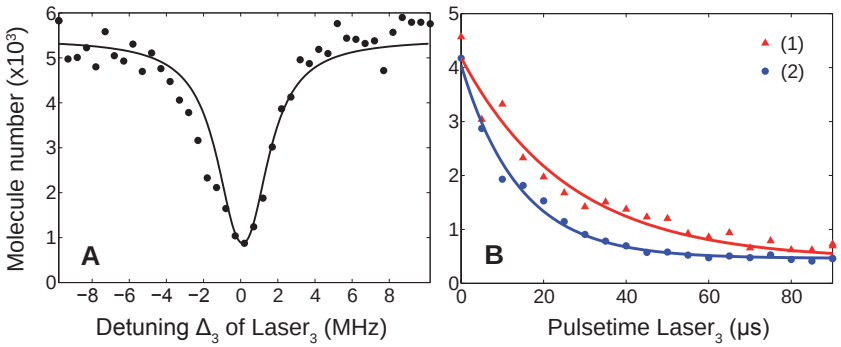

Figure 8.7: Loss resonances for excitation near 1351 nm from $|3>= |v = 73, J = 2 >$ of the $X^1\Sigma_g^+$ ground state potential. **(A)** Loss of molecules in $|3>$ as a function of laser detuning Δ_3 near 1351 nm after a waiting time of $20\,\mu$s. The solid line represents a model calculation matched to the data yielding an excited state natural linewidth of $2\pi \times 2$ MHz. **(B)** Time dependence of molecular loss on resonance at 1351 nm for two different laser intensities. (1) 270 ± 80 mW/cm^2, (2) 570 ± 80 mW/cm^2. The fitted exponential decay gives the decay constants $\tau = 26 \pm 4\,\mu$s for 270 mW/cm^2 and $\tau = 14 \pm 2\,\mu$s for 570 mW/cm^2.

subsequent imaging of the resulting atoms [29].

We transfer the molecules from $|1>$ to the rovibrational level $|3>= |v = 73, J = 2 >$ with the STIRAP technique [1]. For this, about 3 ms after molecule production, with the magnetic field ramping completed, laser L_2 at 1006 nm is pulsed on first and then laser L_1 at 1126 nm. Both lasers are on resonance within a few kHz. The pulse overlap time is about $10\,\mu$s. With peak Rabi frequencies of $\Omega_1 \approx 2\pi \times 3$ MHz and $\Omega_2 \approx 2\pi \times 6$ MHz we transfer about 80 % of the molecules to $|3>$. We find that the molecular sample is not heated as a result of the STIRAP transfer. A residual kinetic energy on the order of $k_B \times 10$ nK comes from the expansion energy of the initial atomic sample. Our current procedure allows us to produce a sample of up to 8000 molecules in state $|3>$ every 12 s. For the loss spectroscopy as detailed below, we irradiate the molecules in $|3>$ with light near 1350 nm for a certain waiting time. We then measure the fraction of molecules that have remained in $|3>$. For this, we transfer the remaining molecules back to $|1>$ using the reverse STIRAP process and determine the number of molecules in $|1>$. Without irradiation with light near 1350 nm we transfer more than 65% of the molecules from $|1>$ to $|3>$ and back to $|1>$ [1].

Loss spectroscopy

Prior to the present experiments, the energies of the levels with predominant $A^1\Sigma_u^+$ character in the region of interest were established to about $\pm$ 0.06 cm^{-1} by fits [34] to data obtained by Fourier transform spectroscopy (FTS) at Laboratoire Aimé Cotton (LAC) using transitions to the $X^1\Sigma_g^+$ state. However, the predominantly $b^3\Pi_{0u}$ levels were only known to about $\pm$ 2 cm^{-1} because this region was above that for which data was obtained from

$2^3\Delta_{1g} \rightarrow b^3\Pi_{0u}$ emission [28], but lower than the regime where $b^3\Pi_{0u}$ levels acquire sufficient singlet character (by spin-orbit mixing) to be observed in the FTS work. Paradoxically, the predominantly $b^3\Pi_{0u}$ levels are of special interest here because they happen to have significant singlet character over regions of the internuclear distance that are most important for transitions of interest in this work.

The coupled channel calculations used to characterize the level structure of the strongly interacting $A^1\Sigma_u^+$ and $b^3\Pi_{0u}$ states employed methods developed from previous work on A and b states of K_2 [29, 30], RbCs [31], Na_2 [32], and Rb_2 [33]. The DVR approach [34] was used to calculate eigenvalues primarily for two coupled channels, although some information on $b^3\Pi_{1u}$ was found in the FTS data from LAC. Similar computational approaches, differing in the detailed numerical methods, have been applied recently also to the A and b states of NaRb [35].

Because of the initial $\pm$ 2 cm^{-1} uncertainty in the positions of $b^3\Pi_{0u}$ levels of interest, we decided to perform a systematic, broad-range search around expected transition energies in the wavelength range from 1329 nm to 1365 nm. For this, we perform double STIRAP from $|1>$ to $|3>$ and back with a waiting time of typically $\tau = 1$ ms. During the waiting time, we irradiate the sample with laser L_3 at an estimated intensity of $5 \cdot 10^4$ mW/cm^2. Laser L_3 is a diode laser with grating feedback. On the timescale of our experiment, the resonator of the laser is sufficiently stable, allowing systematic tuning of the laser without locking the laser to its external resonator. We step the laser frequency in units of typically 20 MHz by tuning the piezo element on the grating. We monitor the laser wavelength with a home-built wavemeter at approximately 300 MHz accuracy. For the initial broad range line search we increased the repetition rate of the experiment by stopping evaporative cooling slightly before condensation sets in. While stepping the laser, taking data points essentially at the cycle rate corresponding to the sample production time, we look for a dip in the molecule number. Once such a dip is found, typically consisting of a few data points, we perform a more precise scan by locking the laser to the external, highly-stable resonator and then the external resonator to the infrared frequency comb. This allows us to detune the laser with kHz precision. Fig.8.7 (A) shows a typical loss resonance near 1351 nm. We reduce the laser intensity such that on resonance at most 80% of the molecules are lost within 20 μs. From such measurements the transition strength as given by the normalized Rabi frequency and the natural linewidth of the excited state can be deduced. The typical width of the excited state molecular levels that we have identified is $2\pi \times 2$ MHz, in agreement with typical expected lifetimes. Fig.8.7 (B) shows a measurement of the time dependence of the molecular loss. Here, we step the waiting time τ from 0 to 50 μs, while the laser is kept on resonance. In total, we have found 7 excited levels belonging to the $(A^1\Sigma_u^+ - b^3\Pi_{0u})$ 0_u^+ coupled state system. They are listed in Table 8.1 along with the dominant overall character (either $A^1\Sigma_u^+$ state or $b^3\Pi_{0u}$ state) of the vibrational wave function as determined from the coupled state

calculations. Within the wavelength range from 1329 nm to 1365 nm, theory predicts the existence of 5 more states of the 0_u^+ coupled state system, whose energies are also displayed in Table 8.1. For most of them, the wave function overlap is not expected to be favorable for STIRAP transfer to X $^1\Sigma_g^+$ $|v=0>$. However, an improved model of the energy level structure, based on all the data except one FTS point with a large residual, fits the observed transitions to a rms residual error of 0.02 cm^{-1}, indicating that additional resonances can be found with searches over very limited ranges of laser frequency.

Dark resonances with $|v=0, J=0>$ and $|v=0, J=2>$

In our recent work [1] we could greatly improve the value for the binding energy of the rovibrational ground state $|5>= |v=0, J=0>$ by determining the binding energy of $|v=73>$ and using well-known data from conventional molecular spectroscopy [36, 37]. Our measurement was limited by the calibration of our wavemeter, not allowing us to determine the number of the teeth of the frequency comb, and by the precision of the spectroscopy data. Searching for $|5>$ in dark state spectroscopy is now a straightforward task as only a range of about 0.002 wavenumbers needs to be scanned. We do this by exciting the transitions from $|3>$ to $|4>$ with laser L_3 and from $|4>$ to $|5>$ with laser L_4 simultaneously. The intensity for L_4 is typically $5 \cdot 10^4$ mW/cm^2. As is well known, the two light fields create a molecule-molecule dark state. The molecules initially in $|3>$ are lost unless laser L_4 is on two-photon resonance, provided that the Rabi frequency Ω_4 on the fourth transition is equal to or greater than Ω_3, the Rabi frequency on the third transition. We look for the resonance condition with the rovibrational ground state $|v=0, J=0>$ for some of the excited levels that we found above. Table 8.1 lists the observed transition wavelengths. We check that we can identify the level with rotational quantum number $J=2$ as the rotational energy splitting is well known. Fig.8.8 shows typical molecular dark resonances when we set L_4 on resonance and step the detuning Δ_3 of L_3 near 1350 nm. From a three-level model matched to the data for the dark resonances, taking into account off-resonant excitations and laser line widths, we determine the molecular transition strengths as given by the normalized Rabi frequencies. One of the two-photon transitions appears to be a particularly good candidate for STIRAP ground state transfer. It involves the excited state level $|4>$ with vibrational number $v'=61$ of the $(A^1\Sigma_u^+ - b^3\Pi_{0u})$ 0_u^+ coupled state system. For the transition from $|3>$ to $|4>$ and from $|4>$ to $|5>$ the normalized Rabi frequencies are $\Omega_3 = 2\pi \times 6$ kHz $\sqrt{I/(\mathrm{mW/cm^2})}$ and $\Omega_4 = 2\pi \times 5$ kHz $\sqrt{I/(\mathrm{mW/cm^2})}$, respectively. These values carry an estimated error of 50% as the laser beam parameters for L_3 and L_4 are not well determined. A comparison with a typical atomic transition strength of $\Omega_a = 2\pi \times 5$ MHz $\sqrt{I/(\mathrm{mW/cm^2})}$ giving $|\Omega_3/\Omega_a|^2 \approx 10^{-6}$ and $|\Omega_4/\Omega_a|^2 \approx 10^{-6}$ reflects the minuteness of the wave function overlap. Nevertheless, their value is sufficient for STIRAP as seen in our recent work [1]. Also, they are of similar

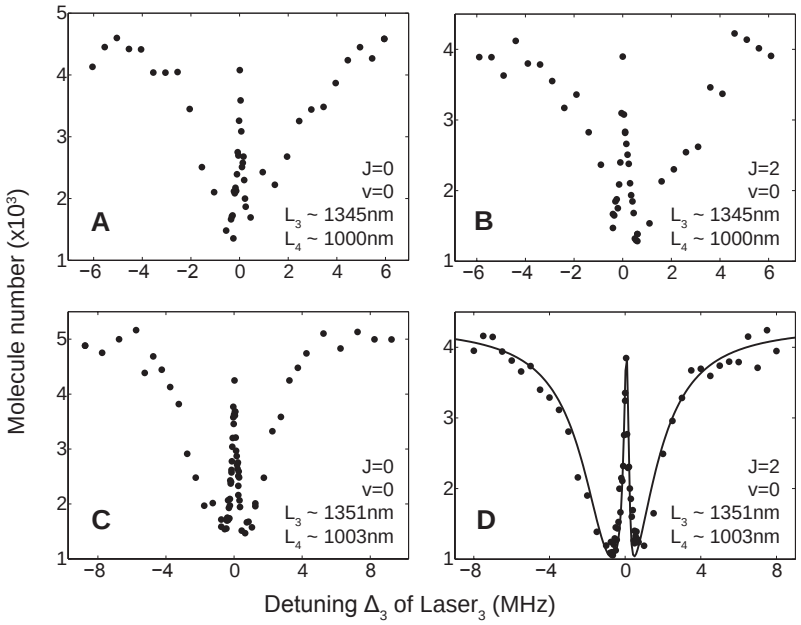

Figure 8.8: Dark resonances involving $X^1\Sigma_g^+$ state levels $|v=73, J=2>$ and $|v=0>$ for two different intermediate levels. **(A** and **B)** Dark resonances with $X^1\Sigma_g^+$ $|v=0, J=0>$ and $|v=0, J=2>$ involving the 0_u^+ excited state level $|v'=63, J=1>$ at an excitation wavelength near 1345 nm. **(C** and **D)** Dark resonances with $X^1\Sigma_g^+$ $|v=0, J=0>$ and $|v=0, J=2>$ involving the excited state level $|v'=61, J=1>$ at an excitation wavelength near 1351 nm. The solid line in **(D)** is the result of a model calculation, solving the three-level master equation including laser bandwidth and loss, matched to the data giving $\Omega_3 = 2\pi\times 6$ kHz $\sqrt{I/(\mathrm{mW/cm^2})}$ and $\Omega_4 = 2\pi\times 4$ kHz $\sqrt{I/(\mathrm{mW/cm^2})}$ for $X^1\Sigma_g^+$ $|v=0, J=2>$. The corresponding calculation for $X^1\Sigma_g^+$ $|v=0, J=0>$ yields $2\pi\times 5$ kHz $\sqrt{I/(\mathrm{mW/cm^2})}$.

magnitude. This facilitates STIRAP, for which the peak Rabi frequencies should be approximately equal for optimum performance.

Conclusion

We observe several two-photon dark resonances that connect the intermediate rovibrational level $|v=73, J=2>$ of the $X^1\Sigma_g^+$ ground state potential with the rovibrational ground state level $|v=0, J=0>$. At least one of the two-photon transitions is sufficiently strong for implementing STIRAP to $|v=0, J=0>$ in the quantum gas regime, paving the way for the realization of a BEC of ground state molecules. STIRAP can in principle be implemented in two ways, either in the form of two sequential two-photon STIRAP steps, or in the form of four-photon STIRAP [38, 39]. An attractive strategy for the production of a BEC of ground state molecules relies on the addition of an optical lattice. Starting from an atomic BEC, pairs of atoms at individual lattice sites are produced in a superfluid-to-Mott-insulator transition

[Gre02]. These pairs can then be very efficiently associated on a Feshbach resonance and subsequently transfered to the rovibronic ground state with STIRAP. The lattice has the advantage of shielding the molecules against inelastic collisions during the association process and subsequent state transfer. As proposed by Jaksch *et al.* [12], dynamical melting of the lattice should ideally result in the formation of a BEC of molecules in the rovibronic ground state in a Mott-insulator-to-superfluid-type transition.

Acknowledgements

We are indebted to R. Grimm for generous support and we thank E. Tiemann for valuable discussions and C. Amiot for providing the FTS data of LAC on Cs_2. We gratefully acknowledge funding by the Austrian Ministry of Science and Research (BMWF) and the Austrian Science Fund (FWF) in form of a START prize grant and by the European Science Foundation (ESF) in the framework of the EuroQUAM collective research project QuDipMol. R.H. acknowledges support by the European Union in form of a Marie-Curie International Incoming Fellowship (IIF). The work at Stony Brook was supported by the US NSF, under grant PHY0652459.

Table 8.1: Levels of the excited 0_u^+ coupled state system in the region 9893 cm^{-1} to 10091 cm^{-1} above $X^1\Sigma_g^+$ $|v=0, J=0>$. The first column gives the coupled channel vibrational numbers of the individual levels. Levels marked with * have not been searched for and the level energies given are those determined from the coupled channels calculations. The column labeled 'C' gives the predominant contribution to the overall vibrational wave function, which is either predominantly $A^1\Sigma_u^+$ or predominantly $b^3\Pi_{0u}$, indicated by A and b, respectively. The number in brackets gives the order within the two progressions of levels with either predominantly $A^1\Sigma_u^+$ or predominantly $b^3\Pi_{0u}$ character. Both the $|J=1>$ and the $|J=3>$ rotational levels were identified for all oberved excited state levels. The wavemeter accuracy gives a typical uncertainty in wavelength of ± 0.002 nm, which translates into ± 0.011 cm^{-1} uncertainty in the value for the energy above $|v=0, J=0>$. The energy relative to $X^1\Sigma_g^+$ $|v=0, J=0>$ of experimentally determined levels is based on the measured excitation wavelength from $X^1\Sigma_g^+$ $|v=73, J=2>$ and the $X^1\Sigma_g^+$ $|v=73>$ level energy from Ref. [37], which introduces an additional uncertainty of 0.001 cm^{-1}. Deexcitation wavelengths are obtained from dark resonance spectroscopy involving the respective intermediate excited state level and the rovibronic ground state $X^1\Sigma_g^+$ $|v=0, J=0>$. n. m.: not measured

v'	C	J	Excitation wavelength from $X^1\Sigma_g^+$ $\|v=73, J=2\rangle$ [nm]	Energy above $X^1\Sigma_g^+$ $\|v=0, J=0\rangle$ [cm^{-1}]	De-excitation wavelength to $X^1\Sigma_g^+$ $\|v=0, J=0\rangle$ [nm]
57	A (7)	1	1365.148	9893.002	n. m.
57	A (7)	3	1365.131	9893.094	n. m.
*58	b (50)	0	1362.893	9905.126	n. m.
*59	A (8)	0	1357.748	9932.927	n. m.
60	b (51)	1	1357.091	9936.497	n. m.
60	b (51)	3	1357.071	9936.606	n. m.
61	b (52)	1	1351.367	9967.707	1003.240
61	b (52)	3	1351.347	9967.816	n. m.
*62	A (9)	0	1350.388	9973.068	n. m.
63	b (53)	1	1345.725	9998.729	1000.128
63	b (53)	3	1345.705	9998.839	n. m.
*64	A (10)	0	1343.082	10013.351	n. m.
65	b (54)	1	1340.162	10029.576	997.052
65	b (54)	3	1340.143	10029.682	n. m.
66	A (11)	1	1335.833	10053.759	994.653
66	A (11)	3	1335.816	10053.853	n. m.
*67	b (55)	0	1334.675	10060.249	n. m.
68	b (56)	1	1329.257	10090.794	991.003
68	b (56)	3	1329.238	10090.902	n. m.

BIBLIOGRAPHY

[1] K. Southwell (ed.), Ultracold matter, Nature (Insight) **416** 205ñ246 (2002).

[2] J. Doyle, B. Friedrich, R.V. Krems, and F. Masnou-Seeuws, Eur. Phys. J. D **31**, 149 (2004).

[3] R.V. Krems, Phys. Chem. Chem. Phys. **10**, 4079 (2008).

[4] S.Y.T. van de Meerakker, H.L. Bethlem, and G. Meijer, Nature Phys. **4**, 595 (2008).

[5] For a review on photoassociation, see: K. M. Jones, E. Tiesinga, P.D. Lett, and P. S. Julienne, Rev. Mod. Phys. **78**, 483 (2006).

[6] A.N. Nikolov, J.R. Ensher, E.E. Eyler, H. Wang, W.C. Stwalley, and P.L. Gould, Phys. Rev. Lett. **84**, 246 (2000).

[7] J.M. Sage, S. Sainis, T. Bergeman, and D. DeMille, Phys. Rev. Lett. **94**, 203001 (2005).

[8] M. Viteau, A. Chotia, M. Allegrini, N. Bouloufa, O. Dulieu, D. Comparat, and P. Pillet, Science **321**, 232 (2008).

[9] J. Deiglmayr, A. Grochola, M. Repp, K. Mörtlbauer, C. Glück, J. Lange, O. Dulieu, R. Wester, and M. Weidemüller, Phys. Rev. Lett. **101**, 133004 (2008).

[10] For an overview, see: Ultracold Fermi Gases, *Proceedings of the International School of Physics Enrico Fermi, Course CLXIV*, edited by M. Inguscio, W. Ketterle, and C. Salomon (IOS Press, Amsterdam, 2008).

[11] R. V. Krems, Int. Rev. Phys. Chem. **24**, 99 (2005).

[12] P. Staanum, S. D. Kraft, J. Lange, R. Wester, and M. Weidemüller, Phys. Rev. Lett. **96**, 023201 (2006).

[13] N. Zahzam, T. Vogt, M. Mudrich, D. Comparat, and P. Pillet, Phys. Rev. Lett. **96**, 023202 (2006).

[14] T. Zelevinsky, S. Kotochigova, and J. Ye, Phys. Rev. Lett. **100**, 043201 (2008).

[15] D. DeMille, S. Sainis, J. Sage, T. Bergeman, S. Kotochigova, and E. Tiesinga, Phys. Rev. Lett. **100**, 043202 (2008).

[16] D. DeMille, Phys. Rev. Lett. **88**, 067901 (2002).

[17] K. Góral, L. Santos, and M. Lewenstein, Phys. Rev. Lett. **88**, 170406 (2002).

[18] M. Baranov, L. Dobrek, K. Góral, L. Santos, and M. Lewenstein, Phys. Scr. **T102**, 74 (2002).

[19] K. Winkler, F. Lang, G. Thalhammer, P. v. d. Straten, R. Grimm, and J. Hecker Denschlag, Phys. Rev. Lett. **98**, 043201 (2007).

[20] K. Bergmann, H. Theuer, and B. W. Shore, Rev. Mod. Phys. **70**, 1003 (1998).

[21] J. G. Danzl, E. Haller, M. Gustavsson, M.J. Mark, R. Hart, N. Bouloufa, O. Dulieu, H. Ritsch, and H.-C. Nägerl, Science **321**, 1062 (2008), published online 10 July 2008; 10.1126/science.1159909.

[22] K.-K. Ni, S. Ospelkaus, M. H. G. de Miranda, A. Peíer, B. Neyenhuis, J.J. Zirbel, S. Kotochigova, P.S. Julienne, D.S. Jin, and J. Ye, published online September 18, 2008, Science DOI: 10.1126/science.1163861.

[23] W.C. Stwalley, Eur. Phys. J. D **31**, 221 (2004).

[24] F. Lang, K. Winkler, C. Strauss, R. Grimm, and J. Hecker Denschlag, Phys. Rev. Lett. **101**, 133005 (2008).

[25] J. Herbig, T. Kraemer, M. Mark, T. Weber, C. Chin, H.-C. Nägerl, and R. Grimm, Science **301**, 1510 (2003); published online 21 August 2003; 10.1126/science.1088876.

[26] M. Mark, F. Ferlaino, S. Knoop, J.G. Danzl, T. Kraemer, C. Chin, H.-C. Nägerl, and R. Grimm, Phys. Rev. A **76**, 042514 (2007).

[27] H. Salami, T. Bergeman, O. Dulieu, D. Li, F. Xie, and L. Li, manuscript in preparation (2008).

[28] F. Xie, D. Li, L. Tyree, L. Li, V. Sovkov, V. S. Ivanov, S. Magnier, and A. M. Lyyra, J. Chem. Phys. **128**, 204313 (2008).

[29] C. Lisdat, O. Dulieu, H. Knöckel and E. Tiemann, Eur. Phys. J. D **17**, 319 (2001).

[30] M. R. Manaa, A. J. Ross, F. Martin, P. Crozet, A. M. Lyyra, L. Li, C. Amiot and T. Bergeman, J. Chem. Phys. **117**, 11208 (2002).

[31] T. Bergeman, C. E. Fellows, R. F. Gutterres and C. Amiot, Phys. Rev. A, **67**, 050501 (2003).

[32] P. Qi, J. Bai, E. Ahmed, A. M. Lyyra, S. Kotochigova, A. J. Ross, C. Effantin, P. Zalicki, J. Vigué, G. Chawla, R. W. Field, T.-J. Whang, W. C. Stwalley, H. Knöckel, E. Tiemann, J. Shang, L. Li, and T. Bergeman, J. Chem. Phys. **127**, 044301 (2007).

[33] H. Salami, T. Bergeman, B. Beser, J. Bai, E. Ahmed, S. Kotochigova, A. M. Lyyra, J. Huennekens, C. Lisdat, O. Dulieu, P. Crozet and A. J. Ross, manuscript in preparation (2008).

[34] D. Colbert and W. H. Miller, J. Chem. Phys. **96**, 1982 (1992).

[35] O. Docenko, M. Tamanis, R. Ferber, E. A. Pazyuk, A. Zaitservkii, A. V. Stolyarov, A. Pashov, H. Knöckel and E. Tiemann, Phys. Rev. A **75**, 042503 (2007).

[36] W. Weickenmeier, U. Diemer, M. Wahl, M. Raab, W. Demtröder, and W. Müller, J. Chem. Phys. **82**, 5354 (1985).

[37] C. Amiot and O. Dulieu, J. Chem. Phys. **117**, 5155 (2002).

[38] B. W. Shore, K. Bergmann, J. Oreg, and S. Rosenwaks, Phys. Rev. A **44**, 7442 (1991).

[39] E. Kuznetsova, P. Pellegrini, R. Côté, M.D. Lukin, and S.F. Yelin, arXiv:0806.0821 (2008).

[40] M. Greiner, O. Mandel, T. Esslinger, T.W. Hänsch, and I. Bloch, Nature **415**, 39 (2002).

[41] D. Jaksch, V. Venturi, J. I. Cirac, C. J. Williams, and P. Zoller, Phys. Rev. Lett. **89**, 040402 (2002).

Precision molecular spectroscopy for ground state transfer of molecular quantum gases

Faraday Discussions (2009)

Johann G. Danzl[1], Manfred J. Mark[1], Elmar Haller[1], Mattias Gustavsson[1], Nadia Bouloufa[2], Olivier Dulieu[2], Helmut Ritsch[3], Russell Hart[1], and Hanns-Christoph Nägerl[1]

[1] *Institut für Experimentalphysik und Zentrum für Quantenphysik, Universität Innsbruck, Technikerstraße 25, A–6020 Innsbruck, Austria.*
[2] *Laboratoire Aimé Cotton, CNRS, Université Paris-Sud, Bât. 505, 91405 Orsay Cedex, France.*
[3] *Institut für Theoretische Physik und Zentrum für Quantenphysik, Universität Innsbruck, Technikerstraße 25, A–6020 Innsbruck, Austria.*

One possibility for the creation of ultracold, high-phase-space-density quantum gases of molecules in the rovibrational ground state relies on first associating weakly-bound molecules from quantum-degenerate atomic gases on a Feshbach resonance and then transfering the molecules via several steps of coherent two-photon stimulated Raman adiabatic passage (STIRAP) into the rovibronic ground state. Here, in ultracold samples of Cs_2 Feshbach molecules produced out of ultracold samples of Cs atoms, we observe several optical transitions to deeply bound rovibrational levels of the excited 0_u^+ molecular potentials with high resolution. At least one of these transitions, although rather weak, allows efficient STIRAP transfer into the deeply bound vibrational level $|v=73>$ of the singlet $X^1\Sigma_g^+$ ground state potential, as recently demonstrated [1]. From this level, the rovibrational ground state level $|v=0, J=0>$ can be reached with one more transfer step. In total, our results show that coherent ground state transfer for Cs_2 is possible using a maximum of two successive two-photon processes or one single four-photon STIRAP process.

Introduction

Ultracold and dense molecular samples in specific deeply bound rovibrational levels are of high interest for fundamental studies in physics and chemistry. They are expected to find applications in high resolution spectroscopy and fundamental tests [2, 3], few-body collisional physics [4, 5], ultracold chemistry [6], quantum processing [4], and in the field of dipolar quantum gases and dipolar Bose-Einstein condensation [28, 9]. Ideally, full control over the molecular wave function is desired, i.e. full (quantum) control over the internal and external

degrees of freedom of the molecules. High phase space densities are needed for molecular quantum gas studies. For many of the envisaged studies and applications, initial preparation of the molecular sample in the rovibronic ground state, i.e. the lowest energy level of the electronic ground state, is desired. Only in this state one can expect sufficient collisional stability.

But how is it possible to produce dense samples of ultracold molecules in the rovibrational ground state? Laser cooling of atoms, which has lead to the production of quantum degenerate atomic Bose and Fermi gases [10], can so far not be adapted to the case of molecular systems as suitable cycling transitions are not available. Versatile non-optical cooling and slowing techniques such as buffer gas cooling and Zeeman slowing in combination with molecule trapping [11, 2, 13] have been developed, but high molecular densities and in particular high phase space densities are yet to be reached. An alternative route to producing ultracold molecular samples is given by first producing ultracold atomic samples and then associating molecules out of the atomic sample. While this technique is so far limited to the production of selected species of dimer molecules, it has the advantage that ultra-low temperatures and high particle densities are easily inherited from the atomic precursor sample. There are essentially two association techniques, photoassociation [14] and magnetically induced Feshbach association [Köh06, 16]. In photoassociation experiments [17, 18, 19, 20], ultracold samples of deeply bound molecules have been created. Additional techniques such as vibrational cooling [19] should allow selective pumping into the rovibrational ground state and open up the prospect for high molecular phase space densities. In Feshbach association experiments [20, 29], high-density samples of weakly bound molecules are produced. For dimer molecules composed of Fermions, collisional stability of the highly excited molecules is assured as a result of a Pauli blocking effect, and molecular Bose-Einstein condensation could be achieved in the limit of extremely weak binding [3].

Here, we are interested in combining the techniques of Feshbach association and coherent molecular state transfer to produce quantum gases of molecules in the rovibrational ground state $|v=0, J=0>$ of the lowest electronic state. As usual, v and J are the vibrational and rotational quantum numbers, respectively. The molecules, produced on a Feshbach resonance and hence initially very loosely bound, are to be transferred in a few successive steps of coherent two-photon laser transfer to the rovibrational ground state, acquiring more and more binding energy in each step. The general idea is sketched in Fig. 8.9A for the case of Cs_2. Each two-photon step involves an excited state level. Population transfer into this level needs to be avoided to prevent loss due to spontaneous emission. One possibility is to use the technique of stimulated Raman adiabatic passage (STIRAP) [23], which is very robust and largely insensitive to laser intensity fluctuations. The scheme has several advantages. First, production of Feshbach molecules out of a quantum degenerate atomic sample can be very efficient [25]. Second, the optical transition rate on the first transition starting from the Fesh-

bach molecules is greatly enhanced in comparison to the free atom case. Further, the scheme is fully coherent, not relying on spontaneous processes, allowing high state selectivity, and involving only a comparatively small number of intermediate levels. A ground state binding energy of typically 0.5 eV for an alkali dimer can be removed essentially without heating the molecular sample, as the differential photon recoil using pairwise co-propagating laser beams driving the two-photon transitions is very small. If losses and off-resonant excitations can be avoided, the scheme essentially preserves phase space density and coherence of the initial particle wave function, allowing the molecular sample to inherit the high initial phase space density from the atomic precursor sample.

Certainly, several challenges have to be met: Going from weakly bound Feshbach to tightly bound ground state molecules corresponds to a large reduction in internuclear distance. Consequently, the radial wave function overlap between successive levels is small, and a compromise has to be found between the number of transitions and the minimum tolerable wave function overlap. To keep the complexity of the scheme low, one or at most two two-photon transitions are desirable. Accordingly, suitable intermediate levels have to be identified that allow a balanced division of wave function overlap, as given by the Franck-Condon factors, between the different transitions. For example, for a four-photon transition scheme with Cs_2 as shown in Fig. 8.9A the Franck-Condon factors are all on the order of 10^{-6}. We emphasize that the identification of the first excited level and hence of the first transition starting from the Feshbach molecules is of crucial importance. Detailed calculations determining the wave function overlap are generally missing, and estimates on the Franck-Condon factors using hypothetical last bound states of either the singlet or triplet potentials of an alkali dimer molecule do not necessarily reflect the transition dipole moments adequately. In addition, for electronic molecular states or energy regions where spectroscopic data is missing, the precise energy of the excited state levels above the atomic threshold is known only with a large uncertainty which can approach the vibrational spacing of a few nanometers. Hence, considerable time has to be spent on searching for weak transitions starting from the initial Feshbach molecules.

In a pioneering experiment, Winkler *et al.* [17] demonstrated that the STIRAP technique can efficiently be implemented with quantum gases of weakly bound Feshbach molecules. In this work, the transferred molecules, in this case Rb_2, were still weakly bound with a binding energy of less than 10^{-4} of the binding energy of the rovibronic ground state, and the intermediate excited state level was close to the excited-atom asymptote. Here, we observe several optical transitions starting from a weakly bound Feshbach level to deeply bound rovibrational levels of the mixed excited $(A^1\Sigma_u^+ - b^3\Pi_u)\ 0_u^+$ molecular potentials of the Cs_2 molecule in a wavelength range from 1118 to 1134 nm, far to the red of the atomic D_1 and D_2 transitions. The Cs_2 molecular potentials are shown in Fig. 8.9A. We observe the levels as loss from an ultracold sample of Cs_2 Feshbach molecules as shown in Fig. 8.9B. We ob-

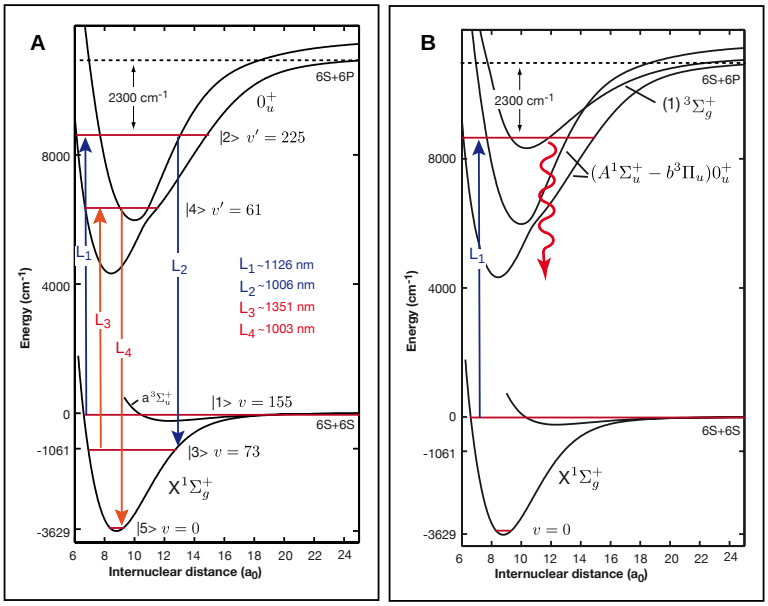

Figure 8.9: (**A**) Simplified molecular level scheme for Cs_2 showing the relevant ground state and excited state potentials involved in rovibrational ground state transfer. Molecules in a weakly bound Feshbach level $|1\rangle = |v \approx 155\rangle$ (not resolved near the $6S_{\frac{1}{2}} + 6S_{\frac{1}{2}}$ two-atom asymptote, but shown in Fig. 8.10) are to be transferred to the rovibrational ground state level $|5\rangle = |v=0, J=0\rangle$ of the singlet $X^1\Sigma_g^+$ potential with a binding energy of 3629 cm^{-1} by two sequential two-photon STIRAP processes involving lasers L_1 and L_2 near 1126 nm and 1006 nm and lasers L_3 and L_4 near 1351 nm and 1003 nm. The intermediate ground state level $|3\rangle = |v=73, J=2\rangle$ has a binding energy of 1061 cm^{-1}. (**B**) Probing candidate levels for $|2\rangle$ belonging to the electronically excited coupled $(A^1\Sigma_u^+ - b^3\Pi_u)\ 0_u^+$ potentials. Here, we search for $|2\rangle$ in loss spectroscopy with laser L_1 in a region near 8890 cm^{-1} above the $6S_{\frac{1}{2}} + 6S_{\frac{1}{2}}$ asymptote, corresponding an excitation wavelength range of 1118 to 1134 nm. The wiggly arrow indicates loss from the excited levels due to spontaneous emission. Also shown is the excited $(1)^3\Sigma_g^+$ potential, for which we find several levels.

serve two progressions, one that we attribute to the $(A^1\Sigma_u^+ - b^3\Pi_u)\ 0_u^+$ potentials and one that we associate to the triplet $(1)^3\Sigma_g^+$ potential. From the loss measurements, we determine the transition strengths and find that the stronger transitions should be suitable for STIRAP to an intermediate, deeply bound rovibrational level of the singlet $X^1\Sigma_g^+$ potential with $v = 73$. Recently, we could implement STIRAP into $|v = 73, J = 2\rangle$ [1]. For the case of the dimer molecule KRb, Ni *et al.* [16] could demonstrate quantum gas transfer all the way into the rovibrational ground state $|v = 0, J = 0\rangle$ of the singlet $X^1\Sigma^+$ molecular potential. Here, the transfer could be achieved in only a single step as a result of the favorable run of the excited state potentials, which is generally the case for heteronuclear molecules composed of alkali atoms [28]. Also recently, transfer to the rovibrational ground state of the lowest triplet state $a^3\Sigma_u^+$ of Rb_2 could be achieved [18].

Preparation of a sample of weakly bound Feshbach molecules

We produce ultracold samples of molecules on two different Feshbach resonances, one near 1.98 mT and one near 4.79 mT [21]. In both cases, essentially following the procedure detailed in Ref.[15], we first produce an ultracold sample of typically 2×10^5 Cs atoms in the lowest hyperfine sublevel $F = 3,\ m_F = 3$ in a crossed optical dipole trap. As usual, F is the atomic angular momentum quantum number, and m_F its projection on the magnetic field axis. The trapping light at 1064.5 nm is derived from a single-frequency, highly-stable Nd:YAG laser. The offset magnetic field value for evaporative cooling is 2.1 mT. We support optical trapping by magnetic levitation with a magnetic field gradient of 3.1 mT/cm. We then produce weakly bound Feshbach molecules out of the atomic sample [29]. We produce a sample every 8 s, i.e. our spectroscopic measurements are performed at a rate of one data point every 8 s. In order to be able to search for optical transitions over large frequency ranges it is advantageous to work with the shortest possible sample preparation times. For this reason we stop evaporative cooling slightly before the onset of Bose-Einstein condensation (BEC), which also makes sample preparation somewhat less critical. The temperature of the initial atomic sample is then typically about 100 nK. At higher temperatures and hence lower phase space densities the molecule production efficiency is reduced, so that there is a trade off between ease of operation and molecule number. We note that for our ground state transfer experiments reported in Ref.[1] we produce a pure atomic BEC at the expense of longer sample preparation times.

The spectrum of weakly-bound Feshbach levels near the two-free-atom asymptote is shown in Fig. 8.10 [21]. For molecule production at the Feshbach resonance at 4.79 mT, we first ramp the magnetic field from the BEC production value to 4.9 mT, about 0.1 mT above the Feshbach resonance. We produce the molecular sample on a downward sweep at a typical sweep rate of 0.025 mT/ms. The resulting ultracold sample contains up to 11000 molecules, immersed in the bath of the remaining ultracold atoms. The resonance at 4.79 mT is a d-wave resonance [21], and hence the molecules are initially of d-wave character, i.e. $\ell = 2$, where ℓ is the quantum number associated with the mechanical rotation of the nuclei. However, there is a weakly bound s-wave Feshbach state ($|s> = |\ell = 0>$) belonging to the open scattering channel right below threshold. This state couples quite strongly to the initial d-wave state, resulting in an avoided state crossing (as shown in the inset to Fig. 8.10), on which the molecules are transferred to the s-wave state $|s>$ upon lowering the magnetic field [21, 1]. Upon further lowering the magnetic field to less than 2.0 mT, the molecules acquire more and more character of a closed channel s-wave state on a second, very broad avoided crossing. Here, we perform spectroscopy in this transition range from open channel to closed channel s-wave character. At a magnetic field value of 2.0 mT, the binding energy of the molecules is near 5 MHz$\times h$ with respect to the $F = 3, m_F = 3$ two-atom asymptote, where h is Planck's constant.

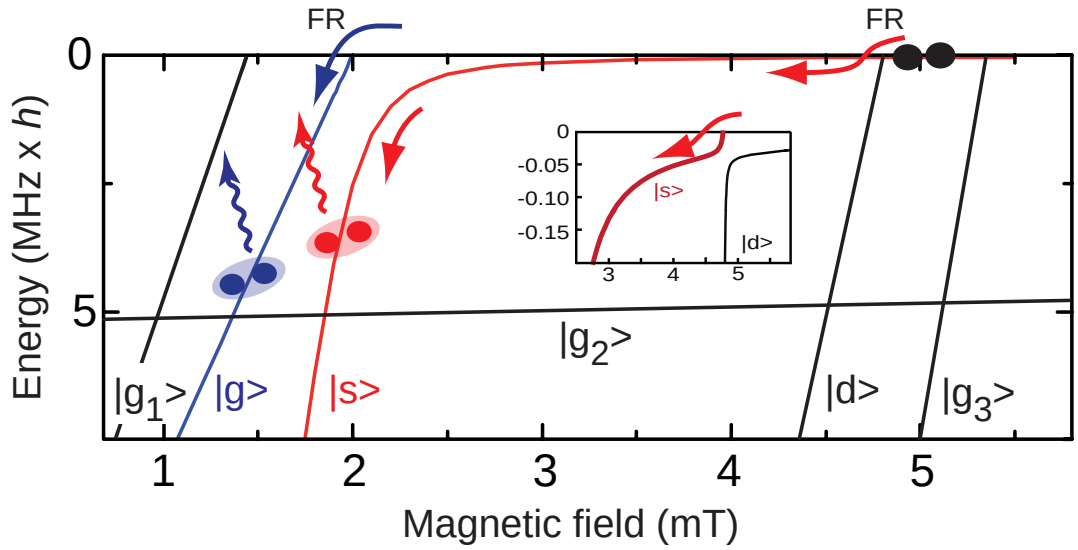

Figure 8.10: Initial Feshbach molecule production: Zeeman diagram showing the energy of weakly bound Feshbach levels [21] and the Feshbach resonances (FR) used in the present work. The binding energy is given with respect to the $F=3, m_F=3$ two-atom asymptote. The molecules are produced either on a d-wave Feshbach resonance at 4.79 mT (see inset) and then transferred to the weakly bound s-wave state $|s>$ on an avoided state crossing, or on a g-wave Feshbach resonance at 1.98 mT, resulting in molecules in level $|g>$. In the first case, further lowering of the magnetic offset field to below 2.0 mT changes the character of the $|s>$ level from open-channel to closed-channel dominated [21]. The levels $|s>$ and $|g>$ are both candidate levels for the initial level $|1>$ shown in Fig. 8.9. For completeness, further g-wave Feshbach levels, $|g_1>$, $|g_2>$, and $|g_3>$ are shown. Level $|g_2>$ connects $|g>$ to $|s>$ and can be used for Feshbach state transfer [21]. Level $|g_3>$ is a further interesting candidate level for $|1>$ with low nuclear spin contribution [21].

For molecule production at the Feshbach resonance at 1.98 mT, we simply ramp the magnetic field down from the initial BEC production value. Again, we produce an ultracold molecular sample with about 11000 molecules. The molecules in $|g>$ have g-wave character, i.e. $\ell=4$. When we lower the magnetic field to 1.6 mT, the binding energy of the molecules is also near 5 MHz$\times h$ with respect to the $F=3, m_F=3$ two-atom asymptote.

For spectroscopy, we release the molecules from the trap after magnetic field ramping is completed and perform all subsequent experiments in free flight without any other light fields on except for the spectroscopy laser.

For molecule detection in both cases, we reverse the magnetic field ramps [29]. The g-wave molecules are dissociated on the g-wave Feshbach resonance at 1.98 mT, and the s-wave molecules are dissociated on the d-wave Feshbach resonance at 4.79 mT. Prior to the reverse magnetic field ramp, we apply a magnetic field gradient of 3.1 mT/cm for about 5 ms to separate the molecular from the atomic sample in a Stern-Gerlach-type experiment. Finally, we detect atoms by standard absorption imaging. The minimum number of molecules that we can detect is on the order of 200 molecules.

Spectroscopy

We perform optical spectroscopy on Feshbach molecules in the wavelength region around 1125 nm. Based on symmetry considerations, there are two sets of electronically excited states that we address in the spectroscopic measurements presented here, namely the $(\mathrm{A}^1\Sigma_u^+ - \mathrm{b}^3\Pi_u)\ 0_u^+$ coupled state system and the $(1)^3\Sigma_g^+$ electronically excited states. We first discuss transitions to the 0_u^+ coupled state system. Transitions to the latter state are discussed in Sec. 8.

Transitions to the $(\mathbf{A}^1\Sigma_u^+ - \mathbf{b}^3\Pi_u)\ 0_u^+$ coupled electronically excited states

We are primarily interested in transitions from Feshbach levels to rovibrational levels of the $(\mathrm{A}^1\Sigma_u^+ - \mathrm{b}^3\Pi_u)\ 0_u^+$ electronically excited states. In the heavy alkali dimers, most notably in Cs_2, the $\mathrm{A}^1\Sigma_u^+$ state and the $\mathrm{b}^3\Pi_u$ state are strongly coupled by resonant spin-orbit interaction [32, 33], yielding the 0_u^+ coupled states in Hund's case (c) notation. The singlet component of the 0_u^+ states allows us to efficiently couple to deeply bound $\mathrm{X}^1\Sigma_g^+$ state levels, specifically to the $|v = 73, J = 2>$ level of the ground state potential, as has recently been shown in a coherent transfer experiment [1]. We have chosen to do spectroscopy in the wavelength range of 1118 nm to 1134 nm above the $6S_{\frac{1}{2}}$+$6S_{\frac{1}{2}}$ dissociation threshold of the Cs_2 dimer. This corresponds to a detuning of roughly 2300 cm^{-1} from the cesium D_1 line and to an energy range of approximately 12572 cm^{-1} to 12450 cm^{-1} above the rovibronic ground state $\mathrm{X}^1\Sigma_g^+$ $|v = 0, J = 0>$. This region was chosen in order to give a balanced distribution of transition dipole moments in a 4-photon transfer scheme to the rovibronic ground state. In addition, the wavelengths of the four lasers used in the transfer experiments were chosen such that they lie within the energy range covered by the infrared fiber-based frequency comb that we use as a frequency reference in the state transfer experiments.

The transitions of interest here lie outside the energy regions for which Fourier transform spectroscopic data was obtained at Laboratoire Aimé Cotton from transitions to the $\mathrm{X}^1\Sigma_g^+$ state [34]. The vibrational progression of the 0_u^+ states is highly perturbed by the resonant spin-orbit coupling and exhibits an irregular vibrational spacing. Molecular structure calculations are complicated by the spin-orbit coupling and calculated term values are highly sensitive to the coupling. Prior to the experiments discussed here the absolute energies of the vibrational levels of the $(\mathrm{A}^1\Sigma_u^+ - \mathrm{b}^3\Pi_u)\ 0_u^+$ excited state levels were poorly known in the region of interest from 1118 nm to 1134 nm. We therefore perform a broad range search by irradiating the weakly-bound Feshbach molecules at a fixed wavelength for a certain irradiation time τ of up to $\tau = 6$ ms and by recording the number of remaining molecules as a function of laser frequency. In one run of the experiment one particular laser frequency is queried. We thus take data points at the repetition rate of our experiment, which is given by the sample preparation time of 8 seconds. Based on the available laser intensity from L_1 and

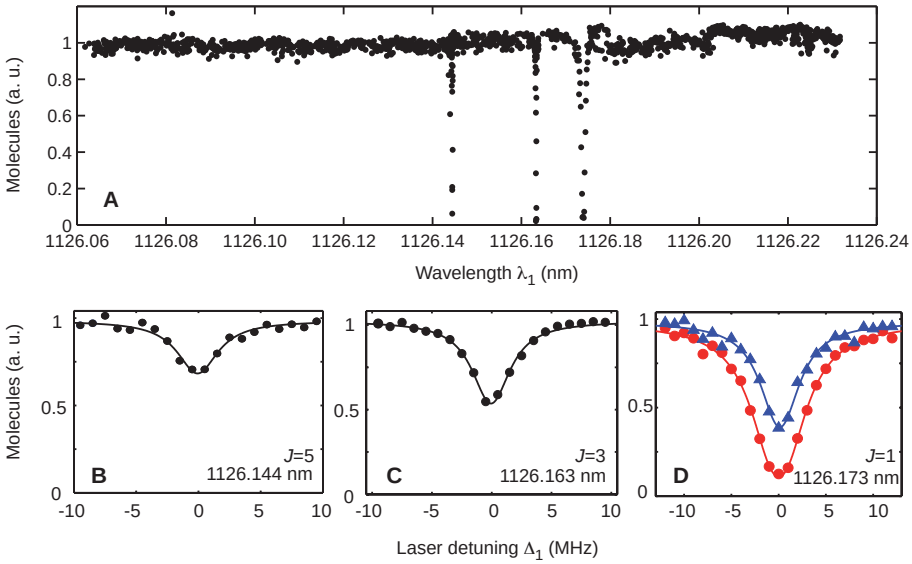

Figure 8.11: Loss resonances for excitation from the initial Feshbach level $|s>$ to the 0_u^+ system. (**A**) Typical scan showing the number of molecules in $|s>$ as a function of laser wavelength λ_1 near 1126 nm. Three resonances can be identified, corresponding to $|J=5>$, $|J=3>$, and $|J=1>$, from left to right. The sample is irradiated with laser light at an intensity of 1×10^6 mW/cm^2 for $\tau = 200$ μs. The laser is locked to a narrow band optical resonator that is tuned via a piezoelectric element with a step size of approximately 40 MHz. Wavelength is measured on a home-built wavemeter. The molecule number is normalized to the atom number measured in the same individual realization of the experiment to cancel out fluctuations that stem from shot-to-shot atom number fluctuations and the baseline is set to 1. (**B**), (**C**), and (**D**) represent measurements of the three individual lines with $|J=5>$, $|J=3>$, and $|J=1>$ at reduced intensity in order to avoid saturation. The solid lines represent fits as described in the text. The spectroscopy laser is stabilized to an optical resonator and the resonator is in turn referenced to an optical frequency comb, which allows precise and reproducible tuning of the frequency. The transition to $|J=1>$ in panel (**D**) is recorded at an intensity of 1.5×10^4 mW/cm^2 (circles) and 6×10^3 mW/cm^2 (triangles), (**B**) and (**C**) are recorded at 1×10^6 mW/cm^2 and 2×10^5 mW/cm^2, respectively. Pulse duration is $\tau = 10$ μs.

an estimate of the dipole transition moments for the strongest expected lines, we chose a frequency step size of about 100 MHz to 150 MHz for initial line searching. We obtain the laser light at 1118 nm - 1134 nm from a grating-stabilized external cavity diode laser. For coarse frequency scanning, the laser is free running and tuned via a piezoelectric element on the grating of the laser. For more precise measurements, we lock the laser to a narrow-band optical resonator that can be tuned via a piezoelectric element. Fig. 8.11A shows a typical loss spectrum starting from Feshbach state $|s>$ for excitation near 1126 nm, measured at a magnetic field of 1.98 mT. In this particular case we find three resonances, which we associate with the rotational splitting of the excited state level, $J = 5, 3, 1$, where J is the rotational quantum number. Based on molecular structure calculations we identify this level as the 225th one of the 0_u^+ progression with an uncertainty of about two in the absolute numbering.

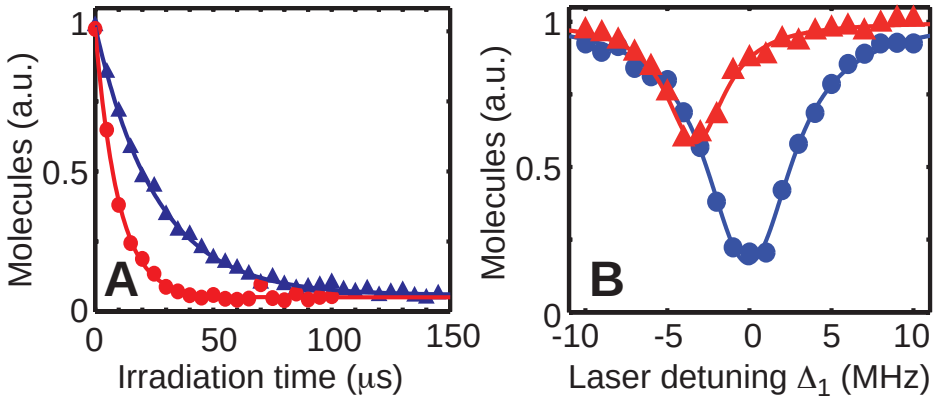

Figure 8.12: Loss of molecules for excitation near 1126.173 nm from Feshbach level $|s>$. (**A**) Time dependence of molecular loss on resonance at 1126.173 nm for two different laser intensities, 5.7×10^5 mW/cm^2 (circles) and 2.1×10^5 mW/cm^2 (triangles). The magnetic offset field is 1.9 mT. The fitted exponential decay gives the decay constants $\tau = 9.7 \pm 0.6$ μs (circles) and $\tau = 25.5 \pm 1$ μs (triangles). (**B**) Loss of molecules in $|s>$ as a function of laser detuning Δ_1 near 1126 nm with an irradiation time of $\tau = 10$ μs for two values of the magnetic field, 1.9 mT (dots) and 2.2 mT (triangles). In both cases, the excited state spontaneous decay rate was determined to $\approx 2\pi \times 2$ MHz. At higher magnetic fields, Feshbach level $|s>$ acquires more open-channel character, reducing radial wave function overlap with the excited rovibrational levels. The shift in transition frequency is the result of a differential magnetic field shift of the Feshbach level $|s>$ and the excited state level.

We zoom in on these three transitions in Fig. 8.11B, C, and D and record loss resonances at reduced laser intensity in order to avoid saturation of the lines. For these measurements, the laser is locked to the narrow-band optical resonator and the resonator in turn is stabilized to the optical frequency comb to assure reproducibility and long term frequency stability. As one can expect, the loss is strongest on the transition to the $|J=1>$ level, and it is weakest on the transition to $|J=5>$. All lines have an excited state spontaneous decay rate of around $2\pi \times 2$ MHz, in agreement with the typical expected lifetimes of excited molecular levels. The transition to $|J=1>$ shown in Fig. 8.11D is of special interest to the current work. It has been used as intermediate excited state level for coherent transfer to $X^1\Sigma_g^+$ $|v=73, J=2>$ in our recent experiments [1].

By fitting a two level model that takes into account decay from the upper level to a series of such measurements obtained with different laser intensities, we determine the transition strength as given by the normalized Rabi frequency. As the Feshbach molecules scatter photons and spontaneously decay to other molecular levels, the number of Feshbach molecules N decays as a function of laser detuning Δ_1 according to

$$N(\Delta_1) = N_0 \exp\left(-\tau\Omega_1^2/(\Gamma(1+4\pi^2\Delta_1^2/\Gamma^2))\right),$$

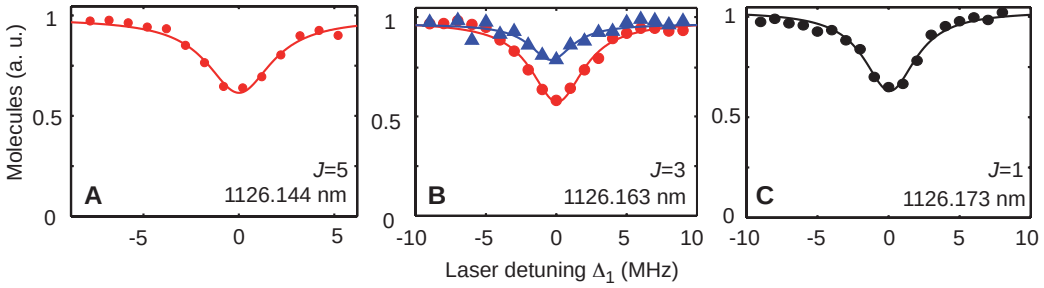

Figure 8.13: Loss resonances for excitation from the initial Feshbach level $|g>$. **(A),(B)**, and **(C)** show the loss for excitation to $|J=5>$, $|J=3>$, and $|J=1>$, corresponding to the resonances shown in Fig. 8.11. The laser intensities are 1.5×10^4 mW/cm^2 for panel **(A)** and for the circles in panel **(B)**. The second resonance in **(B)** (triangles) is measured with 5.6×10^3 mW/cm^2. **(C)** The line at 1126.173 nm is measured at 1×10^6 mW/cm^2. All measurements are done with an irradiation time of $\tau=10$ μs. From a series of such measurements at different intensities we determine the line strengths for $|J=5>$, $|J=3>$, and $|J=1>$ to $\Omega_1=2\pi\times1$ kHz $\sqrt{I/(\mathrm{mW/cm^2})}$, $\Omega_1=2\pi\times1$ kHz $\sqrt{I/(\mathrm{mW/cm^2})}$, and $\Omega_1=2\pi\times0.1$ kHz $\sqrt{I/(\mathrm{mW/cm^2})}$, respectively.

where N_0 is the molecule number without laser irradiation and τ is the irradiation time. From the fit we obtain the Rabi frequency on resonance Ω_1 and the excited state spontaneous decay rate Γ. We determine the normalized Rabi frequency to $\Omega_1=2\pi\times2$ kHz $\sqrt{I/(\mathrm{mW/cm^2})}$ for $|J=1>$, where I is the laser intensity. This value is sufficient to perform STIRAP given the available laser power [1]. The corresponding transition strengths for $|J=3>$ and $|J=5>$ are $\Omega_1=2\pi\times0.3$ kHz $\sqrt{I/(\mathrm{mW/cm^2})}$ and $\Omega_1=2\pi\times0.1$ kHz $\sqrt{I/(\mathrm{mW/cm^2})}$, respectively. The absolute values of these transition strengths bear an estimated uncertainty of 20 % because the laser beam parameters for the spectroscopy laser are not well determined.

We also record the time dependence of the molecular loss on some of the stronger lines. For this, we step the laser irradiation time τ from 0 to 150 μs, while laser L_1 is kept on resonance. The result is shown in Fig. 8.12A for the transition at 1126.173 nm for two different values of the excitation laser intensity.

We note that the transition strength for a particular line starting from Feshbach level $|s>$ strongly depends on the value of the magnetic field, as evidenced in Fig. 8.12B. Loss resonances for the transition at 1126.173 nm at 1.9 mT and 2.2 mT are shown. For ground state transfer [1], we choose a magnetic field of around 1.9 mT, which is somewhat below the magnetic field region where state $|s>$ is strongly curved, but above the avoided state crossing with state $|g_2>$, as seen in Fig. 8.10. The pronounced bending of $|s>$ is the result of a strong avoided crossing between two s-wave Feshbach levels [21]. For magnetic field values beyond 3.0 mT the level $|s>$ can be associated to the $F_1=3, F_2=3$ asymptote, where $F_i, i=1,2$, is the atomic angular momentum quantum number of the i-th atom, respectively. Below 2.0 mT the level $|s>$ can be associated to the $F_1=4, F_2=4$ asymptote. It is hence of closed channel

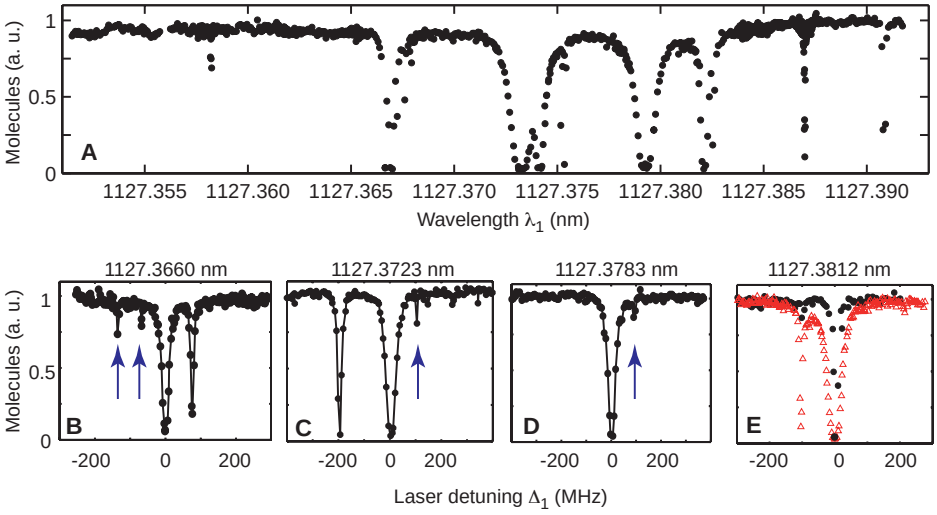

Figure 8.14: Loss of molecules for excitation near 1127.17 nm from Feshbach level $|s>$ to the triplet $(1)^3\Sigma_g^+$ state. (**A**) represents a broad scan with laser irradiation at an intensity of 5×10^5 mW/cm^2 for $\tau = 100$ μs at a step size of 20 MHz. A rich structure due to rotation and excited state hyperfine splitting can be seen which is qualitatively different from the spectrum shown in Fig. 8.11. The lines are greatly broadened by the high intensity and long irradiation time. The spectroscopy laser is locked to a narrow band optical resonator that is stepped via a piezoelectric element. Scans of about 750 MHz were recorded as a function of piezo voltage on the resonator. Voltage was converted to wavelength for each scan by a linear interpolation. (**B**)-(**E**) represent scans over some of the observed features at a reduced intensity of 8×10^4 mW/cm^2 and an irradiation time of $\tau = 10$ μs in order to reduce broadening of the lines. The step size is about 7 MHz. Resonator piezo voltage is converted to frequency with an estimated error of 10 %. The vertical arrows indicate weak lines that have been verified in additional scans with higher power. In panel (**E**) the power was somewhat increased for an additional measurement (triangles) that emphasizes such a weak line. The wavelengths given to identify the zero point on the frequency axis for each subpanel are not meant to imply this level of accuracy which is limited to 0.001 nm by wavemeter calibration. Nevertheless, they give a measure of the energy of the sublines relative to each other.

character and much more deeply bound with respect to its potential asymptote, effectively by twice the atomic hyperfine splitting, improving the radial wave function overlap with the excited state levels. This increases the transition strength. Trivially, the resonance frequency is shifted as the binding energy is reduced for larger magnetic field values. Coupling to the excited state level is reduced from $\Omega_1 = 2\pi \times 2$ kHz $\sqrt{I/(\mathrm{mW/cm^2})}$ to $\Omega_1 = 2\pi \times 1$ kHz $\sqrt{I/(\mathrm{mW/cm^2})}$ when the magnetic field is changed from 1.9 mT to 2.2 mT.

As will be discussed in Sec.8 it is advantageous to be able to choose different Feshbach states as a starting state for ground state transfer experiments. Therefore, we probe transitions from Feshbach level $|g>$ to $(\mathrm{A}^1\Sigma_u^+ - \mathrm{b}3\Pi_u)\ 0_u^+$ levels. Fig. 8.13 shows loss resonances to the same excited state levels as shown in Fig. 8.11, only that now the initial Feshbach level is $|g>$ instead of $|s>$. In this case, the transition to $|J = 3>$ is the strongest, while the transition

to $|J=1>$ is very weak, but can be detected. A comparison of the transition strengths from $|g>$ to the excited state level $|J=3>$, giving $\Omega_1 = 2\pi \times 1$ kHz $\sqrt{I/(\mathrm{mW/cm^2})}$ versus $|s>$ to $|J=1>$ giving $\Omega_1 = 2\pi \times 2$ kHz $\sqrt{I/(\mathrm{mW/cm^2})}$ shows that level $|g>$ could also be potentially used as a starting level for coherent population transfer to deeply bound levels of the ground state but requires longer STIRAP times in order to assure sufficient adiabaticity [23]. The $|J=3>$ excited state level in turn couples to $|J=2>$ in the ground state, as in previous work [1].

In addition to the transition near 1126 nm we find a series of other excited state levels that we assign to the $(\mathrm{A}^1\Sigma_u^+ - \mathrm{b}^3\Pi_u)\ 0_u^+$ coupled state system. These are listed in Table 8.2. The assignment to either the $(\mathrm{A}^1\Sigma_u^+ - \mathrm{b}^3\Pi_u)\ 0_u^+$ system or to the $(1)^3\Sigma_g^+$ electronically excited state discussed below is primarily based on the spacing between neighboring vibrational levels and in addition on the pattern of loss resonances associated with each particular vibrational level. Resonant spin-orbit coupling in the case of the 0_u^+ states leads to an irregular vibrational spacing. In contrast, the $(1)^3\Sigma_g^+$ state is not perturbed by spin-orbit interaction and therefore has a regular vibrational progression. The levels near 1126 nm and near 1123 nm have been used to detect dark resonances with deeply bound levels of the $\mathrm{X}^1\Sigma_g^+$ state [1]. The ability to couple to these essentially purely singlet ground state levels unambiguously assigns the corresponding excited state levels to the 0_u^+ system. The data given in Table 8.2 does not represent a fully exhaustive study of the $(\mathrm{A}^1\Sigma_u^+ - \mathrm{b}^3\Pi_u)\ 0_u^+$ coupled states in the wavelength range of interest. In fact, for the most part we observe those levels of the 0_u^+ system that have a dominant $\mathrm{A}^1\Sigma_u^+$ state contribution, as determined from molecular structure calculations.

Transitions to the $(1)^3\Sigma_g^+$ electronically excited state

The Feshbach levels that serve as starting levels for the spectroscopy are of mixed $\mathrm{X}^1\Sigma_g^+$ and $\mathrm{a}^3\Sigma_u^+$ character. In the wavelength range explored here, excitation to the $(1)^3\Sigma_g^+$ electronically excited triplet state is possible from the $\mathrm{a}^3\Sigma_u^+$ component of the Feshbach molecules. In fact, for a heavy molecule as Cs_2, the $(1)^3\Sigma_g^+$ state is better described by the two separate electronic states 0_g^- and 1_g, denoted by the Hund's case (c) notation. The $(1)^3\Sigma_g^+$ has been previously studied by Fourier transform spectroscopy [35]. This state is not of prime interest for the present work as transitions from this state down to the $\mathrm{X}^1\Sigma_g^+$ ground state are expected to be strongly suppressed, but would be important for STIRAP transfer into the rovibrational ground state level of the shallow triplet $\mathrm{a}^3\Sigma_u^+$ potential [18]. Certainly, it is important to be able to distinguish rovibrational levels belonging to the $(1)^3\Sigma_g^+$ state from the ones belonging to the 0_u^+ system, because otherwise time would be wasted in searching for ground state dark resonances that are very weak or even do not exist. Fig. 8.14A shows a typical loss spectrum for one of the lines that we detected near 1127.37 nm. Due to hyperfine splitting, levels of triplet character exhibit a much richer substructure than the 0_u^+ levels

used for ground state transfer. Several components can be identified as a result of rotational and excited state hyperfine splitting. Zoomed-in regions are shown in Fig. 8.14B, C, D, and E. We have observed a regularly spaced series of optical transitions which we attribute to the $(1)^3\Sigma_g^+$ excited state as listed in Table 8.2. The levels are well reproduced by molecular structure calculations using the Dunham coefficients from Ref.[35]. The vibrational numbering used here is the same as in that work. However, it relies on the absolute energy position of the potential, T_e, which was not determined precisely in Ref. [35].

Conclusion

We have performed optical spectroscopy starting from weakly bound Cs_2 Feshbach molecules into deeply bound rovibrational levels of the mixed excited state 0_u^+ system and the excited triplet $(1)^3\Sigma_g^+$ state. At least one of the observed transitions, namely the one at 1126.173 nm starting from the Feshbach level $|s>$ at an offset magnetic field value of 1.9 mT to the excited level $|v'=225, J=1>$ of the 0_u^+ system, is strong enough to allow efficient STIRAP transfer into deeply bound rovibrational levels of the singlet $X^1\Sigma_g^+$ ground state potential. The use of this transition for STIRAP has recently been demonstrated in Ref.[1]. In that work, the deeply bound rovibrational level $|v=73, J=2>$ of the $X^1\Sigma_g^+$ ground state potential was populated in the molecular quantum gas regime with 80% efficiency. The rovibrational ground state $|v=0, J=0>$ of the $X^1\Sigma_g^+$ ground state potential can thus be reached from the atomic threshold with a maximum of two two-photon STIRAP transfers. Dark resonances connecting $|v=73, J=2>$ to $|v=0, J=0>$ have recently been observed [6], and two-step STIRAP into $|v=0, J=0>$ has recently been implemented [7]. For future experiments, the use of Feshbach level $|g>$ as the initial state might be advantageous. Level $|g>$ can be more easily populated, as the Feshbach resonance connected to this level is at a low magnetic field value of 1.98 mT [21], where the atomic background scattering length has a moderate value of 155 a_0, where a_0 is Bohr's radius. The use of this resonance avoids excitation of collective motion of the atomic BEC as a result of a large mean field interaction near the Feshbach resonance at 4.79 mT [1], where the atomic background scattering length is about 935 a_0. The transition starting from level $|g>$ appears to be strong enough to allow STIRAP, this time via the excited state level $|v'=225, J=3>$ of the 0_u^+ system. An attractive strategy for the production of a BEC of ground state molecules relies on the addition of a three-dimensional optical lattice. Starting from the atomic BEC, pairs of atoms at individual lattice sites can be produced in a superfluid-to-Mott-insulator transition [Gre02] with high efficiencies of up to 50% [12]. These pairs can then be very efficiently associated on a Feshbach resonance [20] and subsequently transferred to the rovibronic ground state with STIRAP. The lattice has the advantage of shielding the molecules against inelastic collisions during the association process and subsequent state transfer. In particular, it should allow long STIRAP pulse du-

rations, allowing us to resolve the weak hyperfine structure of ground state molecules [4]. As proposed by Jaksch *et al.* [12], dynamical melting of the lattice should ideally result in the formation of a BEC of molecules in the rovibronic ground state in a Mott-insulator-to-superfluid-type transition.

Acknowledgements

We are indebted to R. Grimm for generous support and we thank T. Bergeman, H. Salami, J. Hutson, J. Aldegunde, and E. Tiemann for valuable discussions. We gratefully acknowledge funding by the Austrian Ministry of Science and Research (BMWF) and the Austrian Science Fund (FWF) in form of a START prize grant and by the European Science Foundation (ESF) in the framework of the EuroQUAM collective research project QuDipMol. R.H. acknowledges support by the European Union in form of a Marie-Curie International Incoming Fellowship (IIF).

Table 8.2: Observed excited state levels in the wavelength range from 1118 nm to 1134 nm. Transitions were measured from Feshbach state $|s>$ to the first electronically excited state, addressing both $(\mathrm{A}^1\Sigma_u^+ - \mathrm{b}^3\Pi_u)0_u^+$ levels and $(1)^3\Sigma_g^+$ levels. Levels are given according to the excitation wavelength (WL) from $|s>$, which essentially corresponds to the $F=3, m_F=3$ two-atom asymptote. The data is taken at a magnetic field of 1.98 mT. Wavemeter accuracy is about 0.001 nm. The energy of these levels above the rovibronic ground state $\mathrm{X}^1\Sigma_g^+$ $|v=0, J=0>$ is given in the second column, where the binding energy of the rovibronic ground state is taken from Ref.[1]. The assignment to either the coupled $(\mathrm{A}^1\Sigma_u^+ - \mathrm{b}^3\Pi_u)0_u^+$ system or to the $(1)^3\Sigma_g^+$ is based on the vibrational spacing and similarities in the substructure of the levels. The levels marked with $*$ have been used for dark resonance spectroscopy coupling to deeply bound levels of the $\mathrm{X}^1\Sigma_g^+$ state [1]. The ability to couple to such levels unambiguously reflects an important singlet component stemming from the $\mathrm{A}^1\Sigma_u^+$ state and therefore clearly assigns these levels to the 0_u^+ system. The quantum numbers given for the 0_u^+ levels are coupled channels quantum numbers derived from molecular structure calculations and bear an uncertainty of two in the absolute numbering. The calculations show that these levels have about 70% $\mathrm{A}^1\Sigma_u^+$ state contribution. Two further levels observed near 1120.17 nm and 1117.16 nm that belong to the 0_u^+ progression are not given in the table since no further measurements have been done on these levels. The level near 1129.5 nm exhibits a somewhat richer structure than the other levels assigned to 0_u^+ and than exemplified in Fig. 8.11. Levels assigned to the $(1)^3\Sigma_g^+$ state form a regular vibrational progression and show a more complex substructure than the levels attributed to the 0_u^+ system, as exemplified in Fig. 8.14. For these levels, the transition wavelength to one of the most prominent features is given, since an in depth analysis of the rotational and hyperfine structure remains to be done. The vibrational numbering for the $(1)^3\Sigma_g^+$ levels is the same as in Ref [35].

WL [nm]	Energy above $\mathrm{X}^1\Sigma_g^+$ $\|v=0>$ [cm^{-1}]	Assignment
1132.481	12458.875	0_u^+ $\|v'=221, J=1>$
1129.492	12482.245	0_u^+
1126.173$*$	12508.332	0_u^+ $\|v'=225, J=1>$
1123.104$*$	12532.598	0_u^+ $\|v'=226, J=1>$
1133.680	12449.536	$(1)^3\Sigma_g^+$ $\|v'=32>$
1130.510	12474.274	$(1)^3\Sigma_g^+$ $\|v'=33>$
1127.379	12498.838	$(1)^3\Sigma_g^+$ $\|v'=34>$
1124.274	12523.334	$(1)^3\Sigma_g^+$ $\|v'=35>$
1121.196	12547.756	$(1)^3\Sigma_g^+$ $\|v'=36>$
1118.155	12572.013	$(1)^3\Sigma_g^+$ $\|v'=37>$

BIBLIOGRAPHY

[1] J. G. Danzl, E. Haller, M. Gustavsson, M.J. Mark, R. Hart, N. Bouloufa, O. Dulieu, H. Ritsch, and H.-C. Nägerl, *Science*, 2008, **321**, 1062, published online 10 July 2008; 10.1126/science.1159909.

[2] T. Zelevinsky, S. Kotochigova, and J. Ye, *Phys. Rev. Lett.*, 2008, **100**, 043201.

[3] D. DeMille, S. Sainis, J. Sage, T. Bergeman, S. Kotochigova, and E. Tiesinga, *Phys. Rev. Lett.*, 2008, **100**, 043202.

[4] P. Staanum, S. D. Kraft, J. Lange, R. Wester, and M. Weidemüller, *Phys. Rev. Lett.*, 2006,**96**, 023201.

[5] N. Zahzam, T. Vogt, M. Mudrich, D. Comparat, and P. Pillet, *Phys. Rev. Lett.*, 2006, **96**, 023202.

[6] R.V. Krems, *Int. Rev. Phys. Chem.*, 2005, **24**, 99.

[7] D. DeMille, *Phys. Rev. Lett.*, 2002, **88**, 067901.

[8] K. Góral, L. Santos, and M. Lewenstein, *Phys. Rev. Lett.*, 2002, **88**, 170406.

[9] M. Baranov, L. Dobrek, K. G-ral, L. Santos, and M. Lewenstein, *Phys. Scr.* , 2002, **T102**, 74.

[10] K. Southwell (ed.), Ultracold matter, *Nature (Insight)*, 2002, **416**, 205.

[11] J. Doyle, B. Friedrich, R.V. Krems, and F. Masnou-Seeuws, *Eur. Phys. J. D*, 2004, **31**, 149.

[12] R.V. Krems, *Phys. Chem. Chem. Phys.*, 2008, **10**, 4079.

[13] S.Y.T. van de Meerakker, H.L. Bethlema, and G. Meijer, *Nature Phys.*, 2008, **4**, 595.

[14] For a review on photoassociation, see: K. M. Jones, E. Tiesinga, P.D. Lett, P. S. Julienne, *Rev. Mod. Phys.*, 2006 **78**, 483.

[15] T. Köhler, K. Góral, P. S. Julienne, *Rev. Mod. Phys.*, 2006, **78**, 1311.

[16] F. Ferlaino, S. Knoop, and R. Grimm, in: Cold Molecules: Theory, Experiment, Applications, edt. by R. V. Krems, B. Friedrich, and W. C. Stwalley (publication expected in March 2009), preprint at arXiv:0809.3920.

[17] A.N. Nikolov, J.R. Ensher, E.E. Eyler, H. Wang, W.C. Stwalley, and P.L. Gould, *Phys. Rev. Lett.*, 2000, **84**, 246.

[18] J.M. Sage, S. Sainis, T. Bergeman, and D. DeMille, *Phys. Rev. Lett.*, 2005, **94**, 203001.

[19] M. Viteau, A. Chotia, M. Allegrini, N. Bouloufa, O. Dulieu, D. Comparat, P. Pillet, *Science*, 2008, **321**, 232.

[20] J. Deiglmayr, A. Grochola, M. Repp, K. Mörtlbauer, C. Glück, J. Lange, O. Dulieu, R. Wester, and M. Weidemüller, *Phys. Rev. Lett.*, 2008, **101**, 133004.

[21] C. A. Regal, C. Ticknor, J. L. Bohn, and D. S. Jin, *Nature*, 2003, **424**, 47.

[22] J. Herbig, T. Kraemer, M. Mark, T. Weber, C. Chin, H.-C. Nägerl, and R. Grimm, *Science*, 2003, **301**, 1510, published online 21 August 2003; 10.1126/science.1088876.

[23] For an overview, see: Ultracold Fermi Gases, *Proceedings of the International School of Physics Enrico Fermi, Course CLXIV*, edited by M. Inguscio, W. Ketterle, and C. Salomon (IOS Press, Amsterdam, 2008).

[24] K. Bergmann, H. Theuer and B. W. Shore, *Rev. Mod. Phys.*, 1998, **70**, 1003.

[25] M. Mark, T. Kraemer, J. Herbig, C. Chin, H.-C. Nägerl, and R. Grimm, *Europhys. Lett.*, 2005, **69**, 706.

[26] K. Winkler, F. Lang, G. Thalhammer, P. v. d. Straten, R. Grimm, and J. Hecker Denschlag, *Phys. Rev. Lett.*, 2007, **98**, 043201.

[27] K.-K. Ni, S. Ospelkaus, M. H. G. de Miranda, A. Pe'er, B. Neyenhuis, J.J. Zirbel, S. Kotochigova, P.S. Julienne, D.S. Jin, and J. Ye, published online September 18, 2008, *Science* DOI: 10.1126/science.1163861.

[28] W.C. Stwalley, *Eur. Phys. J. D*, 2004, **31**, 221.

[29] F. Lang, K. Winkler, C. Strauss, R. Grimm, and J. Hecker Denschlag, Phys. Rev. Lett. **101**, 133005 (2008).

[30] M. Mark, F. Ferlaino, S. Knoop, J.G. Danzl, T. Kraemer, C. Chin, H.-C. Nägerl, and R. Grimm, *Phys. Rev. A*, 2007, **76**, 042514.

[31] T. Weber, J. Herbig, M. Mark, H.-C. Nägerl, and R. Grimm, *Science*, 2003, **299**, 232.

[32] O. Dulieu and P. Julienne, *J. Chem. Phys.*, 1995, **103**, 60.

[33] C. Amiot, O. Dulieu, and J. Vergès, *Phys. Rev. Lett.* , 1999, **83**, 2316.

[34] H. Salami, T. Bergeman, O. Dulieu, D. Li, F. Xie, and L. Li, manuscript in preparation (2008).

[35] C. Amiot and J. Verges, *Chem. Phys. Lett.*, 1985, **116**, 273.

[36] M. J. Mark, J. G. Danzl, E. Haller, M. Gustavsson, N. Bouloufa, O. Dulieu, H. Salami, T. Bergeman, H. Ritsch, R. Hart, and H.-C. Nägerl, manuscript submitted for publication, 2008, preprint at arXiv:0811.0695.

[37] J. G. Danzl, M. J. Mark, E. Haller, M. Gustavsson, N. Bouloufa, O. Dulieu, H. Salami, T. Bergeman, H. Ritsch, R. Hart, H.-C. Nägerl, manuscript in preparation.

[38] M. Greiner, O. Mandel, T. Esslinger, T.W. Hänsch, and I. Bloch, *Nature*, 2002, **415**, 39.

[39] S. Dürr, 2008, private communication.

[40] G. Thalhammer, K. Winkler, F. Lang, S. Schmid, R. Grimm, and J. Hecker Denschlag, *Phys. Rev. Lett.*, 2006, **96**, 050402.

[41] J. Aldegunde and J. M. Hutson, 2008, preprint at arXiv:0810.4709.

[42] D. Jaksch, V. Venturi, J. I. Cirac, C. J. Williams, and P. Zoller, *Phys. Rev. Lett.*, 2002, **89**, 040402.

Lattice-based ground state transfer: Deeply bound ultracold molecules in an optical lattice

New J. Phys. **11** 055036 (2009)

Johann G. Danzl[1], Manfred J. Mark[1], Elmar Haller[1], Mattias Gustavsson[1], Russell Hart[1], Andreas Liem[2], Holger Zellmer[3], and Hanns-Christoph Nägerl[1]

[1] *Institut für Experimentalphysik und Zentrum für Quantenphysik, Universität Innsbruck, Technikerstraße 25, A–6020 Innsbruck, Austria*

[2] *JT Optical Engine GmbH + Co. KG, Prüssingstraße 41, D–07745 Jena, Germany*

[3] *Hochschule für Technik, Wirtschaft und Kultur Leipzig, Gutenbergplatz 2-4, D–04103 Leipzig, Germany*

We demonstrate efficient transfer of ultracold molecules into a deeply bound rovibrational level of the singlet ground state potential in the presence of an optical lattice. The overall molecule creation efficiency is 25%, and the transfer efficiency to the rovibrational level $|v = 73, J = 2>$ is above 80%. We find that the molecules in $|v = 73, J = 2>$ are trapped in the optical lattice, and that the lifetime in the lattice is limited by optical excitation by the lattice light. The molecule trapping time for a lattice depth of 15 atomic recoil energies is about 20 ms. We determine the trapping frequency by the lattice phase and amplitude modulation technique. It will now be possible to transfer the molecules to the rovibrational ground state $|v=0, J=0>$ in the presence of the optical lattice.

Introduction

The generation of molecular quantum gases and molecular Bose-Einstein condensates (BEC) has been a major goal for the field of atomic and molecular physics. It has been achieved for the case of two fermionic atoms that pair up to form a bosonic dimer molecule in the limit of vanishing binding energy [1, 2] at ultralow temperatures. In this limit, collisional stability is assured, and this has allowed the investigation of the BEC-BCS crossover [3]. Here, we are interested in the opposite limit of deeply bound molecules. Collisional stability is expected only for the rovibronic ground state, and most likely it will be necessary that one prepares the lowest molecular hyperfine sublevel [4] to avoid hyperfine changing collisions. Our approach to producing a quantum gas of ground state molecules is based on laser cooling of atoms to the point of quantum degeneracy, followed by molecule association on a Feshbach resonance and subsequent coherent two-photon molecule transfer [Dan08, 6, 7, 17, 16, 18]. In principle, this approach combines high molecular densities and ultralow temperatures with full state selectivity. For optimization of both the initial molecule creation process and

the transfer process, the use of a three-dimensional optical lattice has been proposed, as illustrated in Fig. 8.15C. In a superfluid-to-Mott-insulator phase transition doubly occupied lattice sites can be favored [6, 12], and collisional relaxation during the transfer can, at least in principle, be fully avoided. It should be possible that one finally creates a molecular BEC by dynamical melting of the lattice after the two-photon transfer [12].

In the present work, we report on two-photon transfer into a deeply bound rovibrational level by means of the stimulated Raman adiabatic passage (STIRAP) technique [23, 17] in the presence of a three-dimensional optical lattice. We extend our previous work of transfering Cs_2 molecules to rovibrational level $|v = 73, J = 2>$ of the $^1\Sigma_g^+$ electronic ground state in the quantum gas regime [Dan08] by first using the superfluid-to-Mott-insulator phase transition to efficiently produce pairs of atoms at the wells of the lattice. The pairs are then associated to weakly bound molecules on a Feshbach resonance. Subsequently, the molecules are transferred by magnetic field ramping to the starting state for optical transfer. From there, they are efficiently transferred to the deeply bound rovibrational level $|v = 73, J = 2>$ by means of STIRAP. Note that in our previous work [Dan08] all experiments were performed in free flight. Fig. 8.15A shows the relevant molecular states for the Cs dimer molecule and the transitions involved. We find that the molecules in $|v = 73, J = 2>$ are trapped in the lattice with a $1/e$-trapping time of about 20 ms, limited by scattering of lattice light. We measure the trapping frequency of the molecules in the lattice and find that the polarizability in $|v = 73, J = 2>$ is about 30% of that of the Feshbach molecules. It will now be possible that one adds a second STIRAP transfer step to reach the rovibronic ground state $|v=0, J=0>$, giving full quantum control over the external and internal degrees of freedom for the molecules.

Preparation of Feshbach molecules in the optical lattice

To produce an ultracold sample of Feshbach molecules trapped at the individual sites of an optical lattice we first produce an atomic BEC with typically 1×10^5 Cs atoms in the lowest hyperfine sublevel $F=3,\ m_F=3$ in a crossed optical dipole trap. As usual, F is the atomic angular momentum quantum number, and m_F its projection on the magnetic field axis. For BEC production, we essentially follow the procedure detailed in Ref.[15]. We set the atomic scattering length to a value of 210 a_0, where a_0 is Bohr's radius, by tuning the magnetic offset field to 2.1 mT. At this value, three-body losses are minimal [16]. We then drive the superfluid-to-Mott-insulator phase transition [17] by exponentially ramping up the power in a three-dimensional optical lattice within about 400 ms while simultaneously ramping up the harmonic confinement in the dipole trap. The lattice is generated by three mutually orthogonal, retro-reflected laser beams at a wavelength of $\lambda = 1064.5$ nm, each with a $1/e$-waist of about 350 μm. For the atoms, we achieve a well depth of up to 40 E_R, where $E_R =$

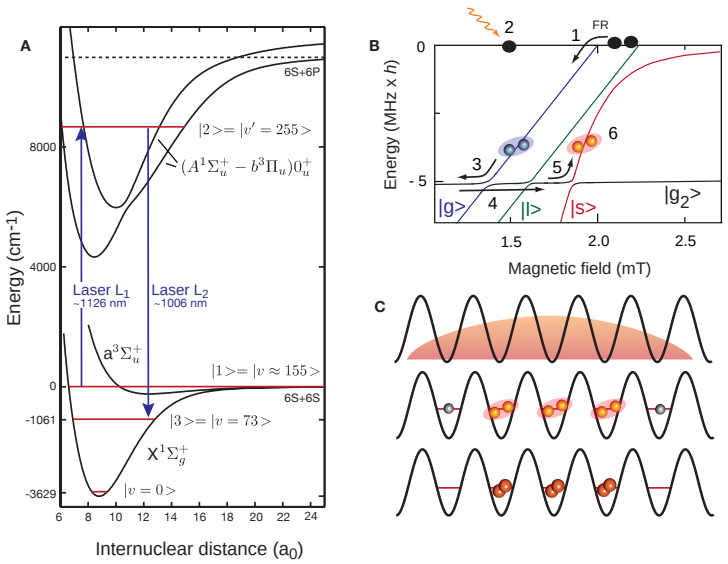

Figure 8.15: A Molecular level scheme for Cs_2. Molecules in a weakly bound Feshbach level $|1>$ are transferred to rovibrational level $|3>= |v=73, J=2>$ of the singlet $X^1\Sigma_g^+$ potential in the presence of an optical lattice. Level $|3>$ with a binding energy of 1061 cm^{-1} is reached in a two-photon STIRAP process with wavelengths near 1126 nm and 1006 nm via the 225th level of the electronically excited $(A^1\Sigma_u^+ – b^3\Pi_u)\, 0_u^+$ potentials. The $X^1\Sigma_g^+$ potential has about 155 vibrational levels. **B** Zeeman diagram showing the energy of all relevant weakly bound molecular levels for initial Feshbach molecular state preparation [21]. The binding energy is given with respect to the $F=3, m_F=3$ two-atom asymptote. The molecules are first produced on a g-wave Feshbach resonance at 1.98 mT in state $|g>$ (1). Residual atoms are removed by a combined microwave and resonant light pulse (2). The molecules are then transferred to the weakly bound s-wave state $|1>= |s>$ (6), the starting state for the STIRAP transfer, via three avoided state crossings involving state $|g_2>$ by slow (3,5) and fast magnetic field ramps (4). **C** Lattice based ground state transfer. Top: The BEC is adiabatically loaded into the three-dimensional optical lattice, creating a Mott-insulator state. Middle: Atoms at doubly occupied sites are converted to Feshbach molecules. Atoms at singly occupied sites are removed thereafter. Bottom: The molecules are subsequently transferred to the deeply bound rovibrational level $|3>= |v = 73, J = 2>$ while shielded from collisions by the lattice potential.

$h^2/(2m\lambda^2) = k_B \times 64\,$nK is the atomic photon recoil energy with the mass m of the Cs atom. h is Planck's constant, and k_B is Boltzmann's constant. Throughout the paper we give lattice depths in units of the atomic recoil energy. The lattice light as well as the light for the dipole trap beams is derived from a single-frequency, narrow-band, highly-stable Nd:YAG laser that is amplified to up to 20 W without spectral degradation in a home-built fiber amplifier [18]. The power in each lattice beam is controlled by an acousto-optical intensity modulator and an intensity stabilization servo. While ramping up the lattice potential, the power in the two dipole trap beams is increased to assure that the central density in the trap is sufficiently high to allow the preferential formation of atom pairs at the central wells of the lattice, but not too high in order to avoid triply occupied sites. We typically ramp the lattice to a depth of 15 to 25 E_R. Typically about 30% of the atoms reside at doubly occupied lattice sites. We

estimate this number from the molecule production efficiency. This value is not optimal yet, as loading from a parabolic potential should give a maximum of 53% [12, 19].

We now produce Feshbach molecules on a Feshbach resonance [20, 29, Köh06] near a magnetic field value of $B = 1.98$ mT [21] in the presence of the optical lattice [20, 6]. Fig. 8.15B shows the relevant weakly bound Feshbach levels. The resonance at 1.98 mT is quite narrow, but it lies at a conveniently low value of the magnetic field, allowing us to simply lower the magnetic offset field from the BEC production value and ramp over the resonance with a rate of about 0.006 T/s. The molecules produced are then in level $|g>$. These molecules have g-wave character, i.e. $\ell = 4$, where ℓ is the quantum number associated with the mechanical rotation of the nuclei [25]. After association, atoms remaining at singly occupied lattice sites are removed by microwave transfer to $F = 4$ and a resonant light pulse. Starting from level $|g>$ we have recently identified transitions to deeply bound excited rovibrational levels of the Cs_2 mixed $(A^1\Sigma_u^+ - b^3\Pi_u)\ 0_u^+$ excited states [7]. These transitions should allow STIRAP transfer to the target rovibrational level $|v = 73, J = 2>$ of the electronic ground state, but for the present work we have decided to use Feshbach level $|s>$ as the starting state as in our previous work [Dan08] so that the transfer performances with and without the presence of the lattice can be compared. To reach level $|s>$ from level $|g>$, we have implemented Feshbach state transfer as realized in Ref.[21] using a combination of slow and fast magnetic field ramps. In brief, we first transfer the molecules from $|g>$ to level $|g_2>$ by lowering the magnetic field B sufficiently slowly to a value of 1.22 mT, thereby following the upper branch of an avoided crossing near 1.33 mT as shown in Fig. 8.15 B. We then increase B abruptly to a value of 1.67 mT, thereby jumping the two crossings with levels $|g>$ and $|l>$. The maximum magnetic field rate of change is ~ 2000 T/s. We finally follow slowly on the upper branch of the avoided crossing with $|s>$ at 1.85 mT, stopping at $B = 1.9$ mT. Our procedure allows us to essentially transfer all molecules from $|g>$ to $|s>$. For molecule detection, we reverse the magnetic field ramps to level $|g>$, dissociate the molecules at the Feshbach resonance at $B = 1.98$ mT and detect the resulting atoms by standard absorption imaging [29].

For comparison with our data obtained below we first measure the lifetime of the weakly-bound Feshbach molecules in the optical lattice. Typical lifetime measurements for these molecules are shown in Fig. 8.16A-C. In such measurements, we record the number of remaining molecules as a function of hold time in the lattice. The lifetime of the molecules depends strongly on which Feshbach level is used and on the value of the magnetic field B. For example, for molecules in level $|g>$ at $B = 1.82$ mT the lifetime is 1.8 s at a lattice depth of 15 E_R, while in level $|s>$ the lifetime is 0.09 s at $B = 1.9$ mT and 10 s at $B = 2.9$ mT for the same lattice depth. We attribute this strong dependence of the lifetime of molecules in $|s>$ to the fact that the molecular character changes strongly from being predominantly closed channel dominated to being open channel dominated as the magnetic field is increased [Köh06],

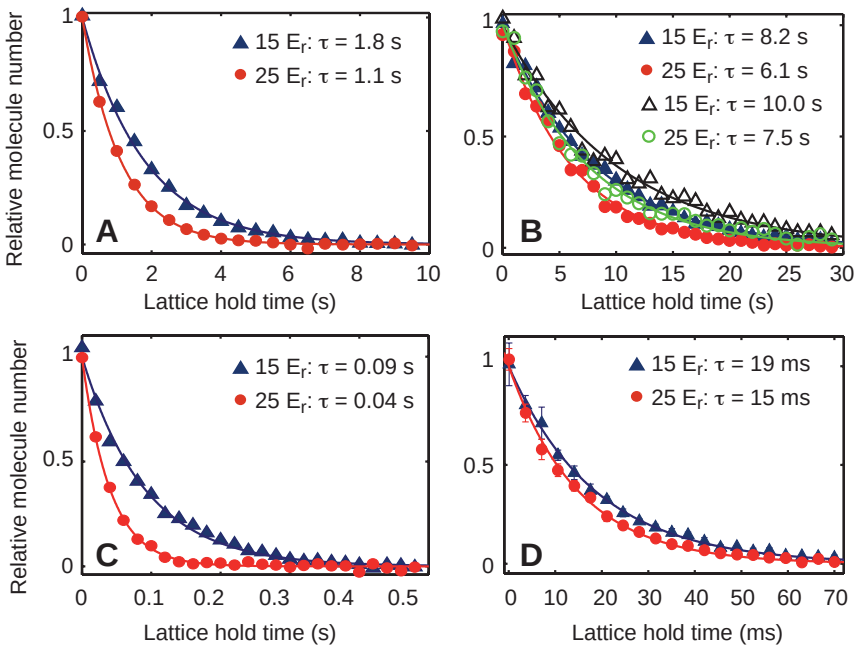

Figure 8.16: Lifetime measurements of ultracold molecules trapped in the optical lattice. A, **B**, and **C** show the decay of trapped Feshbach molecules, while **D** shows the decay for molecules in $|3\rangle = |v=73, J=2\rangle$ of the $X^1\Sigma_g^+$ ground state potential. In all cases, the triangles (circles) correspond to a lattice depth of 15 E_R (25 E_R). All lifetimes τ are determined from exponential fits to the data as shown by the the solid lines. **A** Lifetime of state $|g\rangle$. **B** Lifetime of state $|g_2\rangle$ (filled symbols) and of state $|s\rangle$ at $B = 2.9$ mT (open symbols). **C** Lifetime of state $|s\rangle$ at $B = 1.9$ mT, from where we drive the STIRAP transfer. **D** Lifetime of molecules in the rovibrational level $|3\rangle = |v = 73, J = 2\rangle$. The STIRAP lasers are switched off during the hold time in $|3\rangle$. In **D**, each data point is the average of 4 experimental runs, error bars correspond to the 1σ statistical uncertainty. The typical uncertainty for the lifetimes is one unit of the last digit given.

reducing wave function overlap with excited molecular levels. We always determine the lifetime for two values of the lattice depth, 15 E_R and 25 E_R. In all cases, the lifetime is reduced for higher lattice depth, indicating residual optical excitation by the lattice light. Nevertheless, the long lifetimes reflect the fact that the lattice perfectly shields the molecules from inelastic molecule-molecule collisions, which would otherwise limit the lifetime to a few ms at the given molecular densities [20].

Lattice-based STIRAP transfer

We implement two-photon STIRAP transfer to the deeply bound rovibrational level $|3\rangle = |v = 73, J = 2\rangle$ of the $^1\Sigma_g^+$ electronic ground state potential in a similar way as in our previous work [Dan08], except that now the molecules are trapped at the individual wells of the optical lattice. In brief, laser L_1 near a wavelength of 1126 nm, driving the transition

from $|1>=|s>$ to $|2>$, where $|2>$ is a deeply bound level of the mixed $(A^1\Sigma_u^+ - b^3\Pi_u)\ 0_u^+$ excited states, is pulsed on after laser L_2, which drives the transition from $|3>$ to $|2>$ at 1006 nm, see Fig.8.15A. The pulse (or pulse overlap) time τ_p is typically $\tau_p = 10\ \mu$s for the present experiments. A schematic time course for the transition Rabi frequencies is shown in Fig.8.17C. We estimate the peak Rabi frequencies to be $2\pi \times 3$ MHz for the transition at 1126 nm and $2\pi \times 6$ MHz for the transition at 1006 nm [Dan08]. After a variable hold time τ_h, we reverse the pulse sequence to transfer the molecules back to $|s>$. For short τ_h below $40\ \mu$s we typically leave L_1 on between the two STIRAP pulse sequences. For longer τ_h we switch L_1 off to avoid any residual optical excitation of molecules in $|v=73, J=2>$ and possible effects of dipole forces generated by the tightly focused laser beam L_1.

The result of double STIRAP transfer in the optical lattice is shown in Fig. 8.17 A. Here, $\tau_p = 10\ \mu$s and $\tau_h = 15\ \mu$s. As in our previous work [Dan08], we interrupt the transfer after a given STIRAP time τ_S and record the number of molecules in the initial state $|s>$. The molecules first disappear, and then a sizable fraction of about 65% returns after the reverse STIRAP transfer. Thus, as in our previous work [Dan08], the single pass efficiency is about 80% when both lasers are on resonance. Fig. 8.17B shows the double STIRAP transfer efficiency as a function of the detuning Δ_2 of laser L_2 from the excited intermediate level while laser L_1 is held on resonance (detuning $\Delta_1 \approx 0$). A Gaussian fit yields a full width at half maximum of 830 kHz. With τ_p so short, we do not resolve molecular hyperfine structure in $|v=73, J=2>$.

We find that the molecules transferred to $|v=73, J=2>$ are trapped at the individual wells of the lattice. The $1/e$-lifetime is about 19 ms for a lattice depth of 15 E_R. This is much shorter than the lifetime of Feshbach molecules as shown above, but sufficiently long to allow future implementation of a second lattice-based STIRAP step to the rovibronic ground state $|v=0, J=0>$, for which the lifetime is expected to be much longer as discussed below. We determine the lifetime by repeating the double STIRAP transfer while increasing the hold time τ_h in steps of 3.5 ms. The result is shown in Fig.8.16D. The number of molecules can be well fit by an exponentially decaying function as a function of τ_h. For a higher lattice depth of 25 E_R, the lifetime is reduced to 15 ms. We thus attribute the reduced molecular lifetime to off-resonant scattering of lattice light, exciting the molecules to levels of the $(A^1\Sigma_u^+ - b^3\Pi_u)\ 0_u^+$ states, which then in turn leads to loss into other ground state rovibrational levels that we do not detect. Note that in the wavelength region of our trapping laser, the lifetime is expected to show strong variations as a function of trapping laser wavelength due to the presence of excited state levels. Hence, also the polarizability as discussed in the next section should strongly depend on the wavelength of the laser generating the lattice light.

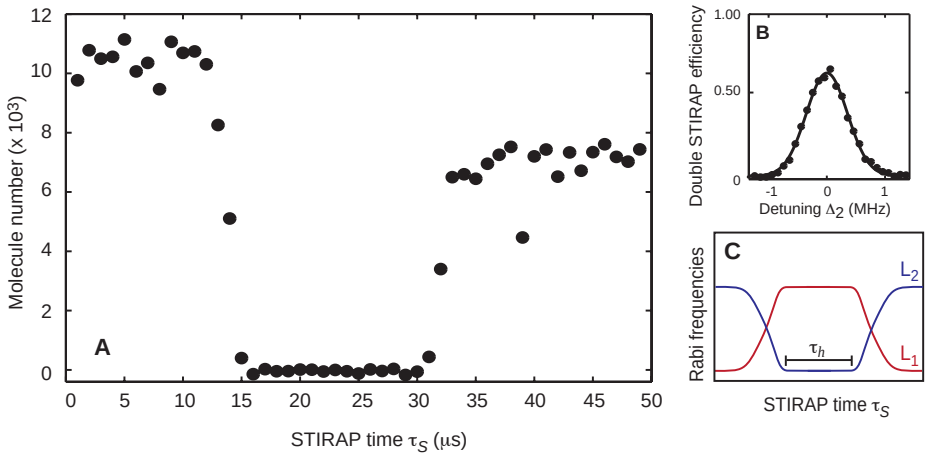

Figure 8.17: STIRAP transfer from the weakly bound state $|1>=|s>$ to the deeply bound rovibrational level $|3>=|v=73, J=2>$ and back to $|1>$ in the optical lattice. A shows the number of molecules in state $|1>$ as a function of STIRAP time τ_S for both lasers on resonance (laser detunings $\Delta_1 \approx 0 \approx \Delta_2$). The measured pulse overlap begins at about 5 μs and ends at about 15 μs. The second pulse overlap starts at 30 μs and ends at about 38 μs. The lattice depth is 15 E_R. Data points represent a single experimental realization, not an average over several runs. The data point at 39 μs represents a "bad shot", which occasionally occurs. **B** Double STIRAP efficiency as a function of the detuning Δ_2 of laser L_2 for $\Delta_1 \approx 0$. The solid line is a Gaussian fit with a full width at half maximum of 830 kHz. **C** schematically shows the timing for the Rabi frequencies, Ω_i, $i = 1, 2$, for lasers L_1 and L_2 during the double STIRAP sequence. For short hold times $\tau_h < 40$ μs laser L_1 is left on after the first STIRAP sequence as shown here. For longer hold times $\tau_h > 40$ μs we shut off L_1 to avoid possible optical excitation.

Determination of molecule trapping parameters

We determine the molecular trapping frequency $\omega_{|v=73>}$ for molecules in $|v = 73, J = 2>$ by modulating the lattice phase and, alternatively, by modulating the lattice amplitude. In the first case, we primarily excite transitions from the lowest band in the lattice to the first excited band and then to higher bands. In the second case, we primarily excite into the second excited band and then to higher bands. For sufficiently strong modulation, molecules are lost from the lattice, as tunneling to neighboring sites and hence inelastic collisions with neighboring molecules become more probable. We thus expect to detect increased molecular loss if the modulation frequency is tuned into resonance with the inter-band transitions. The results are shown in Fig. 8.18. At a lattice depth of 15 E_R, we observe resonant loss at 5.2 kHz in the case of phase modulation and at 10.1 kHz in the case of amplitude modulation of the lattice. Phase modulation at 22 E_R and amplitude modulation at 20 E_R yield resonances at 6.5 kHz and 12.2 kHz, respectively. These values for different trap depths are consistent with each other when compared with a calculation of the band structure. For comparison, to determine the trapping frequency ω_F of the Feshbach molecules in level $|g>$, we measure that phase modulation (amplitude modulation) of a 15 E_R deep lattice leads to loss at

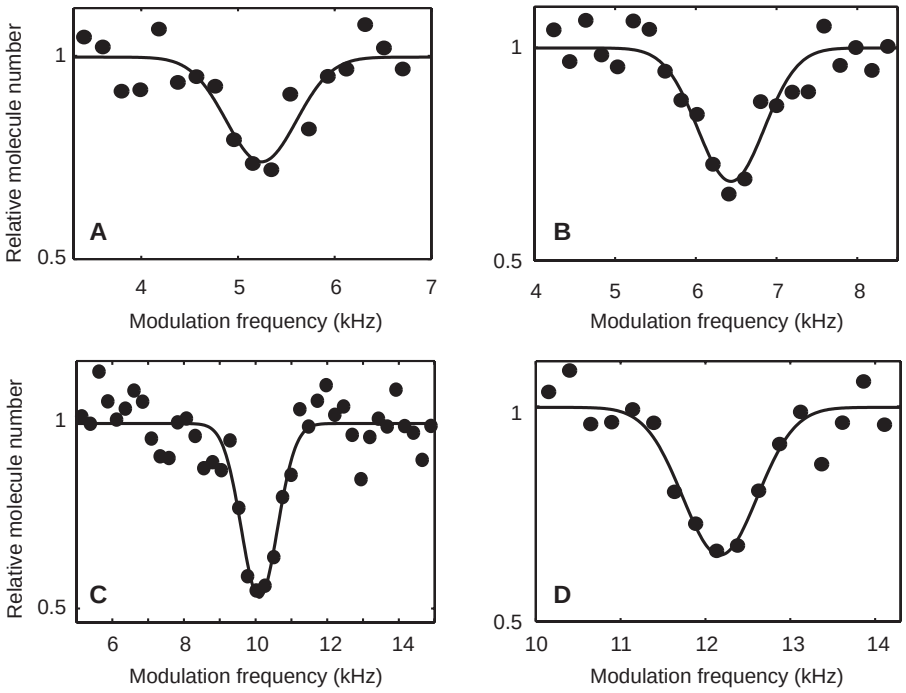

Figure 8.18: Trapping of deeply bound molecules in the wells of the optical lattice. While the molecules reside in level $|3>= |v=73, J=2>$, one of the lattice beams of the 3 dimensional optical lattice is either phase modulated (**A** and **B**) or amplitude modulated (**C** and **D**). As the frequency of the phase or amplitude modulation is scanned, a series of resonances due to transfer to higher bands arise, reflected in a decrease in molecule number. The respective resonances at the lowest modulation frequency are shown here. For phase modulation ("shaking" of the lattice), this corresponds to the first lattice band, for amplitude modulation to the second band. To determine the center frequency, the resonances are fit by a Gaussian. The lattice depth is 15 E_R, 22 E_R, 15 E_R, and 20 E_R in **A**, **B**, **C**, and **D**, respectively.

a modulation frequency of 9.4 kHz (18.4 kHz). Relating the dynamical polarizability $\alpha_{|v=73>}$ of the deeply bound molecules in $|v=73>$ to the dynamical polarizability α_F of the Feshbach molecules via $\alpha_{|v=73>}/\alpha_F = \omega^2_{|v=73>}/\omega^2_F$, we obtain that the molecular polarizability in $|v=73, J=2>$ is $\sim 30\%$ of the polarizability of the Feshbach molecules at the wavelength of our trapping light.

Conclusion

We have transferred an ultracold sample of Cs_2 molecules to the deeply bound rovibrational level $|v=73, J=2>$ of the singlet $X^1\Sigma_g^+$ potential in the presence of an optical lattice. We essentially find the same transfer efficiency as in our previous work [Dan08] where no lattice was used. The transferred molecules are trapped, and we have determined their polarizability in this particular level. The trapping time is sufficiently long to allow for subsequent lattice-based STIRAP transfer to the rovibronic ground state $|v=0, J=0>$ by means of a

second two-photon transition [6]. A lower bound for the STIRAP pulse time and hence for the minimal required trapping time is set by the time needed to resolve the molecular hyperfine structure. This minimal time is the inverse of three times the ground state hyperfine coupling constant $c_4 \approx 14$ kHz [4], giving 24 μs. Hence a compromise can easily be found between Fourier-resolving the molecular hyperfine structure and keeping the STIRAP pulse time sufficiently short in view of finite laser coherence time and finite trapping time. Note that for optimum transfer efficiency also the hyperfine structure of the intermediate state needs to be resolved, which requires longer STIRAP times also for the first transfer step.

For Cs_2 molecules in the rovibronic ground state $|v = 0, J = 0>$ we expect much longer trapping times in the lattice as optical excitation at 1064.5 nm into excited molecular states can only occur in a far off-resonant process. At this wavelength transitions to the $(\mathrm{A}^1\Sigma_u^+ - \mathrm{b}^3\Pi_u)$ 0_u^+ states are relevant. These are possible only to levels that have a sizable singlet contribution stemming from the $\mathrm{A}^1\Sigma_u^+$ state. 0_u^+ levels below the minimum of the $\mathrm{A}^1\Sigma_u^+$ state, corresponding to a wavelength of ~ 1041 nm as measured from the rovibronic ground state [26], have little singlet component and hence these transitions are strongly suppressed. We thus expect the formation of a stable molecular quantum gas in $|v = 0, J = 0>$ when the lattice depth is lowered and the molecules are released into a larger-volume optical dipole trap, possibly allowing the observation of Bose-Einstein condensation of ground state molecules.

Our technique can readily be applied to other molecular systems, e.g. heteronuclear dimers such as RbCs [27] and KRb [16]. These dimers carry a sizable electric dipole moment. In the presence of the lattice, one should thus be able to exploit the long range nature of the dipole-dipole interaction and be able to prepare interesting novel quantum phases with nearest-neighbor interaction [28, 29].

Acknowledgements We are indebted to R. Grimm for generous support and we thank S. Knoop, N. Boloufa, and O. Dulieu for valuable discussions. We gratefully acknowledge funding by the Austrian Ministry of Science and Research (BMWF) and the Austrian Science Fund (FWF) in form of a START prize grant. R.H. acknowledges support by the European Union in form of a Marie-Curie International Incoming Fellowship (IIF).

BIBLIOGRAPHY

[1] Jochim S, Bartenstein M, Altmeyer A, Hendl G, Riedl S, Chin C, Hecker Denschlag J and Grimm R 2003 *Science* **302** 2101

[2] Greiner M, Regal C A and Jin D S 2003 *Nature* **426** 537

[3] For an overview, see: Ultracold Fermi Gases, *Proceedings of the International School of Physics Enrico Fermi, Course CLXIV*, edited by Inguscio M, Ketterle W and Salomon C (IOS Press, Amsterdam, 2008)

[4] Aldegunde J and Hutson J M 2008, preprint at arXiv:0810.4709

[5] Danzl J G, Haller E, Gustavsson M, Mark M J, Hart R, Bouloufa N, Dulieu O, Ritsch H and Nägerl H-C 2008 *Science* **321** 1062, published online 10 July 2008; 10.1126/science.1159909

[6] Mark M J, Danzl J G, Haller E, Gustavsson M, Bouloufa N, Dulieu O, Salami H, Bergeman T, Ritsch H, Hart R and Nägerl H-C 2008, published online February 19 2009, *Appl Phys B* DOI 10.1007/s00340-009-3407-1

[7] Danzl J G, Mark M J, Haller E, Gustavsson M, Bouloufa N, Dulieu O, Ritsch H, Hart R and Nägerl H C 2008 manuscript submitted for publication, preprint at arXiv:0811.2374

[8] Winkler K, Lang F, Thalhammer G, Straten P v d, Grimm R and Hecker Denschlag J 2007 *Phys. Rev. Lett.* **98** 043201

[9] Ni K-K, Ospelkaus S, de Miranda M H G, Peer A, Neyenhuis B, Zirbel J J, Kotochigova S, Julienne P S, Jin D S and Ye J 2008 *Science* **322** 231

[10] Lang F, Winkler K, Strauss C, Grimm R and Hecker Denschlag J 2008 *Phys. Rev. Lett.* **101** 133005

[11] Volz T, Syassen N, Bauer D M, Hansis E, Dürr S, Rempe G 2006 *Nature Physics* **2** 692

[12] Dürr S 2008 private communication.

[13] Jaksch D, Venturi V, Cirac J I, Williams C J, and Zoller P 2002 *Phys. Rev. Lett.* **89** 040402

[14] Bergmann K, Theuer H and Shore B W 1998 *Rev. Mod. Phys.* **70** 1003

[15] Weber T, Herbig J, Mark M, Nägerl H-C and Grimm R 2003 *Science* **299** 232

[16] Kraemer T, Mark M, Waldburger P, Danzl J G, Chin C, Engeser B, Lange A D, Pilch K, Jaakkola A, Nägerl H-C and Grimm R 2006 *Nature* **440** 315

[17] Greiner M, Mandel O, Esslinger T, Hänsch T W and Bloch I 2002 *Nature* **415** 39

[18] Liem A, Limpert J, Zellmer H, Tünnermann A 2003 *Opt. Lett.* **28** 1537

[19] Hansis E 2006, diploma thesis, Technische Universität München, unpublished

[20] Regal C A, Ticknor C, Bohn J L and Jin D S 2003 *Nature* **424** 47

[21] Herbig J, Kraemer T, Mark M, Weber T, Chin C, Nägerl H-C and Grimm R 2003 *Science* **301** 1510, published online 21 August 2003; 10.1126/science.1088876

[22] Köhler T, Góral K and Julienne P S 2006 *Rev. Mod. Phys.* **78** 1311

[23] Mark M, Ferlaino F, Knoop S, Danzl J G, Kraemer T, Chin C, Nägerl H-C and Grimm R 2007 *Phys. Rev. A* **76** 042514

[24] Thalhammer G, Winkler K, Lang F, Schmid S, Grimm R and Hecker Denschlag J 2006 *Phys. Rev. Lett.* **96** 050402

[25] Chin C, Vuletic V, Kerman A J, Chu S, Tiesinga E, Leo P J and Williams C J 2004 *Phys. Rev. A* **70** 2032701

[26] Vergès J and Amiot C 1987 *Journal of Molecular Spectroscopy* **126** 393

[27] Pilch K, Lange A D, Prantner A, Kerner G, Ferlaino F, Nägerl H-C and Grimm R 2008 manuscript submitted for publication, preprint at arXiv:0812.3287

[28] Góral K, Santos L and Lewenstein M 2002 *Phys. Rev. Lett.* **88** 170406

[29] Wall M L and Carr L D 2008 manuscript submitted for publication, preprint at arXiv:0812.1548

An ultracold, high-density sample of rovibronic ground-state molecules in an optical lattice

Nature Physics **6**, 265 (2010)

Johann G. Danzl[1], Manfred J. Mark[1], Elmar Haller[1], Mattias Gustavsson[1], Russell Hart[1], Jesus Aldegunde[2], Jeremy M. Hutson[2] and Hanns-Christoph Nägerl[1]

[1]*Institut für Experimentalphysik und Zentrum für Quantenphysik, Universität Innsbruck, Technikerstraße 25, A–6020 Innsbruck, Austria*

[2]*Department of Chemistry, University of Durham, South Road, Durham, DH1 3LE, England*

Control over all internal and external degrees of freedom of molecules at the level of single quantum states will enable a series of fundamental studies in physics and chemistry [1, 2]. In particular, samples of ground-state molecules at ultralow temperatures and high number densities will allow novel quantum-gas studies [3] and future applications in quantum information science [4]. However, high phase-space densities for molecular samples are not readily attainable as efficient cooling techniques such as laser cooling are lacking. Here we produce an ultracold and dense sample of molecules in a single hyperfine level of the rovibronic ground state with each molecule individually trapped in the motional ground state of an optical lattice well. Starting from a zero-temperature atomic Mott-insulator state [Blo08] with optimized double-site occupancy [6], weakly-bound dimer molecules are efficiently associated on a Feshbach resonance [Chi10] and subsequently transferred to the rovibronic ground state by a stimulated four-photon process with >50% efficiency. The molecules are trapped in the lattice and have a lifetime of 8 s. Our results present a crucial step towards Bose-Einstein condensation of ground-state molecules and, when suitably generalized to polar heteronuclear molecules, the realization of dipolar quantum-gas phases in optical lattices [8, 9, 10].

Recent years have seen spectacular advances in the field of atomic quantum gases. Ultracold atomic samples have been loaded into optical lattice potentials, allowing the realization of strongly-correlated many-body systems and enabling the direct observation of quantum phase transitions with full control over the entire parameter space [Blo08]. Molecules with their increased complexity are expected to play a crucial role in future generation quantum gas studies. For example, the long-range dipole-dipole force between polar molecules gives rise to nearest-neighbour and next-nearest-neighbour interaction terms in the extended Bose-Hubbard Hamiltonian and should thus lead to novel many-body states in optical lattices in the form of striped, checkerboard, and supersolid phases [8, 9, 10].

An important prerequisite for all proposed molecular quantum gas experiments is the capability to fully control all internal and external quantum degrees of freedom of the molecules. For radiative and collisional stability, the molecules need to be prepared in their rovibronic ground state, i.e. the lowest vibrational and rotational level of the lowest electronic state, and preferably in its energetically lowest hyperfine sublevel. As a starting point for the realization of novel quantum phases, the molecular ensemble should be in the ground state of the many-body system. Such state control is only possible at ultralow temperatures and sufficiently high particle densities. While versatile non-optical cooling and slowing techniques have recently been developed for molecular ensembles [11] and photo-association experiments with atoms in magneto-optical traps have reached the rovibrational ground state [1], the achievable molecular phase-space densities are still far away from the point of quantum degeneracy. Here, we exploit the fact that high phase-space densities can readily be achieved for atoms and that atoms can efficiently be associated on Feshbach resonances to form molecules [Chi10] with minimal loss of phase-space density when an optical lattice is present. Subsequent state transfer to a specific hyperfine sublevel of the rovibronic ground state by means of a stimulated multi-photon process then preserves phase-space density and hence the quantum-gas character of the molecular ensemble. This approach is expected to allow the preparation of a molecular ground-state BEC [12]. Note that some loss of phase-space density can be tolerated if the collisional properties of the ground-state molecules, a priori unknown, turn out to be sufficiently favorable to allow for a final stage of evaporative cooling or, alternatively, sympathetic cooling with atoms.

A crucial ingredient for our experiments is the presence of an optical lattice. It provides full control over the motional wave function and prevents collisional loss. It allows us in particular to maximize the efficiency for initial molecule production and the efficiency for ground-state transfer. For sufficiently high efficiency, a molecular Mott-insulator state is approximated by this preparation procedure [12], providing an excellent starting point for the precision measurements [13, 14] and many-body and quantum information experiments [8, 9, 10] envisioned with ground-state molecules. In the quantum gas regime without the use of an optical lattice, molecular state transfer to deeply-bound rovibrational levels of the singlet $^1\Sigma$ ground-state potential has recently been implemented for Cs_2 [15] and KRb [16]. For KRb, the rovibronic ground state was reached, resulting in a near-quantum-degenerate gas of fermionic ground-state molecules [16]. Transfer of molecules in the presence of an optical lattice has been implemented for Rb_2 molecules [17], and the lowest rovibrational level of the shallow triplet $a^3\Sigma_u^+$ potential was reached [18].

Our molecular quantum-gas preparation procedure is summarized in Fig. 8.19. We load a BEC of Cs atoms [Kra04] into a three-dimensional optical lattice and drive the superfluid-to-Mott-insulator phase transition [Blo08]. The atomic number distribution in the Mott-insulator state is inhomogeneous as a result of the external harmonic confinement. Shells with a con-

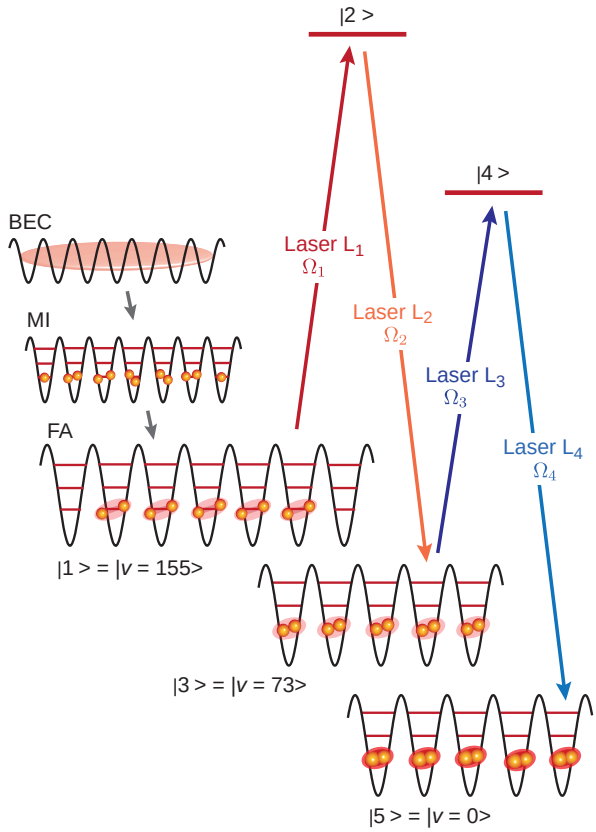

Figure 8.19: Molecular quantum gas preparation procedure. A BEC of Cs atoms is loaded into an optical lattice. By increasing the lattice depth, a Mott-insulator state (MI) with preferentially two atoms per site is created. Feshbach association (FA) subsequently converts atom pairs into weakly-bound molecules in state $|1>$. These are then transferred in the presence of the lattice to a specific hyperfine level $|I = 6, M_I = 6>$ of the rovibronic ground state $|5> = X^1\Sigma_g^+ \; |v = 0, J = 0>$ by a stimulated four-photon process (STIRAP) involving lasers L_i with Rabi frequencies Ω_i $i = 1, 2, 3, 4$, and three intermediate levels $|2>$, $|3>$, and $|4>$.

stant number of precisely n atoms per lattice site, where $n = 1, 2, 3 \ldots$, are separated by narrow superfluid regions [Blo08]. We aim to maximize the size of the two-atom Mott shell in the central region of the lattice in order to obtain the highest number of lattice sites at which there are precisely two atoms (see the Methods section). With up to 45(2)% of the atoms at doubly-occupied lattice sites we come close to the theoretical limit of 53% given the parabolic density profile of the BEC [6]. The atom pairs reside in the motional ground state at each well and are then associated [20] with 94(1)% probability to Cs_2 Feshbach molecules, which are subsequently transferred to the weakly-bound level $|1>$, the starting level for the optical transfer (see the Methods section) [21, 15, 22]. Atoms at singly-occupied sites are removed by a combination of microwave and optical excitation [20]. We now have a pure molecular sample with a high occupation of about 85(3)% in the central region of the lattice

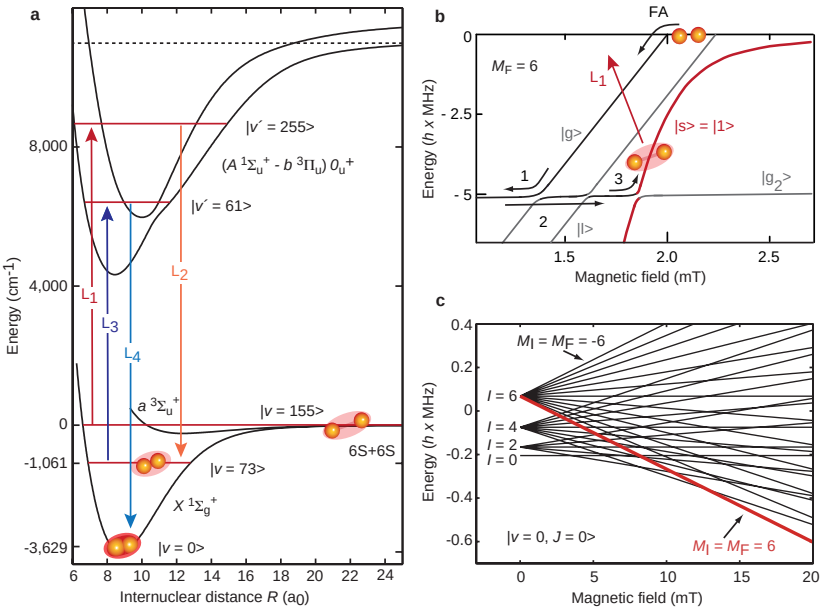

Figure 8.20: Molecular potentials and level schemes for ground-state transfer. a, The four-photon transfer from the weakly-bound Feshbach level $|1\rangle = |\nu \approx 155\rangle$ (not resolved near the 6S+6S asymptote) to the rovibrational ground state $|5\rangle = |\nu = 0, J = 0\rangle$ of the singlet $X^1\Sigma_g^+$ potential involves the deeply bound level $|3\rangle = |\nu = 73\rangle$ of the $X^1\Sigma_g^+$ potential [15] and the levels $|2\rangle = |\nu' = 225, J = 1\rangle$ and $|4\rangle = |\nu' = 61, J = 1\rangle$ of the electronically excited $(A^1\Sigma_u^+ - b^3\Pi_u)\ 0_u^+$ potentials [30, 26]. The laser wavelengths for L_1, L_2, L_3, and L_4 are near 1126 nm, 1006 nm, 1351 nm, and 1003 nm, respectively. **b**, Zeeman diagram for weakly bound molecules near the 6S+6S asymptote. Molecules are associated at a g-wave Feshbach resonance [29] at 1.98 mT (FA) and then transferred to the desired starting level $|1\rangle = |s\rangle$ for optical transfer via three avoided level crossings by slow (arrows 1,3) and fast (arrow 2) magnetic field ramps [21]. The binding energy is given with respect to the $(F_{a_1} = 3, m_{Fa_1} = 3) \times (F_{a_2} = 3, m_{Fa_2} = 3)$ two-atom lowest hyperfine asymptote. All Feshbach levels are characterized by $M_F = 6$. **c**, Calculated Zeeman diagram for the hyperfine manifold of the rovibronic ground state $|5\rangle = |\nu = 0, J = 0\rangle$. The optical transfer goes selectively to level $|I = 6, M_I = 6\rangle$, indicated in red. This level becomes the lowest-energy absolute ground state for magnetic-field values above ~ 13 mT. There are no avoided crossings between different hyperfine sublevels [24].

(see the Methods section). Each molecule is in the motional ground state of its respective well and perfectly shielded from collisional loss.

We employ stimulated Raman adiabatic passage (STIRAP) [23] involving four laser transitions to coherently transfer the molecules into the lowest rovibrational level $|5\rangle = |v = 0, J = 0\rangle$ of the ground state singlet $X^1\Sigma_g^+$ potential as shown in Fig. 8.20a, bridging a binding energy of $hc \times 3628.7\ \text{cm}^{-1} \approx h \times 109$ THz [15]. Here, v and J are the vibrational and rotational quantum numbers, respectively, h is Planck's constant and c is the speed of light. For Cs_2, a homonuclear molecule, the four-photon process is preferred to a direct two-photon process because it allows us to overcome small Franck-Condon overlap. Lasers L_1 through L_4 couple $|1\rangle$ and $|5\rangle$ via three intermediate levels $|2\rangle$,$|3\rangle$, and $|4\rangle$ (see the Methods section). For STIRAP in the presence of the lattice, the lattice light must not impede

the transfer through optical excitation or by creating unwanted coherences. Also, the lattice wavelength has to be chosen such that the dynamical polarizabilities for $|1>$ and $|5>$ are closely matched in order to avoid excitation into higher motional states of the lattice as a result of motional wave-function mismatch [18]. We typically set the lattice depth to a value of 20 E_R for atoms, corresponding to 80 $\tilde{E}_R$ for Feshbach molecules with twice the polarizability and double the mass and 83 $\tilde{E}_R$ for molecules in $|v=0>$ at a lattice wavelength of 1064.5 nm, as determined below. Here, E_R ($\tilde{E}_R$) is the atomic (molecular) recoil energy.

Our experimental configuration ensures that only one particular molecular hyperfine sublevel is populated. The atomic BEC is prepared in the lowest hyperfine sublevel $|F_a = 3, m_{Fa}=3>$, where F_a and m_{Fa} are the total atomic angular momentum and its projection on the magnetic field. Feshbach association and transfer between Feshbach levels via avoided crossings, as illustrated in Fig. 8.20b (see the Methods section), conserve [Chi10] the total angular momentum projection $M_F = m_{Fa_1} + m_{Fa_2} = 6$. Fig. 8.20c shows the hyperfine structure of the target state, i.e. the rovibronic ground state $X^1\Sigma_g^+$ $|v=0, J=0>$. It splits into 28 hyperfine sublevels in the presence of a weak magnetic field, corresponding to the allowed values of the total nuclear spin I = 0, 2, 4, 6 and its $2I+1$ projections M_I for each value of I. The total energy splitting is $\sim h \times 270$ kHz at zero field [24] (see the Methods section). Importantly, there is only a single $M_I = M_F = 6$ sublevel of $|v=0, J=0>$, namely the $|I=6, M_I=6>$ level. This level we selectively populate by exploiting the dipole selection rule $\Delta M_F = 0$ for linear polarization along the axis of quantization. It is the lowest-energy hyperfine sublevel and hence the absolute energy ground state of the Cs dimer for magnetic fields above ~ 13 mT.

There are two possibilities for optical transfer from $|1>$ to $|5>$. Sequential STIRAP (s-STIRAP) uses two consecutive two-photon STIRAP processes, first from $|1>$ to $|3>$ and then from $|3>$ to $|5>$. The second scheme generalizes STIRAP [23, 17] to the five-level system [25]: Four-photon STIRAP (4p-STIRAP) relies on the existence of a dark state of the form $|D> = (\Omega_2\Omega_4|1> - \Omega_1\Omega_4|3> + \Omega_1\Omega_3|5>)/A$ with time-dependent Rabi frequencies $\Omega_i = \Omega_i(t)$ for lasers L_i, $i = 1, 2, 3, 4$, and the appropriate normalization function $A = A(t)$. Similar to standard two-photon STIRAP, a counter-intuitive pulse sequence rotates the initial state $|1>$ adiabatically into the final state, here $|5>$. For this, L_2 and L_3 couple the three intermediate levels while L_4 and L_1 deliver time-dependent overlapping pulses with L_4 preceding L_1. Fig. 8.21b and e show the timings for both schemes including the reverse sequence used for detecting the ground-state molecules after a certain hold time τ_h.

We investigate 4p-STIRAP to $|v=0, J=0>$ by interrupting the transfer sequence after a given 4p-STIRAP time τ and measuring the number of Feshbach molecules, as shown in Fig. 8.21a. The molecules are transferred to $|5>$ in a single step. No molecules in $|1>$ are detected during τ_h as the remaining Feshbach molecules are cleared by L_1 at the end of the transfer. When the pulse sequence is reversed, a large fraction of the molecules returns

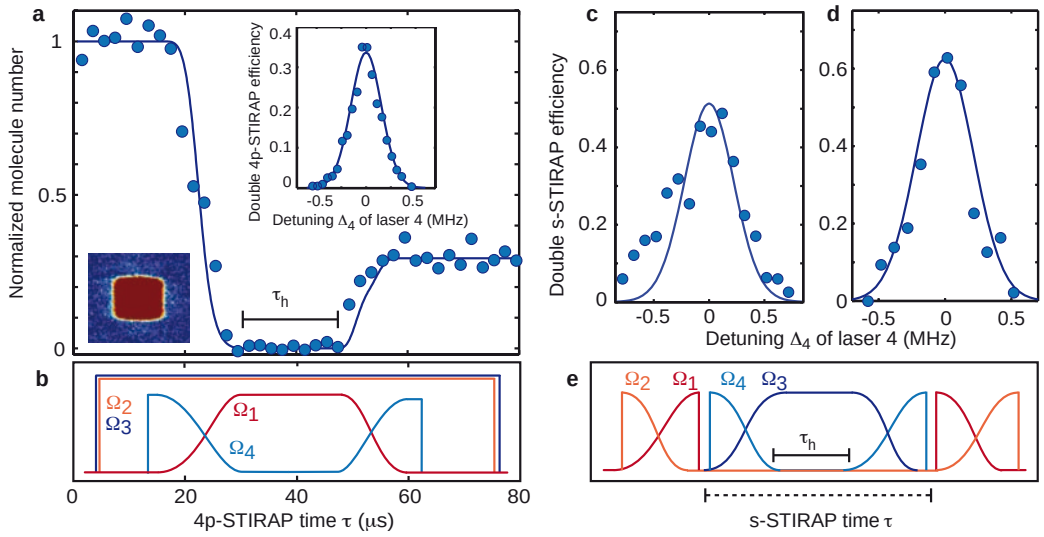

Figure 8.21: STIRAP transfer to the rovibronic ground state $|5>=|\nu=0, J=0>$ **and back. a**, 4p-STIRAP transfer and **b**, schematic timing for the Rabi frequencies Ω_i, $i = 1, 2, 3, 4$: Number of molecules in state $|1>$ as a function of 4p-STIRAP time τ for all 4 lasers on resonance. The lattice depth is 80 $\tilde{E}_R$ and 83 $\tilde{E}_R$ for molecules in levels $|1>$ and $|5>$, respectively. Data points represent a single experimental realization, not an average over several runs. The solid line is a 4p-STIRAP model calculation. τ_h is the hold time in $|5>=|\nu=0, J=0>$. Upper inset: double 4p-STIRAP efficiency as a function of the detuning Δ_4 of laser L_4 and corresponding model calculation. The peak corresponds to a single-pass efficiency of 57%. Lower inset: Band mapping of molecules after the double STIRAP sequence. The absorption images corresponding to data points beyond $\tau = 60$ μs are averaged and smoothed with a Gaussian filter. The colour scale is chosen to emphasize any small population in higher bands. **c**, and **d**, s-STIRAP: Double STIRAP efficiency for the inner two-photon STIRAP from $|3>$ to $|v=0, J=0>$ (**c**) and to $|v=0, J=2>$ (**d**) and back, corresponding to the dotted bar in the timing sequence in **e**, as a function of the detuning Δ_4 of laser L_4. The number of molecules is normalized to the initial number in $|3>$. All measurements are performed at an offset magnetic field of 1.9 mT.

to $|1>$. Typically, 30% of the molecules are recovered after the full double 4p-STIRAP sequence. Almost all reside in the lowest band of the lattice as evidenced by band-mapping experiments [Blo08]. The rectangular shape of the first Brillouin zone can be clearly seen in the momentum-space image shown in the lower inset of Fig. 8.21a. 92(3)% of the molecules can be found in the first Brillouin zone and hence had resided in the lowest lattice vibrational level. Assuming equal efficiencies for both transfers, the single-pass efficiency is 55%. The upper inset of Fig. 8.21a shows the double 4p-STIRAP efficiency versus detuning Δ_4 of L_4 from the ($|4>\rightarrow|5>$)-transition with all other lasers on resonance. With ground-state transfer efficiencies between 55% and 60%, about half of the lattice sites are occupied by a ground-state molecule. The solid lines in Fig. 8.21a represent a simulation of 4p-STIRAP that takes into account excited-state spontaneous decay and laser linewidth. Transfer times are typically 4 μs to 10 μs. The simulation yields that the transfer efficiency is currently limited

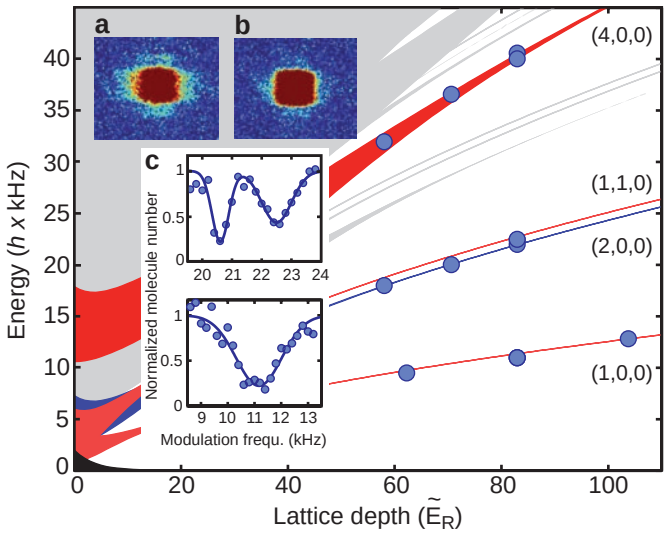

Figure 8.22: Lattice band structure for $|v = 0>$ molecules. Band energies as a function of lattice depth in units of the molecular recoil energy $\tilde{E}_R$ as measured by phase and amplitude modulation of the lattice. The lattice bands are labeled by (k, l, m), where k, l, and m give the number of vibrational quanta along the three spatial directions in the limit of a deep lattice. The horizontal position of the data points (filled circles, representing the position of excitation resonances as shown in inset **c**) is given by the molecular polarizability, which is determined by a fit of the data to the band structure. Inset **a** shows the molecular momentum distribution after transfer to higher lattice bands by resonant lattice amplitude modulation. The distribution represents an average of 5 experimental runs, smoothed with a Gaussian filter. For comparison, inset **b** shows that hardly any population is transferred to higher bands for off-resonant modulation. Inset **c** shows typical excitation spectra for amplitude (top) and phase (bottom) modulation at 83 $\tilde{E}_R$. For these, we determine the number of molecules in the first Brillouin zone as a function of the excitation frequency. The solid lines are Gaussian fits. The resonance at 22.5 kHz corresponds to excitation to the nearly-degenerate bands (2,0,0) and (1,1,0) (not resolved). The resonance at 20.6 kHz is a two-phonon excitation to (4,0,0).

by a combination of laser linewidth, which is about 10 kHz when averaged over 1 s, and imperfect adiabaticity due to finite available laser power to drive the extremely weak transitions of the 5-level scheme [15, 26]. Molecules not transferred to $|5>$ as a result of insufficient phase coherence or limited adiabaticity are excited to either $|2>$ or $|4>$ by one of the lasers and are hence pumped into a multitude of rovibrational levels, which do not couple to the rovibrational ground state. For comparison, the double s-STIRAP efficiency from $|3>$ to $|v = 0, J = 0>$ and $|v = 0, J = 2>$ is shown in Fig. 8.21c and d, respectively. The solid lines represent a calculation matched to the data for standard 3-level STIRAP. With 55%-60%, the total ($|1> \rightarrow |5>$)-transfer efficiency for s-STIRAP is comparable to 4p-STIRAP.

A crucial prerequisite for efficient ground-state transfer without heating is good matching of the motional wave functions for the initial weakly-bound state and the final ground state. A mismatch leads to unwanted excitation of higher lattice vibrational levels or bands and hence to loss of state control. The lattice thus has to be operated at the magic wave-

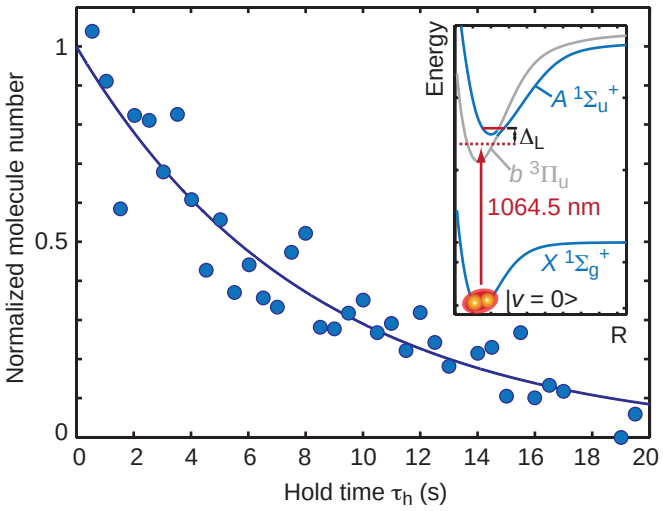

Figure 8.23: Lifetime of trapped ground-state molecules in the optical lattice. Normalized number of molecules in $|5>= |\nu = 0, J = 0>$ as a function of hold time τ_h. The solid line is an exponential fit, yielding a lifetime of $8.1(6)$s. The inset schematically shows the excited-state potentials to which off-resonant optical excitation is possible (cf. Fig. 8.20a). Δ_L is the detuning of the lattice light at 1064.5 nm with respect to the lowest 0_u^+ level with $A^1\Sigma_u^+$ character. During the hold time, all STIRAP laser fields are turned off.

length condition [27], i.e. at a wavelength that gives equal light shifts for the initial and the final molecular states. Our experiment in fact shows, as discussed above, that hardly any population is transferred to higher lattice bands. We now measure the lattice band structure and determine the molecular polarizability of the ground-state molecules (see the Methods section). Molecules residing in the lowest band of the lattice are excited to the first (second) band by phase (amplitude) modulation of the light generating the lattice. Fig. 8.22 shows the measured band energies together with a calculation of the band structure as a function of lattice depth. On resonance, excitation to higher bands can readily be observed in momentum space as shown in inset **a**. For comparison, off-resonant modulation transfers hardly any population into higher bands (see inset **b**). We determine the band energies by taking modulation spectra as shown in inset **c**. We then use the band structure calculation to fit all measured resonance positions with the molecular dynamical polarizability $P_{|v=0>}$ as the single free parameter. These measurements are done for $|v = 0, J = 2 >$. We obtain $P_{|v=0>} = 2.1(1) \times P_a$, where P_a is the atomic polarizability. For the initial, weakly-bound Feshbach molecules in level $|g>$ we obtain $P_{|g>} = 2.0(1) \times P_a$. Hence the magic wavelength condition is well fulfilled.

We measure the lifetime τ_e of the molecules in the lattice by varying the hold time τ_h for up to 20 s and recording the number of remaining molecules as shown in Fig. 8.23. To reduce inelastic light scattering, the lattice depth was adiabatically reduced to about 41.5

$\tilde{E}_R$ after the 4p-STIRAP transfer. An exponential fit gives a $1/e$-lifetime of $\tau_e = 8.1(6)$ s. We attribute this long lifetime to the large detuning $\Delta_L \approx 6.9$ THz from the lowest 0_u^+ level with predominant $A^1\Sigma_u^+$ singlet contribution as shown in the inset to Fig. 8.23. Levels of the 0_u^+ system that lie below this are almost purely of $b^3\Pi_u$ character and thus make negligible contributions to the optical excitation rate.

We are now in a position to determine collisional properties of ultracold ground-state molecules in a fully state-selective way. At magnetic fields beyond 13 mT, where the level $|I = 6, M_I = 6>$ becomes the absolute ground state, the sample should show collisional stability and thus allow the formation of a BEC of ground-state molecules when the lattice is adiabatically removed [12]. For Cs_2, formation of a trimer and an atom in a dimer-dimer collision is predicted to be energetically forbidden (R. Guérout and O. Dulieu, private communication, 2009). The long coherence times and the perfect decoupling from the environment in an optical lattice as demonstrated here will enable a new generation of precision measurements [13, 14]. Furthermore, our results can readily be generalized to heteronuclear systems such as KRb [16] and RbCs [28], opening up the possibility to study dipolar quantum phases in optical lattices.

Methods

Lattice loading

We first follow the procedure detailed in Ref. [22]. In brief, we produce an atomic BEC with typically 1×10^5 Cs atoms in the lowest hyperfine sublevel $|F_a = 3,\ m_{Fa} = 3>$ in a crossed optical dipole trap. We then drive the superfluid-to-Mott-insulator phase transition [Blo08] by exponentially ramping up the power in a three-dimensional optical lattice within about 300 ms. The lattice is generated by three mutually-orthogonal, retro-reflected laser beams at a wavelength of $\lambda = 1064.5$ nm, each with a $1/e^2$-waist of about 350 μm. While ramping up the lattice potential, the power in the two dipole-trap beams is increased to ensure that the central density in the trap is sufficiently high to allow formation of atom pairs at the central wells of the lattice, but not too high to lead to triply occupied sites. Atoms at triply occupied sites would rapidly be cleared out by inelastic three-body collisions. We ramp the lattice to a depth of about 20 E_R before Feshbach association. Here, $E_R = h^2/(2m_a\lambda^2) = k_B{\times}64$ nK is the atomic photon-recoil energy with the mass m_a of the Cs atom and Boltzmann's constant k_B. Up to 45(2)% of the atoms reside at doubly occupied lattice sites. We estimate this number from the number of molecules that we obtain and the molecule production efficiency.

For the molecules, the recoil energy is $\tilde{E}_R = h^2/(2 \times 2m_a\lambda^2)$. The polarizability of Feshbach molecules is twice the atomic polarizability. The same lattice that has a depth of 20 E_R for the atoms has thus a depth of 80 $\tilde{E}_R$ for the Feshbach molecules.

Feshbach association and Feshbach state transfer

We efficiently produce weakly bound Cs_2 Feshbach molecules in the presence of the optical lattice by a magnetic field sweep [Chi10] across a narrow g-wave Feshbach resonance with its pole at a magnetic field value of $B = 1.98$ mT [29, 21]. The molecules are initially in level $|g>$, for which $\ell = 4$. Here, ℓ is the quantum number associated with the mechanical rotation of the nuclei [Chi10]. We subsequently transfer the molecules via level $|g_2>$ with 95(3)% efficiency into level $|s> \equiv |1>$ with $\ell = 0$ by magnetic field ramping [21, 22] as shown in Fig. 8.20b. For this level, the transitions to excited molecular levels are stronger than for the initial level $|g>$ [30]. We obtain up to 2.5 $\times 10^4$ Feshbach molecules in the lattice in the desired starting state. Assuming a perfect filling of the two-atom Mott-shell at the center of the trap, taking into account the efficiencies for molecule production and state transfer, and factoring in weak additional loss during sample purification, 85(3)% of the central lattice sites are occupied. We detect the molecules in $|1>$ by reversing the Feshbach state transfer sequence, dissociating the molecules at the Feshbach resonance and detecting the resulting atoms by standard absorption imaging [29].

Molecular states for ground state transfer

The relevant molecular states for Cs_2 are shown in Fig. 8.20a. Levels $|2>$ and $|4>$ belong to the coupled $(A^1\Sigma_u^+ - b^3\Pi_u)0_u^+$ potentials [15]. We have recently identified suitable transitions linking $|1>$ to $|5>$, where levels $|2>$, $|3>$, and $|4>$ were chosen to give balanced transition strengths on the four optical transitions [30, 26]. For $|3>$ we choose either $|v = 73, J = 2>$ or $|v = 73, J = 0>$ of the $X^1\Sigma_g^+$ ground state with a binding energy of $\sim hc \times 1061$ cm^{-1}.

Hyperfine structure of the rovibronic ground state

The hyperfine levels are calculated using the molecular constants from Ref. [24] by constructing and diagonalizing a Hamiltonian matrix in an uncoupled basis set of functions representing the molecular rotation and the spins of the two nuclei, using the matrix elements given in the Appendix of Ref. [24]. For $J = 0$ states the hyperfine structure is dominated by the scalar spin-spin coupling and the nuclear Zeeman effect, but for $J > 0$ additional terms are important.

STIRAP laser setup

STIRAP lasers L_i with $i = 1, 2, 3, 4$ are continuous-wave grating-stabilized tunable diode lasers, which are stabilized to optical resonators for short-term stability and referenced to an optical frequency comb for long-term stability and reproducibility. We estimate the linewidth of the lasers to be about 10 kHz. In order to ensure minimum momentum recoil imparted on the molecules, the beams for lasers L_1 and L_2 are co-propagating. The beams for L_3 and

L_4 are also co-propagating but run antiparallel to the beams of L_1 and L_2. All beams run horizontally and are linearly polarized with the polarization axis in the vertical direction, parallel to the direction of the magnetic field, which defines the axis of quantization. We operate at Rabi frequencies in the range of $2\pi\times$ (1 to 4) MHz.

Polarizability measurement

For determining the ground state molecular polarizability, transfer to $|v = 0>$ is performed at a fixed lattice depth of 83 $\tilde{E}_R$ for $|v = 0>$ molecules. The lattice depth is then ramped to the desired value within 50 ms. For phase modulation of the lattice, the frequency of one lattice beam is usually modulated with a modulation depth of 2 MHz at the desired frequency for about 10 ms. For amplitude modulation, the intensity is typically modulated by 20% for about 10 ms.

Acknowledgements We thank H. Ritsch, S. Dürr, N. Bouloufa, and O. Dulieu for valuable discussions. We are indebted to R. Grimm for generous support and to H. Häffner for the loan of a charge-coupled camera. We gratefully acknowledge funding by the Austrian Ministry of Science and Research (Bundesministerium für Wissenschaft und Forschung) and the Austrian Science Fund (Fonds zur Förderung der wissenschaftlichen Forschung) in form of a START prize grant and by the European Science Foundation within the framework of the EuroQUASAR collective research project QuDeGPM and within the framework of the EuroQUAM collective research project QuDipMol. R.H. is supported by a Marie Curie International Incoming Fellowship within the 7th European Community Framework Programme.

Author Contributions All authors contributed extensively to the work presented in this paper.

BIBLIOGRAPHY

[1] Carr, L. D., DeMille, D., Krems, R. V. & Ye, J. Cold and ultracold molecules: science, technology and applications. *New. J. Phys.* **11,** 055049 (2009).

[2] Krems, R. V. Cold controlled chemistry. *Phys. Chem. Chem. Phys.* **10,** 4079 – 4092 (2008).

[3] Góral, K., Santos, L. & Lewenstein, M. Quantum phases of dipolar bosons in optical lattices. *Phys. Rev. Lett.* **88,** 170406 (2002).

[4] DeMille, D. Quantum computation with trapped polar molecules. *Phys. Rev. Lett.* **88,** 067901 (2002).

[5] Bloch, I., Dalibard, J. & Zwerger, W. Many-body physics with ultracold gases. *Rev. Mod. Phys.* **80,** 885–964 (2008).

[6] Volz, T. *et al.* Preparation of a quantum state with one molecule at each site of an optical lattice. *Nature Phys.* **2,** 692–695 (2006).

[7] Chin, C., Grimm, R., Julienne, P. & Tiesinga, E. Feshbach resonances in ultracold gases. *arXiv* 0812.1496v2 (2008).

[8] Baranov, M. A. Theoretical progress in many-body physics with ultracold dipolar gases. *Physics Reports* **464,** 71–111 (2008).

[9] Lahaye, T., Menotti, C., Santos, L., Lewenstein, M. & Pfau, T. The physics of dipolar bosonic quantum gases. *Rep. Prog. Phys.* **72,** 126401 (2009).

[10] Pupillo, G., Micheli, A., Büchler, H. P. & Zoller, P. Condensed matter physics with cold polar molecules. Ch. *Cold Molecules: Theory, Experiment, Applications* (CRC Press, Boca Raton, 2009).

[11] Friedrich, B. & Doyle, J. M. Why are cold molecules so hot? *ChemPhysChem* **10,** 604–623 (2009).

[12] Jaksch, D., Venturi, V., Cirac, J. I., Williams, C. J. & Zoller, P. Creation of a molecular condensate by dynamically melting a Mott insulator. *Phys. Rev. Lett.* **89,** 040402 (2002).

[13] DeMille, D. *et al.* Enhanced sensitivity to variation of m_e/m_p in molecular spectra. *Phys. Rev. Lett.* **100,** 043202 (2008).

[14] Zelevinsky, T., Kotochigova, S. & Ye, J. Precision test of mass-ratio variations with lattice-confined ultracold molecules. *Phys. Rev. Lett.* **100,** 043201 (2008).

[15] Danzl, J. G. *et al.* Quantum gas of deeply bound ground state molecules. *Science* **321,** 1062–1066 (2008).

[16] Ni, K.-K. *et al.* A high phase-space-density gas of polar molecules. *Science* **322,** 231–235 (2008).

[17] Winkler, K. *et al.* Coherent optical transfer of Feshbach molecules to a lower vibrational state. *Phys. Rev. Lett.* **98,** 043201 (2007).

[18] Lang, F., Winkler, K., Strauss, C., Grimm, R. & Denschlag, J. H. Ultracold triplet molecules in the rovibrational ground state. *Phys. Rev. Lett.* **101,** 133005 (2008).

[19] Kraemer, T. *et al.* Optimized production of a cesium Bose–Einstein condensate. *Appl. Phys. B* **79,** 1013–1019 (2004).

[20] Thalhammer, G. *et al.* Long-lived Feshbach molecules in a three-dimensional optical lattice. *Phys. Rev. Lett.* **96,** 050402 (2006).

[21] Mark, M. *et al.* Spectroscopy of ultracold trapped cesium Feshbach molecules. *Phys. Rev. A* **76,** 042514 (2007).

[22] Danzl, J. G. *et al.* Deeply bound ultracold molecules in an optical lattice. *New J. Phys.* **11,** 055036 (2009).

[23] Bergmann, K., Theuer, H. & Shore, B. W. Coherent population transfer among quantum states of atoms and molecules. *Rev. Mod. Phys.* **70,** 1003–1025 (1998).

[24] Aldegunde, J. & Hutson, J. M. Hyperfine energy levels of alkali-metal dimers: Ground-state homonuclear molecules in magnetic fields. *Phys. Rev. A* **79,** 013401 (2009).

[25] Malinovsky, V. S. & Tannor, D. J. Simple and robust extension of the stimulated Raman adiabatic passage technique to N-level systems. *Phys. Rev. A* **56,** 4929–4937 (1997).

[26] Mark, M. J. *et al.* Dark resonances for ground-state transfer of molecular quantum gases. *Appl. Phys. B* **95,** 219–225 (2009).

[27] Ye, J., Kimble, H. J. & Katori, H. Quantum state engineering and precision metrology using state-insensitive light traps. *Science* **320,** 1734–1738 (2008).

[28] Pilch, K. *et al.* Observation of interspecies Feshbach resonances in an ultracold Rb-Cs mixture. *Phys. Rev. A* **79,** 042718 (2009).

[29] Herbig, J. *et al.* Preparation of a pure molecular quantum gas. *Science* **301,** 1510–1513 (2003).

[30] Danzl, J. G. *et al.* Precision molecular spectroscopy for ground state transfer of molecular quantum gases. *Faraday Discuss.* **142,** 283–295 (2009).

BIBLIOGRAPHY

[Alb09] A. Alberti, V. V. Ivanov, G. M. Tino, and G. Ferrari, *Engineering the quantum transport of atomic wavefunctions over macroscopic distances*, Nature Physics **5**, 547 (2009).

[Ale05] K. Alekseev, *New approaches to THz bloch oscillator*, Infrared and Millimeter Waves, Conference Digest of the 2004 Joint 29th International Conference on 2004 and 12th International Conference on Terahertz Electronics, 2004. 163–164 (2005).

[Ale06] F. Alet, A. M. Walczak, and M. P. Fisher, *Exotic quantum phases and phase transitions in correlated matter*, Physica A: Statistical and Theoretical Physics **369**, 122 (2006).

[Alt05] E. Altman, A. Polkovnikov, E. Demler, B. Halperin, and M. Lukin, *Superfluid-Insulator Transition in a Moving System of Interacting Bosons*, Physical Review Letters **95**, 020402 (2005).

[And95] M. H. Anderson, J. R. Ensher, M. R. Matthews, C. E. Wieman, and E. A. Cornell, *Observation of Bose-Einstein condensation in dilute atomic vapor*, Science **269**, 198 (1995).

[And97] M. R. Andrews, *Observation of Interference Between Two Bose Condensates*, Science **275**, 637 (1997).

[And98] B. P. Anderson and M. A. Kasevich, *Macroscopic quantum interference from atomic tunnel arrays*, Science **282**, 1686 (1998).

[And09] R. Anderson, C. Ticknor, A. Sidorov, and B. Hall, *Spatially inhomogeneous phase evolution of a two-component Bose-Einstein condensate*, Physical Review A **80** (2009).

[Ash76] N. Ashcroft and N. Mermin, *Solid State Physics*, Cengage Learning Services, 1976.

[Ast04] G. Astrakharchik, D. Blume, S. Giorgini, and B. Granger, *Quasi-one-dimensional Bose gases with a large scattering length*, Physical Review Letters **92**, 030402 (2004).

[Ast05] G. E. Astrakharchik, J. Boronat, J. Casulleras, and S. Giorgini, *Beyond the Tonks-Girardeau Gas: Strongly Correlated Regime in Quasi-One-Dimensional Bose Gases*, Physical Review Letters **95**, 190407 (2005).

[Ast08] G. Astrakharchik and Y. Lozovik, *Super-Tonks-Girardeau regime in trapped one-dimensional dipolar gases*, Physical Review A **77**, 013404 (2008).

[Bar01] K. Barnham and D. Vvedensky, *Low-dimensional semiconductor structures: fundamentals and device applications.*, Cambridge University Press, Cambridge UK, 2001.

[Bat04] R. Battesti, P. Clade, S. Guellati-Khelifa, C. Schwob, B. Grémaud, F. Nez, L. Julien, and F. Biraben, *Bloch Oscillations of Ultracold Atoms: A Tool for a Metrological Determination of h/m_{Rb}*, Physical Review Letters **92**, 253001 (2004).

[Bat05] M. T. Batchelor, M. Bortz, X. W. Guan, and N. Oelkers, *Evidence for the super Tonks-Girardeau gas*, Journal of Statistical Mechanics: Theory and Experiment **2005**, L10001 (2005).

[Bed86] J. G. Bednorz and K. A. Müller, *Possible high Tc superconductivity in the Ba-La-Cu-O system*, Zeitschrift für Physik B: Condensed Matter **64**, 189 (1986).

[Bel00] D. Belitz and T. R. Kirkpatrick, *Quantum phase transitions*, Kluwer, Dordrecht, 2000.

[Ben96] M. Ben Dahan, E. Peik, J. Reichel, Y. Castin, and C. Salomon, *Bloch oscillations of atoms in an optical potential.*, Physical Review Letters **76**, 4508 (1996).

[Ber97] P. Berman, *Atom Interferometry*, New York: Academic, 1997.

[Ber03] T. Bergeman, M. Moore, and M. Olshanii, *Atom-atom scattering under cylindrical harmonic confinement: Numerical and analytic studies of the confinement induced resonance*, Physical Review Letters **91**, 163201 (2003).

[Bil08] J. Billy, V. Josse, Z. Zuo, A. Bernard, B. Hambrecht, P. Lugan, D. Clément, L. Sanchez-Palencia, P. Bouyer, and A. Aspect, *Direct observation of Anderson localization of matter waves in a controlled disorder*, Nature **453**, 891 (2008).

[Biz05] S. Bize, P. Laurent, M. Abgrall, H. Marion, I. Maksimovic, L. Cacciapuoti, J. Grünert, C. Vian, F. P. D. Santos, P. Rosenbusch, P. Lemonde, G. Santarelli, P. Wolf, A. Clairon, A. Luiten, M. Tobar, and C. Salomon, *Cold atom clocks and applications*, Journal of Physics B: Atomic, Molecular and Optical Physics **38**, S449 (2005).

[Bla04] J. S. Blakemore, *Solid state physics.*, Cambridge University Press, Cambridge UK, 2004.

[Blo28] F. Bloch, *Über die Quantenmechanik der Elektronen in Kristallgittern*, Zeitschrift für Physik **52**, 555 (1928).

[Blo08] I. Bloch, J. Dalibard, and W. Zwerger, *Many-body physics with ultracold gases*, Reviews of Modern Physics **80**, 885 (2008).

[Blu02] D. Blume and C. Greene, *Fermi pseudopotential approximation: Two particles under external confinement*, Physical Review A **65**, 043613 (2002).

[Boc99] M. Bockrath, D. Cobden, J. Lu, A. G. Rinzler, R. E. Smalley, L. Balents, and P. McEuen, *Luttinger liquid behavior in carbon nanotubes*, Nature **397**, 598 (1999).

[Bos24] S. Bose, *Plancks Gesetz und Lichtquantenhypothese*, Zeitschrift für Physik A **26**, 178 (1924).

[Boy07] M. Boyd, A. Ludlow, S. Blatt, S. Foreman, T. Ido, T. Zelevinsky, and J. Ye, *Sr87 Lattice Clock with Inaccuracy below 10E-15*, Physical Review Letters **98**, 83002 (2007).

[Bra12] W. Bragg, *The diffraction of short electromagnetic waves by a crystal*, in: *Proceedings of the Cambridge Philosophical Society*, vol. 17, 43–57, 1912.

[Bri30] L. Brillouin, *Les electrons dans les metaux et le classement des ondes de de Broglie correspondantes*, Comptes Rendus Hebdomadaires des Seances de l'Academie des Sciences **191**, 292 (1930).

[Buc03a] A. Buchleitner and A. Kolovsky, *Interaction-Induced Decoherence of Atomic Bloch Oscillations*, Physical Review Letters **91**, 253002 (2003).

[Büc03b] H. Büchler, G. Blatter, and W. Zwerger, *Commensurate-Incommensurate Transition of Cold Atoms in an Optical Lattice*, Physical Review Letters **90**, 130401 (2003).

[Büc10] H. P. Büchler, *Microscopic derivation of Hubbard parameters for cold atomic gases*, Physical Review Letters **104**, 090402 (2010).

[Bur99] S. Burger, K. Bongs, S. Dettmer, W. Ertmer, K. Sengstock, A. Sanpera, G. V. Shlyapnikov, and M. Lewenstein, *Dark Solitons in Bose-Einstein Condensates*, Physical Review Letters **83**, 5198 (1999).

[Bur09] F. J. Burnell, M. M. Parish, N. R. Cooper, and S. L. Sondhi, *Devil's staircases and supersolids in a one-dimensional dipolar Bose gas*, Physical Review B **80**, 1 (2009).

[Cam06] G. K. Campbell, J. Mun, M. Boyd, P. Medley, A. E. Leanhardt, L. G. Marcassa, D. E. Pritchard, and W. Ketterle, *Imaging the Mott insulator shells by using atomic clock shifts.*, Science **313**, 649 (2006).

[Car05] I. Carusotto, L. Pitaevskii, S. Stringari, G. Modugno, and M. Inguscio, *Sensitive measurement of forces at the micron scale using Bloch oscillations of ultracold atoms*, Physical Review Letters **95**, 093202 (2005).

[Cav00] R. J. Cava, *Oxide Superconductors*, J. Am. Ceram. Soc. **83**, 5 (2000).

[Caz04] M. A. Cazalilla, *Bosonizing one-dimensional cold atomic gases*, Journal of Physics B: Atomic, Molecular and Optical Physics **37**, S1 (2004).

[Chi04] C. Chin, V. Vuletić, A. Kerman, S. Chu, E. Tiesinga, P. Leo, and C. Williams, *Precision Feshbach spectroscopy of ultracold Cs2*, Physical Review A **70**, 32701 (2004).

[Chi05] C. Chin, T. Kraemer, M. Mark, J. Herbig, P. Waldburger, H.-C. Nägerl, and R. Grimm, *Observation of Feshbach-Like Resonances in Collisions between Ultracold Molecules*, Physical Review Letters **94**, 13 (2005).

[Chi10] C. Chin, P. Julienne, and E. Tiesinga, *Feshbach resonances in ultracold gases*, Reviews of Modern Physics **82**, 1225 (2010).

[Cla06a] P. Cladé, E. de Mirandes, M. Cadoret, S. Guellati-Khélifa, C. Schwob, F. Nez, L. Julien, and F. Biraben, *Determination of the Fine Structure Constant Based on Bloch Oscillations of Ultracold Atoms in a Vertical Optical Lattice*, Physical Review Letters **96**, 33001 (2006).

[Cla06b] S. R. Clark and D. Jaksch, *Signatures of the superfluid to Mott-insulator transition in the excitation spectrum of ultracold atoms*, New Journal of Physics **8**, 160 (2006).

[Col75] S. Coleman, *Quantum sine-Gordon equation as the massive Thirring model*, Physical Review D **11**, 2088 (1975).

[Cri04] M. Cristiani, O. Morsch, N. Malossi, M. Jona-Lasinio, M. Anderlini, E. Courtade, and E. Arimondo, *Instabilities of a Bose-Einstein condensate in a periodic potential: an experimental investigation*, Optics Express **12**, 4 (2004).

[Cro09] A. Cronin, J. Schmiedmayer, and D. Pritchard, *Optics and interferometry with atoms and molecules*, Reviews of Modern Physics **81**, 1051 (2009).

[Dal10] M. Dalmonte, G. Pupillo, and P. Zoller, *1D Quantum Liquids with Power-Law Interactions: a Luttinger Staircase with Polar Molecules*, arXiv:1004.5035v1 (2010).

[Dan08] J. G. Danzl, E. Haller, M. Gustavsson, M. J. Mark, R. Hart, N. Bouloufa, O. Dulieu, H. Ritsch, and H.-C. Nägerl, *Quantum gas of deeply bound ground state molecules.*, Science (New York, N.Y.) **321**, 1062 (2008).

[Dan10] J. G. Danzl, M. J. Mark, E. Haller, M. Gustavsson, R. Hart, J. Aldegunde, J. M. Hutson, and H.-C. Nägerl, *An ultracold high-density sample of rovibronic ground-state molecules in an optical lattice*, Nature Physics **6**, 265 (2010).

[Dav27] C. Davisson and L. H. Germer, *The Scattering of Electrons by a Single Crystal of Nickel*, Nature **119**, 558 (1927).

[Dav95] K. B. Davis, M. O. Mewes, M. R. Andrews, N. J. van Druten, D. S. Durfee, D. M. Kurn, and W. Ketterle, *Bose-Einstein condensation in a gas of sodium atoms*, Physical Review Letters **75**, 3969 (1995).

[Den99] L. Deng, E. Hagley, J. Denschlag, J. Simsarian, M. Edwards, C. Clark, K. Helmerson, S. Rolston, and W. Phillips, *Temporal, Matter-Wave-Dispersion Talbot Effect*, Physical Review Letters **83**, 5407 (1999).

[Den00] J. Denschlag, J. E. Simsarian, D. L. Feder, C. Clark, L. A. Collins, J. Cubizolles, L. Deng, E. W. Hagley, K. Helmerson, W. P. Reinhardt, S. L. Rolston, B. I. Schneider, and W. D. Phillips, *Generating solitons by phase engineering of a Bose-Einstein condensate*, Science **287**, 97 (2000).

[DeP99] M. DePue, C. McCormick, S. Winoto, S. Oliver, and D. Weiss, *Unity occupation of sites in a 3D optical lattice.*, Physical Review Letters **82**, 2262 (1999).

[Did04] S. A. Diddams, J. C. Bergquist, S. R. Jefferts, and C. W. Oates, *Standards of time and frequency at the outset of the 21st century*, Science **306**, 1318 (2004).

[Eck05] A. Eckardt, T. Jinasundera, C. Weiss, and M. Holthaus, *Analog of Photon-Assisted Tunneling in a Bose-Einstein Condensate*, Physical Review Letters **95**, 200401 (2005).

[Eck09] A. Eckardt, M. Holthaus, H. Lignier, A. Zenesini, D. Ciampini, O. Morsch, and E. Arimondo, *Exploring dynamic localization with a Bose-Einstein condensate*, Physical Review A **79**, 013611 (2009).

[Ehr17] P. Ehrenfest, *How does it becomemanifest in the fundamental laws of Physics that space has three dimensions?*, Proc. Ams. Acad. **20**, 200 (1917).

[Ein25] A. Einstein, *Quantentheorie des einatomigen idealen Gases. Zweite Abhandlung.*, Sitzungber. Preuss. Akad. Wiss. **3** (1925).

[Esa70] L. Esaki and R. Tsu, *Superlattice and negative differential conductivity in semiconductors*, IBM Journal of Research and Development **14**, 61 (1970).

[Est30] I. Estermann and O. Stern, *Beugung von Molekularstrahlen*, Zeitschrift für Physik **61**, 95 (1930).

[Fab09] N. Fabbri, D. Clément, L. Fallani, C. Fort, M. Modugno, K. van der Stam, and M. Inguscio, *Excitations of Bose-Einstein condensates in a one-dimensional periodic potential*, Physical Review A **79**, 1 (2009).

[Fal04] L. Fallani, L. De Sarlo, J. Lye, M. Modugno, R. Saers, C. Fort, and M. Inguscio, *Observation of Dynamical Instability for a Bose-Einstein Condensate in a Moving 1D Optical Lattice*, Physical Review Letters **93**, 140406 (2004).

[Fat08] M. Fattori, C. D'Errico, G. Roati, M. Zaccanti, M. Jona-Lasinio, M. Modugno, M. Inguscio, and G. Modugno, *Atom Interferometry with a Weakly Interacting Bose-Einstein Condensate*, Physical Review Letters **100**, 080405 (2008).

[Fed04] P. Fedichev, M. Bijlsma, and P. Zoller, *Extended Molecules and Geometric Scattering Resonances in Optical Lattices*, Physical Review Letters **92**, 2 (2004).

[Fel92] J. Feldmann, K. Leo, J. Shah, D. Miller, J. Cunningham, T. Meier, G. Von Plessen, A. Schulze, P. Thomas, and S. Schmitt-Rink, *Optical investigation of Bloch oscillations in a semiconductor superlattice*, Physical Review B **46**, 7252 (1992).

[Fer05] C. Fertig, K. O'Hara, J. Huckans, S. Rolston, W. Phillips, and J. Porto, *Strongly Inhibited Transport of a Degenerate 1D Bose Gas in a Lattice*, Physical Review Letters **94**, 3 (2005).

[Fer06] G. Ferrari, N. Poli, F. Sorrentino, and G. Tino, *Long-Lived Bloch Oscillations with Bosonic Sr Atoms and Application to Gravity Measurement at the Micrometer Scale*, Physical Review Letters **97**, 060402 (2006).

[Fer09] F. Ferlaino, S. Knoop, M. Berninger, W. Harm, J. P. D'Incao, H.-C. Nägerl, and R. Grimm, *Evidence for universal four-body states tied to an Efimov trimer*, Phys. Rev. Lett. **102**, 140401 (2009).

[Fey82] R. P. Feynman, *Simulating physics with computers*, International Journal of Theoretical Physics **21**, 467 (1982).

[Fis89] M. Fisher, P. Weichman, G. Grinstein, and D. Fisher, *Boson localization and the superfluid-insulator transition*, Physical Review B **40**, 546 (1989).

[Fix07] J. B. Fixler, G. T. Foster, J. M. McGuirk, and M. A. Kasevich, *Atom interferometer measurement of the newtonian constant of gravity*, Science **315**, 74 (2007).

[Föl06] S. Fölling, A. Widera, T. Müller, F. Gerbier, and I. Bloch, *Formation of Spatial Shell Structure in the Superfluid to Mott Insulator Transition*, Physical Review Letters **97**, 1 (2006).

[Fos04] K. Fossheim and A. Sudbø, *Superconductivity: physics and applications*, John Wiley & Sons Inc., 2004.

[Gan03] D. Gangardt and G. Shlyapnikov, *Stability and Phase Coherence of Trapped 1D Bose Gases*, Physical Review Letters **90**, 1 (2003).

[Geb97] F. Gebhard, *The Mott Metal-Insulator Transition*, Springer Verlag, Berlin, 1997.

[Gem09] N. Gemelke, X. Zhang, C.-L. Hung, and C. Chin, *In situ observation of incompressible Mott-insulating domains in ultracold atomic gases.*, Nature **460**, 995 (2009).

[Geo00] A. Georges, T. Giamarchi, and N. Sandler, *Interchain conductivity of coupled Luttinger liquids and organic conductors*, Physical Review B **61**, 16393 (2000).

[Gia91] T. Giamarchi, *Umklapp process and resistivity in one-dimensional fermion systems*, Physical Review B **44**, 2905 (1991).

[Gia97] T. Giamarchi, *Mott transition in one dimension*, Physica B: Condensed Matter **230-232**, 975 (1997).

[Gia03] T. Giamarchi, *Quantum physics in one dimension*, Clarendon Press, Oxford, 2003.

[Gia04] T. Giamarchi, *Theoretical framework for quasi-one dimensional systems.*, Chemical Reviews **104**, 5037 (2004).

[Gio02] S. Giovanazzi, A. Görlitz, and T. Pfau, *Tuning the dipolar interaction in quantum gases*, Physical Review Letters **89**, 130401 (2002).

[Gir60] M. Girardeau, *Relationship between Systems of Impenetrable Bosons and Fermions in One Dimension*, Journal of Mathematical Physics **1**, 516 (1960).

[Gir09] M. D. Girardeau and G. E. Astrakharchik, *Wave functions of the super Tonks-Girardeau gas and the trapped 1D hard sphere Bose gas*, arXiv:0912.1633 (2009).

[Gog98] A. O. Gogolin, A. M. Tsvelik, and A. A. Nersesyan, *Bosonization and strongly correlated systems*, Cambridge University Press, Cambridge UK, 1998.

[Gör01] A. Görlitz, J. Vogels, A. Leanhardt, C. Raman, T. Gustavson, J. Abo-Shaeer, A. Chikkatur, S. Gupta, S. Inouye, T. Rosenband, and W. Ketterle, *Realization of Bose-Einstein Condensates in Lower Dimensions*, Physical Review Letters **87**, 1 (2001).

[Gou86] P. Gould, G. Ruff, and D. Pritchard, *Diffraction of atoms by light: The near-resonant Kapitza-Dirac effect*, Physical Review Letters **56**, 827 (1986).

[Gre01] M. Greiner, I. Bloch, O. Mandel, T. Hänsch, and T. Esslinger, *Exploring Phase Coherence in a 2D Lattice of Bose-Einstein Condensates*, Physical Review Letters **87** (2001).

[Gre02] M. Greiner, O. Mandel, T. Esslinger, T. W. Hänsch, and I. Bloch, *Quantum phase transition from a superfluid to a Mott insulator in a gas of ultracold atoms.*, Nature **415**, 39 (2002).

[Gre03] M. Greiner, *Ultracold quantum gases in three-dimensional optical lattice potentials*, PhD thesis, Ludwig-Maximilians-Universität München (2003).

[Gre08] M. Greiner and S. Fölling, *Optical lattices*, Nature **453**, 736 (2008).

[Gri00] R. Grimm, M. Weidemüller, and Y. Ovchinnikov, *Optical dipole traps for neutral atoms*, Advances in Atomic, Molecular and Optical Physics **42**, 95 (2000).

[Gri06] A. Griesmaier, J. Stuhler, T. Koch, M. Fattori, T. Pfau, and S. Giovanazzi, *Comparing Contact and Dipolar Interactions in a Bose-Einstein Condensate*, Physical Review Letters **97**, 1 (2006).

[Gün05] K. Günter, T. Stöferle, H. Moritz, M. Köhl, and T. Esslinger, *p-wave interactions in low-dimensional fermionic gases*, Physical Review Letters **95**, 1 (2005).

[Gup02] S. Gupta, K. Dieckmann, Z. Hadzibabic, and D. Pritchard, *Contrast Interferometry using Bose-Einstein Condensates to Measure h/m and α*, Physical Review Letters **89**, 140401 (2002).

[Gur71] L. Gurevich and V. Mostepanenko, *On the existence of atoms in n-dimensional space*, Physics Letters A **35**, 201 (1971).

[Gus08] M. Gustavsson, E. Haller, M. J. Mark, J. G. Danzl, G. Rojas-Kopeinig, and H.-C. Nägerl, *Control of Interaction-Induced Dephasing of Bloch Oscillations*, Physical Review Letters **100**, 080404 (2008).

[Gus10] M. Gustavsson, E. Haller, M. J. Mark, J. G. Danzl, R. Hart, A. J. Daley, and H.-C. Nägerl, *Interference of interacting matter waves*, New Journal of Physics **12**, 065029 (2010).

[Had06] Z. Hadzibabic, P. Krüger, M. Cheneau, B. Battelier, and J. Dalibard, *Berezinskii-Kosterlitz-Thouless crossover in a trapped atomic gas*, Nature **441**, 1118 (2006).

[Hal36] H. V. Halbon Jr and P. Preiswerk, *Preuve expérimentale de la diffraction des neutrons*, Comptes Rendus Acad. Sci. Paris **203**, 73 (1936).

[Hal81] F. D. M. Haldane, *'Luttinger liquid theory' of one-dimensional quantum fluids : I . Properties of the Luttinger model and their extension to the general 1D interacting spinless Fermi gas*, Journal Physics C: Solid State Physics **14**, 2585 (1981).

[Hal09] E. Haller, M. Gustavsson, M. J. Mark, J. G. Danzl, R. Hart, G. Pupillo, and H.-C. Nägerl, *Realization of an excited, strongly correlated quantum gas phase.*, Science **325**, 1224 (2009).

[Hal10a] E. Haller, R. Hart, M. J. Mark, J. G. Danzl, L. Reichsöllner, and H.-C. Nägerl, *Inducing Transport in a Dissipation-Free Lattice with Super Bloch Oscillations*, Physical Review Letters **104**, 4 (2010).

[Hal10b] E. Haller, M. J. Mark, R. Hart, J. G. Danzl, L. Reichsöllner, V. Melezhik, P. Schmelcher, and H.-C. Nägerl, *Confinement-Induced Resonances in Low-Dimensional Quantum Systems*, Physical Review Letters **104** (2010).

[Han79] J. Handyside, *"Gedanken von der wahren Schätzung der lebendigen Kräfte" in "Kant's Inaugural Dissertation and Early Writings on Space"*, Hyperion Books, 1979.

[Han00] D. Han, S. Wolf, S. Oliver, C. McCormick, M. DePue, and D. Weiss, *3D Raman sideband cooling of cesium atoms at high density*, Physical Review Letters **85**, 724 (2000).

[Har04] T. Hartmann, F. Keck, H. J. Korsch, and S. Mossmann, *Dynamics of Bloch oscillations*, New Journal of Physics **6**, 2 (2004).

[Har07] R. A. Hart, X. Xu, R. Legere, and K. Gibble, *A quantum scattering interferometer*, Nature **446**, 892 (2007).

[Her03] J. Herbig, T. Kraemer, M. Mark, T. Weber, C. Chin, H.-C. Nägerl, and R. Grimm, *Preparation of a pure molecular quantum gas.*, Science **301**, 1510 (2003).

[Hof07] S. Hofferberth, I. Lesanovsky, B. Fischer, T. Schumm, and J. Schmiedmayer, *Non-equilibrium coherence dynamics in one-dimensional Bose gases*, Nature **449**, 324 (2007).

[Hub63] J. Hubbard, *Electron Correlations in Narrow Energy Bands*, Proceedings of the Royal Society A: Mathematical, Physical and Engineering Sciences **276**, 238 (1963).

[Hun10] C.-L. Hung, X. Zhang, N. Gemelke, and C. Chin, *Slow Mass Transport and Statistical Evolution of an Atomic Gas across the Superfluid-Mott-Insulator Transition*, Physical Review Letters **104**, 1 (2010).

[Ich04] S. Ichimaru, *Basic principles of plasma physics: a statistical approach*, Westview Press, Oxford, 2004.

[Iij91] S. Iijima, *Helical microtubules of graphitic carbon*, Nature **354**, 56 (1991).

[Ima97] A. Imamoglu, M. Lewenstein, and L. You, *Inhibition of Coherence in Trapped Bose-Einstein Condensates*, Physical Review Letters **78**, 2511 (1997).

[Ino98] S. Inouye, M. R. Andrews, J. Stenger, H.-J. Miesner, D. M. Stamper-Kurn, and W. Ketterle, *Observation of Feshbach resonances in a Bose-Einstein condensate*, Nature **392**, 151 (1998).

[Iuc06] A. Iucci, M. Cazalilla, A. Ho, and T. Giamarchi, *Energy absorption of a Bose gas in a periodically modulated optical lattice*, Physical Review A **73**, 1 (2006).

[Iva08] V. V. Ivanov, A. Alberti, M. Schioppo, G. Ferrari, M. Artoni, M. L. Chiofalo, and G. M. Tino, *Coherent Delocalization of Atomic Wave Packets in Driven Lattice Potentials*, Physical Review Letters **100**, 043602 (2008).

[Jak98] D. Jaksch, C. Bruder, J. Cirac, C. Gardiner, and P. Zoller, *Cold Bosonic Atoms in Optical Lattices*, Physical Review Letters **81**, 3108 (1998).

[Jör08] R. Jördens, N. Strohmaier, K. Günter, H. Moritz, and T. Esslinger, *A Mott insulator of fermionic atoms in an optical lattice.*, Nature **455**, 204 (2008).

[Jul] *P. Julienne (private communication).*

[Kan90] T. Kaneyoshi, *Introduction to surface magnetism.*, CRC Press, 1990.

[Kan95] Y. Kanemitsu and T. Ogawa, *Optical Properties of Low-Dimensional Materials*, World Scientific, Singapore, 1995.

[Kap00] A. Kaplan, I. Marzoli, W. Lamb, and W. Schleich, *Multimode interference: Highly regular pattern formation in quantum wave-packet evolution*, Physical Review A **61** (2000).

[Kas95] A. Kastberg, W. Phillips, S. Rolston, R. Spreeuw, and P. Jessen, *Adiabatic Cooling of Cesium to 700 nK in an Optical Lattice*, Physical Review Letters **74**, 1542 (1995).

[Kea95] B. Keay, S. Zeuner, S. Allen, K. Maranowski, A. Gossard, U. Bhattacharya, and M. Rodwell, *Dynamic Localization, Absolute Negative Conductance, and Stimulated, Multiphoton Emission in Sequential Resonant Tunneling Semiconductor Superlattices*, Physical Review Letters **75**, 4102 (1995).

[Ker00] A. J. Kerman, V. Vuletic, C. Chin, and S. Chu., *Beyond optical molasses: 3D Raman sideband cooling of atomic cesium to high phase-space density.*, Physical Review Letters **84**, 439 (2000).

[Kes10] J. P. Kestner and L.-M. Duan, *Anharmonicity-induced resonances for ultracold atoms and their detection*, New Journal of Physics **12**, 053016 (2010).

[Ket96] W. Ketterle and N. van Druten, *Bose-Einstein condensation of a finite number of particles trapped in one or three dimensions*, Physical Review A **54**, 656 (1996).

[Kha02] L. Khaykovich, F. Schreck, G. Ferrari, T. Bourdel, J. Cubizolles, L. D. Carr, Y. Castin, and C. Salomon, *Formation of a Matter-Wave Bright Soliton*, Science **296**, 1290 (2002).

[Kim05] J. Kim, J. Schmiedmayer, and P. Schmelcher, *Quantum scattering in quasi-one-dimensional cylindrical confinement*, Physical Review A **72**, 1 (2005).

[Kin04] T. Kinoshita, T. Wenger, and D. S. Weiss, *Observation of a one-dimensional Tonks-Girardeau gas*, Science **305**, 1125 (2004).

[Kin06] T. Kinoshita, T. Wenger, and D. S. Weiss, *A quantum Newton's cradle*, Nature **440**, 900 (2006).

[Kle26] O. Klein, *Quantentheorie und fünfdimensionale Relativitätstheorie*, Zeitschrift für Physik **37**, 895 (1926).

[Köh05] M. Köhl, H. Moritz, T. Stöferle, K. Günter, and T. Esslinger, *Fermionic atoms in a three dimensional optical lattice: Observing fermi surfaces, dynamics, and interactions*, Physical Review Letters **94**, 080403 (2005).

[Köh06] T. Köhler, K. Góral, and P. Julienne, *Production of cold molecules via magnetically tunable Feshbach resonances*, Reviews of Modern Physics **78**, 1311 (2006).

[Kol09] A. Kolovsky and H. Korsch, *Dynamics of interacting atoms in driven tilted optical lattices*, arXiv:0912.2587 (2009).

[Kor03] H. Korsch, *An algebraic solution of driven single band tight binding dynamics*, Physical Review A **317**, 54 (2003).

[Kra04] T. Kraemer, J. Herbig, M. Mark, T. Weber, C. Chin, H.-C. Nägerl, and R. Grimm, *Optimized production of a cesium Bose-Einstein condensate*, Applied Physics B **79**, 1013 (2004).

[Kra06] T. Kraemer, M. Mark, P. Waldburger, J. G. Danzl, C. Chin, B. Engeser, A. D. Lange, K. Pilch, A. Jaakkola, H.-C. Nägerl, and R. Grimm, *Evidence for Efimov quantum states in an ultracold gas of caesium atoms.*, Nature **440**, 315 (2006).

[Lah07] T. Lahaye, T. Koch, B. Fröhlich, M. Fattori, J. Metz, A. Griesmaier, S. Giovanazzi, and T. Pfau, *Strong dipolar effects in a quantum ferrofluid.*, Nature **448**, 672 (2007).

[Lam10] G. Lamporesi, J. Catani, G. Barontini, Y. Nishida, M. Inguscio, and F. Minardi, *Scattering in mixed dimensions with ultracold gases*, Physical Review Letters **104**, 5 (2010).

[Lan57] L. D. Landau, *Theory of Fermi-liquids*, Sov. Phys. JETP **3**, 920 (1957).

[Lan59] L. D. Landau, *On the theory of the Fermi-liquid*, Sov. Phys. JETP **8**, 70 (1959).

[Lan09] A. Lange, K. Pilch, A. Prantner, F. Ferlaino, B. Engeser, H.-C. Nägerl, R. Grimm, and C. Chin, *Determination of atomic scattering lengths from measurements of molecular binding energies near feshbach resonances*, Physical Review A **79**, 13622 (2009).

[Leo92] K. Leo, *Observation of Bloch oscillations in a semiconductor superlattice*, Solid State Communications **84**, 943 (1992).

[Li07] W. Li, A. Tuchman, H.-C. Chien, and M. Kasevich, *Extended Coherence Time with Atom-Number Squeezed States*, Physical Review Letters **98** (2007).

[Lie63a] E. Lieb, *Exact Analysis of an Interacting Bose Gas. II. The Excitation Spectrum*, Physical Review **130**, 1616 (1963).

[Lie63b] E. Lieb and W. Liniger, *Exact Analysis of an Interacting Bose Gas. I. The General Solution and the Ground State*, Physical Review **130**, 1605 (1963).

[Lie03] A. Liem, J. Limpert, H. Zellmer, and A. Tünnermann, *100-W single-frequency master-oscillator fiber power amplifier*, Optics Letters **28**, 1537 (2003).

[Lig07] H. Lignier, C. Sias, D. Ciampini, Y. Singh, A. Zenesini, O. Morsch, and E. Arimondo, *Dynamical Control of Matter-Wave Tunneling in Periodic Potentials*, Physical Review Letters **99**, 220403 (2007).

[Lys97] V. Lyssenko, G. Valušis, F. Löser, T. Hasche, K. Leo, M. Dignam, and K. Köhler, *Direct Measurement of the Spatial Displacement of Bloch-Oscillating Electrons in Semiconductor Superlattices*, Physical Review Letters **79**, 301 (1997).

[Mad00] K. W. Madison, F. Chevy, W. Wohlleben, and J. Dalibard, *Vortex Formation in a Stirred Bose-Einstein Condensate*, Physical Review Letters **84**, 806 (2000).

[Mar88] P. Martin, B. Oldaker, A. Miklich, and D. Pritchard, *Bragg scattering of atoms from a standing light wave*, Physical Review Letters **60**, 515 (1988).

[Mat] *Material and methods are available as supporting material on Science Online.*

[Mat99] M. R. Matthews, B. P. Anderson, P. C. Haljan, D. S. Hall, C. E. Wieman, and E. A. Cornell, *Vortices in a Bose-Einstein condensate*, Physical Review Letters **83**, 2498 (1999).

[McG65] J. B. McGuire, *Interacting fermions in one dimension. I. Repulsive potential*, Journal of Mathematical Physics **6**, 432 (1965).

[Mel07] V. Melezhik, J. Kim, and P. Schmelcher, *Wave-packet dynamical analysis of ultracold scattering in cylindrical waveguides*, Physical Review A **76**, 053611 (2007).

[Men02] C. Menotti and S. Stringari, *Collective oscillations of a one-dimensional trapped Bose-Einstein gas*, Physical Review A **66**, 1 (2002).

[Met99] H. Metcalf and P. van der Straten, *Laser Colling and Trapping*, Springer-Verlag New York, New York, 1999.

[Mic07] a. Micheli, G. Pupillo, H. P. Büchler, and P. Zoller, *Cold polar molecules in two-dimensional traps: Tailoring interactions with external fields for novel quantum phases*, Physical Review A **76**, 1 (2007).

[Mor01] O. Morsch, J. Müller, M. Cristiani, D. Ciampini, and E. Arimondo, *Bloch Oscillations and Mean-Field Effects of Bose-Einstein Condensates in 1D Optical Lattices*, Physical Review Letters **87**, 140402 (2001).

[Mor03a] H. Moritz, T. Stöferle, M. Köhl, and T. Esslinger, *Exciting collective oscillations in a trapped 1D gas*, Physical Review Letters **91**, 250402 (2003).

[Mor03b] O. Morsch, J. Müller, D. Ciampini, M. Cristiani, P. Blakie, C. Williams, P. Julienne, and E. Arimondo, *Decay and revival of phase coherence of a Bose-Einstein condensate in a one-dimensional lattice*, Physical Review A **67** (2003).

[Mor05] H. Moritz, T. Stöferle, K. Günter, M. Köhl, and T. Esslinger, *Confinement induced molecules in a 1D Fermi gas*, Physical Review Letters **94**, 210401 (2005).

[Mor06] O. Morsch and M. Oberthaler, *Dynamics of Bose-Einstein condensates in optical lattices*, Reviews of Modern Physics **78**, 179 (2006).

[Mot49] N. F. Mott, *The Basis of the Electron Theory of Metals, with Special Reference to the Transition Metals*, Proceedings of the Physical Society. Section A **62**, 416 (1949).

[Mun07] J. Mun, P. Medley, G. Campbell, L. Marcassa, D. Pritchard, and W. Ketterle, *Phase Diagram for a Bose-Einstein Condensate Moving in an Optical Lattice*, Physical Review Letters **99**, 1 (2007).

[Nai07] P. Naidon, E. Tiesinga, W. F. Mitchell, and P. S. Julienne, *Effective-range description of a Bose gas under strong one- or two-dimensional confinement*, New Journal of Physics **9**, 19 (2007).

[Ni08] K.-K. Ni, S. Ospelkaus, M. H. G. de Miranda, A. Pe'er, B. Neyenhuis, J. J. Zirbel, S. Kotochigova, P. S. Julienne, D. S. Jin, and J. Ye, *A High Phase-Space-Density Gas of Polar Molecules*, Science **322**, 231 (2008).

[Nis08] Y. Nishida and S. Tan, *Universal Fermi Gases in Mixed Dimensions*, Physical Review Letters **101** (2008).

[Nis09] Y. Nishida and S. Tan, *Confinement-induced Efimov resonances in Fermi-Fermi mixtures*, Physical Review A **79**, 3 (2009).

[O'H04] K. M. O'Hara, B. Laburthe Tolra, J. H. Huckans, W. D. Phillips, S. L. Rolston, and J. V. Porto, *Observation of Reduced Three-Body Recombination in a Correlated 1D Degenerate Bose Gas*, Physical Review Letters **92**, 190401 (2004).

[Ols98] M. Olshanii, *Atomic scattering in the presence of an external confinement and a gas of impenetrable Bosons*, Physical Review Letters **81**, 938 (1998).

[Orz01] C. Orzel, A. K. Tuchman, M. L. Fenselau, M. Yasuda, and M. A. Kasevich, *Squeezed states in a Bose-Einstein condensate*, Science **291**, 2386 (2001).

[Par04] B. Paredes, A. Widera, V. Murg, O. Mandel, S. Fölling, I. Cirac, G. V. Shlyapnikov, T. W. Hänsch, and I. Bloch, *Tonks-Girardeau gas of ultracold atoms in an optical lattice*, Nature **429**, 277 (2004).

[Pea05] V. Peano, M. Thorwart, C. Mora, and R. Egger, *Confinement-induced resonances for a two-component ultracold atom gas in arbitrary quasi-one-dimensional traps*, New Journal of Physics **7**, 192 (2005).

[Pet80] A. Peters, K. Chung, and S. Chu, *Measurement of gravitational acceleration by dropping atoms*, Nature **400**, 849 (1980).

[Pet94] K. Petsas, A. Coates, and G. Grynberg, *Crystallography of optical lattices*, Physical Review A **50**, 5173 (1994).

[Pet00] D. Petrov, G. Shlyapnikov, and J. Walraven, *Regimes of Quantum Degeneracy in Trapped 1D Gases*, Physical Review Letters **85**, 3745 (2000).

[Pet01] D. S. Petrov and G. V. Shlyapnikov, *Interatomic collisions in a tightly confined Bose gas*, Physical Review A **64**, 012706 (2001).

[Pet07] D. Petrov, D. Gangardt, and G. V. Shlyapnikov, *Low-dimensional trapped gases*, J. Phys. IV France **1**, 1 (2007).

[Phy03] N. J. Phys., *Superfluidity of Bose-Einstein condensate in an optical lattice: Landau-Zener tunnelling and dynamical instability*, New Journal of Physics **5**, 104 (2003).

[Pin66] D. Pines and P. Nozieres, *The theory of quantum liquids.*, Perseus Books Group, Cambridge, MA, 1966.

[Pit03] L. Pitaevskii and S. Stringari, *Bose-Einstein Condensation*, Oxford University Press, Oxford, 2003.

[Pok79] V. Pokrovsky and A. Talapov, *Ground State, Spectrum, and Phase Diagram of Two-Dimensional Incommensurate Crystals*, Physical Review Letters **42**, 65 (1979).

[Pon06] A. V. Ponomarev and A. R. Kolovsky, *Dipole and Bloch oscillations of cold atoms in a parabolic lattice*, Laser Physics **16**, 367 (2006).

[Rap99] S. Rapsch, U. Schollwöck, and W. Zwerger, *Density matrix renormalization group for disordered bosons in one dimension*, Europhysics Letters **46**, 559 (1999).

[Rev] *Note that the revived Bloch cycles are subject to a phase shift, which depends on the vertical location of the harmonic trap minimum with respect to the lattice minima.*

[Roa04] G. Roati, E. de Mirandes, F. Ferlaino, H. Ott, G. Modugno, and M. Inguscio, *Atom Interferometry with Trapped Fermi Gases*, Physical Review Letters **92**, 1 (2004).

[Roa08] G. Roati, C. D'Errico, L. Fallani, M. Fattori, C. Fort, M. Zaccanti, G. Modugno, M. Modugno, and M. Inguscio, *Anderson localization of a non-interacting Bose-Einstein condensate.*, Nature **453**, 895 (2008).

[Rot95] S. Roth and D. Carroll, *One-dimensional metals: conjugated polymers, organic crystals, carbon nanotubes*, Wiley-VCH, Weinheim, 1995.

[Sac00] S. Sachdev, *Quantum Phase Transitions*, Cambridge University Press, Cambridge UK, 2000.

[Sae08] S. Saeidian, V. Melezhik, and P. Schmelcher, *Multichannel atomic scattering and confinement-induced resonances in waveguides*, Physical Review A **77**, 042721 (2008).

[Sal02] L. Salasnich, a. Parola, and L. Reatto, *Effective wave equations for the dynamics of cigar-shaped and disk-shaped Bose condensates*, Physical Review A **65**, 1 (2002).

[Sal09] T. Salger, S. Kling, T. Hecking, C. Geckeler, L. Morales-Molina, and M. Weitz, *Directed transport of atoms in a Hamiltonian quantum ratchet*, Science **326**, 1241 (2009).

[San04] L. Santos, M. Baranov, J. Cirac, H.-U. Everts, H. Fehrmann, and M. Lewenstein, *Atomic Quantum Gases in Kagomé Lattices*, Physical Review Letters **93**, 4 (2004).

[Sch01] F. Schreck, L. Khaykovich, K. L. Corwin, G. Ferrari, T. Bourdel, J. Cubizolles, and C. Salomon, *Quasipure Bose-Einstein Condensate Immersed in a Fermi Sea*, Physical Review Letters **87**, 80403 (2001).

[Sch08] U. Schneider, L. Hackermüller, S. Will, T. Best, I. Bloch, T. A. Costi, R. W. Helmes, D. Rasch, and A. Rosch, *Metallic and insulating phases of repulsively interacting fermions in a 3D optical lattice.*, Science **322**, 1520 (2008).

[Sch10] J. Schachenmayer, G. Pupillo, and A. J. Daley, *Time-dependent currents of one-dimensional bosons in an optical lattice*, New Journal of Physics **12**, 025014 (2010).

[Sep] *Center-of-mass and relative motion separate for identical particles in a harmonic trap*.

[Sia08] C. Sias, H. Lignier, Y. P. Singh, A. Zenesini, D. Ciampini, O. Morsch, and E. Arimondo, *Observation of Photon-Assisted Tunneling in Optical Lattices*, Physical Review Letters **100**, 040404 (2008).

[Sme03] A. Smerzi and A. Trombettoni, *Nonlinear tight-binding approximation for Bose-Einstein condensates in a lattice*, Physical Review A **68**, 023613 (2003).

[Spi07] I. Spielman, W. Phillips, and J. Porto, *Mott-Insulator Transition in a Two-Dimensional Atomic Bose Gas*, Physical Review Letters **98**, 1 (2007).

[Ste08] H. Steinberg, G. Barak, A. Yacoby, L. N. Pfeiffer, K. W. West, B. I. Halperin, and K. Le Hur, *Charge fractionalization in quantum wires*, Nature Physics **4**, 116 (2008).

[Stö04] T. Stöferle, H. Moritz, C. Schori, M. Köhl, and T. Esslinger, *Transition from a Strongly Interacting 1D Superfluid to a Mott Insulator*, Physical Review Letters **92**, 1 (2004).

[Str] *The momentum distribution of a fully dephased interacting ensemble carries high-contrast substructure which will be discussed in a forthcoming publication* .

[Sya08] N. Syassen, D. M. Bauer, M. Lettner, T. Volz, D. Dietze, J. J. García-Ripoll, J. I. Cirac, G. Rempe, and S. Dürr, *Strong dissipation inhibits losses and induces correlations in cold molecular gases*, Science **320**, 1329 (2008).

[Tak06] I. Takesue, J. Haruyama, N. Kobayashi, S. Chiashi, S. Maruyama, T. Sugai, and H. Shinohara, *Superconductivity in Entirely End-Bonded Multiwalled Carbon Nanotubes*, Physical Review Letters **96** (2006).

[Tan01] Z. K. Tang, L. Zhang, N. Wang, X. X. Zhang, G. H. Wen, G. D. Li, J. N. Wang, C. T. Chan, and P. Sheng, *Superconductivity in 4 angstrom single-walled carbon nanotubes*, Science **292**, 2462 (2001).

[Tem08] E. Tempfli, S. Zöllner, and P. Schmelcher, *Excitations of attractive 1D bosons: binding versus fermionization*, New Journal of Physics **10**, 103021 (2008).

[Tho02] Q. Thommen, J. Garreau, and V. Zehnlé, *Theoretical analysis of quantum dynamics in one-dimensional lattices: Wannier-Stark description*, Physical Review A **65**, 053406 (2002).

[Tie00] E. Tiesinga, C. Williams, F. Mies, and P. Julienne, *Interacting atoms under strong quantum confinement*, Physical Review A **61**, 1 (2000).

[Tin96] M. Tinkham, *Introduction to superconductivity.*, McGraw-Hill, New York, 1996.

[Tip86] F. J. Tipler and J. Barrow, *The anthropic cosmological principle*, Oxford University Press, Oxford UK, 1986.

[Voi08] J. Voit, *One-dimensional Fermi liquids*, Reports on Progress in Physics (2008).

[Voj03] M. Vojta, *Quantum phase transitions*, Reports on Progress in Physics **66**, 2069 (2003).

[Vul98] V. Vuletić, C. Chin, A. Kerman, and S. Chu, *Degenerate Raman sideband cooling of trapped cesium atoms at very high atomic densities*, Physical Review Letters **81**, 5768 (1998).

[Wac02] A. Wacker, *Semiconductor superlattices: a model system for nonlinear transport*, Physics Reports **357**, 1 (2002).

[Was93] C. Waschke, H. Roskos, R. Schwedler, K. Leo, H. Kurz, and K. Köhler, *Coherent submillimeter-wave emission from Bloch oscillations in a semiconductor superlattice*, Physical Review Letters **70**, 3319 (1993).

[Web03] T. Weber, J. Herbig, M. Mark, H.-C. Nägerl, and R. Grimm, *Bose-Einstein condensation of cesium.*, Science **299**, 232 (2003).

[Whi59] G. Whitrow, *The structure and evolution of the universe.*, Harper & Row, New York, 1959.

[Wic02] A. Wicht, J. M. Hensley, E. Sarajlic, and S. Chu, *A Preliminary Measurement of the Fine Structure Constant Based on Atom Interferometry*, Physica Scripta **T102**, 82 (2002).

[Wid] *We define the full width to be the root-mean-square (rms) diameter of the distribution*.

[wik09] *cntsem.jpg*, Wikipedia, The Free Encyclopedia, *http://en.wikipedia.org/wiki/Carbon_nanotube* (2009).

[Wil96] S. R. Wilkinson, C. F. Bharucha, K. W. Madison, Q. Niu, and M. G. Raizen, *Observation of atomic Wannier-Stark ladders in an accelerating optical potential.*, Physical Review Letters **76**, 4512 (1996).

[Wit05] D. Witthaut, M. Werder, S. Mossmann, and H. Korsch, *Bloch oscillations of Bose-Einstein condensates: Breakdown and revival*, Physical Review E **71**, 036625 (2005).

[Wu01] B. Wu and Q. Niu, *Landau and dynamical instabilities of the superflow of Bose-Einstein condensates in optical lattices*, Physical Review A **64** (2001).

[Yu00] M. Yu, *Strength and Breaking Mechanism of Multiwalled Carbon Nanotubes Under Tensile Load*, Science **287**, 637 (2000).

[Yur05] V. Yurovsky, *Feshbach resonance scattering under cylindrical harmonic confinement*, Physical Review A **71**, 012709 (2005).

[Zam79] A. Zamolodchikov, *Factorized S-matrices in two dimensions as the exact solutions of certain relativistic quantum field theory models*, Annals of Physics **120**, 253 (1979).

[Zam95] A. B. Zamolodchikov, *Mass scale in the sine-Gordon model and its reductions*, Int. J. Mod. Phys. **A10**, 1125 (1995).

[Zan88] A. Zangwill, *Physics at surfaces.*, Cambridge University Press, Cambridge UK, 1988.

[Zen34] C. Zener, *A theory of the electrical breakdown of solid dielectrics*, Proceedings of the Royal Society of London. Series A, Containing Papers of a Mathematical and Physical Character (1905-1934) **145**, 523 (1934).

[Zen09] A. Zenesini, H. Lignier, D. Ciampini, O. Morsch, and E. Arimondo, *Coherent Control of Dressed Matter Waves*, Physical Review Letters **102**, 100403 (2009).

[Zha08] R. Zhang, R. Sapiro, R. Mhaskar, and G. Raithel, *Role of the mean field in Bloch oscillations of a Bose-Einstein condensate in an optical lattice and harmonic trap*, Physical Review A **78** (2008).

[Zhe04] Y. Zheng, E. Let, M. Kostrun, J. Javanainen, and M. Kos, *Low-Acceleration Instability of a Bose-Einstein Condensate in an Optical Lattice*, Physical Review Letters **93**, 230401 (2004).

DANKSAGUNG

Experimente mit ultrakalten Atomen haben heutzutage eine Komplexität erreicht, die von einzelnen Personen nicht mehr zu bewältigen ist. Voraussetzung für das Gelingen ist immer eine gute Zusammenarbeit und ein Gemeinschaftsgefühl. Ich möchte mich deshalb bei allen Personen herzlich bedanken, die in den letzten Jahren zu dieser Arbeit beigetragen haben. Mein besonderer Dank gilt

Hanns-Christoph Nägerl, für die phantastische Betreuung. Er hat immer Zeit, Hilfe und Lösungen auf Lager und hat uns seine volle Unterstützung zukommen lassen, die weit über das rein Fachliche hinausging. Insbesondere möchte ich mich dafür bedanken, dass er uns den Freiraum zu eigenen Entscheidungen gelassen hat, so dass wir uns mit unserem Experiment identifizieren konnten.

Rudi Grimm, für die hervorragende Gruppenorganisation, die Infrastruktur und die Unterstützung unseres Experiments. Die Atmosphäre in der Arbeitsgruppe war immer entspannt, Team-orientiert und stimulierend, mit vielfältigen Möglichkeiten zu physikalischen Diskussionen und zum wissenschaftlichen Austausch.

Mattias, dem ersten Doktorand an unserem Experiment, für den warmherzigen Empfang und die langen gemeinsamen Laborabende mit schwedischer Musik. Mattias hat das Experiment maßgeblich aufgebaut und die Grundlagen für die hier beschriebenen Ergebnisse gelegt.

Manfred und **Hans**, für das gute Team, für die gegenseitige Unterstützung und für den gemeinsamen Umbau des Labors. Dieser Umbau stellt für mich eine wesentliche Zäsur im Werdegang des Experiments dar und hat die meisten späteren Messungen erst ermöglicht.

Russell, für die vielen stimulierenden Diskussionen, sowohl über die Physik als auch über den Rest dieser Welt.

das restliche Cäsium III Team, Peter, Toni, Gabriel, Lukas, Andy, Oliver und Mohamed für die bisherige und hoffentlich noch anhaltende gute Zusammenarbeit.

Toni und **Helmut**, für die hilfsbereite, kompetente und schnelle Unterstützung aus der Werkstatt.

Christine und **Karin**, für den Überblick über Gelder und Gehälter. So manche Erinnerung von ihnen hat ein finanzielles Chaos verhindert.

Conny, für die langen physikalischen Diskussionen und insgesamt für die letzten fünf Jahre.

und ganz besonders **meinen Eltern** und **meiner Schwester**.